Title
Interacting Effects of Inertia and Gravity on Bubble Dynamics

Author
Rousselet, Yohann Lilian

Publication Date
2014

Peer reviewed|Thesis/dissertation

UNIVERSITY OF CALIFORNIA

Los Angeles

Interacting Effects of Inertia and Gravity on Bubble Dynamics

A dissertation submitted in partial satisfaction of the

requirements for the degree Doctor of Philosophy

in Mechanical Engineering

by

Yohann Lilian Rousselet

2014

ABSTRACT OF THE DISSERTATION

Interacting Effects of Inertia and Gravity on Bubble Dynamics

by

Yohann Lilian Rousselet

Doctor of Philosophy in Mechanical Engineering

University of California, Los Angeles, 2014

Professor Vijay K. Dhir, Chair

Knowledge of the physical mechanisms governing bubble dynamics and two-phase heat transfer is critical in order to accurately predict and scale the performance of two-phase systems, most importantly in low-g environments. To better understand flow boiling, especially under microgravity conditions, the dynamics of single and multiple bubbles under different levels of bulk liquid velocity, surface orientation, contact angle, and substrate materials are studied in this work. Microfabricated cavities at the center of a flat heating surface are used to generate bubbles. Silicon and aluminum are used as substrate materials, with contact angles of 56^o and 19^o, respectively, with water as test liquid. The investigated bulk liquid velocities ranged from 0 m/s to 0.25 m/s, while surface orientation varies from horizontal to vertical, through 30^o, 45^o and 60^o, and cavity spacing from 0.4 mm to 1.2 mm, in upflow conditions. Bulk liquid temperature was set

close to saturation temperature, with bulk liquid subcooling less than 1 ^{o}C, and wall superheat was maintained between 5.0 ^{o}C and 6.0 ^{o}C.

Based on the experimental data, a simple force balance model was developed, and is used to develop a model to predict bubble lift off. These forces are the lift force (F_l), the buoyancy force (F_b), the surface tension force (F_s), the contact pressure force (F_{cp}), and the inertia of both the vapor and the liquid displaced by the growing bubble. It is showed that at the instant when bubble lift off is initiated, the sum of forces acting on the bubble is equal to zero (and then becomes positive in the direction normal to the heater). This force balance is used to develop an expression for bubble lift off diameter. It also is found that for single and merged bubbles, when lift off occurs, buoyancy and lift forces are the only forces acting on the bubble, regardless of orientation, contact angle and flow velocity, and that for all cases, the ratio $(F_b + F_l) / A_l$ is constant and equal to 2.25 N/m^2, where A_l is the bubble surface area at lift off.

The dissertation of Yohann Lilian Rousselet is approved.

Adrienne G. Lavine

Harold G. Monbouquette

Laurent G. Pilon

Vijay K. Dhir, Committee Chair

University of California, Los Angeles

2014

TABLE OF CONTENTS

LIST OF FIGURES

LIST OF TABLES

NOMENCLATURE

A	area
C_d	drag coefficient
C_l	lift coefficient
C_{vm}	virtual mass coefficient
D	diameter
f	bubble release frequency
F	force
g	gravitational acceleration
h	local heat transfer coefficient
h_{fg}	latent heat of vaporization
Ja	Jakob number
k	thermal conductivity
l_o	characteristic length scale
Nu	Nusselt number
P	pressure
Pr	Prandtl number
q	heat flux
r	radius
Ra	Rayleigh number
Re	Reynolds number
Re_b	bubble Reynolds number

t	time
t^*	reduced time
S	viscous shear stress
T	temperature
U_{bulk}	bulk flow velocity
$U(y)$	local flow velocity
u^*	friction velocity
U^*	scaling velocity
v	velocity
V	volume
x	axial distance along heater surface
x_{cav}	distance between cavities
x_l	sliding distance
y	normal distance to heater surface
W	weight

Greek Symbols

α	thermal diffusivity
β	dynamic contact angle or thermal expansion coefficient
γ	shear rate
δ_t	hydrodynamic boundary layer thickness
δ_t	thermal boundary layer thickness
θ	static contact angle

ρ	density
σ	surface tension
φ	heater inclination
ν	kinematic viscosity

Subscripts and Superscripts

c	curvature
d	departure, downstream or drag
e	earth normal gravity
h	hydraulic or heater
l	lift off or liquid
s	sliding or static
sat	saturation
sub	subcooled
v	vapor
w	wall
x	direction parallel to the heater surface
y	direction normal to the heater surface

ACKNOWLEDGEMENTS

I would like to thank Professor Vijay k. Dhir for giving me the opportunity to work on this project, and for his guidance and support throughout my tenure in the Boiling Heat Transfer Laboratory, well as the members of my committee. I would also like to thank Dr. Gopinath R. Warrier for his insight and feedback, as well as for his invaluable technical support in the laboratory.

I would like to express my gratitude to Dr. Sathish Manickam, whose help and advice allowed me to adapt quickly to a new environment when I joined the Boiling Heat Transfer Laboratory. I would like to give a special thank to Dr. Eduardo Aktinol for the many discussions that we shared, for his constant encouragement, and for our continuing friendship.

I would like to thank my fiancée Laurie, whose unwavering support, constant encouragement and optimism provided me with the necessary motivation and confidence to achieve my goals. I am also forever indebted to my parents, Claudine and Jean Luc, and my sister Sophie, who pushed me to pursue this endeavor, and supported me from across the world.

This work was supported by NASA through the Microgravity Fluid Physics Research Program.

VITA

2007 B.S., Thermal Science and Energy Engineering,
Institut Universitaire de Technologie 1, Université Joseph Fourier, Grenoble, France.

2010 M.S., Energy and Environmental Engineering,
Institut National des Sciences Appliquées, Lyon, France.

2013 M.S., Mechanical Engineering,
University of California, Los Angeles.

Publications

Journal Articles:

Y. Rousselet, V.K. Dhir, "Numerical modeling of a Co-Current Cascading Rotary Dryer," Submitted to Food and Bioproducts Processing (2014)

Y. Rousselet, G.R. Warrier, V.K. Dhir, "Subcooled Pool Film Boiling Heat Transfer from Small Horizontal Cylinders at Near-Critical Pressures," Int. J. Heat Mass Transfer 72 (2014) 531–543.

Y. Rousselet, G.R. Warrier, V.K. Dhir, "Natural Convection from Horizontal Cylinders at Near-Critical Pressures: Part 1 – Experimental Study," J. Heat Transfer 135 (2) (2012) 022501.

G.R. Warrier, **Y. Rousselet**, V.K. Dhir, "Natural Convection from Horizontal Cylinders at Near-Critical Pressures: Part 2 – Numerical Simulations," J. Heat Transfer 135 (2) (2012) 022502.

N. Gondrexon, **Y. Rousselet**, M. Legay, P. Boldo, S. Le Person, A. Bontemps, "Intensification of Heat Transfer Process: Improvement of Shell-and-Tube Heat Exchanger Performances by Means of Ultrasound," Chemical Engineering and Processing: Process Intensification, 49 (9) (2010) 936–942.

Peer-Reviewed Conference Papers:

Y. Rousselet, G.R. Warrier, V.K. Dhir, "An experimental Study of Heat Transfer from Small Horizontal Cylinders at Near-Critical Pressures," ASME/JSME 2011 8th Thermal Engineering Joint Conference, Hawaii, USA (2011).

G.R. Warrier, **Y. Rousselet**, V.K. Dhir, "A numerical Investigation of Heat Transfer from Small Horizontal Cylinders at Near-Critical Pressures," ASME/JSME 2011 8th Thermal Engineering Joint Conference, Hawaii, USA (2011).

N. Gondrexon, **Y. Rousselet**, P. Boldo, A. Bontemps, "Intensification of Heat Transfer Process: Improvement of Shell-and-Tube Heat Exchanger Performances by Means of Ultrasound," 2nd International Congress on Green Process Engineering - 2nd European Process Intensification Conference, Venice, Italy (2009).

Y. Rousselet, N. Gondrexon, P. Boldo, A. Bontemps, "Amélioration du Coefficient d'Échange Global d'un Échangeur par Champ Ultrasonore. Mise en Œuvre dans une Géométrie Faisceau de Tubes/Calandre," Dixième Congrès de la Société Française de Thermique, Toulouse, France (2008).

Y. Rousselet, N. Gondrexon, P. Boldo, A. Bontemps, "Enhancement of Heat Transfer Coefficient by Ultrasound: Design and Performances of a New Type of Heat Exchanger," Abstract Book, 11th Meeting of the European Society of Sonochemistry, La Grande Motte, France (2008).

Chapter 1
Introduction

The high heat removal rates encountered during the nucleate boiling process makes it a desirable mode of heat removal for several industrial applications involving high heat fluxes. Even after more than fifty years of extensive research, nucleate boiling remains an extremely active area of research. In spite of the fact that numerous studies have focused on forced convection nucleate boiling, our understanding of the fundamentals of the processes involved is still incomplete. One of the key objectives of the research on forced convection nucleate boiling is the development of mechanistic models to predict the boiling heat transfer under reduced gravity conditions.

Most of the studies available in the literature present empirical and semi-empirical correlations for the forced convection nucleate boiling heat transfer coefficient, usually in situations involving multiple bubbles. These correlations depend on several adjustable parameters, and are usually only valid for very specific geometries and experimental conditions. Moreover, these correlations do not describe or offer any insight on the physics of the boiling phenomena. The development of a mechanistic model would allow for a large range of physical parameters to be accounted for including magnitude of gravity and provide a reliable prediction of forced convection nucleate boiling heat transfer.

Flow nucleate boiling is a complex phenomenon; bubble growth is fast, and interactions between bubbles, as well as surface conditions and geometry, have considerable effect on the boiling process. In order to develop an accurate model for flow

boiling, the complexity of boiling process has to be increased in steps. The first major step in the mechanistic modeling of forced convection nucleate boiling is to study the dynamics of a single bubble. An isolated bubble will allow for an easier study of the main parameters that influence flow boiling heat transfer: wall superheat, liquid subcooling, inclination of the heating surface with respect to the gravity vector, and liquid bulk velocity. For each of these key parameters, several aspects need to be studied: bubble departure and lift-off diameter, bubble growth rate and release frequency, and bubble sliding distance and velocity.

Obtaining extensive data for single and multiple bubbles in forced convection nucleate boiling is a particularly challenging endeavor, but is crucial for the development of a mechanistic model of flow nucleate boiling. This data would also provide the information necessary for the validation of analytical models and numerical simulations.

1.1 Background

1.1.1 Bubble nucleation

From the early study of liquid and vapor entrapment by Bankoff (1958), to the one by Cornwell (1977), or later Wang and Dhir (1993), it has been generally accepted that on smooth surface, an imperfection or cavity could trap gas when immersed into a liquid. It is commonly acknowledged that gas/vapor entrapment has a major effect on the conditions for the onset on nucleate boiling. The criterion defining the capacity of a cavity to trap gas remains, on the other hand, greatly debated.

Some of the earliest studies on nucleation characteristics in boiling were conducted by Hsu (1962), Bergles and Rohsenow (1964), Sato and Matsumura (1964), and Davis

and Anderson (1966). The nucleation criterion developed by Hsu (1962) was based on the analysis of a truncated spherical bubble located at the mouth of a cavity. The assumption was made that in order for the bubble to grow, the minimum temperature surrounding the embryo, the temperature at the top of the bubble, should at least be equal to the saturation temperature of the vapor inside the bubble. Hsu (1962) also postulated that the pressure inside the bubble has to be greater than that of the surrounding liquid, a direct consequence of the curvature of the vapor-liquid interface. The criterion proposed by Hsu (1962) provides a range of cavity radii nucleating for a specific wall superheat, and is given as

$$\left\{r_{c,\min}, r_{c,\max}\right\} = \frac{\delta_t}{4}\left(\frac{T_w}{T_w + T_{sub}}\right)\left[1 \pm \sqrt{1 - \frac{12.8\sigma T_{sat}\left(P_l\right)\left(T_w + T_{sub}\right)}{\rho_v h_{fg} \delta_t T_w^{\,2}}}\right] \tag{1.1}$$

This criterion was modified by Bergles and Rohsenow (1964) to account for flow, using a tangency criterion for the determination of the minimum wall superheat required for nucleation, and forced convection data for the calculation of the thermal boundary layer thickness. Their criterion is identical to the one developed in a separate study by Sato and Matsumura (1964)

$$\left\{r_{c,\min}, r_{c,\max}\right\} = \frac{\delta_t}{2}\left(\frac{T_w}{T_w + T_{sub}}\right)\left[1 \pm \sqrt{1 - \frac{8\sigma T_{sat}\left(P_l\right)\left(T_w + T_{sub}\right)}{\rho_v h_{fg} \delta_t T_w^{\,2}}}\right] \tag{1.2}$$

with the liquid saturation temperature calculated at the top of a spherical bubble. Their criterion showed good agreement with experimental data for flow boiling on a vertical upflow heater. More recently, Kandlikar *et al.* (1997) showed that Bergles and Rohsenow's model (1964) provided a satisfactory prediction of the minimum wall superheat required for nucleation.

Davis and Anderson (1966) defined the problem starting from Hsu's model, but were the first to consider the contact angle (θ) as a variable. There analysis resulted in the definition of the following criterion for the range of active cavities

$$\left\{r_{c,\min}, r_{c,\max}\right\} = \frac{\delta_t \sin(\theta)}{2\left(1+\cos(\theta)\right)}\left(\frac{T_w}{T_w + T_{sub}}\right)\left[1 \pm \sqrt{1 - \frac{8\sigma T_{sat}\left(P_l\right)\left(T_w + T_{sub}\right)}{\rho_v h_{fg} \delta_t T_w{}^2}}\right] \tag{1.3}$$

Davis and Anderson (1966) reported accurate predictions of nucleation inception for subcooled flow nucleate boiling.

The effect of cavity size on nucleate boiling incipience was studied by Singh *et al.* (1976) and in a follow up study (Singh *et al*., 1977). It was reported that for a large depth/width ratio, the wall superheat required for bubble nucleation was in agreement with the static equilibrium criterion. On the other hand, for smaller depth/width ratios and lower contact angle fluids, the recorded wall superheats at nucleation were systematically higher than the predicted ones.

Basu *et al.* (2002) carried out subcooled flow nucleate boiling experiments on a vertical copper flat plate and a zircalloy-4 nine-rod bundle, with water as the test fluid. For the vertical plate experiments the static contact angle was varied from 29^o to 88^o by controlling the oxidation of the heater surface. The heat flux and wall superheat required for bubble inception were found to be dependent on flow rate, liquid subcooling, and contact angle. Based on their data, as well as data from the literature for boiling of water, R113, R11 and FC72, on surfaces made from various materials, they developed the following correlation

$$\left(T_w - T_{sat}\right)_{ONB} = \frac{2\sigma T_{sat}}{R_C^* N \rho_v h_{lv}} \tag{1.4}$$

where R_C^* is given as

$$R_C^* = \left(\frac{2\sigma T_{sat} k_l}{h_{lv} q_w \rho_v} \right)_{ONB}^{1/2} \tag{1.5}$$

and N is a correction factor accounting for the effect of the contact angle

$$N = 1 - \exp\left(-\left(\frac{\pi\varphi}{180} \right)^3 - 0.5\left(\frac{\pi\varphi}{180} \right) \right) \tag{1.6}$$

The developed correlation predicting the wall superheat at inception showed good agreement with their experimental data and the data available in the literature.

1.1.2 Bubble growth

Pioneering work on bubble dynamics in pool nucleate boiling was performed by Fritz (1935). Based a rudimentary force balance, including the effects of the buoyancy force (force lifting the bubble from the surface) and the surface tension force (force holding the bubble to the wall), he developed a simple expression for the bubble lift-off diameter, given as

$$D_l = 0.0208\theta \left(\frac{\sigma}{g\left(\rho_l - \rho_v\right)} \right)^{0.5} \tag{1.7}$$

where θ is the contact angle in degrees. A considerable number of experimental and analytical studies following the same model have since been conducted. Numerous studies have focused on bubble dynamics during forced convection nucleate boiling, most of which were conducted for vertical upflow or downflow conditions, as well as for horizontal flow conditions.

One of the earliest studies using high speed photography was conducted by Gunther (1951). The effect of flow velocity and subcooling on bubble growth and collapse were studied. Gunther (1951) reported a decrease in bubble size and growth rate with increase in liquid bulk velocity.

Koumoutsos *et al.* (1968) studied bubble departure on a horizontal copper heater (L = 26 mm, W = 15 mm) at temperatures close to saturation temperature, in an attempt to determine a criterion for bubble departure in forced-convection nucleate boiling. Velocity was varied from 0.0363 m/s to 0.358 m/s, with wall superheat varied from 10^{o}C to 15^{o}C, while maintaining the liquid inlet temperature at 99.3 ^{o}C. Although no sliding was observed at low velocities, sliding was reported for velocities between 0.25 m/s and 0.358 m/s they observed bubbles ellipsoidal about at axis inclined in the direction of flow. They reported the formation of a neck joining the bubble to the surface, shortly before departure. They were able to successfully predict the thickness of the neck based on the hydrodynamic stability theory. They developed a bubble and neck model, based on a force balance, and found out that drag force was much smaller than surface tension and buoyant forces. From their analysis, they obtained a semi-empirical relationship for the bubble radius at lift off (r_l), given as

$$\frac{r_l}{r_{l,pool}} = \left[1 - \varepsilon \frac{\rho_v V_l \nu_l}{\sigma}\right]^{n/2} \tag{1.8}$$

where ε and n are coefficients determined from experimental data, and $r_{l,0}$ is the pool boiling lift off diameter radius, for given fluid. They report a good agreement between the bubble departure diameters obtained from their experiments and the predicted ones using the results of their analytical solution.

Abdelmessih et al. (1972) studied bubble growth and collapse on a stainless steel vertical flat surface (L = 57.75 mm, W = 6.35 mm), in upflow conditions. The test fluid was water maintained at a $2^{o}C$ subcooling, with a liquid bulk velocity ranging from 0.91m/s to 2.3m/s and a wall heat flux ranging from 187.4 kW/m^2 to 460.6 kW/m^2. The top surface of the heater was smoothed and a small depression of 0.178 mm diameter was made with a carboloy needle. Videos were recorded using a 700 frames per second frame rate. A decrease in active nucleation sites, bubble size and life span was observed with increase in liquid bulk velocity, while an increase in heat flux at constant velocity produced the opposite effects. It was reported that velocity had no effect on bubble nucleation frequency, while increase in heat flux resulted in increase in frequency, before reaching a maximum value.

Bubbles dynamics in a vertical cylindrical annular channel in upflow direction were studied by Akiyama and Tachibana (1974). Vapor bubbles were obtained with water flowing at velocities ranging from 0.1 to 5 m/s, with liquid subcooling ranging from $20^{o}C$ to $80^{o}C$ and a wall heat flux of 750 kW/m^2 to 2900 kW/m^2, under atmospheric pressure. They observed that bubble lifetime and maximum diameter changed monotonously with velocity and subcooling, decreasing linearly with the logarithm of the velocity and liquid subcooling.

Cooper, Mori and Stone (1983) conducted forced convection nucleate boiling of n-hexane, at earth normal gravity as well as at 0.4 % of earth normal gravity. This low gravity environment was obtained through the use of a drop table. Governing parameters of bubble dynamics were found to be growth rate, motion in the liquid and buoyancy force. They reported rolling or sliding motion of bubbles, and argued that such motion

caused a rather unpredictable departure from the wall. However, they were able to develop an expression describing the bubble growth rate

$$\frac{\left(dV/dt\right)}{A} \approx \frac{b}{\sqrt{t}} \tag{1.9}$$

where

$$b = Ja\sqrt{\alpha}, \qquad Ja = \frac{\rho_l c_{pl}\left(T_w - T_{sat}\right)}{\rho_v h_{fg}} \tag{1.10}$$

Chung and Bankoff (1990) studied the effect of bubble sliding during highly subcooled nucleate boiling. The aim of their study was to determine whether conduction and convection between the bubbles, or latent heat transport through the bubbles, dominated the heat transfer process. They reported an enhancement of microlayer evaporation under the bubble by a factor of two compared to that of a stationary bubble with a continuous microlayer. They concluded that the latent heat transport mechanism may be dominant at large bulk subcoolings. Assuming a constant bubble radius and a step function lifetime, they developed the following equation for the total heat transfer to a sliding bubble

$$Q_{sliding} = \frac{4\sqrt{2}k_l \Delta T_w \left(D/2\right)^{5/2}}{\sqrt{\pi\alpha V_{bubble}}}\left[\frac{V_{bubble}t_{bubble}}{D}B\left(\frac{5}{4},\frac{1}{2}\right) - \frac{1}{3}B\left(\frac{7}{4},\frac{1}{2}\right)\right] \tag{1.11}$$

where t_{bubble} is the lifetime of the bubble and B the Bessel function.

Klausner *et al.* (1993) studied flow boiling with R-113, for mass flux ranging from 112 to 287 kg/m^{2}s and heat flux ranging from 11.0 to 26.0 kW/m^2. After careful statistical analysis of the results, they attempted a force balance on the departing bubble to predict the mean departure diameter. The majority of the bubbles slid along the heater surface prior to departure. Results showed a strong influence of liquid bulk velocity and

wall superheat on the bubble departure diameter. Increasing velocity led to lower departure diameter and increasing wall superheat led to larger diameters. They noted that at the point of departure, the surface tension force in the flow direction is generally small.

In a follow up study, Klausner and Zeng (1993) focused on nucleation site density. They determined that in addition to established critical parameter that is the cavity radius, a length scale related to thermal boundary layer thickness should be introduced for proper characterization of the nucleation site density. Their paper also included a complete review of the literature focused on bubble dynamics in pool and flow boiling.

Bibeau and Salcudean (1994) studied vertical upflow nucleate boiling in a cylindrical annular test section, using water as test fluid. They varied velocity from 0.08 m/s to 1.2 m/s, inlet pressure from 2 to 3 bars, subcooling from 10^{o}C to 60^{o}C and heat flux between 100 kW/m^2 to 1200 kW/m^2. Based on visual observations, the bubble lifetime was described in two parts: a first phase including the growth and sliding period of the bubble lifetime (with the bubble initially growing during sliding), and a second phase composed of the bubble lift off process. They observed a very fast initial bubble growth rate. After lift off, a rapid collapse of the bubble was reported, due to the liquid subcooling. Decrease in liquid bulk velocity and heat flux systematically led to increase in bubble diameter, bubble lifetime, sliding distance and sliding time.

Zeitoun (1994) studied subcooled flow boiling of water in a vertically mounted annular test section. Using high-speed photographic techniques, Zeitoun (1994) measured bubble detachment diameter, bubble surface area and volume, and was able to correlate the mean bubble diameter as a function of the heat flux, subcooling, and flow velocity. The expression for the mean bubble diameter was given as

$$\frac{D_b}{\sqrt{\sigma/(g\Delta\rho)}} = \frac{0.0683\left(\rho_l/\rho_v\right)^{1.326}}{Re^{0.324}\left[Ja + \dfrac{149.2\left(\rho_l/\rho_v\right)^{1.326}}{Bo^{0.487}\,Re^{1.6}}\right]} \tag{1.12}$$

with Ja as in Eq. (1.10). Zeitoun (1994) observed that bubble size in subcooled nucleate flow boiling was determined by the competition between evaporation at both the heating surface and at liquid-vapor interface at the sides of the bubble and condensation at the liquid-vapor bubble interface at the top of the bubble.

Experiments on bubble detachment from an artificial cavity in a plane wall of a vertical rectangular channel were performed by Van Helden *et al*. (1995). Water and nitrogen were used as test fluids, and various liquid bulk velocities were investigated. Steam bubbles were generated by local heating of an artificial cavity, while nitrogen bubbles of about the same size were introduced in the flowing bulk liquid by injection. They reported differences in lift off behaviors between vapor and nitrogen bubbles. Vapor bubbles were projected into the liquid, while nitrogen bubbles slid parallel to the wall. As reported in earlier studies, their results showed that the bubble detachment radius decreased with increase in bulk liquid velocity. As part of their attempt to model the forces acting on a bubble in the moment preceding lift off, they fitted growth rate a bubble as a function of time to a power function of the form

$$R(t) = R_0 + C_\gamma t^\gamma \tag{1.13}$$

with R_0 a constant of the order of the cavity radius, C_γ the growth constant and γ the growth exponent. These three coefficients were found by applying a least-squares fit to the measured bubble radius. Typical γ values ranged from 1.0 to 1.5.

Nucleation characteristic during forced convection nucleate boiling, as well as bubble growth were investigated by Kandlikar *et al.* (1996), and later in a follow up study (Kandlikar *et al.* (1997)). They conducted experiments for nucleate boiling of water on a 10 mm diameter aluminum rod. They concluded that increase in flow rate, as well as decrease in liquid subcooling, deactivates larger cavities, while increase in wall superheat activates more cavities.

Thorncroft *et al.* (1998) conducted subcooled forced convection boiling experiments of FC 87 on a nichrome heating surface, in a vertical upflow and downflow conditions Mass flux was varied between 190 kg/m^2s and 666 kg/m^2s, subcooling between 1^oC and 5^oC and heat flux ranging from 1.3 kW/m^2 to 14.6 kW/m^2. Bubble dynamics were observed to be very significantly different for upflow and downflow conditions. In upflow, bubbles departing from the nucleation sites stared to slide but in most cases did not lift off. Nucleation site density increased with heat flux. On the other hand, in downflow configuration, bubbles either lifted off directly from the nucleation site, or after sliding, depending on the flow and thermal conditions. Larger heat transfer coefficients were obtained for upflow than downflow, for similar experimental condition. They concluded that the process of bubble sliding led to an enhancement of energy transfer from the heater to the liquid.

Continuing the work done on the effects of vapor bubble sliding on heat transfer, Thorncroft and Klausner (1999) stated that bubble dynamics in forced convection are strongly influenced by bulk flow behavior and bulk flow turbulent heat transport is influenced by bubble dynamics. Instead of using the classical method of combining turbulent forced convection heat transfer to nucleate boiling heat transfer analysis, both

phenomena are not independent and therefore should be analyzed together. They found that that bubble sliding could account for as much as half of the total energy transfer during forced convection nucleate boiling

Maity (2000) studied the dynamics of a single bubble under various levels of bulk liquid velocity, surface orientation, liquid subcooling and wall superheat. A single bubble was generated by activating a designed cavity micromachined on a strip of silicon wafer. The range of bulk liquid velocities investigated was from 0.07 m/s to 0.25 m/s, surface orientations from horizontal to vertical through 30^o, 45^o, 60^o as well as one case of inclined downward facing upflow (135^o), bulk liquid subcooling from 0.2^oC to 5^oC and wall superheat from 4.6^oC to 5.9^oC. Departure and lift off diameters were observed to be closely related to bulk liquid velocity and orientation of the heater surface. Bubble diameter and bubble sliding velocity at lift off were observed to be strongly dependent on bulk liquid velocity and surface orientation.

Situ *et al.* (2004) conducted subcooled forced convection water boiling experiments in a vertical annular channel. Mass flux was varied from 497 kg/m^2s to 570 kg/m^2s, with liquid subcooling ranging from 2.0 ^oC to 6.6 ^oC and a wall heat flux from 54.0 kW/m^2 to 108.0 kW/m^2. High speed videos of the boiling process were recorded at 5000 fps. Their results show an increase in bubble departure frequency with increase in heat flux, in some cases reaching an asymptotic limit around 1000 bubbles/s.

In a follow up study, Situ *et al.* (2005) carried out a force balance analysis of forced convective subcooled flow boiling. Their analysis showed that the forces governing lift off of the bubble are growth force and shear lift force. Based on their analysis, they

developed a dimensionless bubble lift-off diameter as a function of Jacob number and Prandtl number, for vertical surface, given as

$$\left(\frac{u_r D_{lo}}{v_l}\right)\sqrt{C_{sl}} = \frac{4\sqrt{22/3}m^2}{\pi} Ja_e^2 \, Pr_l^{-1} \tag{1.14}$$

where C_{sl} is the shear lift coefficient, u_r is the relative velocity between bubble center of mass and the liquid phase and m is an empirical constant. The effective Jakob number is defined as

$$Ja_e = \frac{\rho_l C_{p,l} S\left(T_w - T_{sat}\right)}{\rho_v h_{fg}} \tag{1.15}$$

with S the suppression factor. Good agreement was found between their model and experimental results.

Donnelly *et al.* (2009) focused on the enhancement of heat transfer due to the sliding motion of a bubble on an inclined heated plate in a quiescent pool of water. Using thermochromic liquid crystals, as well as a high speed camera, they obtained a time varying 2D temperature map of the test surface. They showed that heat transfer was enhanced for two reasons: the bubble acting as a bluff body, and the increased mixing created by the wake generated behind the bubble. The influence of the heater inclination was also studied. A steeper angle led to a higher bubble velocity, which in turns resulted in a greater heat transfer enhancement.

The formation of N-pentane micro-bubbles on a small heater located at the bottom wall of a horizontal channel was investigated by Duhar *et al.* (2009). Experiments were conducted in pool boiling conditions, as well as for velocities ranging from 0.025 to 0.1 m/s. Wall superheat was varied between 7.9 ^{o}C and 20.2 ^{o}C. The bubble growth and detachment in the shear flow were recorded with a high-speed video camera at 2000 fps.

The experimental results were used as a basis for the development of an analytic expression for the bubble radius at lift off for very small bubbles (R < 0.4 mm).

1.1.3 Contact angle

The affinity of a liquid for a solid is referred to as the wettability of a fluid. This characteristic of a fluid is quantified by a parameter called the contact angle, defined as the angle between the liquid-vapor interface and the solid surface. Contact angle depends on the three interfacial tensions. The equilibrium contact angle is experimentally obtained by measuring the contact angle of a static liquid droplet on a flat surface. In the case of a moving droplet, or for a growing (or shrinking) vapor bubble in a liquid, the observed values of the contact angle differ from the equilibrium value. These so-called dynamic values of the contact angle are named advancing and receding contact angles, for growing and shrinking droplets, respectively. The difference between the advancing and receding contact angles is known as contact angle hysteresis.

However, analysis of the dynamic contact angles is complicated by the introduction of forced convection in the case of flow nucleate boiling. Under flow, different contact angles are observed at the upstream and downstream fronts of the bubble. A reasonable hypothesis is that the angles at the upstream and downstream fronts of the bubble are comprised between the values of the advancing and receding contact angles. It is shown in the literature that contact angle affects nucleation, bubble departure and lift off diameters, and bubble generation frequency. Although upstream and downstream contact angles are crucial parameters for any mechanistic model of flow boiling, there are very few systematic studies of this key parameter in the literature.

Al-Hayes and Winterton (1981) conducted an extensive series of measurements of gas bubble diameters on detachment into flowing liquid, using water, water with surface active agent, and ethylene glycol as test fluids. They investigated contact angles ranging from 22^o to 90^o. Based on their results, they developed a novel approach to calculate surface tension force using different contact angles at the upstream and downstream fronts of the bubble. Upstream and downstream contact angles for a departing bubble were not measured; as a result, advancing and receding contact angles of a liquid droplet were used in the development of their model.

Klausner *et al.* (1993) studied vapor bubble departure on a 457 mm long horizontal nichrome heater, using R113 as test fluid. While the investigated experimental conditions were varied significantly, with velocity as high as 1 m/s and wall superheat ranging from 10^oC to 21^oC, they reported average upstream and downstream contact angles for a typical bubble to be around 45^o and 36^o, respectively. The uncertainty in their measurement of contact angle was about ± 10º.

Bibeau and Salcudean (1994) studied bubble ebullition in vertical upflow in a cylindrical annular test section. They used water as test fluid, for velocities ranging from 0.08 m/s to 1.2 m/s, inlet pressure of 2 to 3 bars, subcooling of 10^oC to 60^oC and a heat flux between 100 kW/m^2 to 1200 kW/m^2. On average, they observed that upstream contact angle increased from 43º to 53º and downstream contact angle grew from 40º to 44º, then decreased a when the bubble elongated in normal direction before lift off. In this study, upstream and downstream contact angles were inaccurately referred to as advancing and receding contact angle. It has to be noted that they reported difficulties to obtain accurate measurements of contact angles, due to the reflection of the bubble on the

heater surface and the light distortion due to the temperature gradients near the heated wall.

As in Bibeau and Salcudean's (1994) study, Van Helden et al. (1995) inaccurately referred to upstream and downstream contact angles as advancing and receding contact angles, respectively. They conducted an experimental study of bubble detachment from a plane wall in vertical upflow, using saturated water, for velocities ranging from 0.16 m/s to 0.85 m/s. They also studied the injection of nitrogen bubbles into the same test section. They reported that in most cases, upstream contact angle was larger than downstream contact angle. The upstream contact angle was mostly constant or increased slightly, while the downstream contact angle decreased with increase in flow velocity. On the other hand, they noted that for nitrogen bubbles, both upstream contact angle and downstream contact angle decrease for increasing bubble diameter.

A combined experimental and analytical study of vapor bubbles in subcooled water was conducted by Kandlikar and Stumm (1995). Their boiling surface consisted of a flat surface of a 10 mm diameter copper heater. Although they used a polished heater with two artificial cavities, nucleation occurred at various locations on the heater surface. They suggested the use of upstream and downstream instead of advancing and receding to characterize the dynamic contact angles formed at both edges of the bubble. They observed that upstream contact angle was consistently greater than downstream contact angle at all flow velocities, the difference increasing at first with velocity, and later decreasing. A control volume approach was introduced to quantify the forces acting on a departing bubble. In their analysis, splitting the bubble into two separate control volumes,

front and rear, allowed them to use different contact angle for each control volume (upstream and downstream), which allowed them to account for bubble distortion.

In a similar study, Qiu and Van der Geld (1997) observed that upstream contact angle is higher than downstream contact angle. In their study, nitrogen bubbles were injected at the side of a heater.

Jia and Dhir (2004) studied the dynamics of contact angle during growth and liftoff of single bubbles in forced convection nucleate boiling, with an experimental setup similar to the one used by Maity (2000) . The effects of orientation as well as liquid bulk velocity on contact angle were investigated. For a horizontal surface, the difference between upstream and downstream contact angles increased with time for low flow velocity, while it remained constant for higher flow velocity. For a vertical surface, regardless of flow velocity, the difference between upstream and downstream contact angles increased with time at first, and decreased to almost zero for the rest of the bubble lifetime.

1.1.4 Effect of gravity

Our capacity to design and operate two-phase systems in reduced gravity environments is currently very limited. This is primarily due to the lack of understanding of how the physical processes scale with respect to the level of gravity. The role of buoyancy can only be investigated in variable gravity conditions. Available data is limited, as very few experiments have been conducted in similar conditions, must of which very focused on pool nucleate boiling.

Kirk *et al.* (1995) conducted subcooled forced convection nucleate boiling experiments with R-113 using both thin film semi-transparent gold on quartz and gold coated cooper substrate flat heaters at varying orientations. Subcooling was varied from 2.2 ^{o}C to 11.1 ^{o}C, four bulk velocities from 0.041 m/s to 0.324 m/s were studied, for various orientations spanning 360^{o} and three levels of wall superheat. They commented that a decrease in heat transfer occurred when normal component of buoyant force is increased. When this component becomes negative, heat transfer is enhanced only at low heat flux, and only if the liquid bulk velocity is large enough to sweep away the bubbles. Also, the effect of velocity is shown to be dependent on orientation. A limiting velocity exists beyond which the orientation and hence gravity can be completely ignored.

Ma and Chung (2001) conducted single bubble experiments at terrestrial gravity and microgravity, using FC72 as test fluid. Microgravity conditions ($g = 10^{-4}g_e$) were obtained using a 2.1 s drop tower. Their heater consisted in a thin gold film. Bubble nucleation, growth, and departure in microgravity for various experimental conditions were regarded using a high speed camera. From the analysis of the experimental data, they obtained the following expression for the transient bubble diameter during growth

$$\frac{D}{l_o} = c_b \,\mathrm{Re}^{-1/3}\left(\frac{q_w}{l_o \rho_l h_{fg}} t\right)^{1/3} \tag{1.16}$$

where l_o is the capillary length defined as $lo = \sqrt{\sigma / g\left(\rho_l - \rho_v\right)}$. They observed that at high flow rate, the bubble generation frequency, and bubble shape tend to be similar with those in normal gravity.

The behavior of single vapor bubbles on a wall sheared by a two-dimensional horizontal flow in a micro-gravity environment was investigated by Yoshikawa and Colin

(2010). Experiments were performed using with a subcooled HFE-7000 at a low pressure (between 1 bar and 2 bars) as a test fluid. Single vapor bubbles were generated at the mouth of a 50 μm diameter cavity artificially created on a gold layer sputtered on a glass substrate. Results from experiment in a microgravity environment (realized by parabolic flights of an aircraft, $g = 10^{-2}\ g_e$) were compared to data obtained at earth normal gravity, for vertical and horizontal configurations. Longer growth times and larger lift off diameters were reported for the experiments conducted at low gravity. They observed sliding of the bubbles at earth normal gravity, while no sliding was reported at low gravity ($g = 10^{-2}\ g_e$). Similarly to the results reported by Ma and Chung (2001), they observed a bubble growth rate of $D \propto t^{1/3}$. They showed that their calculations of the forces acting on the bubbles resulted in a break of the force balance at the bubble departure, validating the mechanistic approach they employed. Van der Geld *et al.* (2012) presented a follow up study to that of Yoshikawa and Colin (2010), and extended their analysis of the forces acting on the bubble in microgravity and terrestrial conditions, and found satisfactory agreement between their predictions and their experimental results.

1.1.5 Force balance

As shown by the extensive literature available regarding boiling heat transfer, fundamental knowledge of the mechanisms governing bubble growth and detachment from heated surfaces is essential for our understanding of this physical process. The effects of bubble growth, sliding and lift off on heat transfer are considerable; hence there is a need for an accurate prediction of bubble diameter as a function of time. In order to develop a mechanistic model of bubble growth in forced convection nucleate boiling,

various authors have included an energy balance on vapor bubbles in making a force balance on bubbles.

Most of these studies have focused on three major forces acting on a bubble, namely the buoyancy, surface tension and inertia/drag forces. It is not uncommon, though, for other forces to be included as well. The forces acting on a bubble can be classified in two categories. Firstly, the static forces, namely buoyancy, surface tension, hydrodynamic pressure force and contact pressure forces, are present even in the absence of fluid motion around the bubble. The other three forces, known as dynamic forces (they result from motion of the fluid around the bubble), are the added mass force (composed of the bubble growth force, the drag force and the lift force.

The forces acting on a bubble during flow nucleate boiling on a horizontal surface are represented in Fig. 1.1. F_b is the buoyancy force, F_s the surface tension force, F_h the hydrodynamic pressure force, F_{cp} the contact pressure force, F_{am} the added mass force, F_d the drag force, and F_l the lift force. β_u and β_d represent upstream and downstream contact angle, respectively, and ϕ the polar angle around the bubble. The bubble inclination angle φ, represented by a dotted line across the bubble length, is not labeled in Fig. 1. The forces acting on the bubble projected in the x and y directions are

$$\sum F_x = F_{b,x} + F_{s,x} + F_{d,x} + F_{l,x} + F_{am,x} \tag{1.17}$$

$$\sum F_y = F_{b,y} + F_{h,y} + F_{cp,y} + F_{s,y} + F_{d,y} + F_{l,y} + F_{am,y} \tag{1.18}$$

Various authors have attempted to predict bubble growth, including bubble departure and lift off. Major studies were conducted by Al-Hayes and Winterton (1981), Auton *et al*. (1988), Klausner *et al.* (1993), Mei and Klausner (1994), Thorncroft *et al*. (2001), and Situ et al. (2005), among others. This large number of studies resulted in a wide variety

of expressions of the forces acting on a bubble. A thorough review of these studies was performed by Montout (2009).

Sliding of the bubble, observed in a large majority of the studies, is caused by an initial break in the static force balance in the direction parallel to the heater wall, while lift off of the bubble is a result of a break in the force balance in the direction normal to the heater wall.

1.2 Objectives

Understanding the physical processes governing vapor bubble growth and lift off on heated surfaces is critical for the modeling of heat transfer during nucleate boiling. Bubble dynamics have a determining influence on crucial parameters like heat transfer coefficient and maximum heat flux. As highlighted in the literature review in the previous section, two types of approaches have been adopted to develop models for the growth of bubbles in forced convection nucleate boiling. The first one is empirical correlations based on experimental data. The disadvantage of these correlations is that they rarely model the relevant physical mechanisms involved, and their application is mostly limited to the conditions for which they were developed. The second approach is the development of mechanistic models to predict bubble growth as well as bubble dynamics. This approach, based on the physical mechanism involved in the boiling process, is expected to be reliable and applicable to a wide variety of conditions.

An accurate model for bubble growth has yet to be developed. Most attempts to model bubble growth have failed for two reasons. Firstly, for most experiments the boiling process occurred from multiple nucleation sites. The interactions between bubbles

affected the bubble growth rate, and departure and lift off diameters. In most cases, when mechanistic modeling of bubble growth was attempted, theoretical analysis of a single bubble was conducted. The obtained analytical expressions failed to accurately model the experimental data, which were obtained for bubbles greatly disturbed by neighboring bubbles. On the other hand, studies involving single bubbles were either incomplete (the effect of one or more key parameters, such as gravity, was overlooked), or encountered the inevitable difficulties related to single bubble flow boiling experiments. The scales involved are extremely small and the process of bubble growth is very fast. As a result, there is hardly any systematic data available in the literature regarding the influence of system parameters (for example, surface wettability, liquid subcooling, wall superheat, flow velocity, gravity, etc.) on the growth and departure of single bubbles during in forced convection nucleate boiling, especially as they relate to interacting effects of gravity and inertia.

This study was designed to address these modeling issues. Two boiling surfaces, one made of silicon and the other made of aluminum, each with micromachined cavities at the center, were used to generate an isolated single vapor bubble, as well as two bubbles aligned along the direction of the flow, for bubble merger experiments. With the use of high speed imaging of the bubble growth process, this study provides detailed data for fundamental parameters such as upstream and downstream contact angles, bubble growth rate, departure and lift off diameters, as well as sliding distance and sliding velocity. This data will be the basis for the development of a mechanistic model for bubble growth under flow conditions, and to validate numerical simulations. The emphasis is put on understanding how bubble growth is affected by gravity level. At earth normal gravity,

the gravity components parallel and normal to the heater surface are changed by varying the inclination of the heater surface. Also, the experimental setup was mounted inside a support rack designed for low gravity flight, in order to conduct reduced gravity experiments during parabolic flight campaigns.

The increased focus on the use of boiling processes in space applications creates an urgent need for a better understanding of the physical mechanisms governing bubble dynamics and two-phase heat transfer in reduced gravity conditions. This knowledge is critical in order to accurately predict and scale the performance of two-phase systems in low-g environments. It is hoped that the findings of this study will help in a better understanding of flow boiling especially under microgravity conditions.

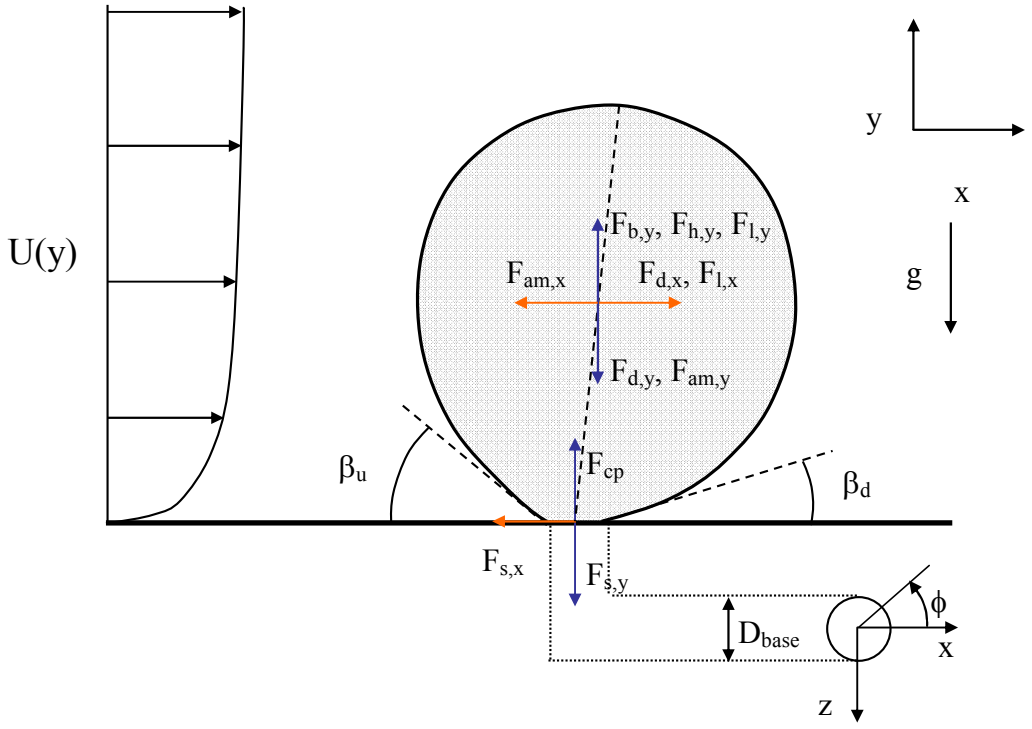

Fig. 1.1 Schematic of forces applied to a growing bubble attached to a heating surface in shear flow.

Chapter 2
Experimental Apparatus and Procedure

The experimental setup is designed to operate in a specific range of experimental conditions, namely:

- Liquid bulk velocity varying from 0 m/s to 0.3 m/s,
- Liquid subcooling varying from 0 ^{o}C to 10 ^{o}C,
- Wall superheat up to 15^{o}C,
- Pressure varying from 1 bar to 2 bar,
- Gravitational orientation adjustable from horizontal to vertical

Also, this experimental setup must comply with the structural design requirements established by NASA to participate in its Reduced Gravity Program.

2.1 Experimental apparatus

2.1.1 Equipment rack

The equipment rack used as structural support for this experimental setup is a Next Generation Horizontal Aircraft Rack (NGHAR100), designed and built by NASA. Front, side and top views of the rack, as well as dimensions in inches, are shown in Fig. 2.1. The overall dimensions of the rack are L = 1.72 m (68 in), W = 0.66 m (26 in), and H = 0.95 m (36 in). This equipment rack is entirely made of Aluminum 6061-T6. The maximum allowable weight (at earth normal gravity) of the entire rack is 340.5 kg (750 lb), including the weight of the empty, which is 46.3 kg (102 lb). The total weight of the experimental setup, including the test fluid, in flight-ready conditions is 204.3 kg (450 lb).

The equipment rack, as well as the entire test equipment (fasteners, individual components, frames, etc), are designed to withstand the following g-loads in "hard" takeoff and landing configurations:

- Forward 9-g's,
- Aft 3-g's,
- Down 6-g's,
- Lateral 2-g's,
- Up 2-g's.

The capability of this rack to withstand these loads was shown while conducting the structural verification of the experimental setup, through stress analysis. A fitting factor of 1.15 was applied to every load, and a factor of safety against ultimate strength (tension and shear) of 2.0 was taken. The equipment rack is designed to be attached to the aircraft floor in four places.

2.1.2 Flow loop

A schematic of the flow loop is shown in Fig. 2.2. The flow loop is designed to provide the test fluid from a reservoir with a capacity of 0.015 m^3. Most of the test fluid used for the experiment is stored in a reservoir (shown in Fig. 2.3 without insulation), and this is also where the fluid is heated up to the required temperature. One 1500 W, 115 V Tempco TSP02245 heater is used, controlled by an Ogden ETR-9200 controller. If cooling of the return water is required, a Lytron C-4120G10 heat exchanger is also controlled by the controller. The temperature measured using a type-J sheath thermocouple (Omega) located at the outlet of the reservoir (labeled T_{res} in Fig. 2.2) is

compared by the controller to the set temperature, and heat of cooling powers are adjusted accordingly.

A Micropump magnetic drive gear pump, power by a Fasco 350 W motor is used to circulate the test fluid through the test section. Rubber pads are installed under the pump to limit vibrations that could disturb the bubble growth in the test section. The flow loop is constituted of a flow control and a flow bypass valve to control the flow rate through the test section. Control of the flow rate is done manually. The liquid flow rate is measured in gallons per minute (gpm, with an accuracy of +/- 0.05 % of the reading) using a turbine flowmeter (Flowmetric FM series), with a maximum capacity of 4 gpm. The flowmeter was calibrated by the manufacturer before it was installed. The flow rate was recorded in gallons per. An Omegalux 1500 W, 115 V in-line preheater is used to adjust the temperature of the test fluid circulating through the test section. There are two ways to control the preheater: manually using a 115 V variac, or automatically through the data acquisition system (DAS), using an average of the temperatures at the outlet of the preheater (T_{pre}) and at the inlet of the test section (T_{in}). The automatic control of the preheater is only used during low gravity experiments, due to its lack of precision. To avoid any hydrodynamic entry length problems, the liquid flows through a 0.355 m (15 in) long square developing section, before entering the square test section (0.02 x 0.02 m^2). The fluid exiting the test section (at temperature T_{out}) flow through a heat exchanger before returning to the reservoir. Type-K thermocouple probes (Omega) of outer diameter 1.52 mm (0.06 in) are used to measure T_{pre}, T_{in} and T_{out}. Apart from the test section, the entire flow loop is insulated to prevent heat losses.

2.1.3 Nitrogen reservoir/Pressure control

As shown in Figs 2.2 and 2.3, the reservoir is divided in two parts: a bottom one, occupied by the test fluid, and a top one occupied by nitrogen. These two parts are separated by a bellows. The purpose of the nitrogen circuit, schematized in Fig 2.2, is to provide control of the pressure inside the test fluid loop. The liquid pressure is measured by a SETRA 205-2 pressure transducer (0 to 2.7 bar, with an accuracy of +/- 0.003 bar). Based on this value, the DAS, through control of the nitrogen inlet and outlet valves, fills/empties the nitrogen reservoir to lower/elevate the bellows, increasing/decreasing the pressure inside the flow loop.

There are two other means of controlling the pressure in the test fluid loop. Firstly, by setting a maximum allowable value on the pressure relief valve. Secondly, by manually opening the valve controlling the venting of the bellows.

2.1.4 Test section

2.1.4.1 Chamber

The test section chamber is designed to accommodate a rectangular flow section (0.02 x 0.02 x 0.3 m^2), heated on the bottom. The test section is equipped of polycarbonate windows on each side to allow visualization of the heater and a perforated (four holes, 8.64 cm apart) Phenolic Garolite (G10) cover plate on the top, equipped with Copper bushings to accommodate traversing type-K thermocouples (D = 0.5 mm, or 0.197 in). These thermocouples are attached to traversing micrometers to measure the thermal profile in the liquid above the test surface. This configuration being too fragile for flight conditions, similar thermocouples are used in a set position instead. The bottom part is

closed by the heater assembly, composed of a heating surface bonded to a G10 base. Figure 2.4(a) shows a schematic of the assembled test section, as well as the main dimensions in inches, and Fig. 2.4(b) shows an exploded view of the test section with an aluminum test surface.

2.1.4.2 Test surfaces

Two types of test surfaces are employed: one made of three rectangular polished <100> silicon wafers, another one made of aluminum. Both materials possess similar advantages in their use as test surfaces: they are relatively easy to machine and polish (required to avoid trapping gas other than in the artificial cavity), current micromachining techniques are more than capable of drilling the microscale cavities required for the experiments, and their thermal properties are well known (refer to Table 1).

Silicon test surface:

The test surface is composed of three rectangular (1.8 cm x 10 cm), 1 mm thick polished <100> silicon wafers. Commercially circular wafers were diced into desired rectangular dimensions at the UCLA Center for High Frequency Laboratory. The center wafer contains a cavity with a diameter of 10 μm and a depth of 100 μm, micromachined using DRIE technique by Lenox Laser.

Stress analysis strain gages (obtained from Vishay Precision Group, Inc), with a resistance of 120 Ohms and various sizes, are used as microheaters to maintain a uniform temperature on the test surface. The layout of these heaters, as well as thermocouples, on the silicon wafers is shown in Fig. 2.5. To ensure proper bonding of the gages on the

backside of the heater, it is carefully prepared using specific products obtained from Vishay Precision Group, Inc. The gages are laid out on the prepared surface, previously coated with M-Bond 610 Adhesive, and cured at high temperature, under important pressure. Copper wires are soldered to the strain gage heater terminals, and connected to the DAS for supply of DC power (through two dbk 2 4-channel output cards), and voltage and current measurement. As seen in Fig. 2.7, the strain gage heaters are divided in eight groups, corresponding to the eight power output of the dbk 2 cards. A small-size, standalone heater is located underneath the cavities (to initiate nucleation), while larger groups of bigger gages are employed far away from the cavities, were coarser temperature control is acceptable. There are two ways to control the power supply. The surface temperature is determined by 14 type-K glass braid thermocouples bonded to the silicon wafers by Omegabond 200 (Omega) at specific locations along the wafers' centerline. There are two ways two control surface temperature, both using the DAS: manually by setting the voltage given to each group, or using PID control build in the program and setting a desired wall temperature. Automated control is required for experiments aboard the low gravity aircraft.

A hollow G10 based is used as support structure for the wafers. The thermal conductivity of G10 is about 0.16 W/mK. The wafers with heaters and thermocouples already installed are bonded to the G10 base using RTV60 high temperature two-part silicone elastomer (Momentive). The RTV60 is evacuated during 10 to 15 minutes prior to the bonding process to remove any entrapped air bubbles. The required curing time for the assembly is 24 hours at room temperature. The bonding process is a delicate one. The thermal conductivity of RTV60 is given as 0.70 W/mK. The fragile lead wires coming

from the strain gage heaters and the thermocouple wires from the back of the wafers have to be pulled through holes at the bottom of the G10 base. Ensuring that the wafers are correctly aligned and flush mounted on the G10 base before curing is the most critical process of the assembly and is particularly difficult. A schematic of the assembly is shown in Fig. 2.6. The dimensions of the top part of the assembly (in contact with the test fluid), are L = 0.31 m (12.2 in) and W = 0.02 m (5.1 in).

Aluminum test surface:

There are motivations for the assembly of an aluminum heater. By using a different surface material, the effect of surface characteristics on bubble growth can be studied. Secondly, it provides an opportunity to improve the test surface design employed for the silicon heater.

As opposed to silicon wafers, aluminum can be shaped is any from desired. Generation of bubbles at the edge of the silicon wafers was observed in previous studies using a similar design (Maity (2000) and Jia and Dhir (2004)). This is due to the fact that these wafers are flush mounted on the G10 base, causing air to be trapped at the interface between the G10 base and the wafers. This entrapped air, combined to the high temperature of the wafers, leads to the formation of extraneous bubbles. While they don't affect the flow field or the bubble growth, they create difficulties in visualizing of the bubbles generated at the artificial cavity. In order to limit generation of such bubbles while using the aluminum test surface, the aluminum plate is designed as a hollowed out block (with 1 mm thick walls), that fits on top of a G10 support structure. The dimensions of the plate are L = 0.307 m (12.1 in), W = 0.019 m (00.75 in), and H = 0.635 m (0.25 in).

The overall dimensions of the assembly are similar to that of the silicon test surface. The final assembly is shown in Fig. 2.6, while the aluminum plate and the G10 are represented separated from each other in Fig. 2.4. As seen in Fig. 2.6 the side walls of the aluminum plate are only partly covered by the G10 base, eliminating bubble nucleation from the edge of the upper surface. The aluminum plate was diamond polished by Nu-Tek Precision Optical Corporation, and a cavity with a diameter of 10 μm and a depth of 100 μm was laser drilled at the center of the top wall by Laserod. A thin layer of 3M Scotch-Weld Epoxy Adhesive 2216 is applied at the junction of the G10 and the aluminum to prevent infiltration of the test fluid inside the G10 base. The gaps at the front and back of the plate are filled with the same product, to avoid any disturbance of the flow. The aluminum plate already equipped with heaters and thermocouples is bonded to the G10 base using 3M Scotchcast Electrical Resin 251 (previously evacuated during 10 to 15 minutes). The bonding process is completed in three layers to avoid putting too much strain on the wires during solidification of the resin. The curing time for each layer is 15 to 20 hours at 75 ^{o}C. The thermal conductivity of the resin is about 0.35 W/mK.

The layout of the strain gage heaters, as well as thermocouples, the aluminum plate is shown in Fig. 2.7. The installation process of strain gages on aluminum is the same to that on silicon. Sixteen type-K glass braid thermocouples are along the plate's centerline to measure the wall temperature. In order to obtain a good 2D temperature profile inside the support structure, and estimate the loses through the bottom of the assembly, nine type-K glass braid thermocouples are embedded in the Electrical Resin 251 layer, at

known locations along the centerline of the G10 base, at various depth levels. The locations of these thermocouples are shown in Fig. 2.8.

2.1.5 Data acquisition system/Camera

The DAS is a daqbook 2000 (from Measurement Computing Corporation). It is composed of numerous input and output modules embedded in 2 daqbook 200 modules and one dbk 82 analog expansion chassis, controlling and gathering data from the experiment. The gathered data is sent to a DELL laptop computer where it is analyzed, recorded and displayed in an appropriate manner, i.e. graphs and charts, inside a Dasylab data acquisition software window. Dasylab is a software program developed by Measurement Computing Corporation. Types of gathered data are acceleration (not relevant when at earth normal gravity), heater voltage and current, temperature readings from the various thermocouples, pressure and flow rate. Two dbk 2 4-channel D/A voltage-output cards (from Measurement Computing Corporation) are used to supply power to the heaters. The voltage output of the dbk 2 cards is only 0-10 V, so a custom made amplifier, with a gain of 4, is used to amplify the voltage. The voltage supplied to each heater group is limited to 25 V, to avoid destruction of the strain gages.

The high speed camera utilized to visualize bubble growth is a Fastech Troubleshooter HR. The video recording software used is MIDAS 4.0 (from Xcitex). The relevant frame rates and images resolutions supported by the camera are: 1000 fps and 640 x 480, and 2000 fps and 1280 x 256.

2.1.6 Test fluids

The selected test fluids are de-ionized (DI) water and FC72 (also known as PF5060). The saturation temperatures of DI water and FC72 (at P = 101.325 kPa), are 100 ^{o}C and 56 ^{o}C, respectively. Some thermophysical properties for DI water and FC72 are given in Table 2 for saturated conditions at one atmosphere. The latent heat of vaporization, as well as surface tension, is one order of magnitude greater for DI water than for FC72. Also, FC72 is a very well-wetting fluid with most surfaces, while wettability characteristics for water sensitive to both surface material and surface finish.

2.2 Experimental procedure and data reduction

2.2.1 Thermocouple calibration

Before thermocouples are installed on the experimental setup, or bonded to the test surfaces, they are calibrated using a dry block thermocouple calibrator (Omega). The DAS temperature readings are adjusted using the results of the calibration.

2.2.2 Estimation of static contact angles

The static contact angles, for each fluid/material configuration, are determined before the experiment. Contact angle measurements require a clean and dry surface, as well as a properly degassed test fluid (to limit the effect of dissolved gas on contact angle). The test surfaces are cleaned using acetone or isopropyl alcohol, and blow dried using compressed air to remove any dust or cleaning agent remaining. Cotton swabs are used on the silicon wafers during the cleaning process, but not on the aluminum plate.

Aluminum is much softer than silicon; hence any small particle present on the surface could scratch it.

A small syringe is used to place drops of degassed test fluid on the clean surface. Digital pictures of the droplets are taken using the high speed camera, and analyzed using ImageJ, an open source image processing and analysis software, to estimate the contact angle. Measurements are repeated in order to reduce measurement uncertainty.

Picture of DI water and FC72 droplets on silicon and aluminum surfaces are shown in Fig. 2.9. Typical static contain angle values are: 56^{o} for DI water on silicon, 19^{o} for DI water on aluminum, and 7^{o} for FC72 on silicon and aluminum.

2.2.3 Procedure

To properly degas the test fluid, the reservoir heater is turned on and the test fluid is boiled for about an hour, without flow, at the start of every experiment. Deaeration of the test liquid is completed by turning on the pump and running the fluid (at a moderate velocity of about 0.1 m/s) through the flow loop for another hour. After proper degassing, the velocity is set using the bypass and flow control valves. The liquid is then heated up (or cooled down) to reach the desired subcooling, using the preheater to maintain subcooling between ±0.5°C of the set value.

Once the desired flow conditions are obtained, the wall superheat is set on the DAS and the strain gages are powered according. Nucleation of the cavities is usually achieved by providing more power to the single heater located underneath the cavities. As soon as bubbles are obtained the power is decreased to lower wall superheat to the required value. The wall temperature is kept at the desired value by means of the DAS PID controller.

As soon as steady state conditions are reached, the acceleration, heater voltage and current, temperature readings from the various thermocouples, pressure and flow rate da ta acquired through the DAS are recorded. High speed movies of the bubbles are simultaneously obtained by the high speed camera (at 1000 fps or 2000 fps, depending on the heater type) and saved.

For the experiments where the test section is equipped of traversing micro-thermocouples, the thermocouples are moved in towards the heater surface until they just almost the surface and then moved out in steps of 0.025 mm (close to the surface, then larger one) until they measure the bulk liquid temperature. Similarly, these temperatures are monitored and recorded using the DAS.

Once an experimental run is completed, wall superheat, liquid subcooling and velocity are adjusted to the next conditions desired.

2.2.4 Data reduction

The bubbles in each nucleation cycle or analyzed using ImageJ. The picture of an object of known dimensions is used as scaling reference. The various parameters measured for each bubble are shown in Fig. 2.10. Bubble dimensions (height, width, surface, base diameter, as well as sliding distance) are estimated by measuring the number of pixels and then it to physical dimensions. The bubble is assumed to be an inclined ellipsoid; hence the bubble equivalent diameter is taken as the diameter of the sphere whose volume is equal to this ellipsoid, given as

$$D = \sqrt[3]{D_x^2 D_y} \tag{2.1}$$

where D_x is the bubble diameter in the x direction and D_y is the bubble diameter in the y direction. The surface A of the bubble can also be used to estimate the equivalent diameter of the bubble, as $D = (4A/\pi)^{0.5}$. An ImageJ built-in function is used to determine the bubble area, but it requires a level of contrast and picture difficult to attain on every run. The equivalent diameter is used to calculate the bubble growth rate.

Bubble velocity at time t_2 is calculated as

$$U_{bubble}\Big|_{t_2} = \frac{x_l\Big|_{t_2} - x_l\Big|_{t_1}}{t_2 - t_1} \tag{2.2}$$

with x_l the sliding distance of the bubble from the nucleation site and t the time. The upstream and downstream contact angles are measured using a built-in protractor functionality in ImageJ.

2.2.5 Uncertainty analysis

The accuracy of the bulk temperature and wall temperature measurements is ± 0.1 °C, while the accuracy of the pressure measurement is ± 0.3 kPa. The relative uncertainty of the volumetric flow rate measurement is given as +/- 0.05 % after calibration by the manufacturer. The dimensions of the test section dimensions (notably height and width) are measured using calipers with an accuracy of ± 0.1 mm. The uncertainty in micrometer displacement, while obtaining the thermal profile in the liquid, is 0.025 mm. The uncertainty in temporal measurements is given by the frame rate of the camera software (± 1 ms at 1000 fps and ± 0.5 ms at 2000 fps). The uncertainty in spatial measurements (bubble diameter, base diameter and sliding distance) is taken as 4 pixels, a reasonable estimate given the resolution and focus quality of the pictures. This uncertainty depends on the level of zoom of the camera. A close up view will result in a

smaller uncertainty than a view from farther away. The uncertainty in sliding velocity is calculated from spatial as well as temporal uncertainties. The uncertainty on contact angle is taken as ± 5^o for bubbles smaller than 10 pixels high, and ± 2^o for larger ones. The level of zoom and quality of focus is also a determining factor for the accuracy of these measurements.

The uncertainty in the experimental data is calculated using the method proposed by Kline and McClintock (1953). The uncertainty in bulk liquid velocity is calculated as

$$U_{bulk} = \frac{\dot{V}}{l_1 l_2} \rightarrow \frac{\delta U_{bulk}}{U_{bulk}} = \sqrt{\left(\frac{\delta \dot{V}}{\dot{V}}\right)^2 + \left(\frac{\delta l_1}{l_1}\right)^2 + \left(\frac{\delta l_2}{l_2}\right)^2} \tag{2.3}$$

where $\dot{V}$ is the volumetric flow rate, and l_1 and l_2 are cross sectional dimension of the test section. The uncertainty on the flow velocity measurement is less than 1 %. The uncertainty in bubble diameter (calculated using Eq. (2.1)) is given as

$$\frac{\delta D}{D} = \sqrt{\left(\frac{2D}{3D_x}\delta D_x\right)^2 + \left(\frac{D}{3D_y}\delta D_y\right)^2} \tag{2.4}$$

Finally, the uncertainty in sliding velocity (determined using Eq.(2.2)) is calculated as

$$\frac{\delta U_{bubble}\big|_{t_2}}{U_{bubble}\big|_{t_2}} = \sqrt{\left(\frac{U_{bubble}\big|_{t_2}}{\left(x_l\big|_{t_2} - x_l\big|_{t_1}\right)}\delta\left(x_l\big|_{t_2} - x_l\big|_{t_1}\right)\right)^2 + \left(\frac{U_{bubble}\big|_{t_2}}{\left(t_2 - t_1\right)}\delta\left(t_2 - t_1\right)\right)^2} \tag{2.5}$$

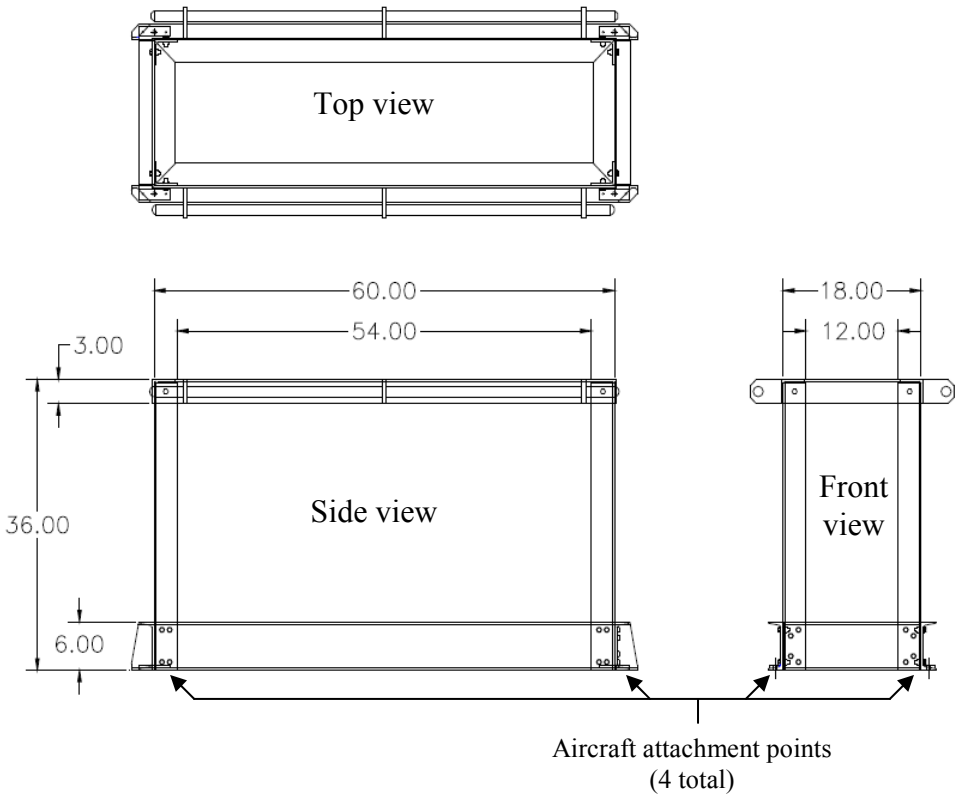

Fig. 2.1 Schematic of the equipment rack (all dimensions in inches).

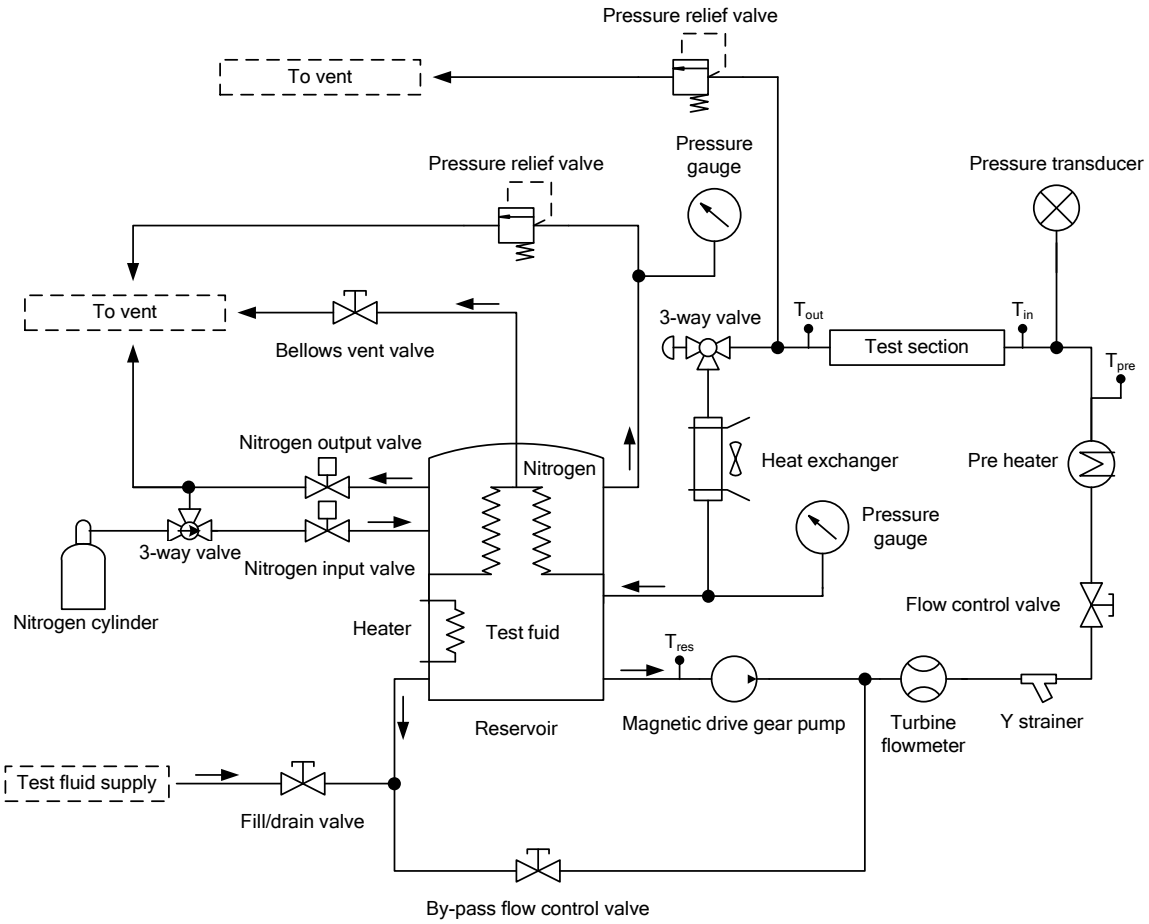

Fig. 2.2 Schematic of the flow loop (arrows indicate flow direction).

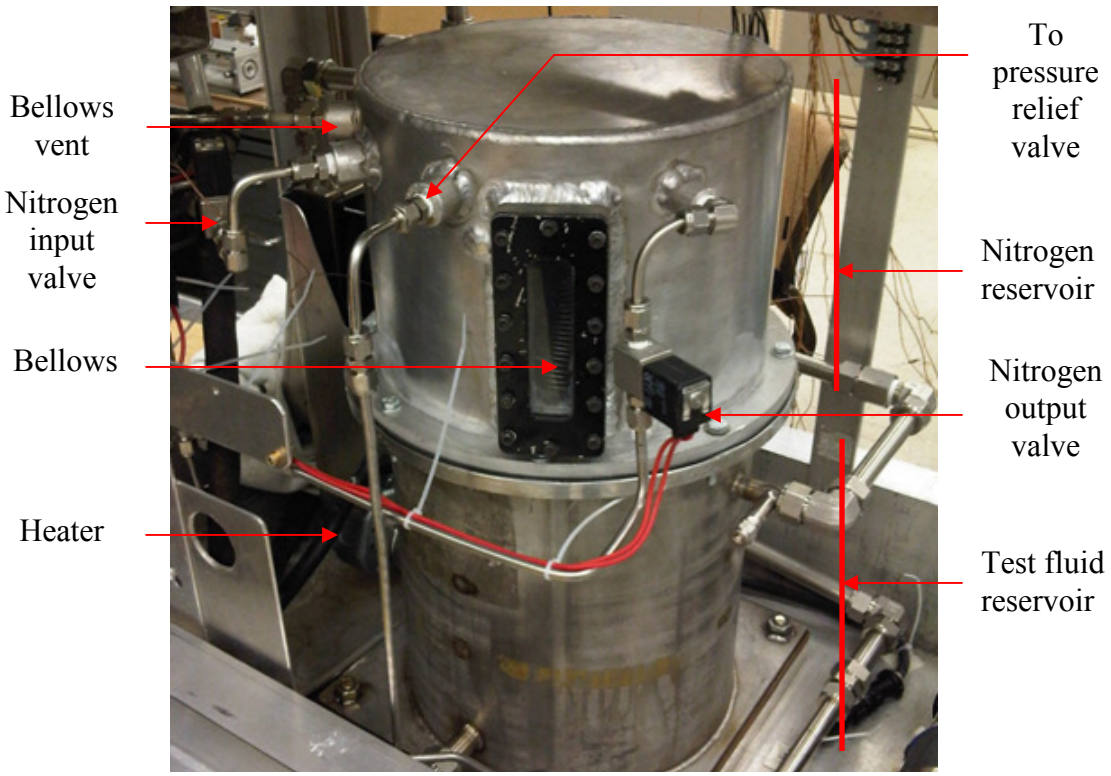

Fig. 2.3 Picture of the reservoir.

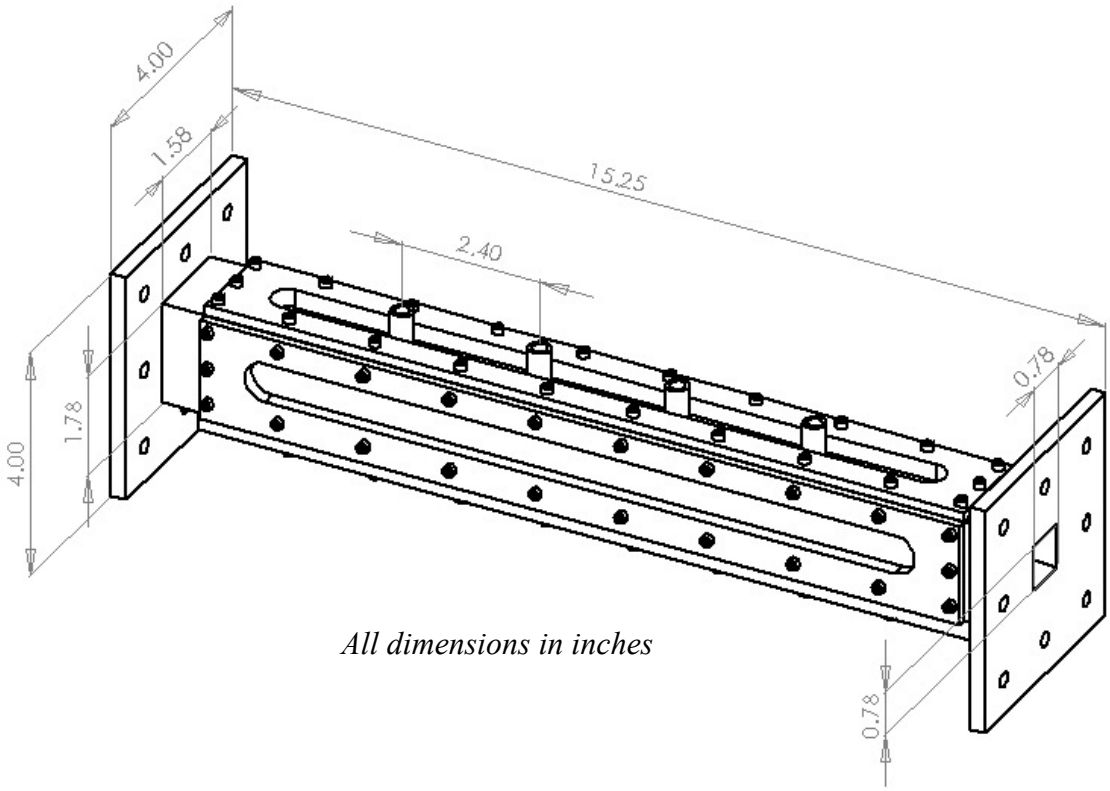

(a)

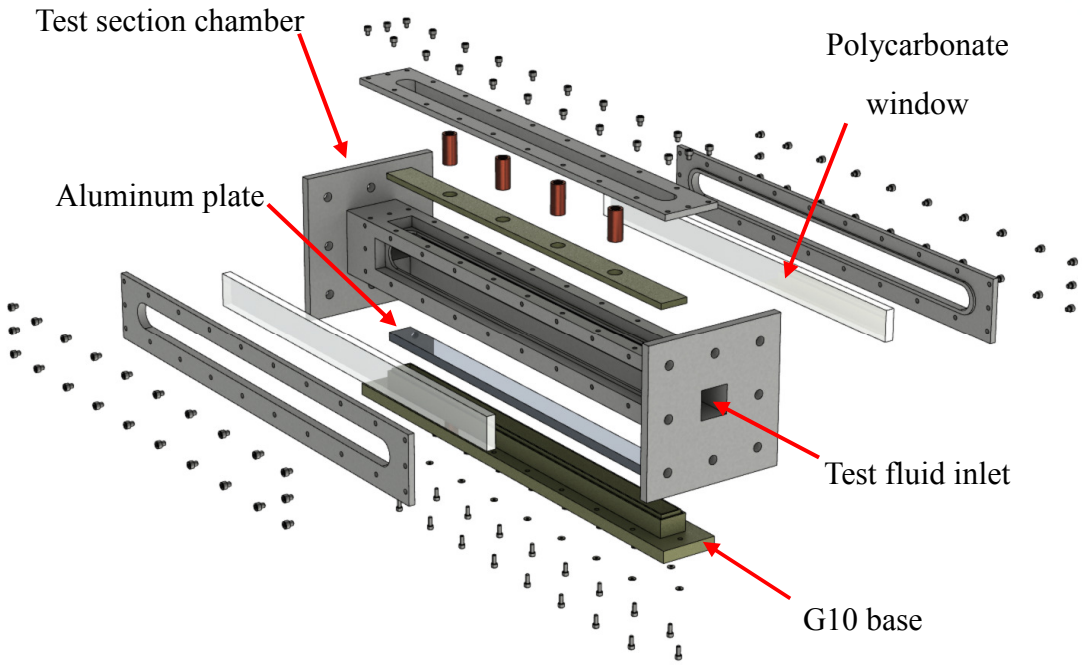

(b)

Fig. 2.4 (a) Schematic of the test section, and (b) exploded view of the test section (with aluminum test surface).

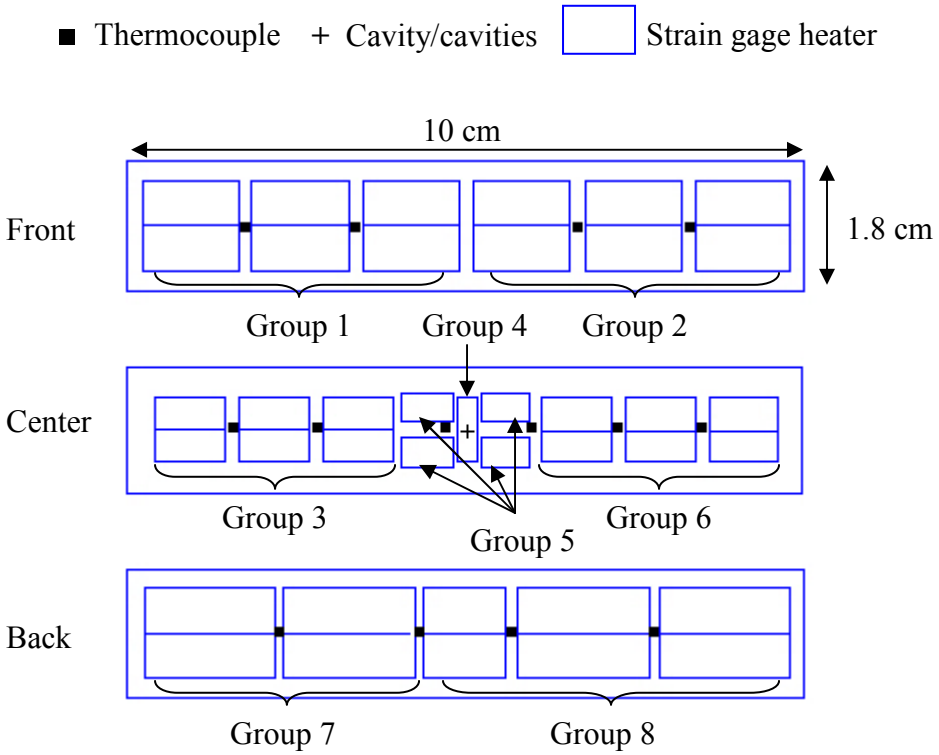

Fig. 2.5 Layout of the cavity / cavities, heaters and thermocouples on the silicon wafers.

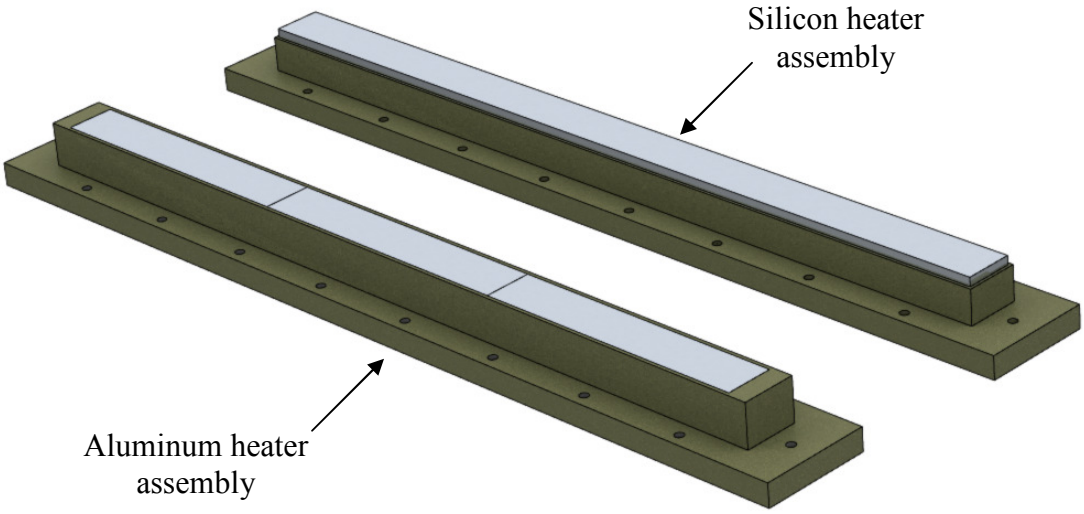

Fig. 2.6 Schematic of the heater assemblies.

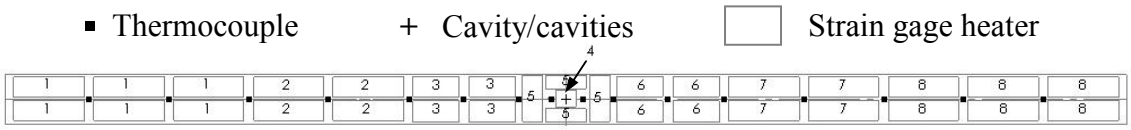

Strain gages numbers correspond to each heating group

Fig. 2.7 Layout of the cavity, heaters, and thermocouples on the aluminum plate.

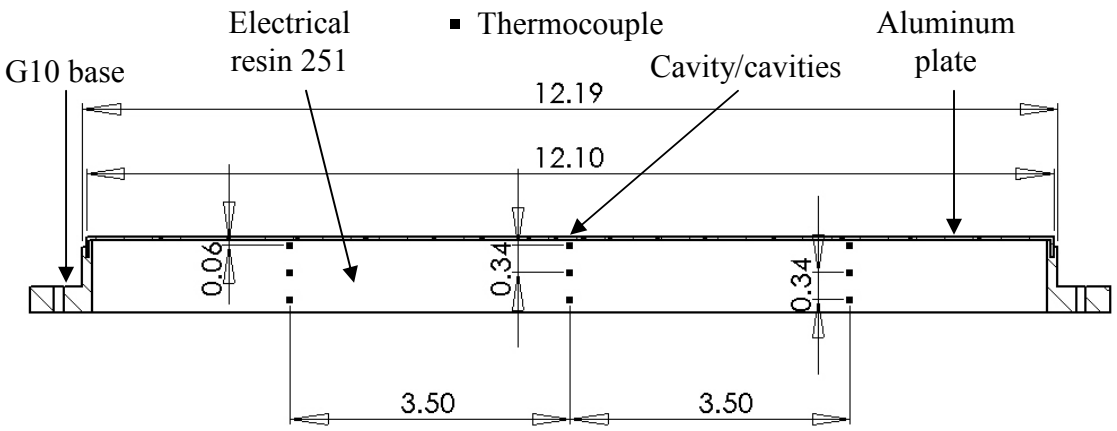

All dimensions in inches

Fig. 2.8 Aluminum test surface assembly and placement of thermocouples at various axial locations.

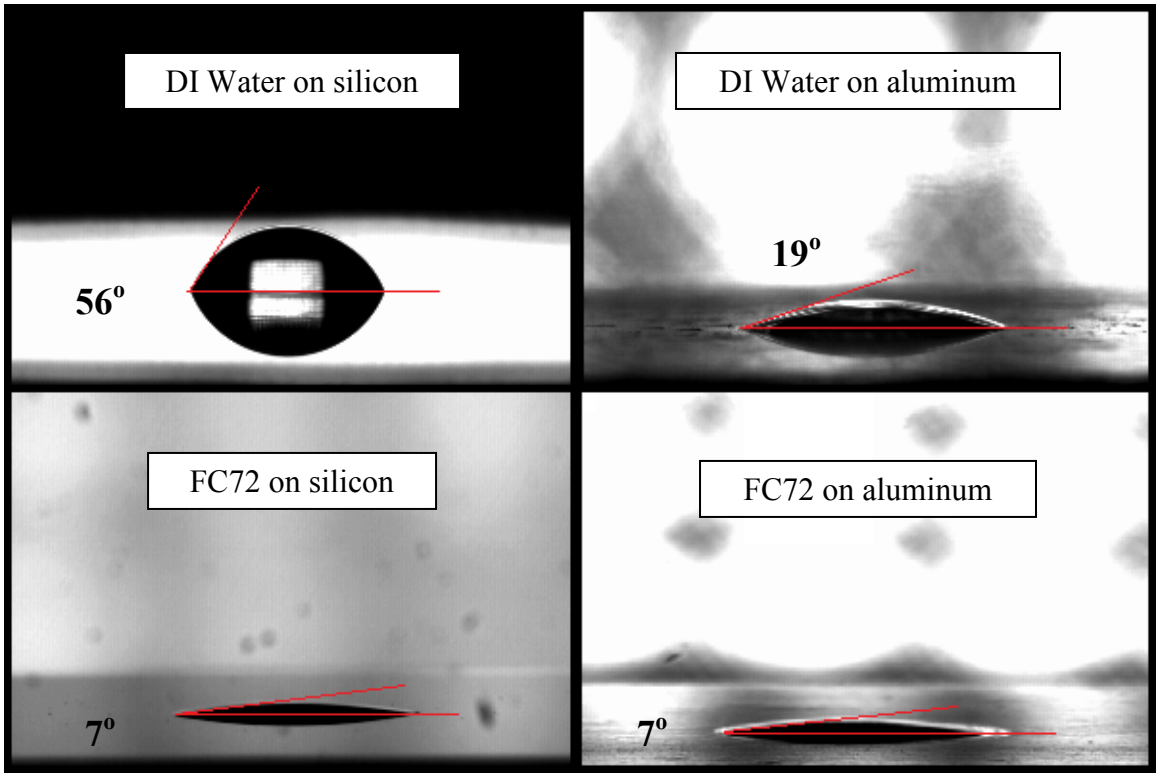

Fig. 2.9 Contact angle estimation, for DI Water and FC72 on silicon and aluminum surfaces.

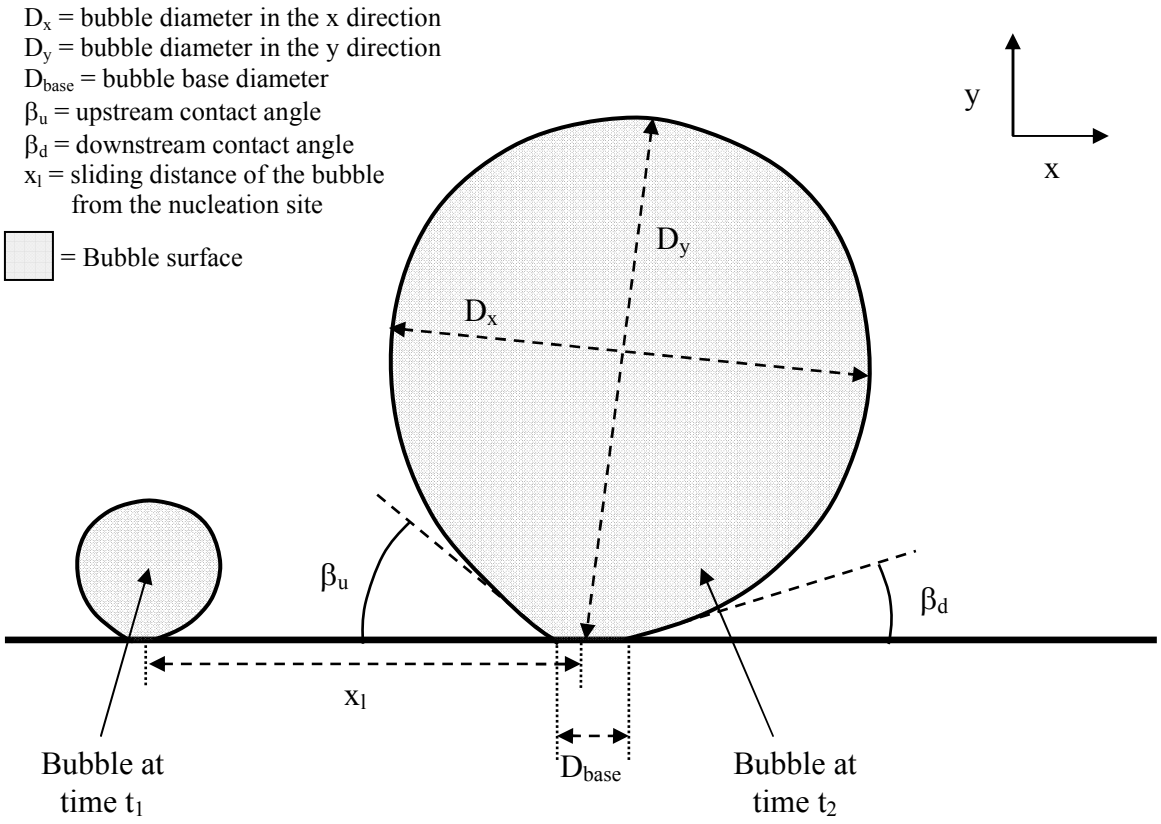

Fig. 2.10 Schematic showing relevant measured quantities.

Table 2.1 Thermal properties of silicon and aluminum.

Parameter	Silicon	Aluminum
k (W/mK)	157	237
c (J/kgK)	712	890
ρ (kg/m^3)	2300	2700
α (m^2/s)	95.8×10^{-6}	8.4×10^{-5}

Table 2.2 Thermophysical properties of saturated DI water and FC72 at atmospheric pressure.

Parameter	DI water	FC72
ρ_v (kg/m^3)	0.598	13.13
ρ_l (kg/m^3)	958.37	1594
k_v (W/mK)	0.025	-
k_l (W/mK)	0.679	0.057
h_{fg} (kJ/kg)	2257.9	95.02
σ (N/m)	0.0589	0.00841

Chapter 3
Results and Discussion – Single Bubble Water Experiments

Experiments were conducted for various flow various velocities, for horizontal (0^o) to vertical (90^o) surface inclinations (through 30^o, 45^o and 60^o), and for two surface materials, at near saturated condition ($\Delta T_{sub} \leq 1.0$ K), and almost constant wall superheat ($5.0 \text{ K} \leq \Delta T_w \leq 6.0$ K), using water as test fluid. Measured quantities include bubble growth rate, bubble base diameter, bubble departure diameter (bubble diameter at which the bubble departs the nucleation site), upstream and downstream contact angles, bubble sliding distance (distance a bubble slides between departure from the nucleation site and lift-off from the heater surface), bubble lift-off diameter (diameter at which the bubble lifts off from the heater surface). The bubble velocity during sliding and at lift off is calculated from measurement of distance travelled by bubble in a given time.

3.1 Experimental results – Silicon test surface

3.1.1 Horizontal surface

This section describes the experiments carried out on a horizontal silicon surface, for a bulk flow velocity varying from 0.076 m/s to 0.25 m/s.

U_{bulk} = 0.076 m/s

A typical ebullition cycle is shown in Fig. 3.1, for bulk liquid velocity of 0.076 m/s, a wall superheat of 5.5 ^oC and liquid subcooling of 0.6 ^oC. It can be seen from Fig. 3.1 that the bubble is nearly spherical in the initial growth stage, and as growth continues, it becomes tilted in the direction of the flow, resulting in an asymmetrical growth until lift

off. This asymmetrical growth is characterized by an increase in the upstream contact angle and a decrease in downstream contact angle, as shown in Fig 3.2(e) for three different growth cycles. Also plotted in Fig 3.2 are bubble diameter, sliding distance, sliding velocity and bubble base diameter as a function of time. As can be seen in Fig. 3.2, the bubble starts to slide from its nucleation site 11 ms after nucleation, for a diameter of about 1.1 mm. The bubble sliding velocity increases as the bubble slides on the heater surface. The bubble growth continues during sliding. Lift off occurs after 27 ms, for a bubble diameter of 1.6 mm. The sliding velocity at lift off is about 0.06 m/s and the bubble has slid nearly more than 0.4 mm from its nucleation site. As shown in Fig. 3.2 the bubble base diameter increases at first, peaks at 0.25 mm (at 10 ms), then decreases with time until lift off.

U_{bulk} = 0.1 m/s

Experimental results for 0.1 m/s liquid bulk velocity are presented in Fig. 3.3, for a wall superheat of 5.6 ^{o}C and liquid subcooling of 0.4 ^{o}C. The bubble departs from the cavity mouth after 9 ms, at a diameter of 1 mm. After sliding more than 0.4 mm, the bubble lifts off at a velocity of 0.08 m/s. The lift off diameter is 1.4 mm, for a lift off time of 20 ms. The downstream contact angle decreases monotonously, while the upstream contact angle remains constant during bubble growth. The maximum bubble base diameter is 0.2 mm.

U_{bulk} = 0.135 m/s

Figure 3.4 shows results obtained for a higher flow velocity, 0.135 m/s, for a wall superheat of 5.4 ^{o}C and a liquid subcooling of 0.3 ^{o}C. The bubble lifts off after 15 ms, at a diameter of 1.2 mm. The sliding distance is 0.55 mm, and sliding velocity at lift off 0.09 m/s. The bubble departed after 4 ms, at a diameter of 0.65 mm. The base diameter reaches a maximum of 0.18 mm. The downstream contact angle decreases monotonously. The upstream contact angle increases at first, attains a maximum value and subsequently decreases.

U_{bulk} = 0.25 m/s

Figure 3.5 shows results obtained for the highest flow velocity studied for the horizontal silicon surface, 0.25 m/s. Wall superheat is 5.8 ^{o}C and liquid subcooling is 0.3 ^{o}C. The bubble departs after 3 ms, at 0.55 mm. It slides for 0.8 mm and lifts off at 0.19 m/s. The lift off time and diameter are 10 ms and 0.95 mm, respectively. The maximum bubble base diameter is 0.16 mm. Both downstream and upstream contact angle decrease with time.

Effect of flow velocity

Several parameters, including departure and lift off diameters, sliding distance and velocity at lift off, and peak base diameter, are plotted in Fig. 3.6 to highlight the effect of velocity on bubble dynamics on an upward facing horizontal surface. Also, the bubble growth as a function of time is shown in Fig. 3.6(a) for all four studied flow velocities. Velocity has a slight effect on growth rate. The bubble growth is faster for lower flow

velocities. A possible explanation is that increase in velocity leads to decrease in thermal boundary layer thickness, decreasing heat transfer. From Fig. 3.6, it is clear that as velocity increases, both departure and lift off diameter decreases non-linearly. Departure and lift off time decrease with increase in velocity. For the bubble to start sliding, the drag force has to overcome the effect of surface tension force holding the bubble at the cavity mouth. The drag force increases with increasing in bubble diameter, up to a value sufficient for the bubble to start sliding. Similarly, the drag force increases with liquid bulk velocity, resulting in smaller departure diameters. Departure and lift off diameters and times are much smaller than for pool boiling conditions, as shown by the data from Ramanujapu and Dhir (1999) (for $\Delta T_w = 6.5\ ^oC$, $\theta = 54^o$) as well as Qiu *et al*. (2002) (for $\Delta T_w = 7.1\ ^oC$, $\theta = 55^o$).

Bubble lift off occurs when the lift force and the buoyancy force are able to overcome the surfaces tension force which attaches the bubble to the surface. Lift force increases with increase in relative velocity. As a result, bubble lift off diameter is smaller at higher velocities.

The effect of velocity on sliding distance is unclear: at low velocities (0.076 m/s and 0.1 m/s), sliding distance increases with increase in velocity while for 0.135 m/s and 0.25 m/s the opposite is seen. The sliding velocity at lift off increases with liquid bulk velocity, but remains lower than the flow velocity. This increase in sliding velocity, coupled with decrease in lift off diameter with increase in velocity shows the dependence of lift force on multiple parameters. Maximum bubble base diameter is seen to decrease with increase in velocity, which is coherent with the fact that higher flow velocities result in smaller bubbles.

Comparison with data from the literature

Comparisons with data from the literature are shown in Fig 3.7. Figure 3.7(a) shows a comparison of departure and lift diameters from the present study with data from Kandlikar and Stumm (1995) (for ΔT_{sub} = 40 ^{o}C, unknown ΔT_{w} and $\theta = 55^{o}$), Maity (2000) (for $\Delta T_{w} = 5.5 \pm 0.4$ ^{o}C, $\Delta T_{sub} = 0.5 \pm 0.3$ ^{o}C, and $\theta = 61^{o}$) and Jia and Dhir (2004) (for $\Delta T_{w} = 5.3 \pm 0.2$ ^{o}C, $\Delta T_{sub} = 0.2 \pm 0.2$ ^{o}C, and θ was not reported). Maity (2000) and Jia and Dhir (2004) experiments are very similar to that of the present study: they both studied single bubble nucleation and behavior in flow boiling of water on polished silicon wafers. Kandlikar and Stumm's data were obtained in flow boiling of water on a horizontal copper surface, at high velocities and subcoolings. The comparison in Fig. 3.7(a) shows that data from the present study has similar trend with the data from the literature. Also, results from Maity (2000) and Jia and Dhir (2004) are very close to the ones obtained in this study, which is expected given the similarities between all three studies.

Figure 3.7(b) shows the comparison between data from the present study and data from Koumoutsos *et al.* (1968). Their data was obtained during experiments on flow boiling of water on a horizontal copper surface, for $\Delta T_{w} = 15.0 \pm 0.2$ ^{o}C, $\Delta T_{sub} = 0.5 \pm 2.0$ ^{o}C, and unknown θ. They presented their lift off diameter data normalized with respect to lift off diameter under pool boiling conditions ($D_{l,o}$, not reported). A similar trend is observed, but the lift off diameter values reported by Koumoutsos *et al.* (1968) are higher than that from the present study ($D_{l,o}$ = 2.6 mm), for the same flow velocity. It might be due to the fact that they used a smaller pool boiling lift off diameter, and also that their

wall superheat is much higher. Increase in wall superheat results in larger lift off diameters, for pool and flow nucleate boiling.

3.1.2 Vertical surface

Experiments described in this section were carried out on a vertical silicon surface, for a flow velocity varying from 0 m/s (pool boiling conditions) to 0.25 m/s.

U_{bulk} = 0 m/s

Figure 3.8 shows results obtained for pool boiling conditions, for a wall superheat of 5.2 ^{o}C and a liquid subcooling of 0.9 ^{o}C. The bubble lifts off after 35 ms, at a diameter of 4.5 mm. The sliding distance is 4.9 mm, and the velocity at lift off is 0.2 m/s. Note that for vertical upflow, bubbles were observed to slide even for pool boiling conditions. Consequently, in all cases the bubble sliding velocity at lift off was observed to increase beyond the velocity obtained for pool boiling, and in all cases the sliding velocity was found to be larger than the bulk liquid velocity. The bubble departed after 1.5 ms, at a diameter of 1.5 mm. In all cases, the bubble departs almost instantaneously after nucleation. Therefore there is no effect of bulk liquid velocity on bubble departure time. The base diameter reaches a maximum of 1.3 mm. Both downstream and upstream contact angles decrease monotonously. In one case, as seen from Fig. 3.8, the bubble lifts off from the heater surface after 9 ms, and stays in the liquid before reattaching to the surface 19 ms after nucleation. Similar behavior was reported by Bibeau and Salcudean (1994) and Maity (2000). Bibeau and Salcudean (1994) reported such occurrences as

random and rare, while Maity (2000) observed such behavior repeatedly, for specific velocities and orientations.

U_{bulk} = 0.076 m/s

The ebullition cycle for bulk liquid velocity of 0.076 m/s, a wall superheat of 5.6 ^{o}C and liquid subcooling of 0.7 ^{o}C, is shown in Fig. 3.9. The bubble departs from the cavity mouth after 1.5 ms, at a diameter of 0.75 mm. After sliding more than 13 mm, the bubble lifts off at a velocity of 0.34 m/s, larger than the bulk liquid velocity of 0.076 m/s. The lift off diameter is 3.2 mm, for a lift off time of 62 ms. The downstream contact angle decreases monotonously, while the upstream contact angle remains constant during bubble growth. The maximum bubble base diameter is 0.83 mm.

U_{bulk} = 0.1 m/s

Experimental results for 0.1 m/s liquid bulk velocity are presented in Fig. 3.10, for a wall superheat of 5.5 ^{o}C and liquid subcooling of 0.6 ^{o}C. The bubble departs from the cavity mouth after 1 ms, at a diameter of 0.55 mm. After sliding for around 11 mm, the bubble lifts off at a velocity of 0.4 m/s. The lift off diameter is 2.6 mm, for a lift off time of 56 ms. The downstream and upstream contact angles decrease monotonously during bubble growth. The maximum bubble base diameter is 0.68 mm.

U_{bulk} = 0.135 m/s

Figure 3.11 shows results obtained for a flow velocity of 0.135 m/s, a wall superheat of 5.4 ^{o}C and a liquid subcooling of 0.8 ^{o}C. The bubble lifts off after 50 ms, at a diameter

of 2.25 mm. The sliding distance is 10.5 mm, and lift off velocity is 0.45 m/s. The bubble departed after 1 ms, at a diameter of 0.48 mm. The base diameter reaches a maximum of 0.58 mm. The downstream contact angle decreases monotonously. The upstream contact angle remains constant at first, and decreases towards the downstream value.

U_{bulk} = 0.25 m/s

Figure 3.12 shows results obtained for the highest flow velocity studied for the vertical silicon surface, 0.25 m/s. The wall superheat and liquid subcooling are 5.7 ^{o}C and 0.6 ^{o}C, respectively. The bubble departs after 1 ms, at 0.35 mm. It slides for 8.4 mm and lifts off at 0.58 m/s. The lift off time and diameter are 32 ms and 1.58 mm, respectively. The maximum bubble base diameter is 0.5 mm. The downstream contact angle decreases monotonously. The upstream contact angle remains constant at first, and decreases towards the downstream value.

Effect of flow velocity

Departure and lift off diameters, sliding distance and velocity at lift off, and peak base diameter, are plotted in Fig. 3.13 to highlight the effect of velocity on bubble dynamics, for vertical upflow conditions. The bubble growth as a function of time is shown in Fig. 3.13(a) for all five studied flow velocities. As shown earlier for a horizontal surface, velocity has a slight effect on growth rate, when the bulk liquid velocity is non-zero. For pool boiling conditions, the growth rate is much larger than for flow boiling. Overall, the bubble growth is faster for lower flow velocities. A possible explanation is that increase in velocity leads to decrease in thermal boundary layer thickness, decreasing heat transfer.

From Fig. 3.13, it is clear that for flow boiling conditions, as velocity increases, both departure and lift off diameters decrease non-linearly. Similarly, lift off time decreases with increase in velocity, and departure time remains constant at around 1 ms. On the other hand, Fig. 3.13 shows that for pool boiling conditions, the lift off times are much smaller than for the lowest flow velocity studied. This is a consequence of the faster pool boiling bubble growth rate. Even though the bubble sliding velocity is smaller, the bubble diameter required for the bubble to detach from the heater surface is reached faster.

The effect of velocity on sliding distance is unclear: at low velocities (0 and 0.076 m/s), sliding distance increases with increase in velocity while for 0.1 m/s to 0.25 m/s the opposite is seen. The sliding velocity at lift off increases with liquid bulk velocity, and is higher than the flow velocity. This increase in sliding velocity, coupled with decrease in lift off diameter with increase in velocity shows the dependence of lift force on multiple parameters. Maximum bubble base diameter is seen to decrease with increase in velocity, which is coherent with the fact that higher flow velocities result in smaller bubbles.

Comparison with data from the literature

Comparisons with data from the literature are shown in Fig 3.14. Figure 3.14(a) shows a comparison of departure diameters from the present study with data from Bibeau and Salcudean (1994) (for $10\ ^{o}C \leq \Delta T_{sub} \leq 30\ ^{o}C$, unknown ΔT_w and φ), Maity (2000) (for $\Delta T_w = 5.5 \pm 0.4\ ^{o}C$, $\Delta T_{sub} = 0.5 \pm 0.3\ ^{o}C$, and $\theta = 61^{o}$) and Jia and Dhir (2004) (for $\Delta T_w = 5.3 \pm 0.2\ ^{o}C$, $\Delta T_{sub} = 0.2 \pm 0.2\ ^{o}C$, and unknown φ). Results from Bibeau and Salcudean (1994), at low velocity, and Jia and Dhir (2004) are in good agreement with

the ones obtained in this study. On the other hand, results from Maity are systematically larger than the ones obtained in the study and that available in the literature.

Figure 3.14(b) shows a comparison between lift off diameter data from the present study and that from the literature. Data shown in Fig. 3.14(b) were reported by Abdelmessih *et al.* (1972) (for ΔT_{sub} = 1.9 ^{o}C, unknown ΔT_w and θ), Akiyama and Tachibana (1974) (for $\Delta T_{sub} = 23 \pm 0.5$ ^{o}C, unknown ΔT_w and θ), Bibeau and Salcudean (1994) (for 10 ^{o}C $\leq \Delta T_{sub} \leq$ 30 ^{o}C, unknown ΔT_w and θ), Van Helden *et al.* (1995) (for $\Delta T_{sub} \approx 0$ ^{o}C, $\Delta T_{sub} \leq$ 2 ^{o}C and unknown θ), Maity (2000) (for $\Delta T_w = 5.5 \pm 0.4$ ^{o}C, $\Delta T_{sub} = 0.5 \pm 0.3$ ^{o}C, and $\theta = 61^{o}$), Jia and Dhir (2004) (for $\Delta T_w = 5.3 \pm 0.2$ ^{o}C, $\Delta T_{sub} = 0.2 \pm 0.2$ ^{o}C, and unknown θ), Situ *et al.* (2005) (for $\Delta T_{sub} = 3.5 \pm 2.0$ ^{o}C, and unknown ΔT_w and θ), and Ahmadi *et al.* (2012) (for $\Delta T_w = 14.9 \pm 6.5$ ^{o}C, $\Delta T_{sub} = 14.3 \pm 4.1$ ^{o}C and $\theta = 18^{o}$). All of the data from the literature shows that lift off diameter decreases with increase in flow velocity. On the other hand, there is a large variation in the magnitude of bubble lift off diameters. This is due to the fact that most experiments were conducted for different ΔT_w, ΔT_{sub} and/or φ, parameters that affect greatly bubble lift off diameter.

3.1.3 Effect of velocity and orientation on bubble dynamics

Bubble departure

The coupled effects of orientation and velocity on bubble departure diameter are shown in Fig. 3.15. The change in magnitude of gravity (in normal and parallel direction to the surface) created by a change in orientation affects the departure diameter. For vertical surface, there is no component of gravity normal to the heater surface, and for horizontal surface there is no component of gravity parallel to the heater surface. The

departure diameter decreases with velocity, irrespective of orientation. For given velocity, departure diameter decrease with increase in orientation (from horizontal to vertical). This is due to the fact that the contribution of buoyancy to bubble departure increases with inclination, and therefore decreases departure diameter. For horizontal surface, drag force is the only force promoting bubble sliding, and counteracting surface tension force, while for vertical surface both drag and buoyancy act parallel to the heater surface and promote bubble sliding.

Bubble lift off

Figure 3.16 shows the effect of orientation and velocity on lift off diameter. Lift off diameter increases with both flow velocity and orientation. As stated earlier, the normal component of gravity disappears with increase in orientation, resulting in no direct contribution from buoyancy towards lift off. As a consequence, the bubble needs to grow to a larger size for the lift force to be able to compensate the forces keeping the bubble on the surface. For horizontal surface, buoyancy and lift forces counteract surface tension force, and promote bubble lift off, while for vertical surface only lift force acts normal to the heater surface and promote bubble lift off. Also, for the highest flow velocity (0.25 m/s), it appears that the effect of orientation on lift off diameter is reduced.

Bubble sliding distance

Sliding distance increases with orientation, as shown in Fig. 3.17. This effect appears to be stronger at low flow velocities.

Bubble velocity at lift off

Bubble velocity at lift off increases with both orientation and flow velocity, rather monotonically, as can be seen from Fig. 3.18. For horizontal surface, the bubble velocity at lift off remains slower than flow velocity, but for vertical surfaces, sliding velocity at lift off becomes larger than flow velocity in all cases. This is due to the fact that for horizontal surface, the only detaching force acting parallel to the heater is drag, while for vertical surface both drag and buoyancy forces a detaching forces parallel to the heater surface. Note that bubble velocity at lift off is a crucial parameter in determining the lift force.

Maximum bubble base diameter

In general, bubble base diameter decreases with increase in velocity, and increases with increase in inclination, as shown in Fig. 3.19. Base diameter is an important parameter in calculation of forces attaching the bubble to the heater surface, as well as in calculating heat transfer. Base diameter depends on bubble size, as well as contact angle.

3.2 Single bubble lift off modeling

Numerous authors have attempted to predict bubble lift off diameter, most of them by either developing empirical correlations or semi-empirical force balance-based models. This widespread interest has yielded a wide variety of expressions of bubble lift off diameter as well as the forces acting on a bubble from nucleation to lift off. There is to date no consensus on which model to use, since they all either rely too heavily on

empirical data or are overly-complicated. In this section, a force-balance based approach is taken to develop a simple and accurate model for bubble lift-off diameter.

3.2.1 Simplified force balance model

Lift off of the bubble is a result of a break in the force balance in the direction normal to the heater wall (y-direction). If a simple force balance approach is taken, these forces are the lift force (F_l), the buoyancy force (F_b), the surface tension force (F_s), the contact pressure force (F_{cp}), and the inertia of both the vapor and the liquid displaced by the growing bubble. Bubble lift off is initiated once the following criterion is met

$$\Sigma F_y = F_{l,y} + F_{b,y} + F_{s,y} + F_{cp,y} - \left(\rho_v + C_{vm}\rho_l\right)\frac{\partial}{\partial t}\left(V_b v_b\right) \geq 0 \tag{3.1}$$

where the last term represents the inertia of the growing bubble and of the liquid surrounding it, and V_b is the bubble volume in m^3. The vertical bubble velocity v_b is approximated as dD/dt. The virtual mass coefficient C_{vm} is taken as 11/16, as recommended by Davidson and Schüler (1960) and Han and Griffith (1965), and is used to account for the mass of liquid surrounding the bubble that is displaced during bubble growth.

3.2.1.1 Lift force

Lift force is the force experienced by the bubble due to the non-uniformity of the flow and to the relative velocity between the bubble and the liquid. The component of the lift force normal to the heater wall is a determining factor in bubble lift off, particularly for a vertical surface when the buoyancy force does not have a component normal to the heater

wall. Similarly, in microgravity conditions, where buoyancy is negligible, the lift force would be the only force responsible for bubble lift off.

Orientation of the lift force

As shown earlier, the bubbles always lift off, irrespective of flow velocity and inclination. Most importantly, for vertical conditions (and other inclinations, other than horizontal), the bubbles lift off with a sliding velocity larger than that of the liquid. Similar results have been reported in the literature by Bibeau and Salcudean (1994), Van Helden *et al.* (1995), Maity (2000), Jia and Dhir (2004), and Ahmadi *et al.* (2012). However, Klausner *et al.* (1993), Mei and Klausner (1994), Thorncroft *et al*. (1998 and 2001) have reported that for vertical upflow conditions, bubble lift off occurs rarely, and may be due to neighboring bubbles perturbing the flow or turbulent currents. They noted that in vertical forced flow conditions, the bubble sliding velocity was typically superior to the bulk liquid velocity. They argued that when the bubble leads the flow, the lift force pushes the bubble towards the wall while when the bubble trails the flow, it pushes the bubble away from the wall.

Patankar *et al.* (2001) performed numerical simulations of single spherical particles lift off at a wall in Shear and Couette flows and showed that for Couette flow, the pressure (P) and viscous shear stress (S) are larger were the velocity incident on the particle is largest, which means when the velocity difference between the particle and the fluid is the most important. The pressure and viscous shear stress difference on the particle surface resulted in a lift force pushing the particle away from the wall. Similar observations were reported by Zhu (2000) for the lift off of a spherical particle in Couette

flow. These results were shown to be relevant to vapor bubbles during flow boiling by Li (2005), who performed numerical simulations of single bubble saturated nucleate flow boiling, and reported that for vertical upflow conditions, at the instant before lift off the pressure at the liquid vapor interface was larger at the base of the bubble than at the top, thus creating a lift force pushing the bubble away from the heated wall. These results are applicable to the current problem. Figure 3.20 shows the velocity profiles for cases were the bubble trails the flow and when the bubble leads the flow, on a vertical. It can be seen that in both cases, the pressure P_1, near the wall, is larger than the pressure P_2, the top of the bubble, by the fluid approaches the bubble with a larger velocity at the bottom. Similarly, the viscous shear stress S_1 is larger than S_2, in both cases. Therefore, whether the bubble trails or leads the flow, a lift force generated by pressure and viscous shear stress will act towards ejecting the bubble from the surface. A similar conclusion was reached by Auton (1987).

A possible explanation for the absence of systematic bubble lift off reported in some studies may be a liquid subcooling value so large that it prevents the bubble from reaching large enough size for lift off to occur.

Lift force equation

The y-component of the lift force for a sphere in shear flow was derived by Auton (1987) as

$$F_{l,y} = \frac{4}{3}\pi r^3 C_l \rho_l \dot{\gamma}_{y=r} \left| U(y=r) - U_{bubble} \right| \tag{3.2}$$

where r is the bubble radius, C_l is the lift coefficient, U_{bubble} is the bubble sliding velocity, U(y=r) is the local flow velocity at y = r, and $\dot{\gamma}_{y=r}$ is the shear rate at y = r. The shear rate is given as

$$\dot{\gamma}_y = \frac{dU(y)}{dy} \tag{3.3}$$

Auton (1987) recommended a constant lift coefficient of 0.5. Naciri (1992) expended Auton's (1987) work to ellipsoids, and demonstrated a close equivalence between C_{vm} and C_l, and showed that for quasi-spherical particles, a constant lift coefficient of 0.5 is valid, as postulated by Auton (1987), for bubble Reynolds numbers inferior to 1000. A constant lift coefficient equal to 0.5 is chosen for the present study, For $Re_b < 1000$. For $Re_b > 1000$, Naciri reported a quasi-linear increase in C_l with increase in Re_b. In the present study, most cases do not exceed $Re_b = 1000$, and the maximum C_l value is found to be equal to 1.25, as seen in Fig. 3.21. Figure 3.21 shows the lift coefficient as a function of bubble Reynolds number for the present study, for all velocities, orientations and surface materials. For the sake of completeness, a popular but quite complicated expression of the lift coefficient was formulated by Klausner *et al.* (1993). This expression for the lift coefficient was used by Mei and Klausner (1994), Thorncroft *et al.* (1998 and 2001), and is given as

$$C_l = 3.877\left(\frac{r\dot{\gamma}_r}{|U(r)-U_{bubble}|}\right)^{0.5}\left(\mathrm{Re_b}^{-2} + 0.14\left(\frac{r\dot{\gamma}_r}{|U(r)-U_{bubble}|}\right)^2\right)^{0.25} \tag{3.4}$$

with Re_b the bubble Reynolds number given as

$$\mathrm{Re_b} = \frac{D|U(r)-U_{bubble}|}{\nu_v} \tag{3.5}$$

Numerous lift coefficient expressions can be found in the literature, and were reviewed by Hibiki and Ishii (2007).

Based on the hydraulic diameter, the Reynolds number for every experimental condition is turbulent (Re_{dh} > 5000 for every forced convection experiment). The liquid velocity profile near the wall is calculated using Reichardt (1951) turbulent flow profile expression

$$U(y) = u^* \left[\kappa^{-1} \ln\left(1 + \kappa y^+\right) + c\left(1 - e^{-y^+/\chi} - \frac{y^+ e^{-0.33y^+}}{\chi}\right)\right] \tag{3.6}$$

where $y^+ = u^* y / \nu$, where u^* is the friction velocity. The von Karman constant $\kappa = 0.41$, $\chi = 11$ and $c = 8.67$. Although this expression was developed for single phase flows, the presence of a single bubble should not disrupt the flow significantly, as demonstrated Yoshikawa and Colin (2010). They performed PIV measurement of the velocity field in a rectangular duct of 5x40 mm^2 cross section during single bubble flow boiling experiments, and reported the accuracy of the velocity field predicted by Reichardt's (1951) model and their experimental results, for Re_{dh} > 5000. The friction velocity u^* is calculated using the expression developed by Petukhov (1970)

$$u^* = U\left(\frac{1}{2.236\,\mathrm{Re}_{Dh} - 4.639}\right) \tag{3.7}$$

3.2.1.2 Buoyancy force

The buoyancy force in the direction normal to the heater is modeled classically as follows

$$F_{b,y} = \frac{4}{3}\pi r^3 \left(\rho_l - \rho_v\right) g \cos\left(\frac{\pi\varphi}{180}\right) \tag{3.8}$$

where φ is the heater orientation in degrees and g is the acceleration due to gravity. As one can see from Eq. (3.8), for a vertical surface the buoyancy force does not have a component normal to the heater surface. Therefore it does not participate directly in bubble lift off, but will affect bubble sliding velocity, ultimately contributing to the lift off of the bubble from the heater wall.

3.2.1.3 Surface tension force

The surface tension force is a capillary force that maintains the bubble attached to the surface, thus preventing it from sliding and lifting off. It is oriented towards the heater wall, along the liquid/vapor/solid contact line. For pool boiling conditions, the bubble base is axisymmetric, and the surface tension force in the y-direction can be expressed as

$$F_{s,y} = -D_{base}\sigma\pi\sin(\beta) \tag{3.9}$$

where D_{base} is the bubble base diameter, σ is the surface tension in N, and β is the dynamic contact angle, in radians. But as shown in the previous chapter, vapor bubbles in flow boiling conditions are inclined, and the contact angle varies along the liquid/vapor/solid contact line. To account for this contact angle variation, Klausner *et al.* (1993) developed an expression for the local contact angle, given as

$$\begin{aligned} &\beta(\Phi) = \beta_u + (\beta_d - \beta_u)\frac{\Phi}{\pi} \\ &0 \le \Phi \le \pi \end{aligned} \tag{3.10}$$

where β_u and β_d are the upstream and downstream contact angles, respectively, in radians, and Φ is the angle along the bubble base. Using this approximate expression for the contact angle, the surface tension force acting on a vapor bubble during flow boiling was derived by Klausner *et al.* (1993) as

$$F_{s,y} = -\int_{0}^{\pi} D_{base}\sigma \sin(\beta)\,d\Phi$$
$$F_{s,y} = -D_{base}\sigma \frac{\pi}{\beta_u - \beta_d}\left(\cos(\beta_d) - \cos(\beta_u)\right) \tag{3.11}$$

This expression accounts for the difference in upstream and downstream contact angles that is observed during flow boiling.

3.2.1.4 Contact pressure force

The contact pressure force is a force that acts normal to the heater wall and is due to the pressure difference between the inside and the outside of the bubble, resulting from the contact are between the bubble and the heater wall. A thorough derivation was presented by Siedel (2012); it is given as

$$F_{cp,y} = \frac{\sigma}{2r_c}\pi {D_{base}}^2 - \frac{4}{3}\pi(D\left(\pi \frac{{D_{base}}^2}{4}\right)\left(\rho_l - \rho_v\right) g \cos\left(\frac{\pi\varphi}{180}\right) \tag{3.12}$$

where r_c is the radius of curvature of the liquid-vapor interface at the top of the bubble. The radius of curvature of the liquid-vapor interface at the top of the bubble is taken such that $r_c = 0.75r$. The second term is a correction of the buoyancy force due to the absence of liquid/vapor contact at the base of the bubble, when the bubble is attached to the wall

3.2.2 Application of the force balance to bubble growth cycles

3.2.2.1 Flow boiling

In order to verify if the forces introduced in the earlier sections are accurate in describing the bubble growth and lift off processes during flow boiling, and to see if the simplified force balance approach is a valid one, these forces were computed for each

cases presented in this study. Some of the most relevant cases are presented in this section.

Figure 3.22 shows the forces acting on a bubble growing on a horizontal silicon heater, for bulk liquid velocities of 0.076 m/s (Fig. 3.22(a)) and 0.25 m/s (Fig. 3.22(b)). Similarly, Fig. 3.23 shows the forces acting on a bubble growing on a vertical silicon heater, for bulk liquid velocities of 0.076 m/s (Fig. 3.23(a)) and 0.25 m/s (Fig. 3.23(b)). As shown in Figs. 3.22 and 3.23, the sum of the forces acting on the bubble becomes positive at the same time than the bubble base starts to shrink. The initiation of bubble lift off is characterized by a shrinking of the bubble base, and is due to the fact that the surface tension force is no longer capable of overcoming the forces pushing the bubble away from the surface. This result is of significance since it shows that the simplified force-balance approach is capable of quantifying with precision when the lift off process starts. Note that for all cases, the inertia term has little to no influence on the bubble lift off process, and therefore could be neglected.

As can be seen in Fig. 3.22(a), for $\varphi = 0^o$, and $U_{bulk} = 0.076$ m/s, the buoyancy force is much larger than the contact pressure force and the lift force, at the instant where the sum of the forces acting on the bubble becomes positive. Therefore, the lift off process in this case is controlled by buoyancy. Note that for $\varphi = 0^o$, and $U_{bulk} = 0.076$ m/s, the lift force decreases a few milliseconds before lift of. This is a result of the bubble sliding velocity approaching that of the liquid. One can surmise that in microgravity conditions, the bubble sliding velocity will reach a value close to that of the bulk liquid but will never become larger, due to the negligible contribution of buoyancy. Therefore the velocity gradient would be very small and the viscous sheer stress would be the

dominating factor in the lift force required for the bubble to lift off. For $\varphi = 0^o$, and U_{bulk} = 0.25 m/s, Fig. 3.22(b) shows that the contribution of buoyancy and lift forces towards lift off is similar, at the instant where the sum of the forces acting on the bubble becomes positive, and that both forces are smaller than the contact pressure force. Therefore, the initiation of the lift off process in this case is dominated by the contact pressure force, and receives identical contributions from buoyancy and lift forces. Figure 3.23 shows that for all velocities, lift force becomes extremely large for $\varphi = 90^o$, due to the large sliding velocity of the bubble, that is being pushed by the buoyancy force acting in the direction parallel to the heater surface, and that lift force dominates the lift off process.

3.2.2.2 Pool boiling

Similarly to the approach taken in the previous section, the forces acting on a bubble growing on a heated vertical surface silicon surface in pool boiling were computed. However, in order to express the lift force, one needs to be able to determine the local flow velocity at y = r, U(r), and the shear rate at y = r, $\dot{\gamma}_r$.

For both silicon and aluminum surfaces, the cavity is located at 15 mm from the leading edge. As a result, based on an axial location x = 15 cm, the Rayleigh number for every experimental condition is laminar ($Ra_x < 10^9$), where Ra_x is defined as

$$Ra_x = \frac{\beta\left(T_w - T_\infty\right) g x^3}{\nu\alpha} \tag{3.13}$$

where g is the acceleration due to gravity m/s^2, given as $g = 9.81\sin(\pi\varphi/180)$, with φ the orientation in degrees, β is the thermal expansion coefficient in K^{-1}, ν is the kinematic viscosity in m^2/s, and α is the thermal diffusivity in m^2/s. The liquid velocity profile near the wall is assumed to be of the following form

$$U(y) = u^* \left[\frac{y}{\delta} \left(1 - \frac{y}{\delta} \right)^2 \right] \tag{3.14}$$

where u^* is the scaling velocity and δ is the hydrodynamic boundary layer thickness. The scaling velocity u^* and the hydrodynamic boundary layer thickness δ are determined using laminar boundary layer analysis, and are expressed as

$$\begin{aligned} u^* &= Xx^{0.5}; \quad \delta = Dx^{0.25} \\ X &= \frac{80\alpha}{D^2} \\ D &= 3.94 \left[\frac{(20/21)\alpha^2 + \nu\alpha}{g\beta(T_w - T_\infty)} \right]^{0.25} \end{aligned} \tag{3.15}$$

From Eq. (3.14), the shear rate at y = r, $\dot{\gamma}_r$, is calculated as

$$\gamma_r = U^* \left(\frac{1}{\delta} - 4\frac{y}{\delta^2} + 3\frac{y^2}{\delta^2} \right) \tag{3.16}$$

Figure 3.24 shows the forces acting on a bubble growing on a vertical silicon heater for pool boiling conditions Similarly to the results shown in Figs. 3.22 and 3.23, Fig. 3.24 shows that for pool boiling on a vertical surface, the sum of the forces acting on the bubble becomes positive at the same time than the bubble base starts to shrink. This result shows that the simplified force-balance approach is capable of quantifying with precision when the lift off process starts for pool boiling on a vertical surface. Note that the inertia term has little to no influence on the bubble lift off process, and therefore could be neglected in the simple force balance model. The lift force is becomes extremely large, due to the large sliding velocity of the bubble, that is being pushed by the buoyancy force acting in the direction parallel to the heater surface. As a result, for a vertical wall, lift off

is controlled by the lift force, and indirectly by buoyancy since it causes the bubble to the slide along the heater wall.

3.2.3 Modeling of bubble lift off diameter

As shown in Figs. 3.22, 3.23 and 3.24, bubble lift off is initiated when the buoyancy force, lift force and contact pressure force overcome the surface tension force in the direction normal to the heater surface. This break in the force balance coincides with a decrease in bubble base diameter, and leads ultimately to bubble lift off. Numerous authors, such as Mei and Klausner (1994), Thorncroft *et al*. (1998 and 2001), Duhar *et al.* (2009), Montout (2009), Yoshikawa and Colin (2010), amongst others, attempted to model bubble lift off diameter as the diameter for which the sign of the force balance changes. However, none of the existing models available in the literature can accurately predict bubble lift off diameter. A similar approach is taken in the present study.

Figure 3.25 shows the comparison between $F_b + F_s + F_{cp}$ and F_s, at the instant where bubble lift off is initiated (i.e. when bubble base diameter is maximum). As can be seen in Fig. 3.25, and as was shown in Figs. 3.22, 3.23 and 3.24, the detaching forces acting on the bubble are equal to the attaching forces, regardless of orientation. Therefore this force balance can be used to determine bubble diameter when lift off is initiated. The force balance at the instant bubble base is maximum is

$$F_{b,y} + F_{l,y} + F_{cp,y} = F_{s,y}$$

$$\begin{pmatrix} \frac{4}{3}\pi r^3 (\rho_l - \rho_v) g \cos\left(\frac{\pi\varphi}{180}\right) + \frac{\sigma}{2r_c}\pi D_{base,max}{}^2 \\ + \frac{4}{3}\pi r^3 C_l \rho_l \dot{\gamma}_{y=r} \left| U(y=r) - U_{bubble} \right| \\ - \frac{4}{3}\pi (D\left(\pi \frac{D_{base,max}{}^2}{4}\right)(\rho_l - \rho_v) g \cos\left(\frac{\pi\varphi}{180}\right) \end{pmatrix} = \begin{pmatrix} -D_{base,max}\sigma \frac{\pi}{\pi(\beta_u - \beta_d)/180} \\ \times \begin{pmatrix} \cos(\pi\beta_d/180) \\ -\cos(\pi\beta_u/180) \end{pmatrix} \end{pmatrix} \quad (3.17)$$

where φ and β are in degrees, and $F_{s,y}$ is given for flow boiling conditions, or pool boiling on an inclined surface, as in Eq. (3.11). For pool boiling conditions on a horizontal surface, where no sliding occurs and bubbles are axisymmetrical, Eq. (3.9) should be used. In order to obtain an expression for the bubble equivalent diameter D, maximum base bubble diameter D_{base} needs to be expressed as a function of D. Figure 3.26 shows the variation of $D_{base,max}$ with D, for horizontal and vertical silicon surfaces. As can be seen from Fig. 3.26, $D_{base,max} = D / 3$. Hence Eq. (3.17) becomes

$$\begin{pmatrix} \left(\frac{1}{2}\pi\left((\rho_l - \rho_v) g \cos\left(\frac{\pi\varphi}{180}\right) + C_l \rho_l \dot{\gamma}_{y=D/2} \left| U(y=D/2) - U_{bubble} \right|\right)\right) D^2 \\ \left(-\frac{1}{9}\pi^2 (\rho_l - \rho_v) g \cos\left(\frac{\pi\varphi}{180}\right)\right) \\ + \pi\sigma\left(\frac{1}{2.25} - \frac{1}{\pi(\beta_u - \beta_d)/180}\left(\cos(\pi\beta_d/180) - \cos(\pi\beta_u/180)\right)\right) \end{pmatrix} = 0 \quad (3.18)$$

The positive root of Eq. (3.18) gives the value of the bubble diameter when bubble base is maximum. For pool boiling on a horizontal surface, Eq. (3.18) becomes

$$\left(\frac{1}{2}\pi - \frac{1}{9}\pi^2\right)(\rho_l - \rho_v) g \cos\left(\frac{\pi\varphi}{180}\right) D^2 + \pi\sigma\left(\frac{1}{2.25} - \sin\left(\frac{\pi\beta}{180}\right)\right) = 0 \quad (3.19)$$

Equations (3.18) and (3.19) can then be used to predict bubble lift off diameter. As shown in Fig. 3.27, bubble lift off diameter is 1.25 times larger than bubble diameter when bubble base is maximum.

However, in order to predict lift off diameter using a model that does not require any empirical data such as β, U_{bubble}, $U(y)$ and γ_y, one needs to be able to model bubble growth and sliding. It is not the object of the present study, and therefore it will not be addressed.

Another interesting finding of Figs. 3.22, 3.23 and 3.24, is that when bubble lift off occurs, the only non-negligible forces acting on the bubble are the lift and buoyancy forces. Therefore, one can surmise that bubble lift off diameter is a function of the sum of the lift force and the buoyancy force acting on the bubble right before it lifts off from the heater surface.

Figure 3.28 shows the forces acting on a bubble at lift off, as a function of flow velocity, for horizontal (Fig. 3.28(a)) and vertical (Fig. 3.28(b)) silicon surfaces. These forces are presented in reduced form, in which F_b, F_l and $F_b + F_l$ are divided by the bubble surface area at lift off A_l, given as

$$A_l = 4\pi r_l^2 \tag{3.20}$$

where r_l is the bubble lift off radius in m. For given conditions, the results from the three experimental runs presented in earlier in this chapter were averaged and plotted in Fig. 3.28. The error bars represent the maximum discrepancy between the averaged values and the three corresponding experimental run results. As can be seen in Fig. 3.28(a), for horizontal surface, the contribution of buoyancy force to lift off decreases with increase in flow velocity, while the contribution of lift force to lift off increases with increase in flow velocity. Although buoyancy dominates for all flow velocities shown in Fig. 3.28(a), it shows that for horizontal surface, a large enough flow velocity could result in lift off being independent of buoyancy, and therefore independent of the level of gravity.

Figure 3.28 shows that irrespective of orientation and flow velocity, $(F_b + F_l) / A_l$ is constant, and equal to 2.25 N/m^2. This result means that for the bubble to lift off, the combined effect of gravity and inertia is the same, regardless of flow velocity and gravity. This is a significant result, as it means that a simple relationship between inertia, gravity and lift off diameter can be developed. From Fig. 3.28, the following relationship can be expressed

$$\frac{F_b + F_l}{A_l} = \frac{1}{3} r_l \left(\rho_l - \rho_v\right) g \cos\left(\frac{\pi\varphi}{180}\right) + \frac{1}{3} r_l C_l \rho_l \dot{\gamma}_{r_l} \left|U(r_l) - U_{bubble}\right| = 2.25 \text{ N/m}^2 \quad (3.21)$$

hence the lift off radius r_l is given as

$$r_l = 2.25\left(\frac{1}{3}\left(\rho_l - \rho_v\right) g \cos\left(\frac{\pi\varphi}{180}\right) + \frac{1}{3} C_l \rho_l \dot{\gamma}_{r_l} \left|U(r_l) - U_{bubble}\right|\right)^{-1} \quad (3.22)$$

Note that Eq. (3.22) is a function of fluid properties, heater orientation and bulk liquid velocity. However, the bubble sliding velocity at lift off is also required for all flow conditions, as well as bubble lift off radius, in order to calculate the product $C_l \dot{\gamma}_{r_l} \left|U(r_l) - U_{bubble}\right|$. In order to make this model a general one that would not require any empirical information, one would need to develop a model to predict bubble sliding velocity, as well as bubble growth rate. To do so, one possible approach would be to develop a simple model based on the forces acting on the bubble in the x-direction, parallel to the heater wall. However, as written earlier in this Section, it is not the object of this study, and therefore will not be attempted.

3.3 Experimental results – Aluminum test surface

The experiments conducted on a silicon test surface, presented in the previous sections, were reproduced using an aluminum test surface, to investigate the effects of contact angle on bubble dynamics. Flow velocity is varied from 0 m/s to 0.25 m/s, for horizontal and vertical surfaces. The integrality of the experimental data for aluminum surface is available in Appendix B.

3.3.1 Bubble dynamics

Bubble departure

Data for bubble departure diameter is shown in Fig. 3.29, for various orientations, flow velocities and heater material. As can be seen in Fig. 3.29, orientation has a weaker effect on bubble departure diameter for low contact angle than for a larger one. Also, it is important to note that the values of departure diameter are similar for both surfaces, and that departure times are much smaller for aluminum than for silicon (refer to data in appendices A and B). Uncertainty is therefore important, and these results are to be considered with caution.

Bubble lift off

Figure 3.30 shows the effect of orientation and velocity on lift off diameter. Data for silicon and aluminum are plotted in Fig. 3.30. Contact angle doesn't appear to have an effect on the trend of the curves. Lift off diameter increases with inclination, for constant flow velocity, and decreases with increase in flow velocity, for constant orientation. What changes with contact angle is the magnitude of lift off diameter. For similar conditions,

lift off diameter is much smaller for a lower contact angle. This is due to the fact that as the contribution of surface tension force decreases with decrease in contact angle. As a result a smaller bubble volume is required for lift off, since lift force should be able to exceed the forces keeping the bubble on the surface. Lift off times for silicon and aluminum are shown in Fig. 3.31. As for lift off diameter, the trend is the same for lift off time for both materials, but the values are different. The lift off times for aluminum are much smaller than that for silicon. Growth rate is not affected dramatically by contact angle, which means that smaller lift off diameters result in shorter growth periods.

Bubble sliding distance

The effects of orientation, flow velocity and contact angle on sliding distance are shown in Fig. 3.32. The trend is the same for low and high contact angle. Again, the difference is in the magnitude of the sliding distance. For low contact angle, the growth period is much shorter than for larger contact angle and similar parameters. This in turn leads to a shorter sliding distance, since sliding time is reduced. This effect appears to be stronger at low flow velocities. As for silicon, the effect of flow velocity on sliding distance is hard to quantify, and depends on orientation.

Bubble velocity at lift off

Comparison between velocities at lift off for silicon and aluminum, as a function of orientation and flow velocity, is shown in Fig. 3.33. Bubble velocity at lift off increases monotonously with flow velocity and orientation in both cases. Also, for both surface materials, in horizontal conditions the bubble velocity at lift off remains lower than flow

velocity, ands sliding velocity becomes larger than flow velocity, for vertical surfaces. Also, for horizontal surface, contact angle appears to have no effect on sliding velocity. On the other hand, an interesting difference between the results for aluminum and silicon occurs for vertical surface: bubble sliding velocity is larger for lower contact angle.

Maximum bubble base diameter

Maximum bubble base diameter for both aluminum and silicon surfaces is shown in Fig. 3.34. Bubble diameter decreases with decrease in contact angles. Because of the low contact angle, bubbles are smaller and more spherical. A smaller base diameter is a consequence of this shape and size.

3.3.2 Application of the force balance to bubble growth cycles

3.3.2.1 Flow boiling

Figure 3.35 shows the forces acting on a bubble growing on a horizontal aluminum heater, for bulk liquid velocities of 0.076 m/s (Fig. 3.35(a)) and 0.25 m/s (Fig. 3.35(b)). Similarly, Fig. 3.36 shows the forces acting on a bubble growing on a vertical aluminum heater, for bulk liquid velocities of 0.076 m/s (Fig. 3.36(a)) and 0.25 m/s (Fig. 3.36(b)). Similarly to the observations made for silicon surfaces in Figs. 3.22 and 3.23, Figs. 3.35 and 3.36 show that the sum of the forces acting on the bubble becomes positive at the same time than the bubble base starts to shrink. Buoyancy and contact pressure forces dominate the initiation of the lift off process for $\varphi = 0^o$, and $U_{bulk} = 0.076$ m/s, while for $\varphi = 0^o$, and $U_{bulk} = 0.25$ m/s, Fig. 3.35(b) shows that the contribution of buoyancy and lift forces towards the initiation of lift off is similar, and that both forces are smaller than the

contact pressure force. Figure 3.36 shows that for all velocities, lift force becomes extremely large for $\varphi = 90^{o}$, as shown in Fig. 3.23 for silicon surfaces.

3.3.2.2 Pool boiling

Figure 3.37 shows the forces acting on a bubble growing on a vertical aluminum heater for pool boiling conditions Similarly to the results shown in Figs. 3.22 to 3.24 for silicon surfaces, and Figs 3.35 to 3.36 for aluminum surfaces, for pool boiling on a vertical aluminum surface, the sum of the forces acting on the bubble becomes positive at the same time than the bubble base starts to shrink. The lift force is becomes extremely large, due to the large sliding velocity of the bubble, that is being pushed by the buoyancy force acting in the direction parallel to the heater surface. As a result, for a vertical wall, lift off is controlled by the lift force, and indirectly by buoyancy since it causes the bubble to the slide along the heater wall.

3.3.3 Modeling of bubble lift off diameter

Figure 3.38 shows the comparison between $F_b + F_s + F_{cp}$ and F_s, at the instant where bubble lift off is initiated (i.e. when bubble base diameter is maximum). As can be seen in Fig. 3.38, the detaching forces acting on the bubble are equal to the attaching forces, regardless of orientation and contact angle. Also, as seen in Figs. 3.39 and 3.40, $D_{base,max} = D / 3$ and $D_l = 1.25 \times D$, regardless of orientation and contact angles. Therefore, Eqs. (3.18) and (3.19) can be used as a base to develop a model that could predict bubble lift off diameter.

As shown in Figs. 3.22 to 3.24 for silicon surfaces, and Figs 3.35 to 3.37 for aluminum surfaces, when bubble lift off occurs, the only non-negligible forces acting on the bubble are the lift and buoyancy forces. Figure 3.41 shows the forces acting on a bubble at lift off, as a function of flow velocity, for horizontal (Fig. 3.41(a)) and vertical (Fig. 3.41(b)) aluminum surfaces. These forces are presented in reduced form, in which F_b, F_l and $F_b + F_l$ are divided by the bubble surface area at lift off A_l, as in Fig. 3.28 for silicon surfaces.

As can be seen in Fig. 3.41(a), for horizontal surface, the contribution of buoyancy force to lift off decreases with increase in flow velocity, while the contribution of lift force to lift off increases with increase in flow velocity. Also, for a liquid velocity of 0.25 m/s, the contribution from buoyancy and lift forces is identical. This means that for a higher velocity, lift off would be dominated by lift force over buoyancy force, even for a horizontal heater. Figure 3.41 also shows that irrespective of orientation and flow velocity, $(F_b + F_l) / A_l$ is constant. Similarly to what was observed in Fig 3.28 for horizontal and vertical silicon surfaces, Fig. 3.41(b) shows that $(F_b + F_l) / A_l = 2.25$ N/m^2 for vertical aluminum surface. For horizontal aluminum surfaces, however, it is found that $(F_b + F_l) / A_l = 1.75$ N/m^2. This discrepancy is due to the fact that the relative contribution from lift force to lift off is much larger for horizontal aluminum surface than for horizontal silicon surface. Bubble sliding velocity approaches that of the flow for horizontal surfaces, resulting in a much higher uncertainty in calculating relative velocity (and thus lift force), which could explain this difference. Therefore one can assume that regardless of contact angle and flow velocity, $(F_b + F_l) / A_l = 2.25$ N/m^2 for horizontal and vertical surfaces, and that Eq. (3.22) is always applicable.

3.4 Experimental results – Inclined aluminum and silicon surfaces (30^o, 45^o, and 60^o)

To study the effect of the magnitude of the gravity component normal and parallel to the heater surface, in addition to the effect of velocity and contact angle, several orientations (30^o, 45^o, 60^o) were also investigated, for velocities ranging from 0 m/s to 0.25 m/s, and for aluminum and silicon surfaces. The integrality of the experimental data is available in Appendices A and B. The results obtained are discussed in the following section.

3.4.1 Bubble dynamics

Bubble departure

The coupled effects of orientation and velocity on bubble departure diameter are shown in Fig. 3.42. The change in magnitude of gravity (in normal and parallel direction to the surface) created by a change in orientation affects the departure diameter. The normal component of gravity decreases and the parallel component increases with increase in inclination (form 0^o to 90^o upflow, through 30^o, 45^o and 60^o). The departure diameter decreases with velocity, irrespective of orientation. Most importantly, departure diameter decreases with increase in orientation (from vertical to horizontal). This is due to the fact that the contribution of buoyancy to bubble departure increases with inclination, which in turns decrease departure diameter.

Bubble lift off

Figure 3.43 shows the effect of orientation and velocity on lift off diameter. Lift off diameter increases with both flow velocity and orientation. As stated earlier, the normal component of gravity decreases with increase in orientation, resulting in a smaller contribution of buoyancy towards lift off. As a consequence, the bubble needs to grow to a larger size for the lift force to be able to compensate the forces keeping the bubble on the surface. Also, for the highest flow velocity (0.25 m/s), it appears that the effect of orientation on lift off diameter is reduced. Lift off times for silicon and aluminum are shown in Fig. 3.44. As for lift off diameter, lift off time decreases with increase in flow velocity, and increases with increase in surface inclination.

Bubble sliding distance

Sliding distance increases with orientation, as shown in Fig. 3.45. This effect appears to be stronger at low flow velocities. On the other hand, the effect of velocity on sliding distance is unclear, and depends on orientation. For horizontal surface, sliding distance is almost independent of velocity, while for 45^{o} to 90^{o} inclined surfaces sliding distance decreases with velocity.

Bubble velocity at lift off

Bubble velocity at lift off increases with both orientation and flow velocity, rather monotonically, as can be seen from Fig. 3.46. For horizontal surface, the bubble velocity at lift off remains slower than flow velocity, but as inclination increases, sliding velocity

at lift off becomes larger than flow velocity in all cases. The bubble velocity at lift off is a crucial parameter in determining the lift force.

Maximum bubble base diameter

In general, bubble base diameter decreases with increase in velocity, and increases with increase in inclination, as shown in Fig. 3.47. Base diameter is an important parameter in calculation of forces attaching the bubble to the heater surface, as well as in calculating heat transfer. Base diameter depends on bubble size, as well as contact angle.

3.4.2 Application of the force balance to bubble growth cycles

3.4.2.1 Flow boiling

Figure 3.48 shows the forces acting on a bubble growing on a 45^o inclined aluminum heater, for bulk liquid velocities of 0.076 m/s (Fig. 3.48(a)) and 0.25 m/s (Fig. 3.48(b)). Similarly, Fig. 3.49 shows the forces acting on a bubble growing on a 45^o inclined silicon heater, for bulk liquid velocities of 0.076 m/s (Fig. 3.49(a)) and 0.25 m/s (Fig. 3.49(b)). Figure 3.48 and 3.49 show that the sum of the forces acting on the bubble becomes positive at the same time than the bubble base starts to shrink. Buoyancy and contact pressure forces dominate the initiation of the lift off process for U_{bulk} = 0.076 m/s, while for U_{bulk} = 0.25 m/s, Figs. 3.48(b) and 3.49(b) show that the contribution of buoyancy and lift forces towards the initiation of lift off is similar, and that both forces are smaller than the contact pressure force.

3.4.2.2 Pool boiling

Figure 3.50 shows the forces acting on a bubble growing on a 45^o inclined aluminum heater for pool boiling conditions, and Fig. 3.51 shows the forces acting on a bubble growing on a 45^o inclined silicon heater for pool boiling conditions Similarly to the results shown in Figs. 3.24 and 3.37 for vertical surfaces, the sum of the forces acting on the bubble becomes positive at the same time than the bubble base starts to shrink, for pool boiling on a 45^o inclined surface. However, as opposed to the vertical surface results, the contribution of lift force toward the initiation of bubble lift off is very small compared to that of contact pressure and buoyancy forces. Also, buoyancy force is much larger than lift force when the bubble lifts off from the heater surface.

3.4.3 Modeling of bubble lift off diameter

Figure 3.52 shows the comparison between $F_b + F_s + F_{cp}$ and F_s, at the instant where bubble lift off is initiated (i.e. when bubble base diameter is maximum). As can be seen in Fig. 3.52, the detaching forces acting on the bubble are equal to the attaching forces, regardless of orientation ($0^o \leq \varphi \leq 90^o$) and contact angle (19^o and 56^o). Also, as seen in Figs. 3.53 and 3.54, $D_{base,max} = D / 3$ and $D_l = 1.25 \times D$, regardless of orientation and contact angles. Therefore, Eqs. (3.18) and (3.19) can be used as a base to develop a model that could predict bubble lift off diameter.

Figure 3.55 shows the forces acting on a bubble at lift off, as a function of flow velocity, for 30^o inclined (Fig. 3.55(a)), 45^o inclined (Fig. 3.55(b)), and vertical (Fig. 3.55(c)) aluminum surfaces. Similarly, Fig. 3.56 shows the forces acting on a bubble at lift off, as a function of flow velocity, for 30^o inclined (Fig. 3.56(a)), 45^o inclined (Fig.

3.56(b)), and vertical (Fig. 3.56(c)) silicon surfaces. These forces are presented in reduced form, in which F_b, F_l and $F_b + F_l$ are divided by the bubble surface area at lift off A_l.

Figures 3.55 and 3.56 show that the contribution of buoyancy force to lift off decreases with increase in flow velocity, while the contribution of lift force to lift off increases with increase in flow velocity, irrespective of orientation. Also, comparison between Figs. 3.55 and 3.56 shows that for given condition, the relative contribution of lift force to bubble lift off is larger for aluminum surface than for silicon surface. Figures 3.55 and 3.56 also show that irrespective of orientation, flow velocity, and heater material, $(F_b + F_l) / A_l$ is constant. Similarly to what was observed in Figs. 3.28 and 3.41 for horizontal and vertical aluminum and silicon surfaces, Figs. 3.551 and 3.56 show that $(F_b + F_l) / A_l = 2.25$ N/m^2. For 30^o inclined silicon surface, and pool boiling conditions, it is found that $(F_b + F_l) / A_l = 3.10$ N/m^2. This large difference can be attributed to the measurement uncertainty, which is particularly large for pool boiling conditions.

As a result, regardless of orientation, contact angle and flow velocity, $(F_b + F_l) / A_l = 2.25$ N/m^2, as shown in Fig. 3.57. In Fig. 3.57, the sum of buoyancy and lift forces divided by bubble surface area is plotted as a function of flow velocity, for all orientations, flow velocities and surface materials. As can be seen in Fig. 3.57, almost all of the data is within ± 15%, which shows that Eq. (3.22) is always applicable, regardless of heater material, surface orientation and flow velocity.

3.5 Experimental results – Reduced gravity experiments

Reduced gravity experiments, using a horizontal aluminum surface, were conducted in April 2012 aboard the Zero-G Corporation aircraft, during a parabolic flight experimental campaign, conducted by NASA. The same test rig was used for these experiments. Unfortunately, on the two consecutive days that the experiments were conducted, the laptop computer used for data collection (data acquisition and high speed video) malfunctioned during the reduced gravity phases of the flights. Because of the technical difficulties encountered, no experimental data were obtained at reduced gravity levels.

3.6 Chapter conclusions

From the above results and discussion, the following key observations can be made:

Bubble dynamics

- Irrespective of orientation and contact angle, departure and lift off diameters decrease with increase in bulk liquid velocity.
- At a given velocity, orientation has almost no effect on departure diameter.
- Contact angle has no effect on departure diameter. On the other hand, decrease in contact angle leads to decrease in lift off diameter.
- For given conditions, bubble lift off diameter increases when the gravity component normal to the heater is decreased. The effect gravity on lift off diameter is reduced at high liquid bulk velocities.

- For the majority of cases, the bubble sliding distance increases with increase in bulk liquid velocity and decrease in the magnitude of the component of gravity normal to the heater.
- For given conditions, sliding distance decreases with decrease in contact angle
- The bubble velocity at lift off increases with increase in flow velocity, as well as with increase in component of gravity parallel to heater surface. With increase in component of gravity parallel to the surface, bubble velocity becomes larger than bulk liquid velocity.
- Increase in component of gravity parallel to the surface and decrease in contact angle lead to higher bubble velocity at lift off, for similar conditions.

Force balance and lift off diameter modeling

- The validity of a simple force balance model to predict bubble lift off was demonstrated. These forces are the lift force (F_l), the buoyancy force (F_b), the surface tension force (F_s), the contact pressure force (F_{cp}), and the inertia of both the vapor and the liquid displaced by the growing bubble. Based on these forces two approaches were developed to model bubble lift off diameter.
- Bubble lift off is initiated at the instant when the sum of these forces becomes positive in the y-direction (normal to the heater). It coincides to the moment when the bubble base starts to shrink. It is found that at this instant, $D_{base} = D / 3$.
- Based on this force balance an expression for bubble diameter is developed. From this expression, one can determine the bubble lift off diameter, using the

following relationship: $D_l = 1.25 \times D$ (at $D_{base} = D_{base,max}$), for two contact angles (19^o and 56^o), $0^o \leq \varphi \leq 90^o$, and 0 m/s $\leq U_{bulk} \leq$ 0.25 m/s.

- When lift off occurs, buoyancy and lift forces are the only forces acting on the bubble, and regardless of orientation, contact angle and flow velocity, the ratio $(F_b + F_l) / A_l = 2.25$ N/m^2, where A_l is the bubble surface area at lift off.
- Based on this result, a simple bubble lift off diameter expression, applicable for two contact angles (19^o and 56^o), $0^o \leq \varphi \leq 90^o$, and 0 m/s $\leq U_{bulk} \leq$ 0.25 m/s, was developed.

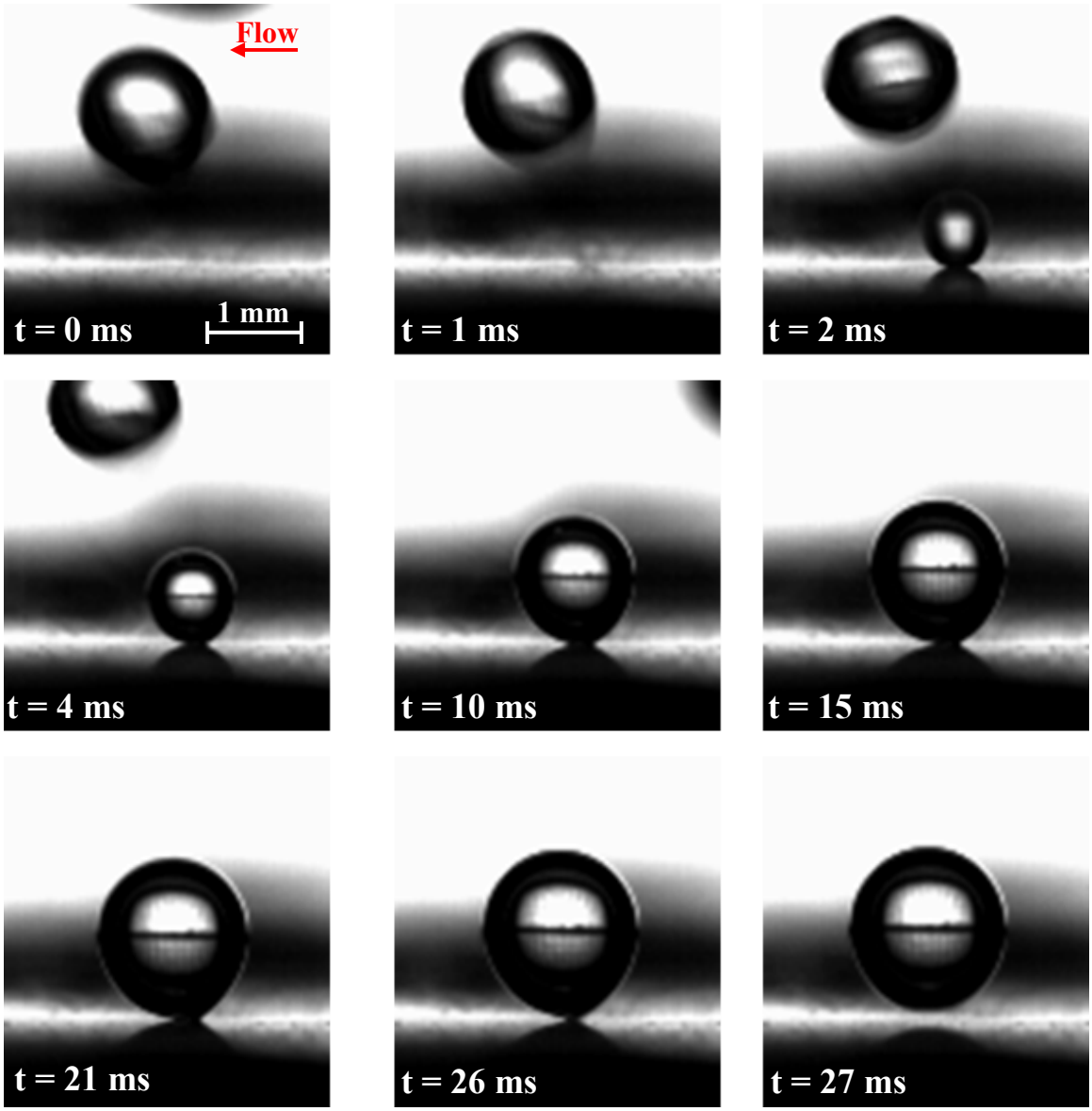

Figure 3.1 Bubble growth cycle for horizontal silicon surface, U_{bulk} = 0.076 m/s, ΔT_w = 5.5 ^oC, and ΔT_{sub} = 0.6 ^oC.

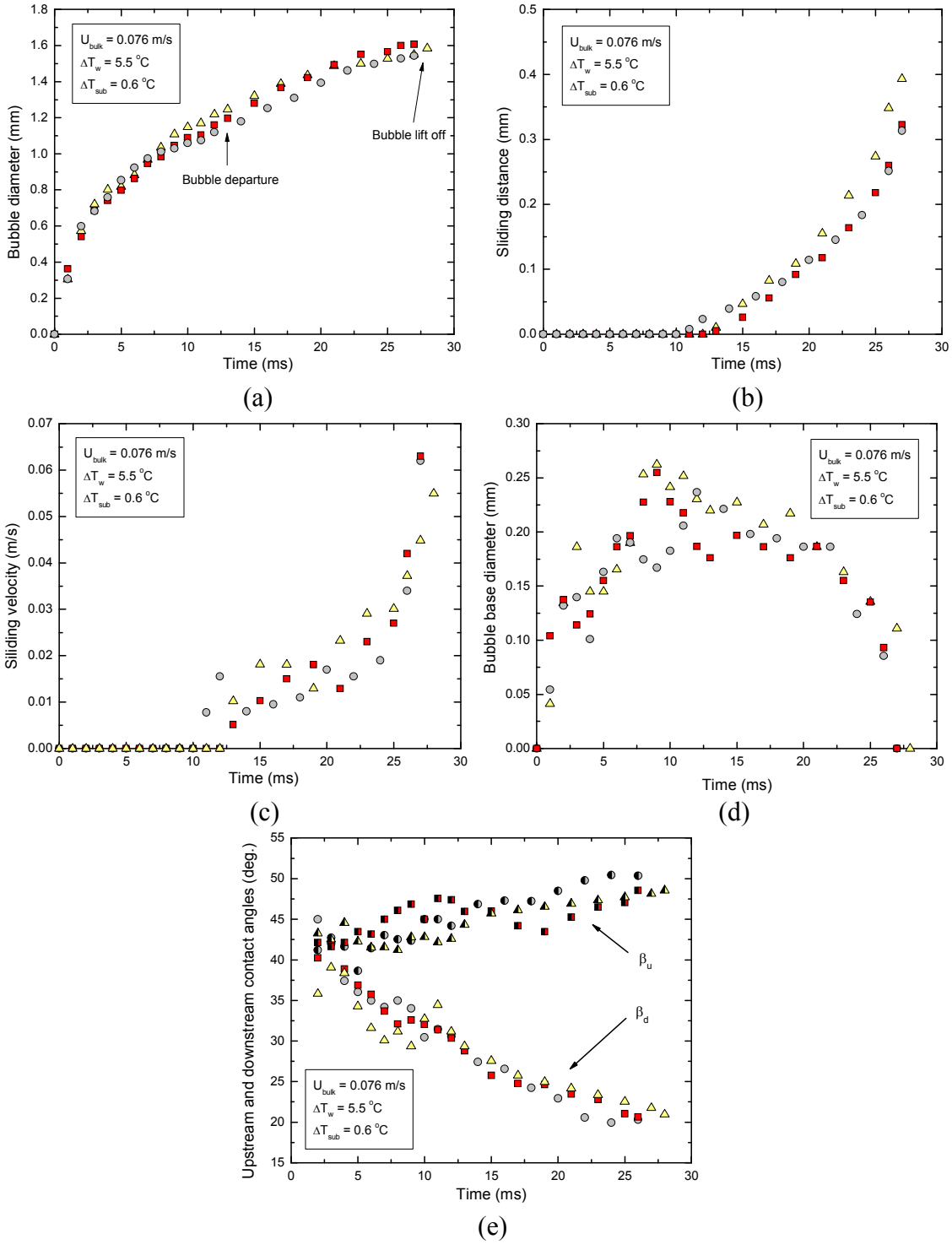

Figure 3.2 Measured quantities for horizontal silicon surface: (a) bubble diameter, (b) sliding distance, (c) sliding velocity, (d) bubble base diameter and (e) upstream and downstream contact angles, for U_{bulk} = 0.076 m/s, ΔT_w = 5.5 °C, and ΔT_{sub} = 0.6 °C.

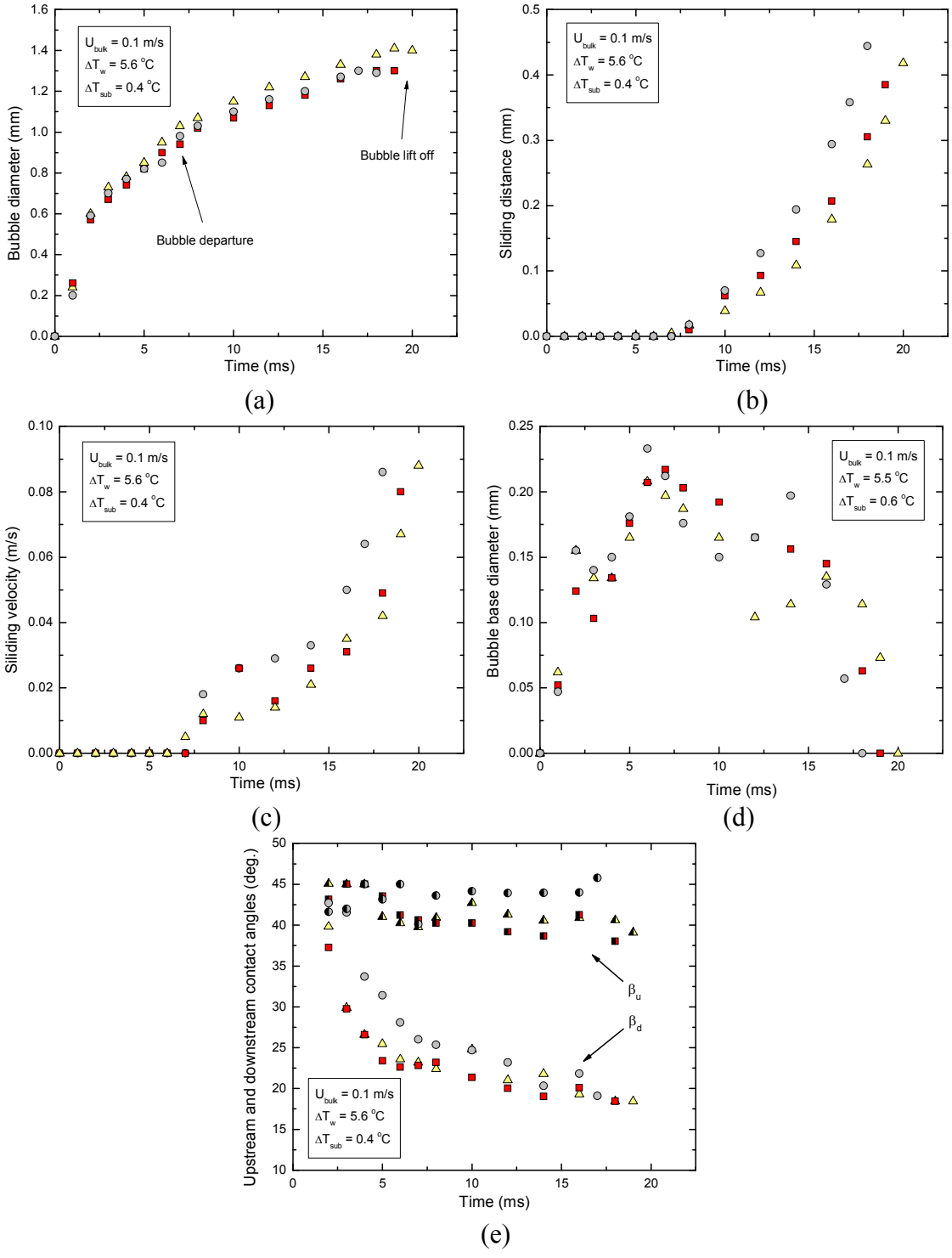

Figure 3.3 Measured quantities for horizontal silicon surface: (a) bubble diameter, (b) sliding distance, (c) sliding velocity, (d) bubble base diameter and (e) upstream and downstream contact angles, for U_{bulk} = 0.1 m/s, ΔT_w = 5.6 °C, and ΔT_{sub} = 0.4 °C.

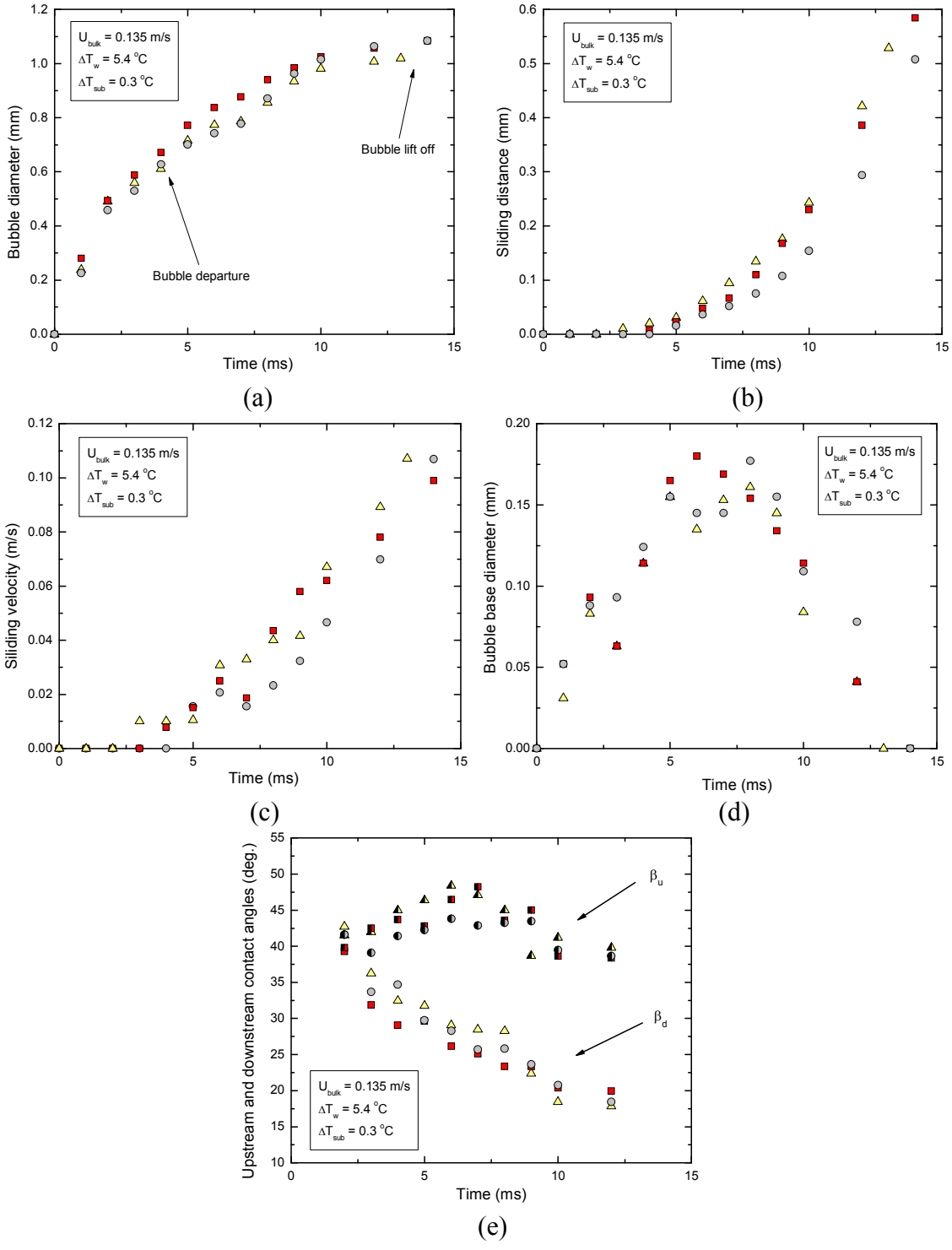

Figure 3.4 Measured quantities for horizontal silicon surface: (a) bubble diameter, (b) sliding distance, (c) sliding velocity, (d) bubble base diameter and (e) upstream and downstream contact angles, for U_{bulk} = 0.135 m/s, ΔT_w = 5.4 °C, and ΔT_{sub} = 0.3 °C.

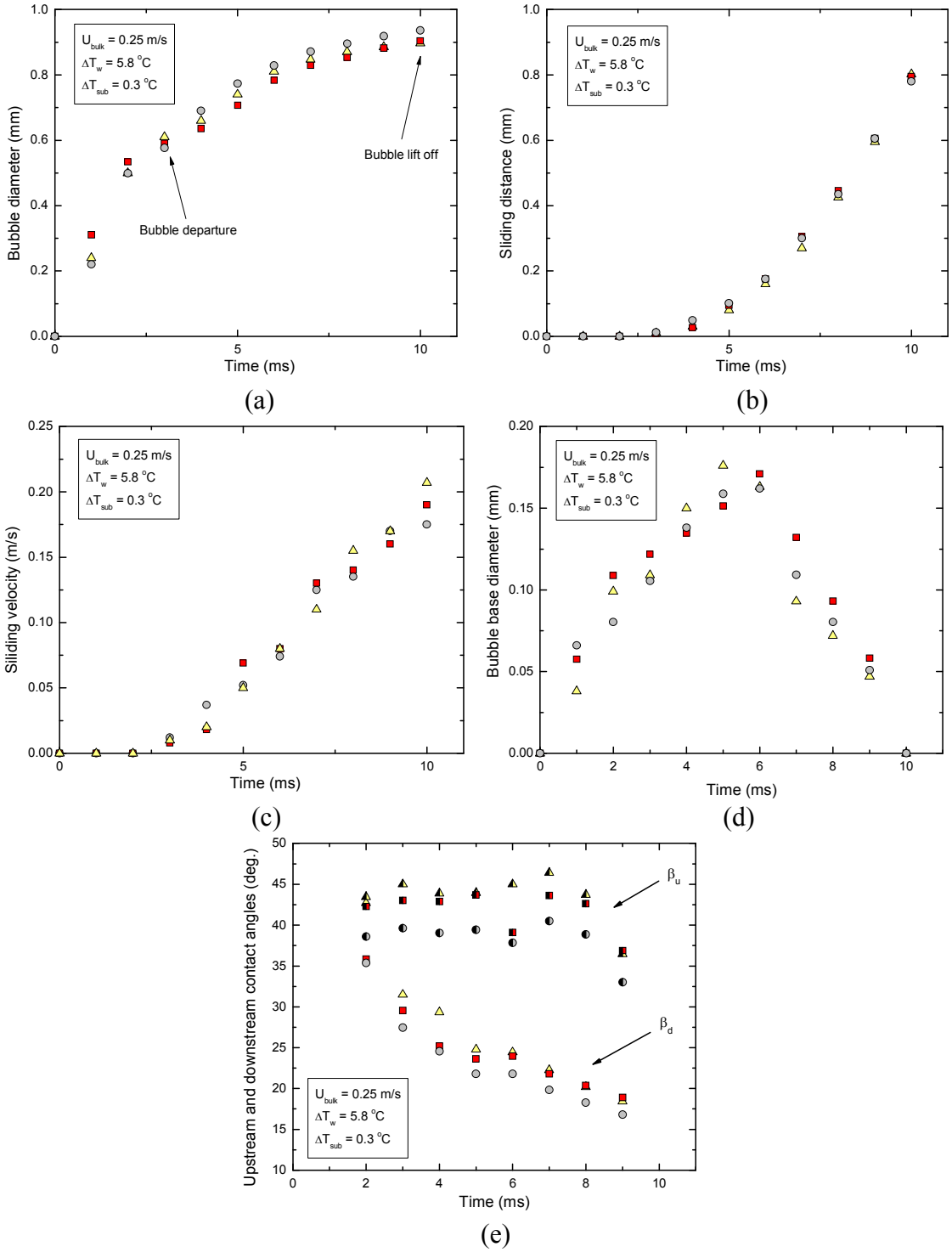

Figure 3.5 Measured quantities for horizontal silicon surface: (a) bubble diameter, (b) sliding distance, (c) sliding velocity, (d) bubble base diameter and (e) upstream and downstream contact angles, for U_{bulk} = 0.25 m/s, ΔT_w = 5.8 °C, and ΔT_{sub} = 0.3 °C.

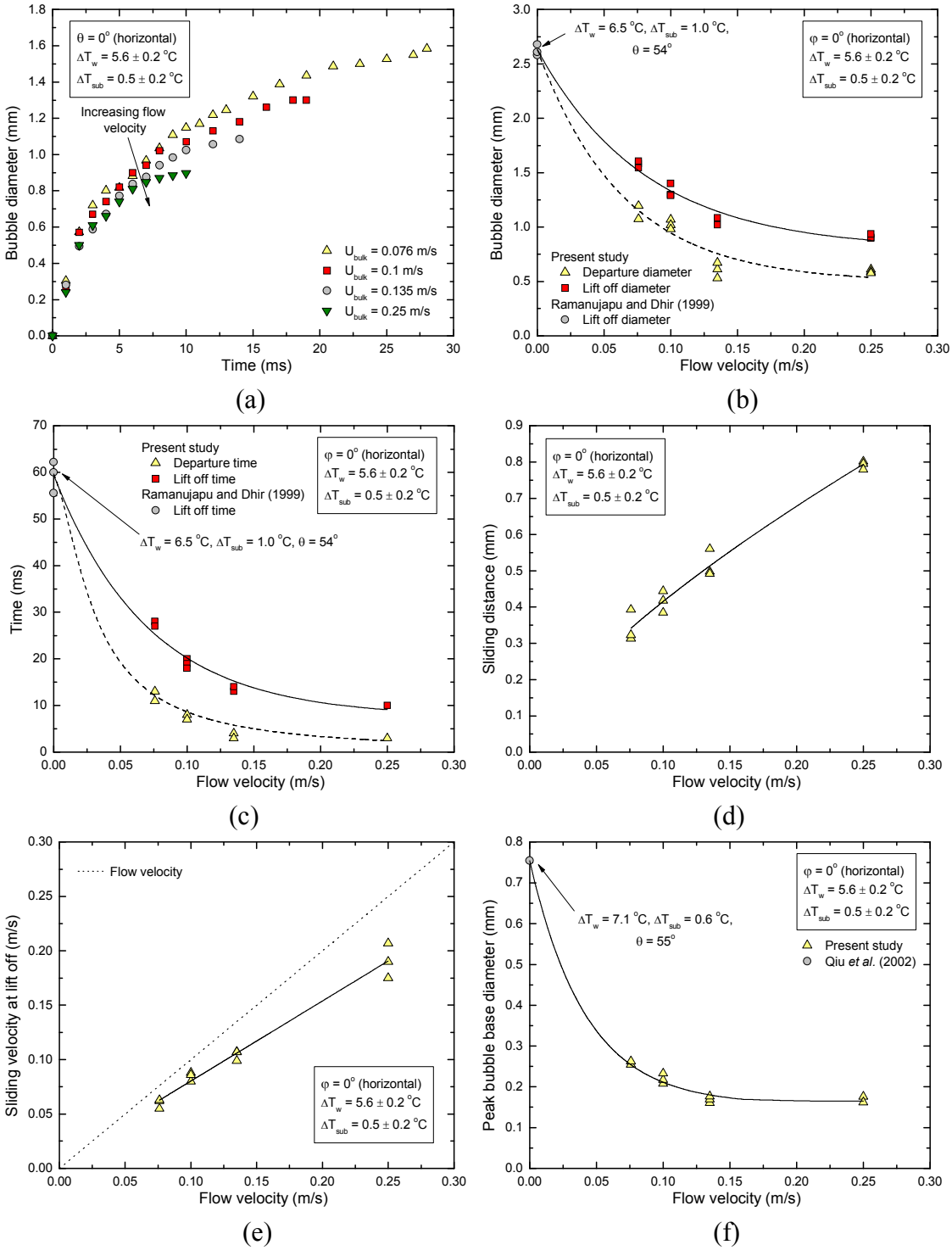

Figure 3.6 Effect of liquid bulk velocity on (a) variation of bubble diameter with time, (b) bubble departure and lift off diameters, (c) departure and lift off times, (d) sliding distance, (e) sliding velocity at lift off and (f) peak bubble base diameter – Horizontal silicon surface.

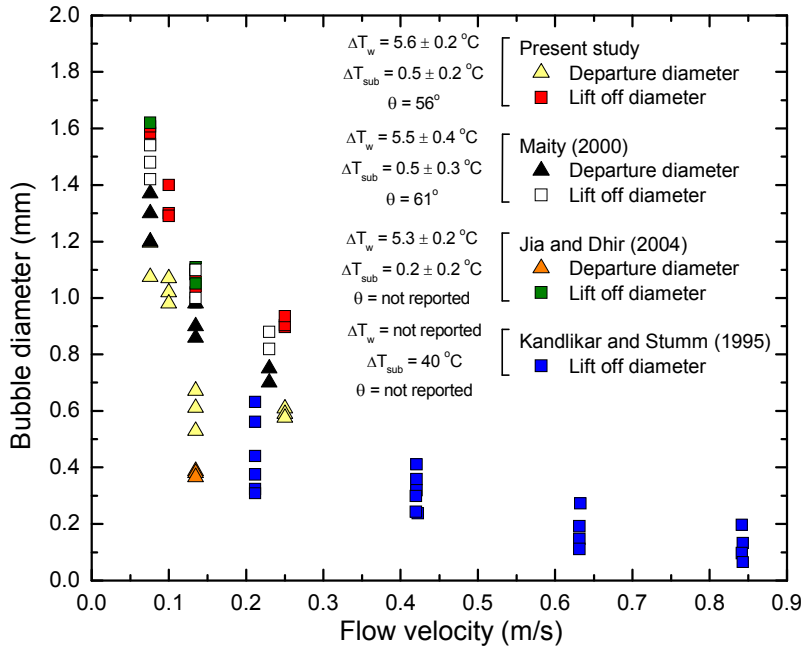

(a)

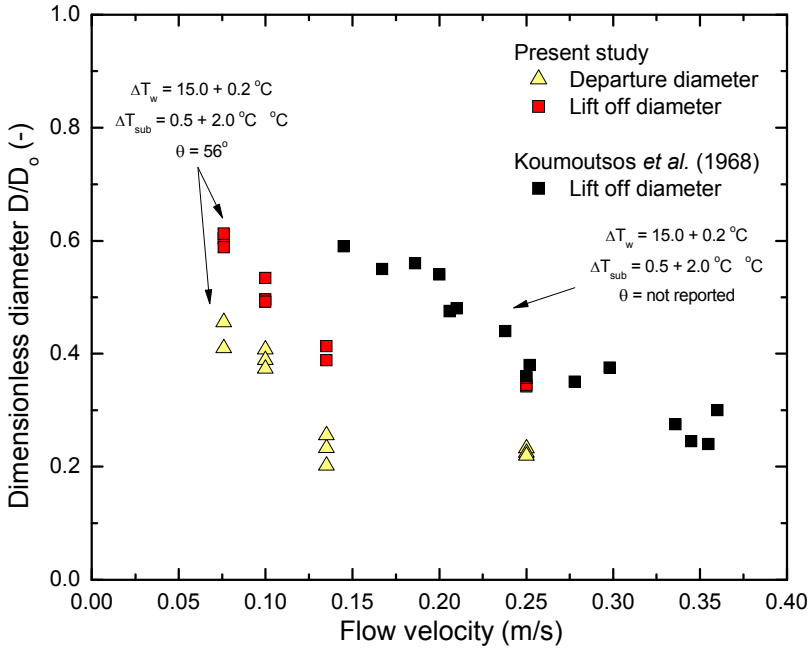

(b)

Figure 3.7 Comparison of departure and lift off diameters data from the present study (horizontal silicon surface) with data from the literature: (a) Kandlikar and Stumm (1995), Maity (2000), Jia and Dhir (2004), and, (b) Koumoutsos *et al.* (1968).

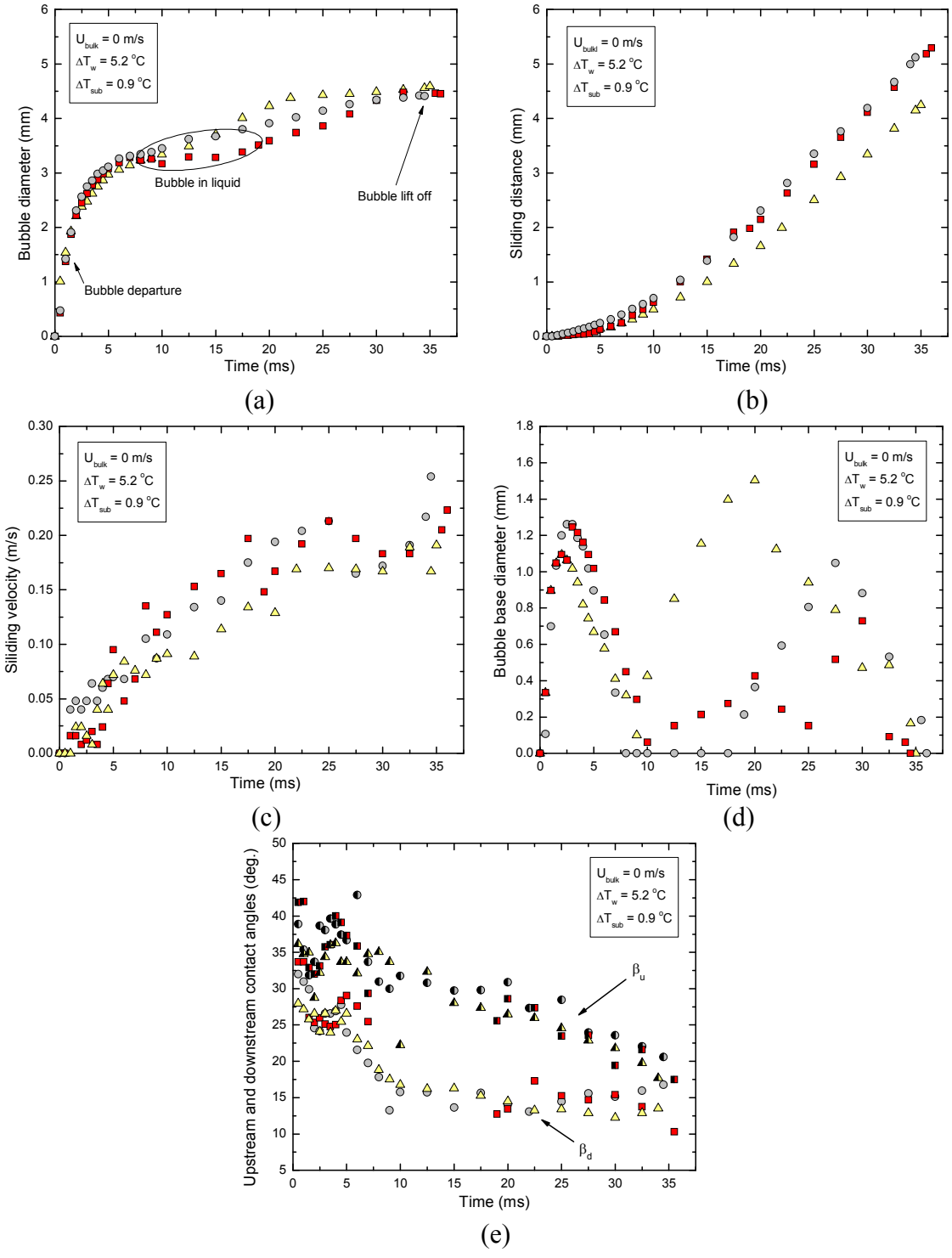

Figure 3.8 Measured quantities for vertical silicon surface: (a) bubble diameter, (b) sliding distance, (c) sliding velocity, (d) bubble base diameter and (e) upstream and downstream contact angles, for U_{bulk} = 0 m/s, ΔT_w = 5.2 °C, and ΔT_{sub} = 0.9 °C.

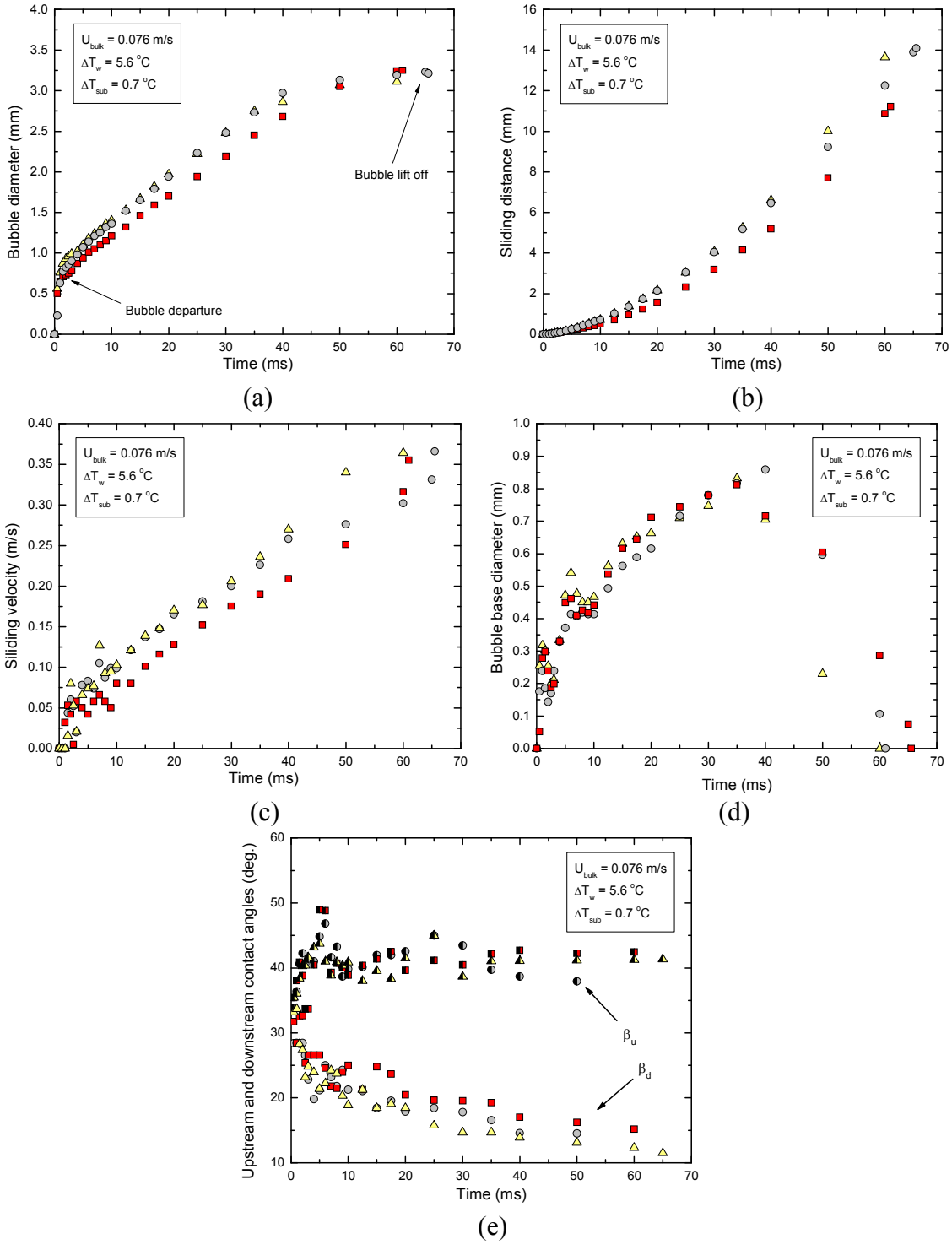

Figure 3.9 Measured quantities for vertical silicon surface: (a) bubble diameter, (b) sliding distance, (c) sliding velocity, (d) bubble base diameter and (e) upstream and downstream contact angles, for U_{bulk} = 0.076 m/s, ΔT_w = 5.6 °C, and ΔT_{sub} = 0.7 °C.

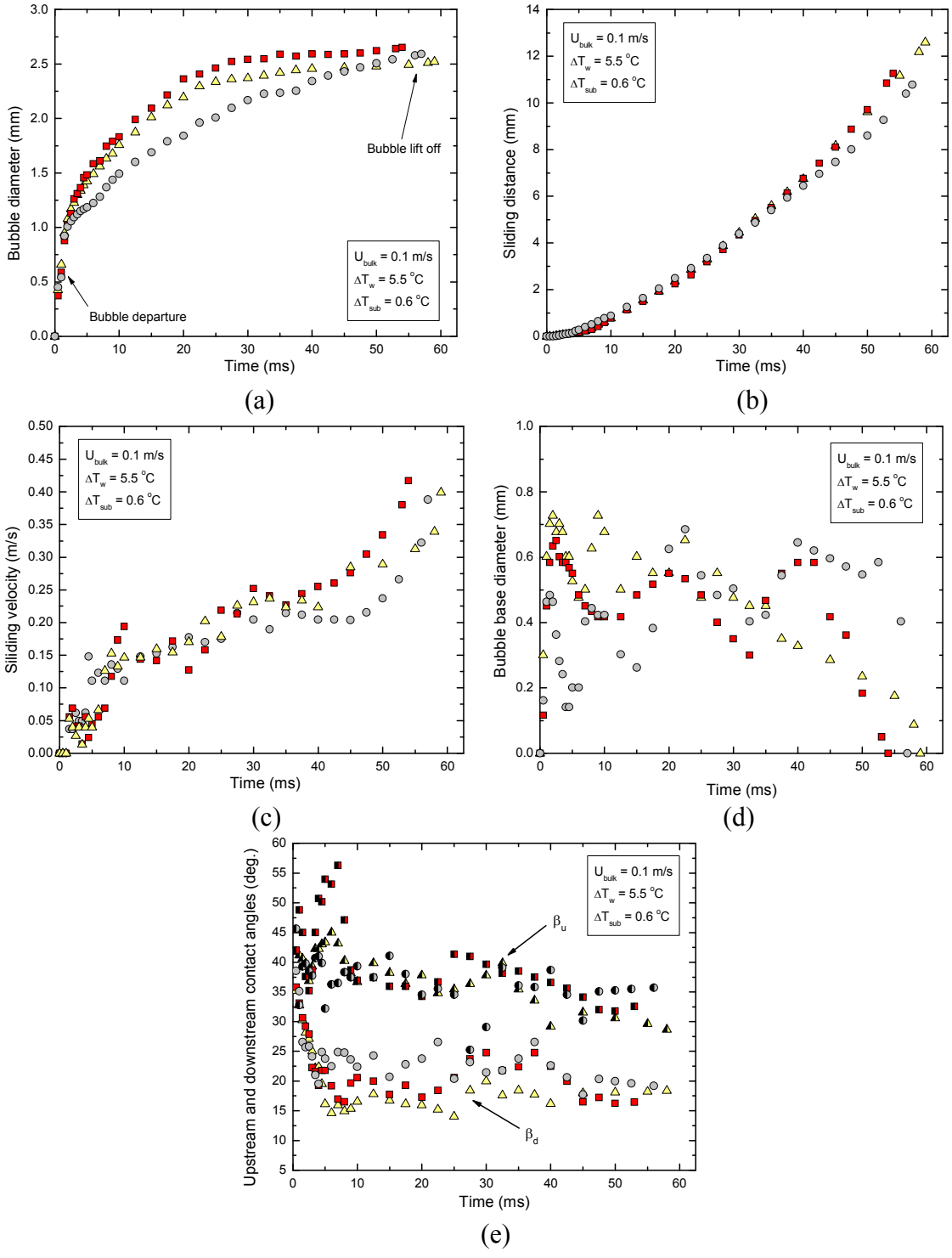

Figure 3.10 Measured quantities for vertical silicon surface: (a) bubble diameter, (b) sliding distance, (c) sliding velocity, (d) bubble base diameter and (e) upstream and downstream contact angles, for U_{bulk} = 0.1 m/s, ΔT_w = 5.5 °C, and ΔT_{sub} = 0.6 °C.

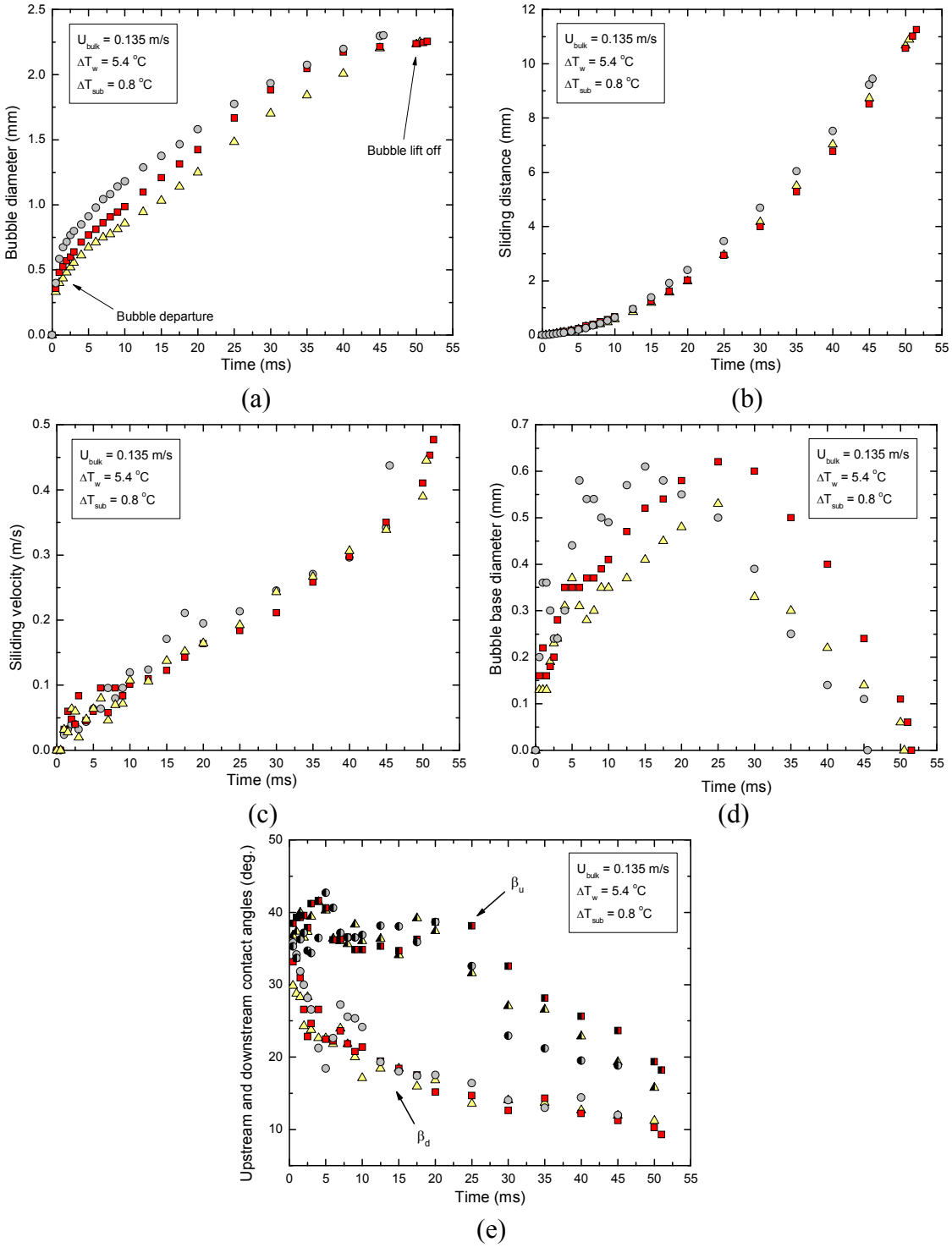

Figure 3.11 Measured quantities for vertical silicon surface: (a) bubble diameter, (b) sliding distance, (c) sliding velocity, (d) bubble base diameter and (e) upstream and downstream contact angles, for U_{bulk} = 0.135 m/s, ΔT_w = 5.4 °C, and ΔT_{sub} = 0.8 °C.

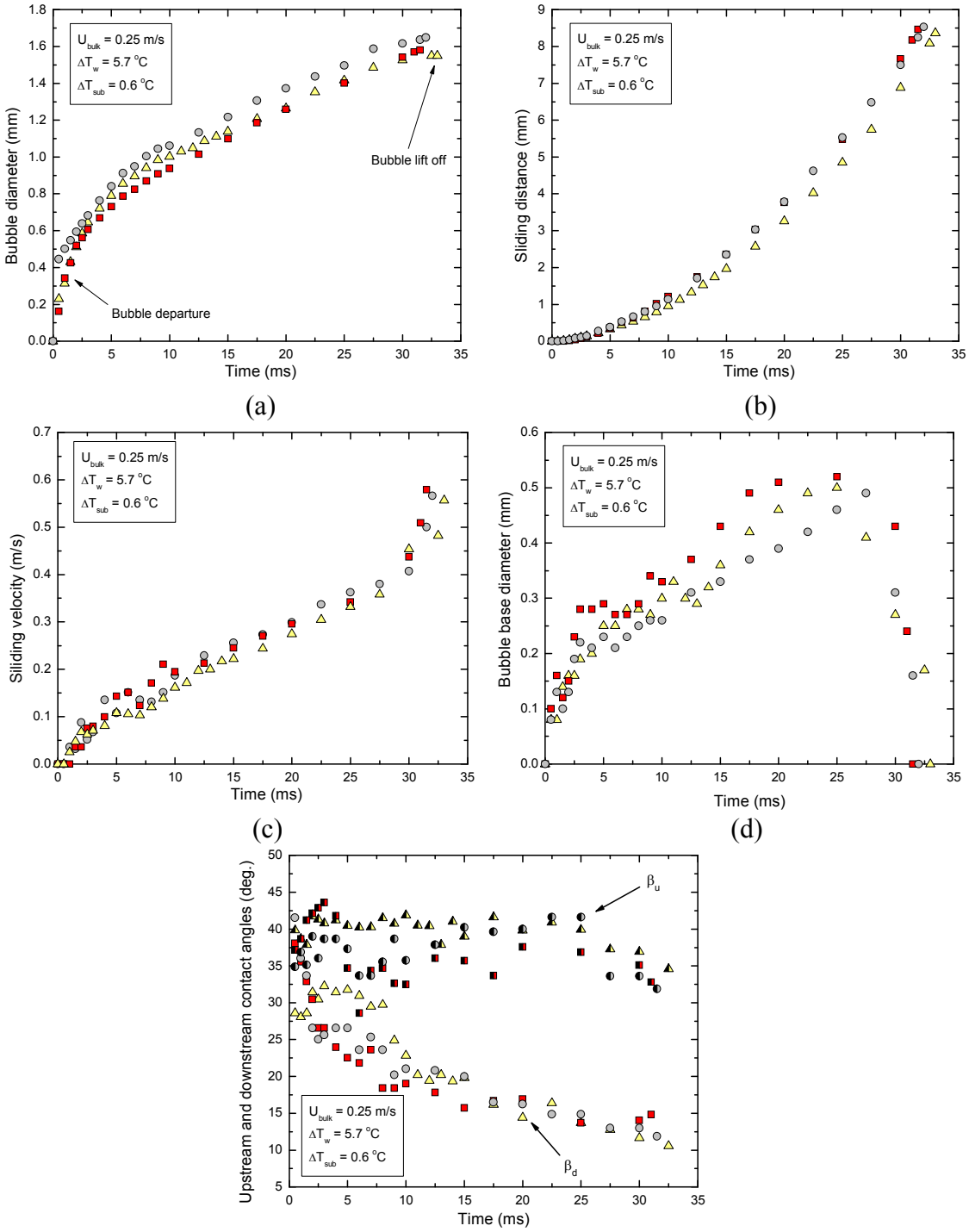

Figure 3.12 Measured quantities for vertical silicon surface: (a) bubble diameter, (b) sliding distance, (c) sliding velocity, (d) bubble base diameter and (e) upstream and downstream contact angles, for U_{bulk} = 0.25 m/s, ΔT_w = 5.7 °C, and ΔT_{sub} = 0.6 °C.

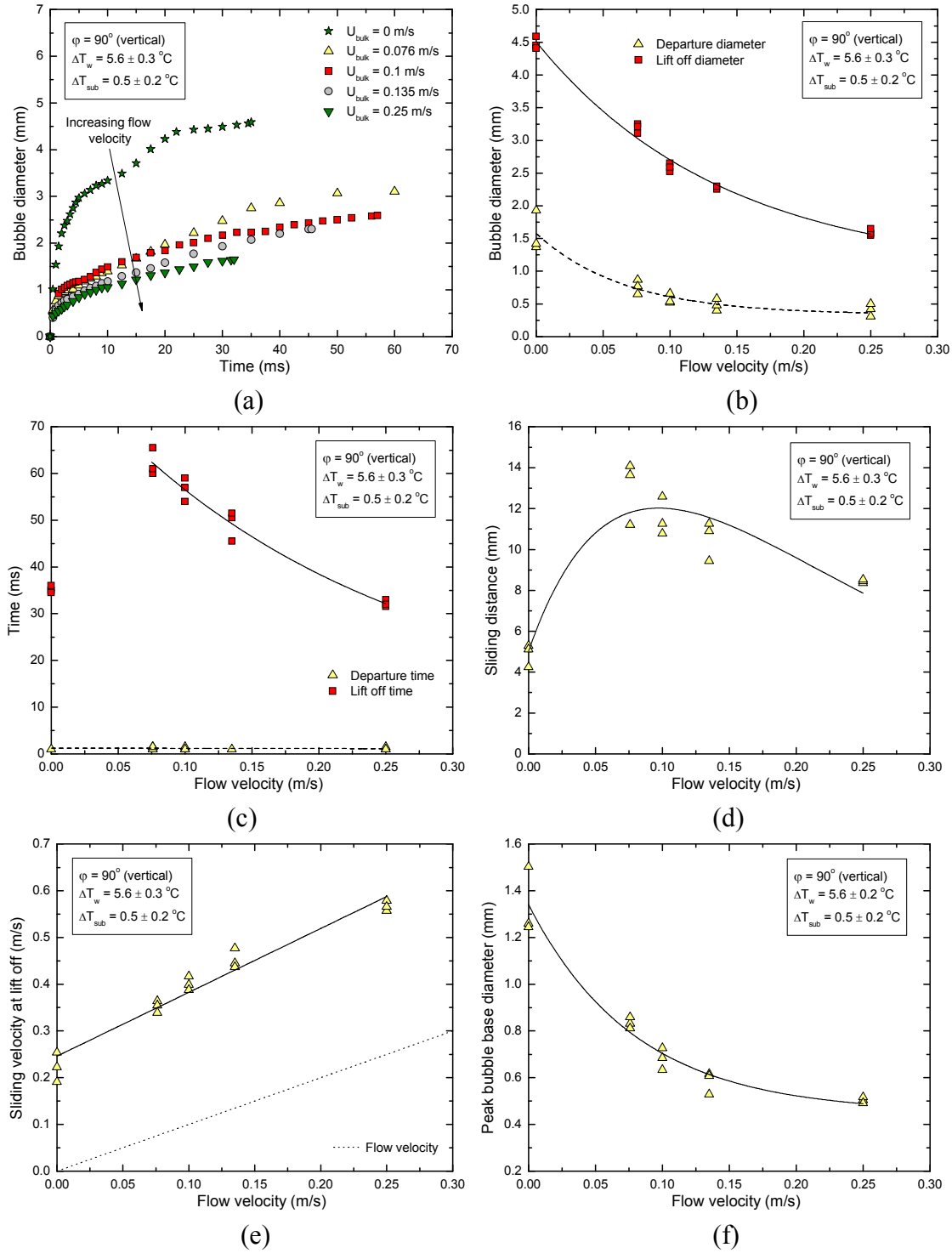

Figure 3.13 Effect of liquid bulk velocity on (a) variation of bubble diameter with time, (b) bubble departure and lift off diameters, (c) departure and lift off times, (d) sliding distance, (e) sliding velocity at lift off and (f) peak bubble base diameter – Vertical silicon surface.

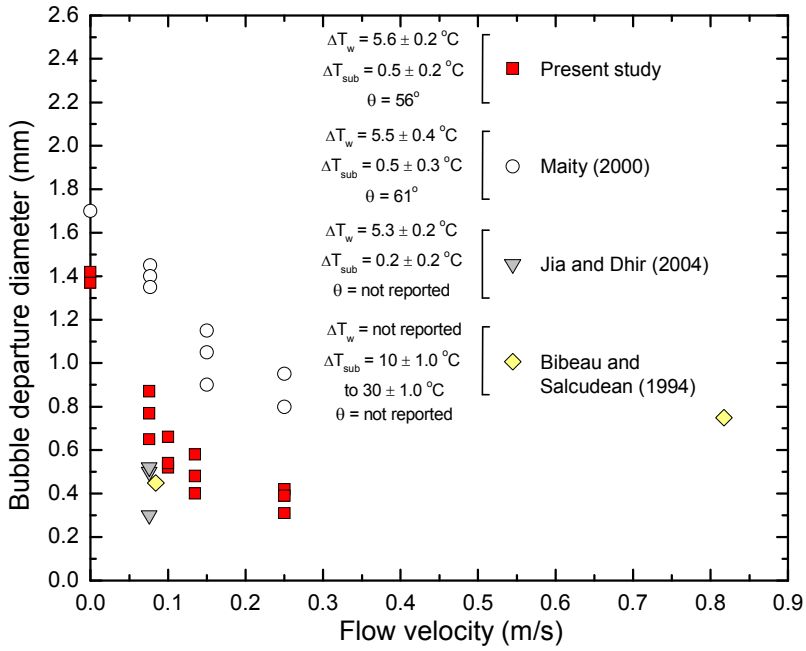

(a)

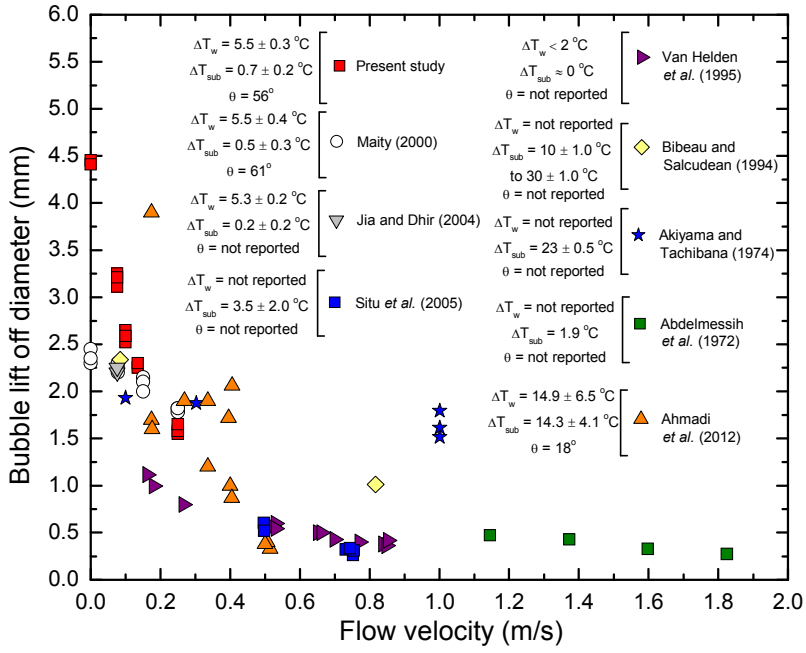

(b)

Figure 3.14 (a) Comparison of departure diameter data from the present study (vertical silicon surface) with data from the literature: Bibeau and Salcudean (1994), Maity (2000), and Jia and Dhir (2004), and (b) comparison of lift off diameter data from the present study (vertical silicon surface) with data from the literature: Abdelmessih *et al.* (1972), Akiyama and Tachibana (1974), Bibeau and Salcudean (1994), Van Helden (1995), Maity (2000), Jia and Dhir (2004), Situ *et al.* (2005) and Ahmadi *et al.* (2012).

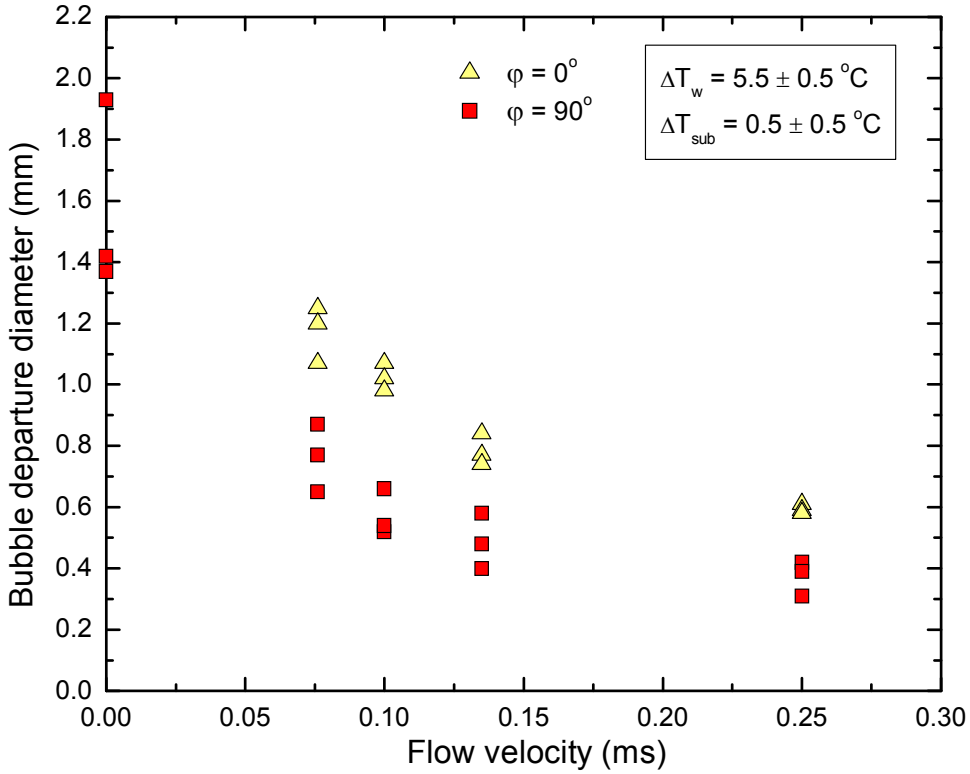

Figure 3.15 Effect of liquid bulk velocity and orientation on bubble departure diameter – Silicon surface.

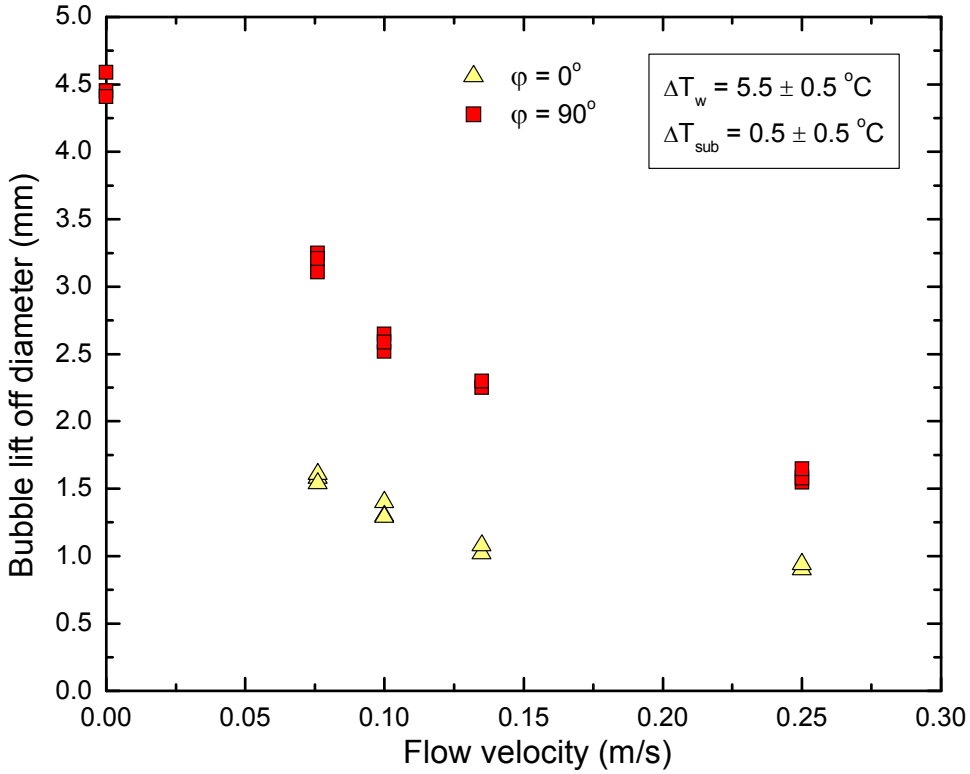

Figure 3.16 Effect of liquid bulk velocity and orientation on bubble lift off diameter – Silicon surface.

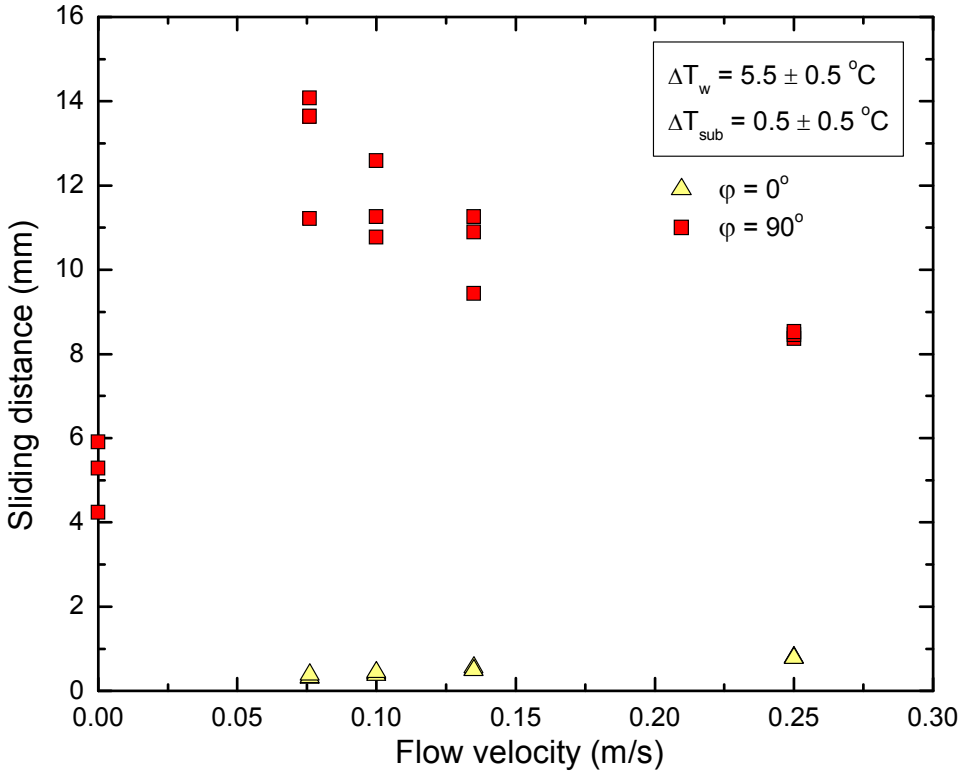

Figure 3.17 Effect of liquid bulk velocity and orientation on sliding distance – Silicon surface.

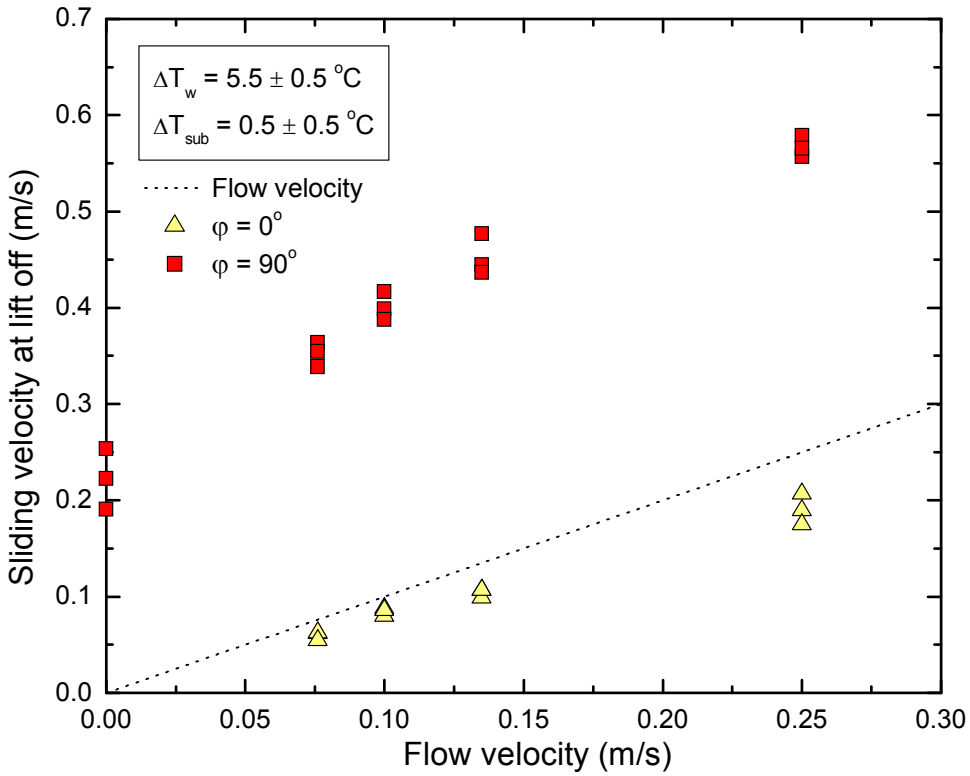

Figure 3.18 Effect of liquid bulk velocity and orientation on sliding velocity at lift off – Silicon surface.

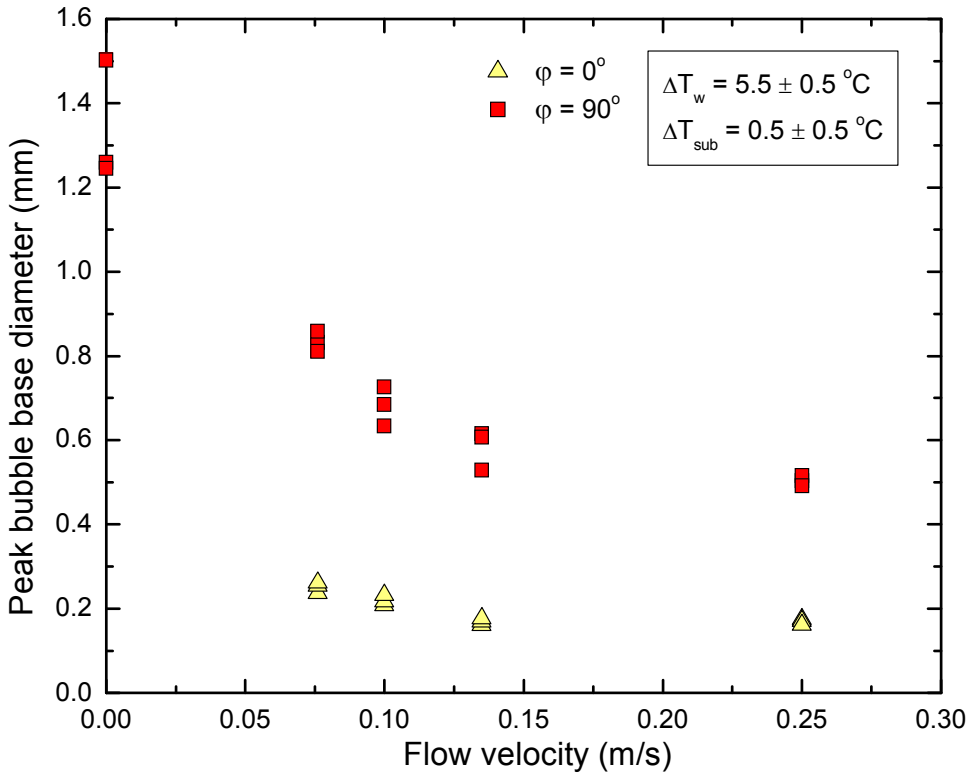

Figure 3.19 Effect of liquid bulk velocity and orientation on peak bubble base diameter – Silicon surface.

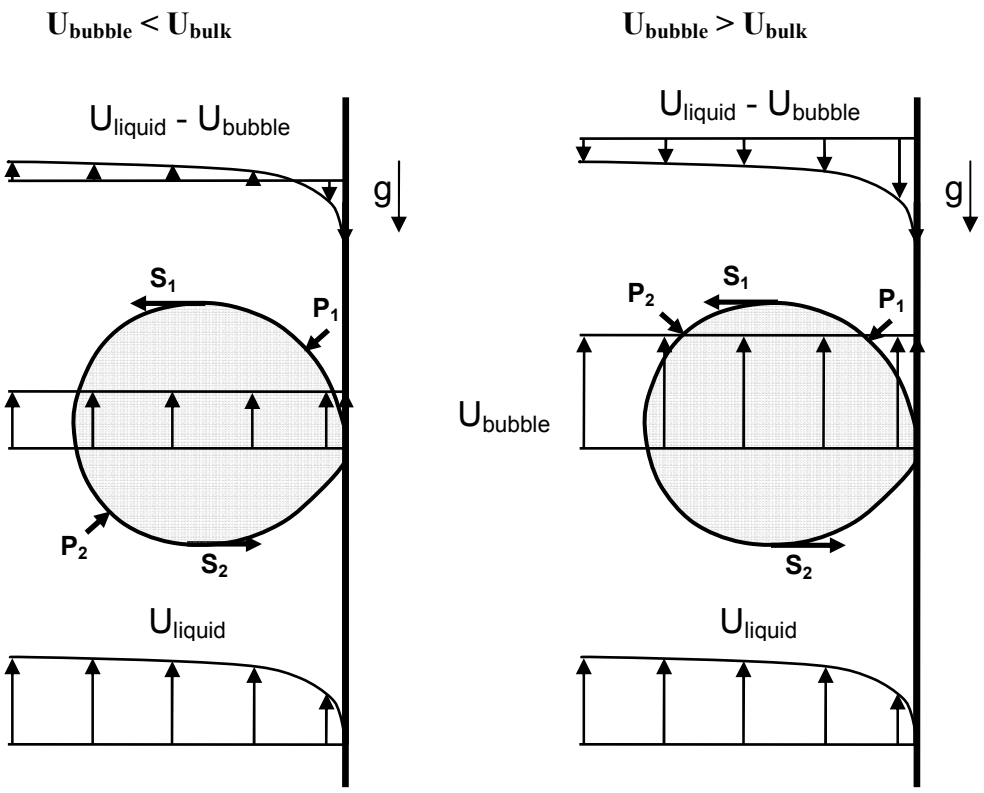

Figure 3.20 Velocity profiles, pressure and viscous shear stress components – Bubble sliding on a vertical wall.

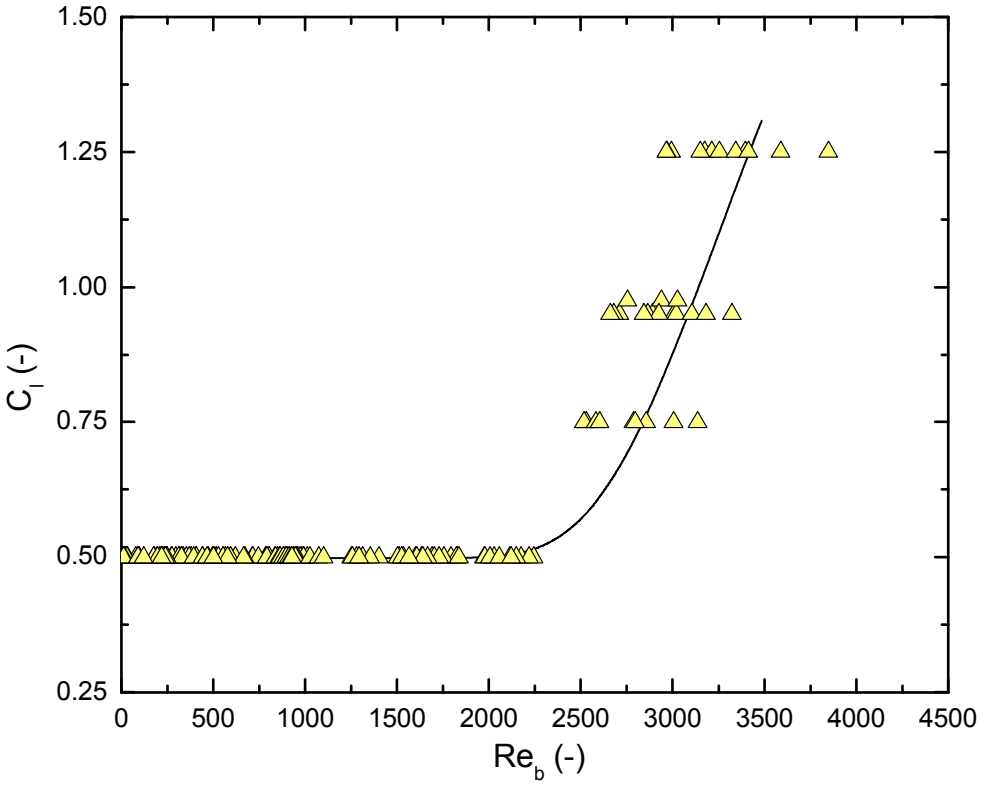

Figure 3.21 Lift coefficient as a function of bubble Reynolds number – data from the present study.

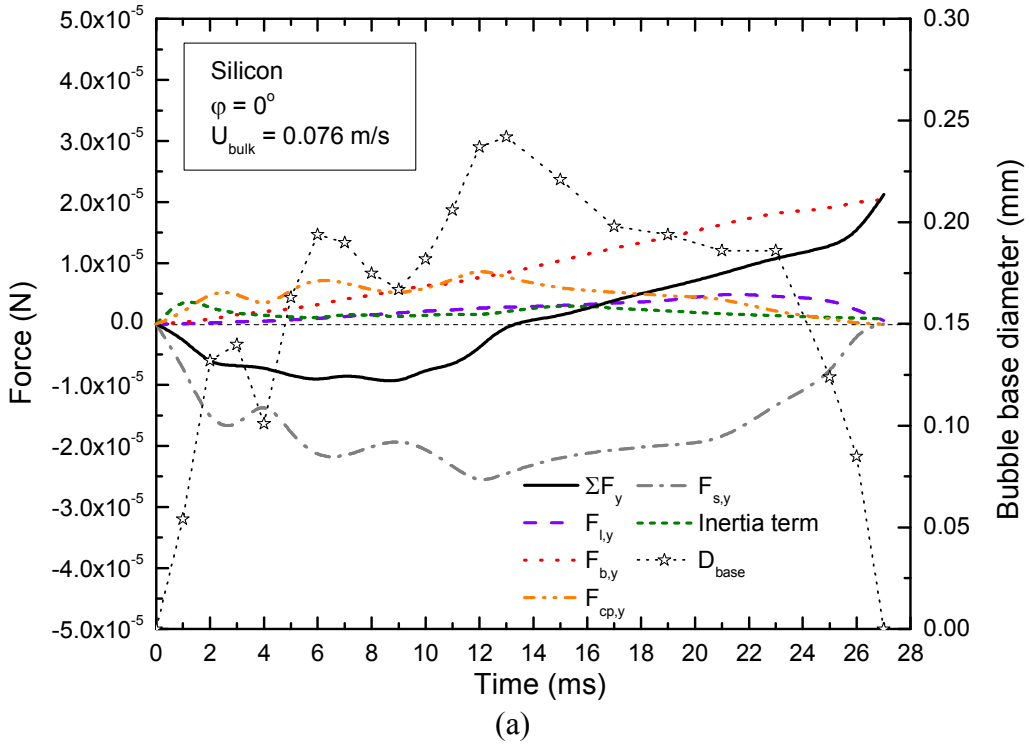

(a)

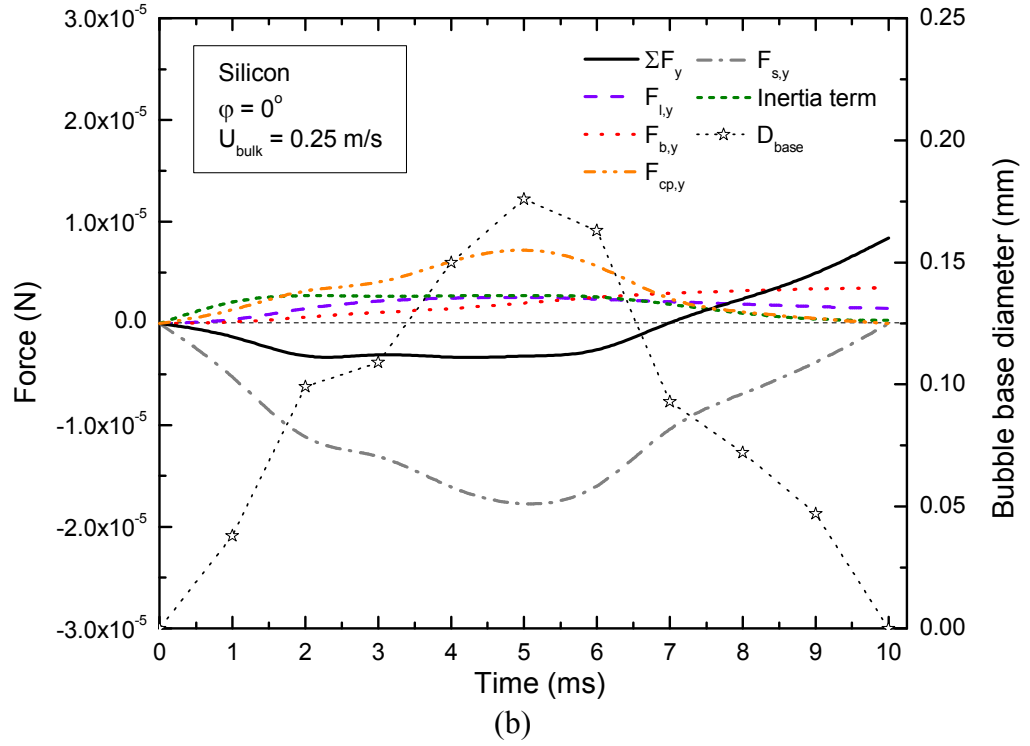

(b)

Figure 3.22 Forces acting on a growing bubble, and bubble base diameter, as a function of time, for horizontal surface and (a) U_{bulk} = 0.076 m/s, (b) U_{bulk} = 0.25 m/s – Silicon surface.

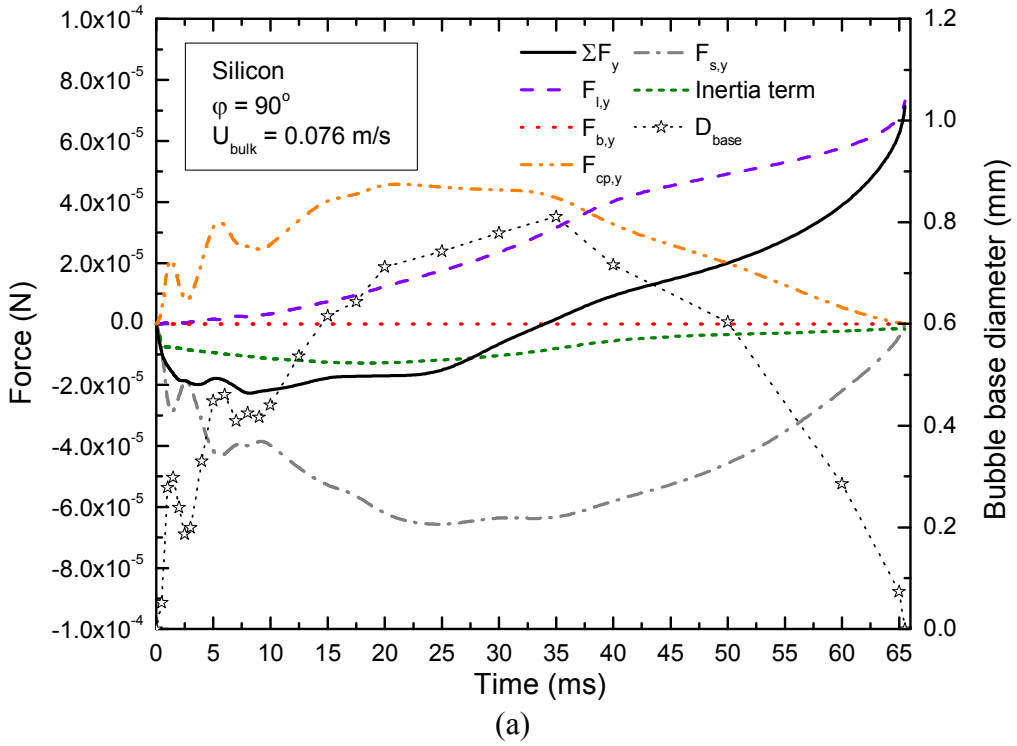

(a)

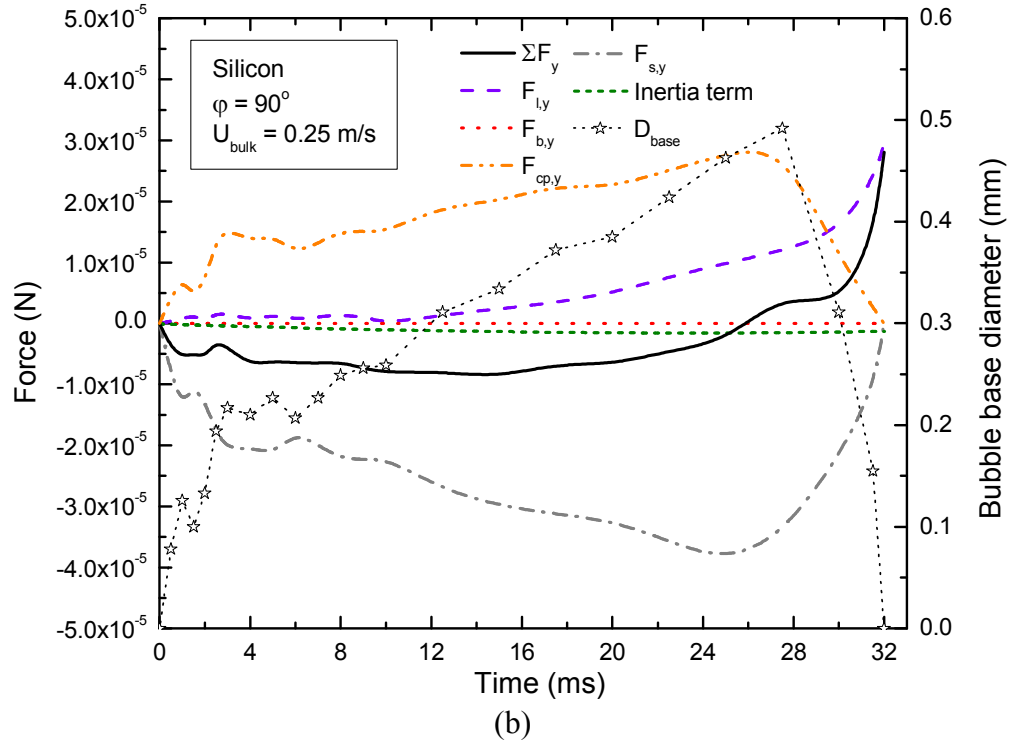

(b)

Figure 3.23 Forces acting on a growing bubble, and bubble base diameter, as a function of time, for vertical surface and (a) U_{bulk} = 0.076 m/s, (b) U_{bulk} = 0.25 m/s – Silicon surface.

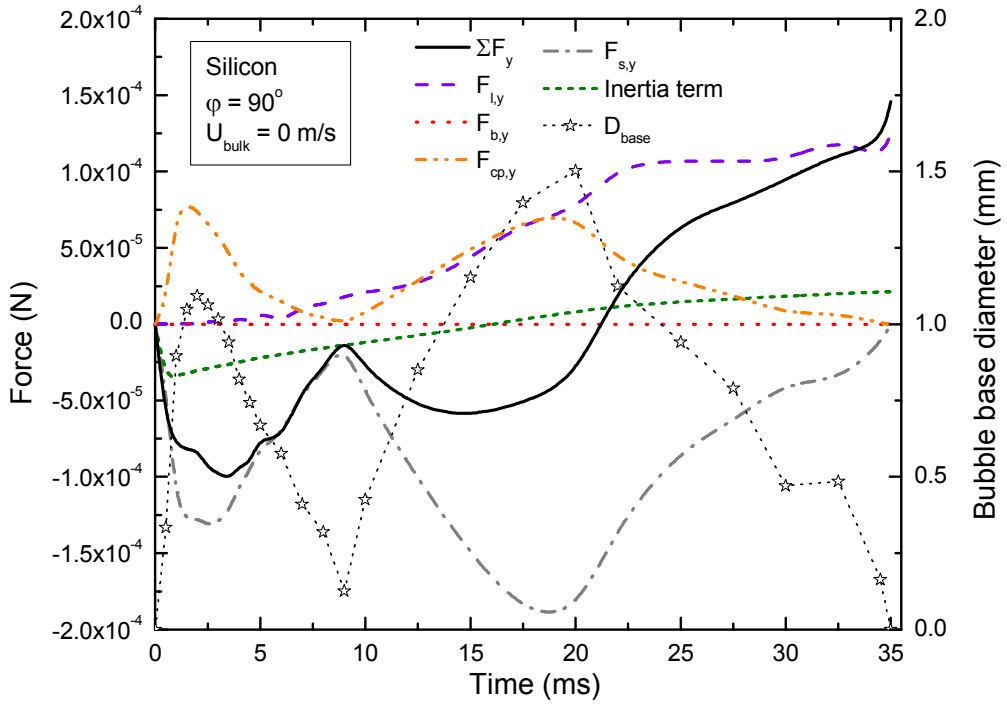

Figure 3.24 Forces acting on a growing bubble, and bubble base diameter, as a function of time, for vertical surface and pool boiling conditions – Silicon surface.

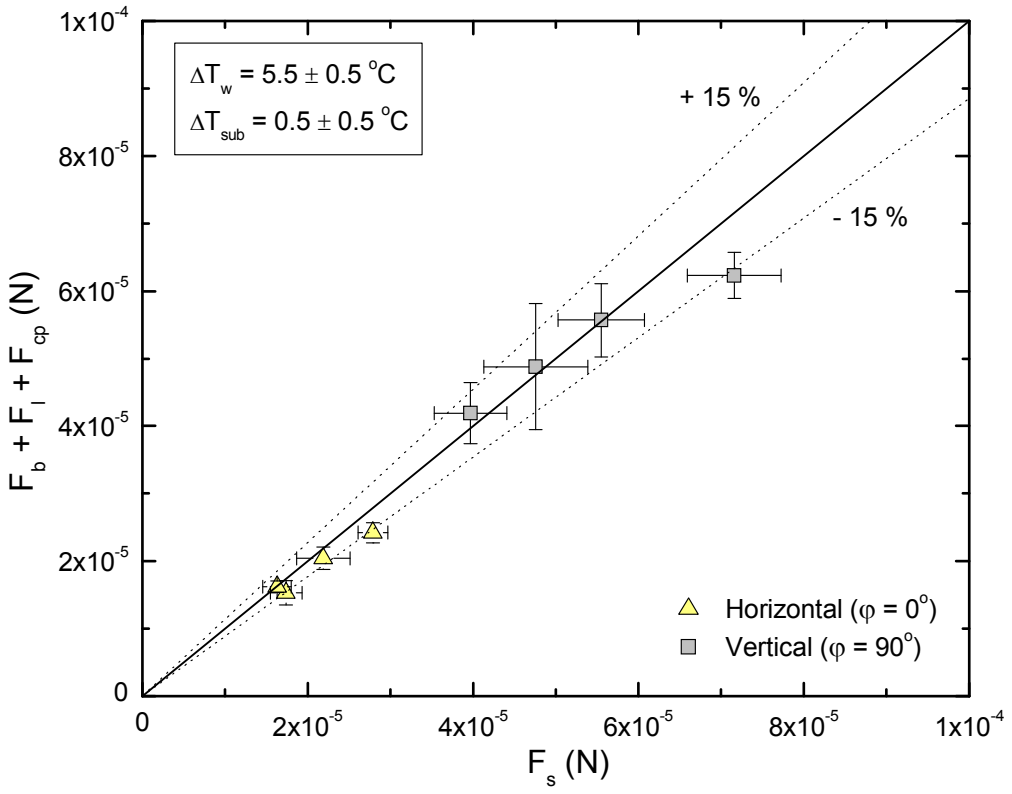

Figure 3.25 Comparison between detaching and attaching forces actual on a bubble, when bubble base diameter is maximum, for horizontal and vertical surfaces – Silicon surface.

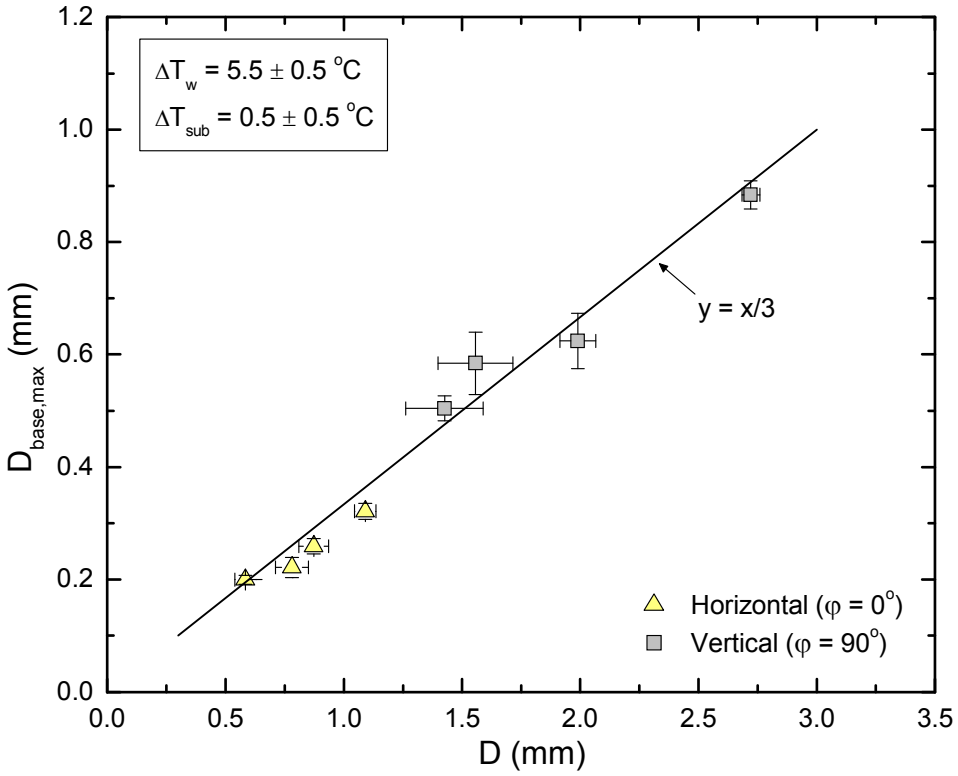

Figure 3.26 Maximum bubble base diameter as a function of bubble diameter, for horizontal and vertical surfaces – Silicon surface.

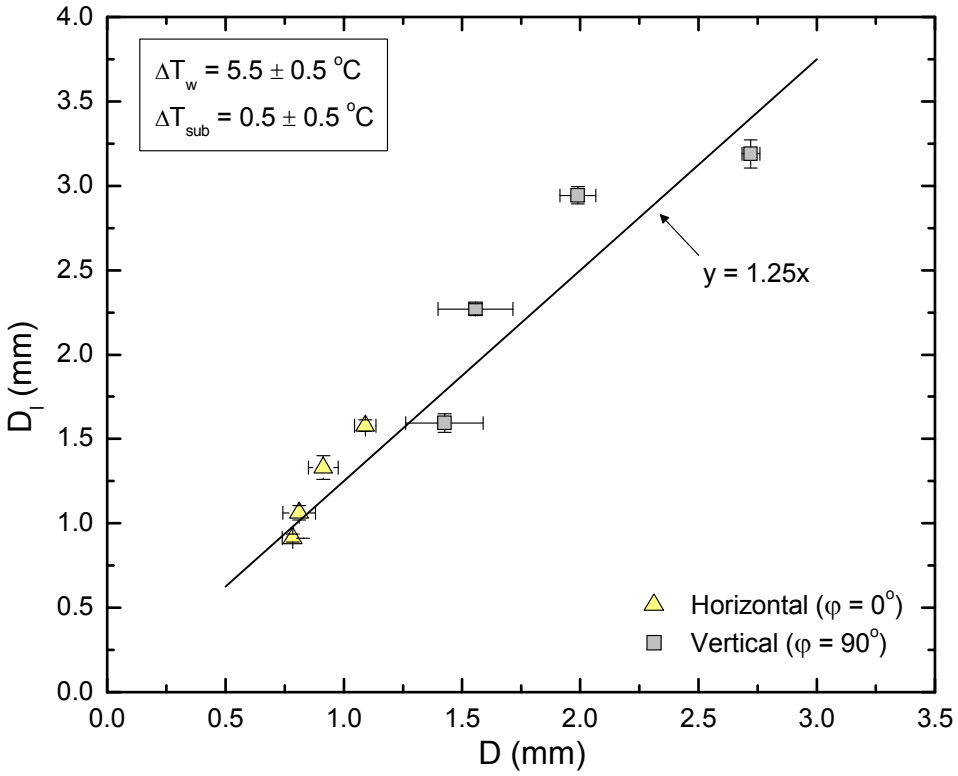

Figure 3.27 Bubble lift off diameter as a function of bubble diameter at D_{base} = $D_{base,max}$ diameter, for horizontal and vertical surfaces – Silicon surface.

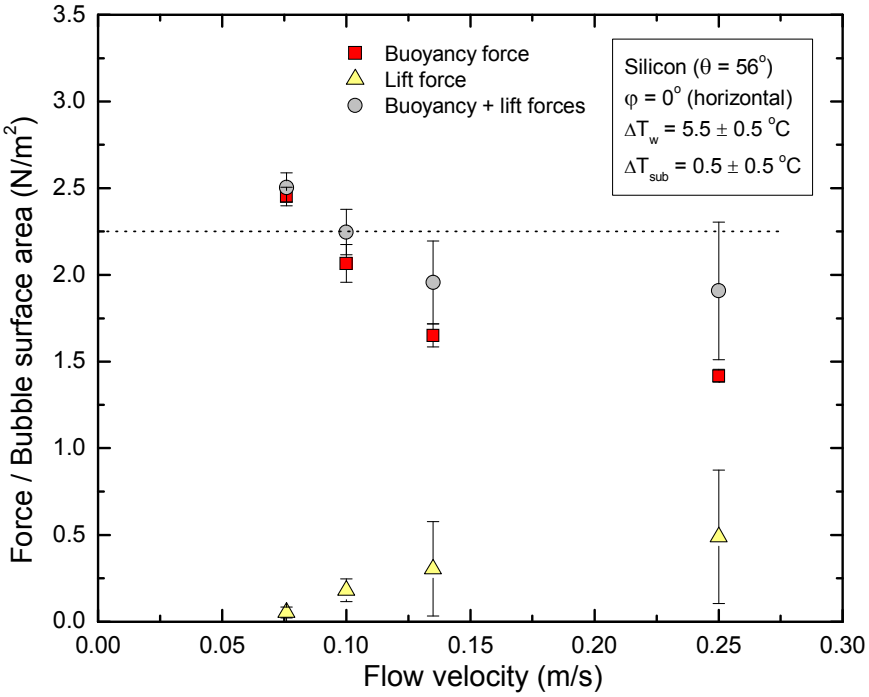

(a)

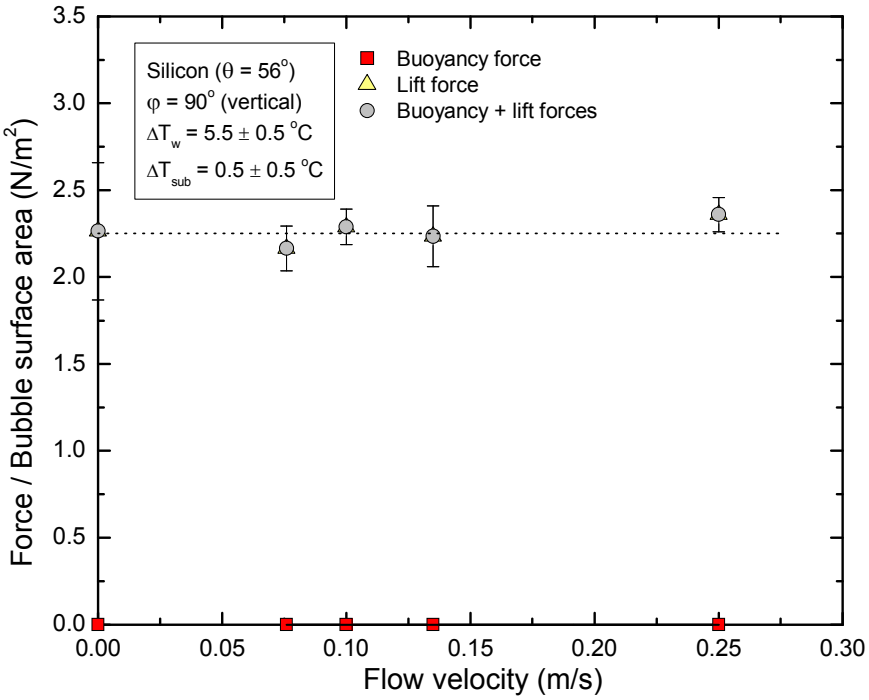

(b)

Figure 3.28 Forces acting on a bubble at lift off as a function of flow velocity, for (a) horizontal surface, and (b) vertical surface – Silicon surface.

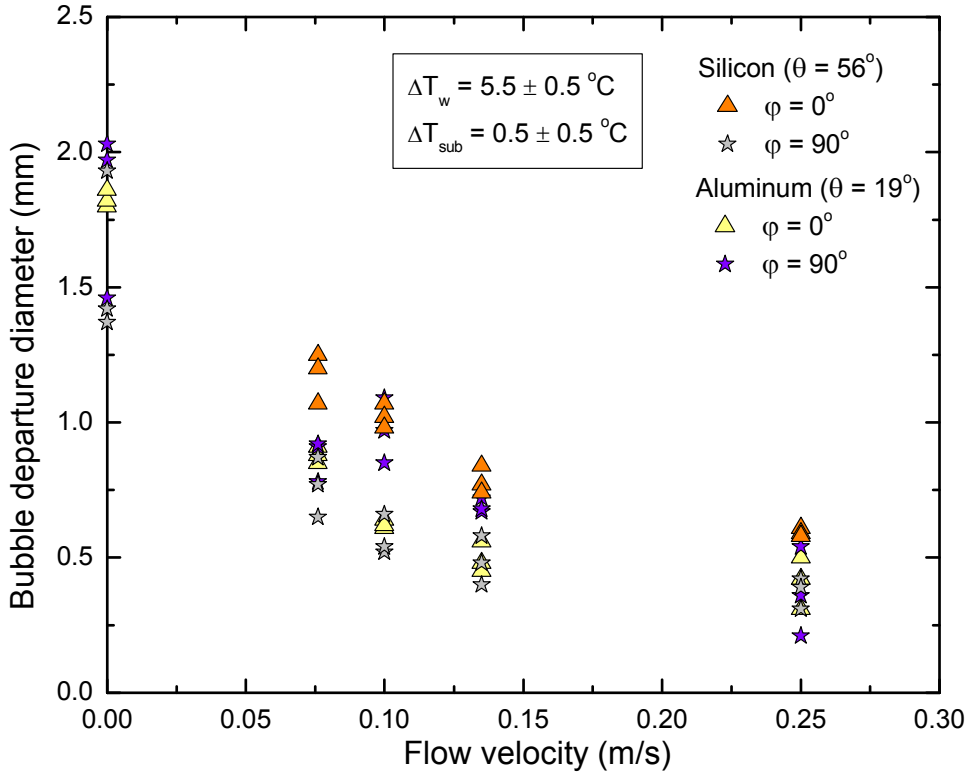

Figure 3.29 Effect of liquid bulk velocity, orientation and contact angle on bubble departure diameter – Aluminum and silicon surfaces.

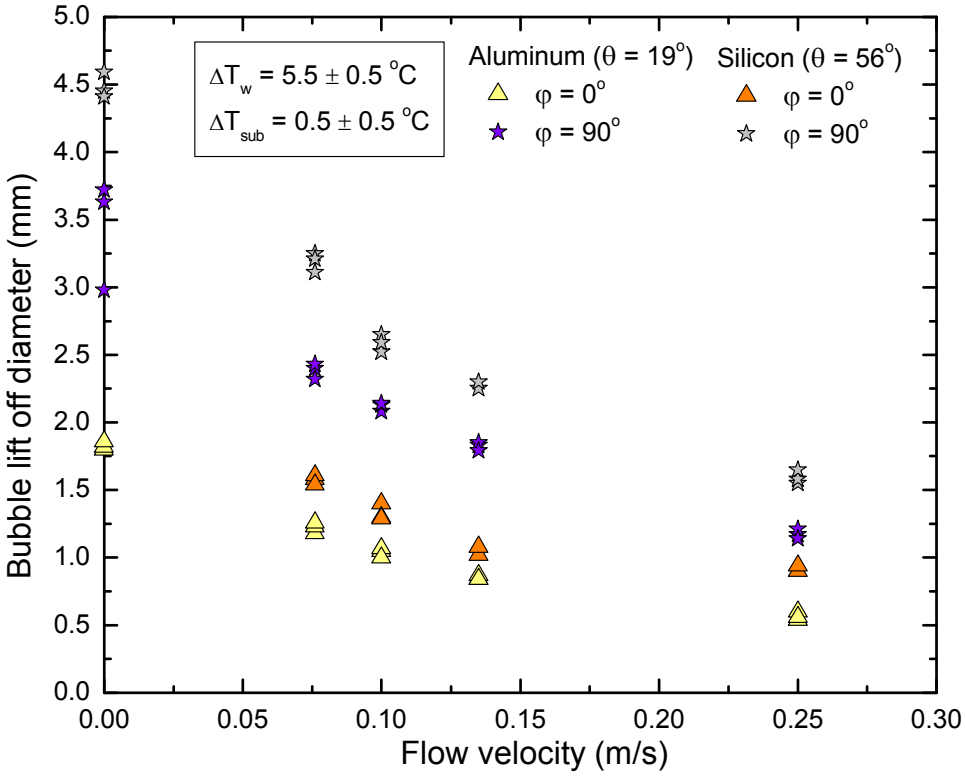

Figure 3.30 Effect of liquid bulk velocity, orientation and contact angle on bubble lift off diameter – Aluminum and silicon surfaces.

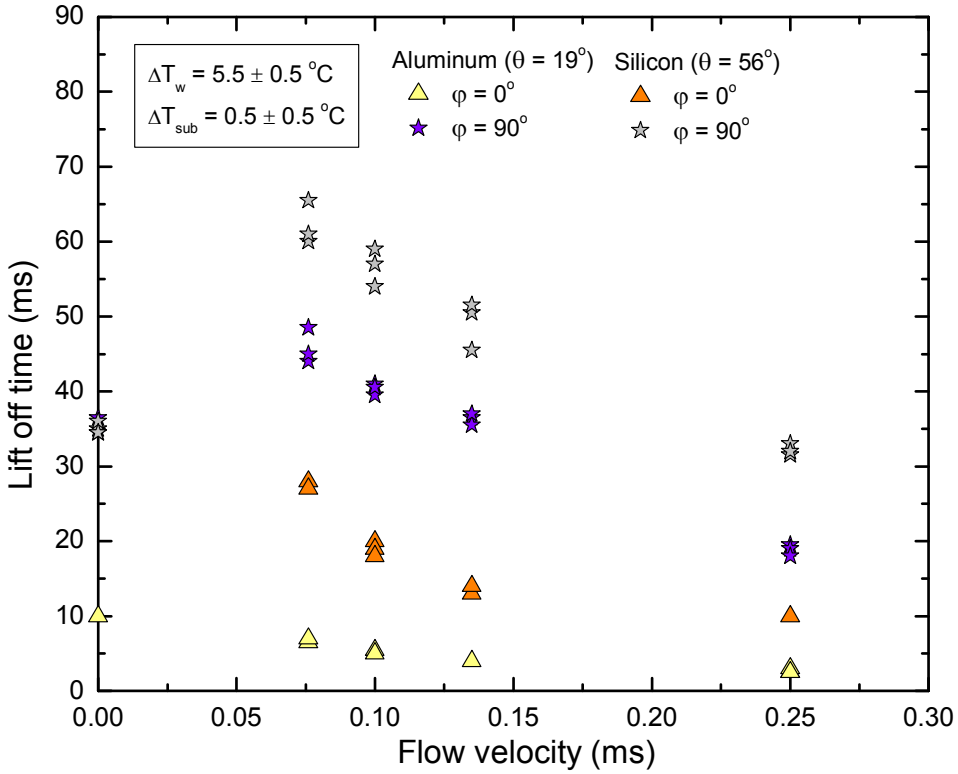

Figure 3.31 Effect of liquid bulk velocity, orientation and contact angle on lift off time – Aluminum and silicon surfaces.

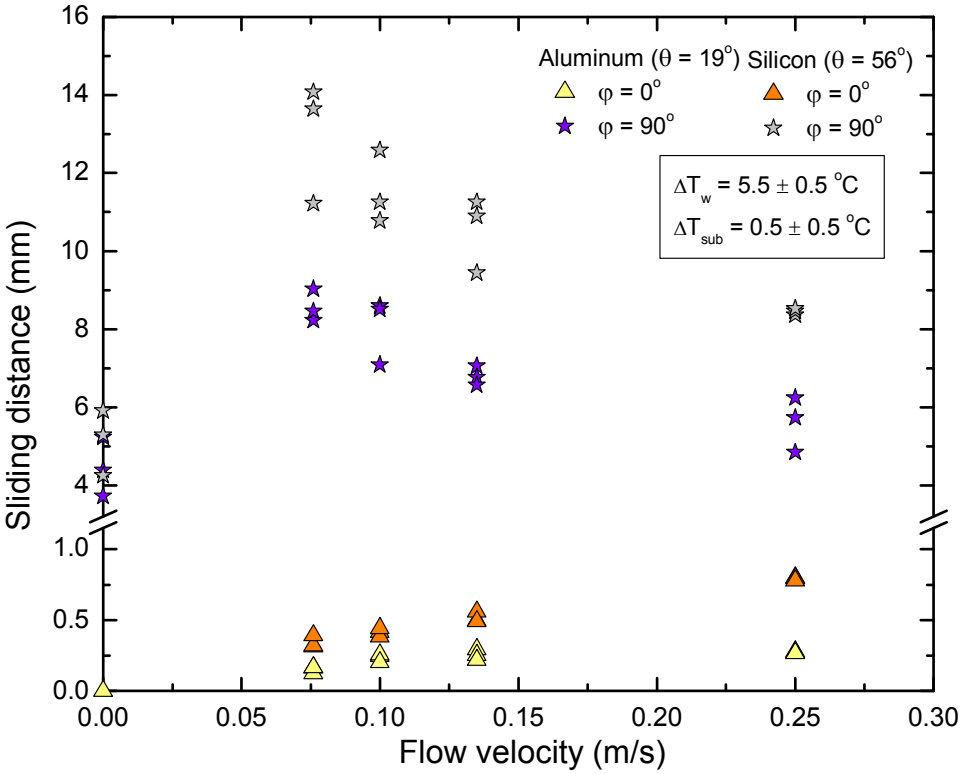

Figure 3.32 Effect of liquid bulk velocity, orientation and contact angle on sliding distance – Aluminum and silicon surfaces.

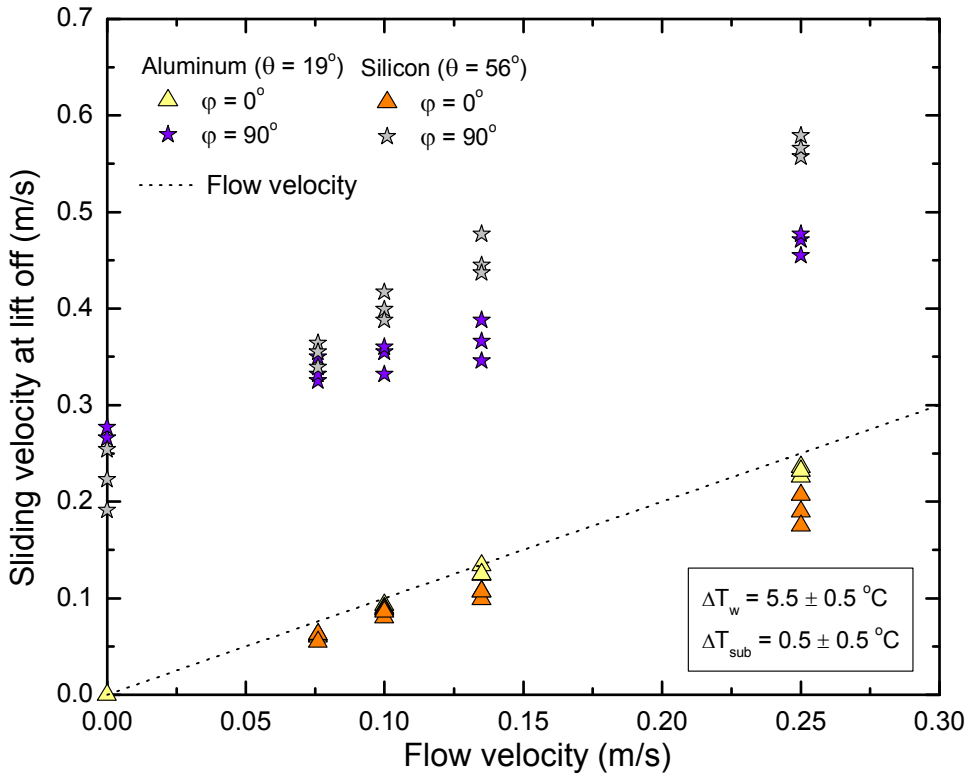

Figure 3.33 Effect of liquid bulk velocity, orientation and contact angle on sliding velocity at lift off – Aluminum and silicon surfaces.

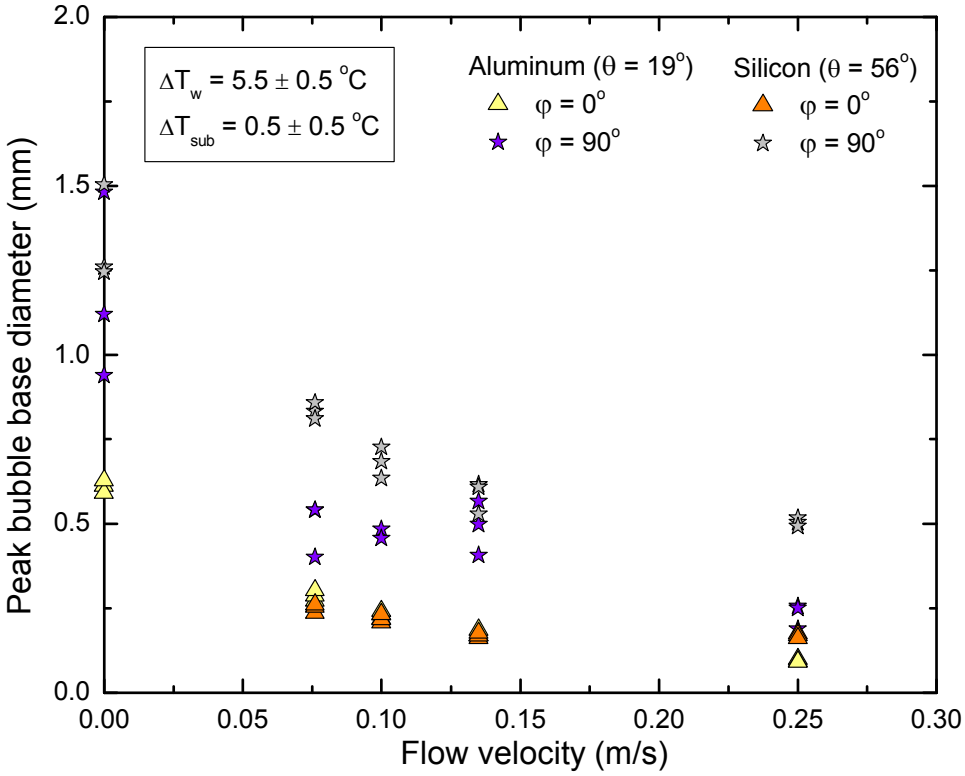

Figure 3.34 Effect of liquid bulk velocity, orientation and contact angle on peak bubble base diameter – Aluminum surface.

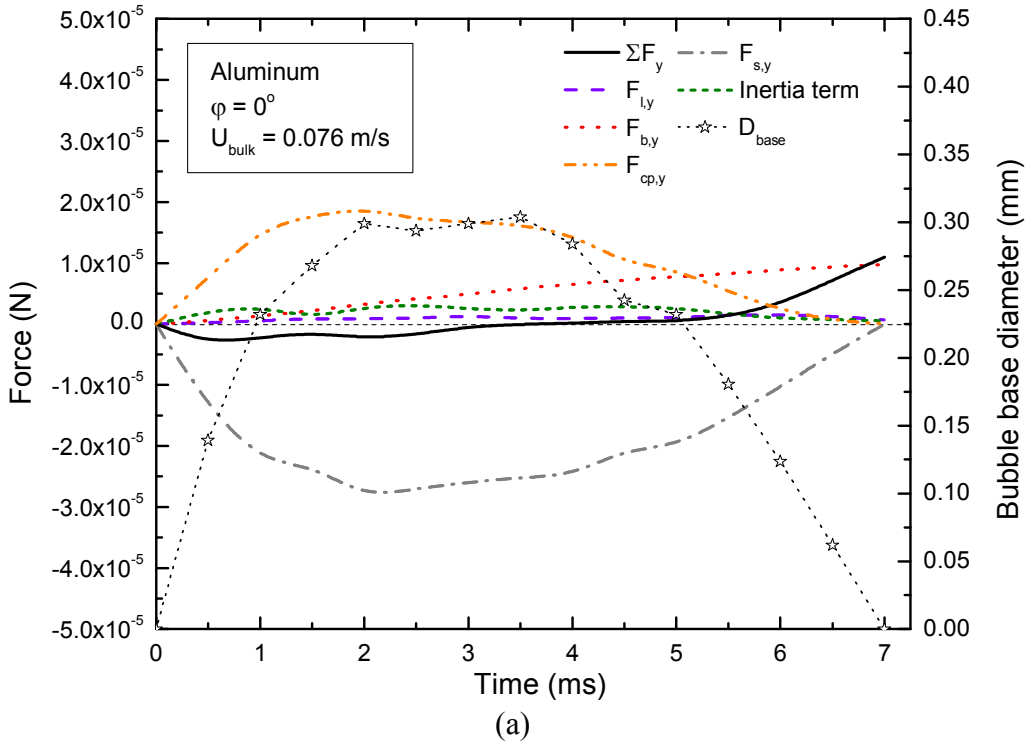

(a)

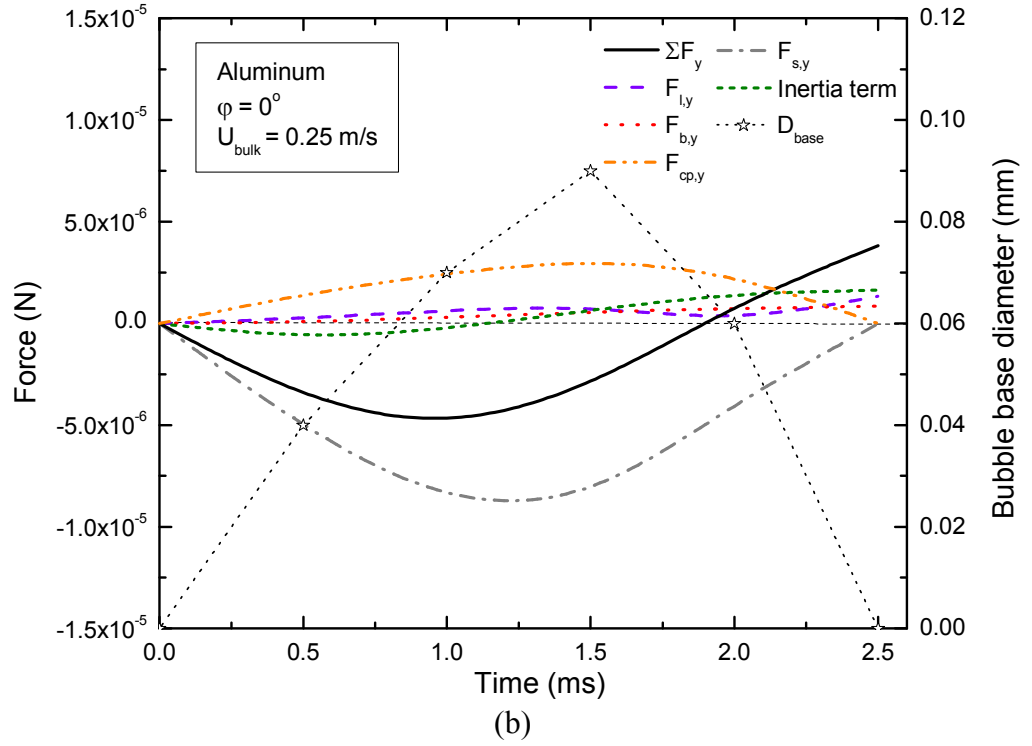

(b)

Figure 3.35 Forces acting on a growing bubble, and bubble base diameter, as a function of time, for horizontal surface and (a) U_{bulk} = 0.076 m/s, (b) U_{bulk} = 0.25 m/s – Aluminum surface.

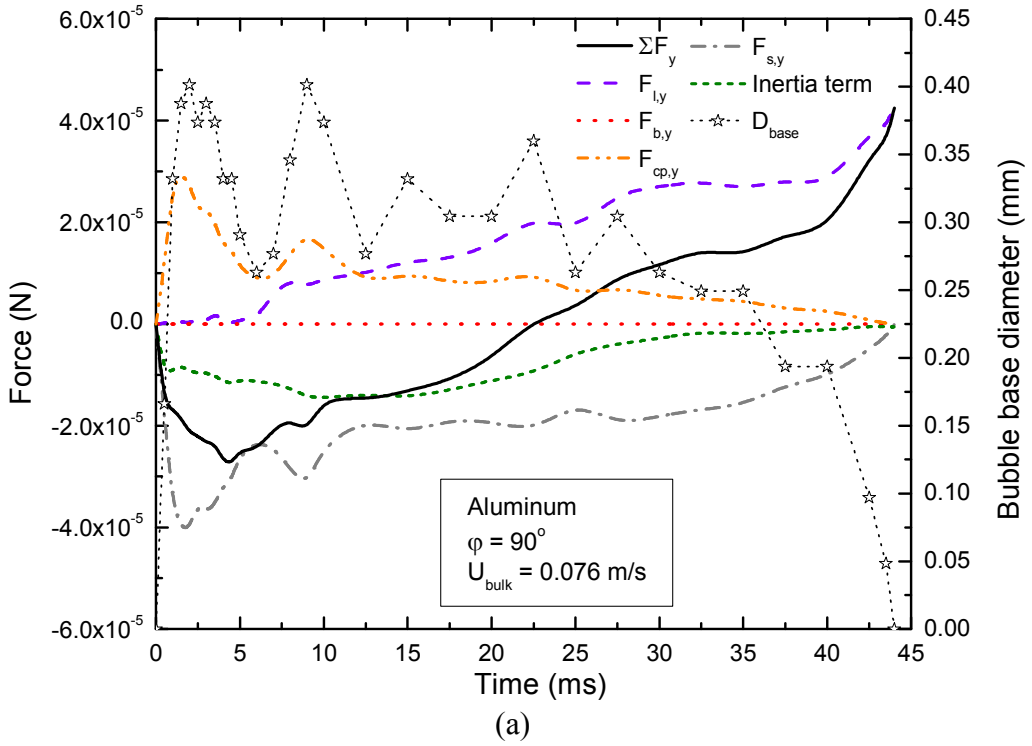

(a)

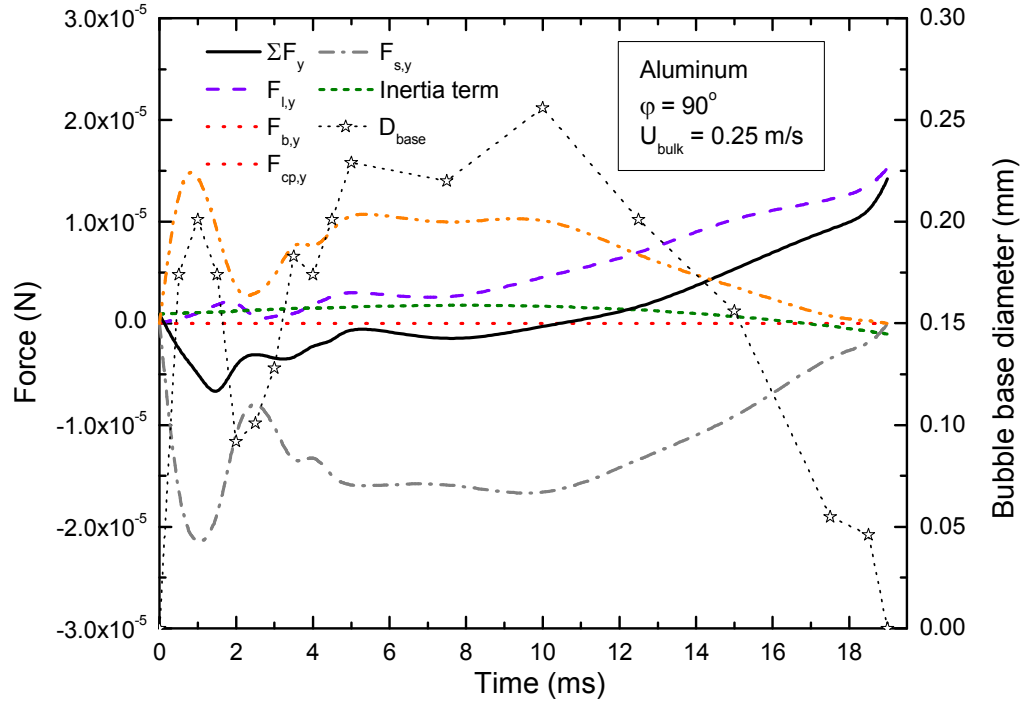

(b)

Figure 3.36 Forces acting on a growing bubble, and bubble base diameter, as a function of time, for vertical surface and (a) U_{bulk} = 0.076 m/s, (b) U_{bulk} = 0.25 m/s – Aluminum surface.

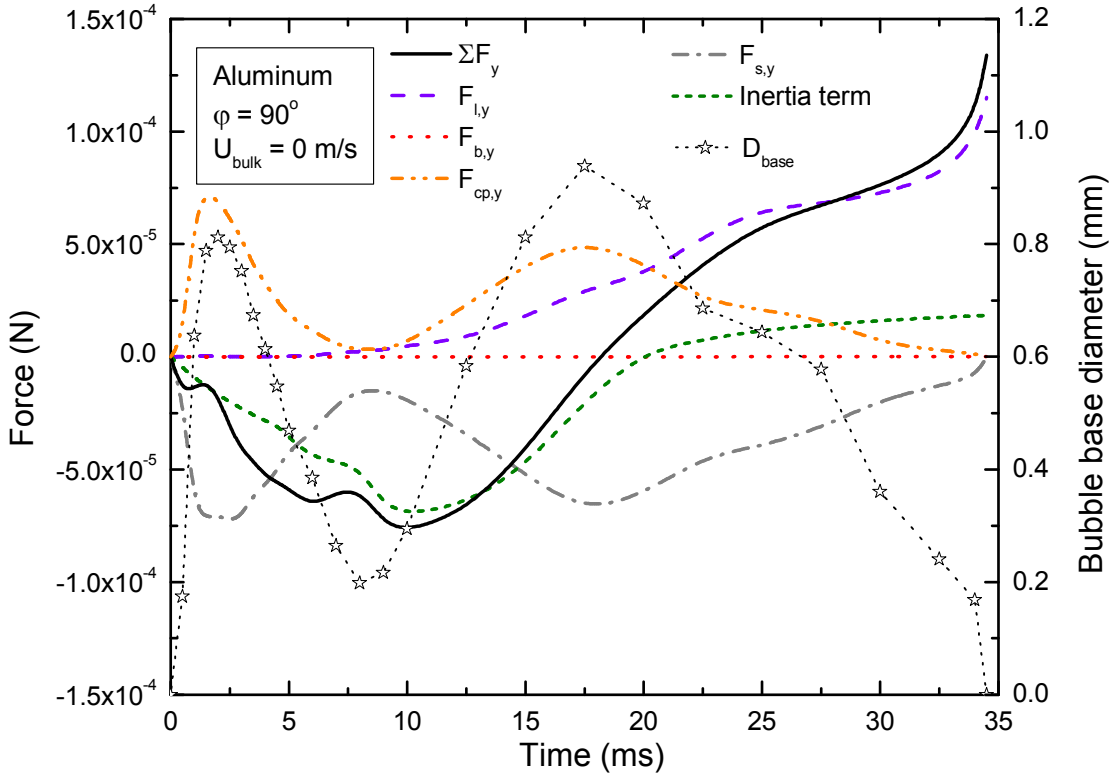

Figure 3.37 Forces acting on a growing bubble, and bubble base diameter, as a function of time, for vertical surface and pool boiling conditions – Aluminum surface.

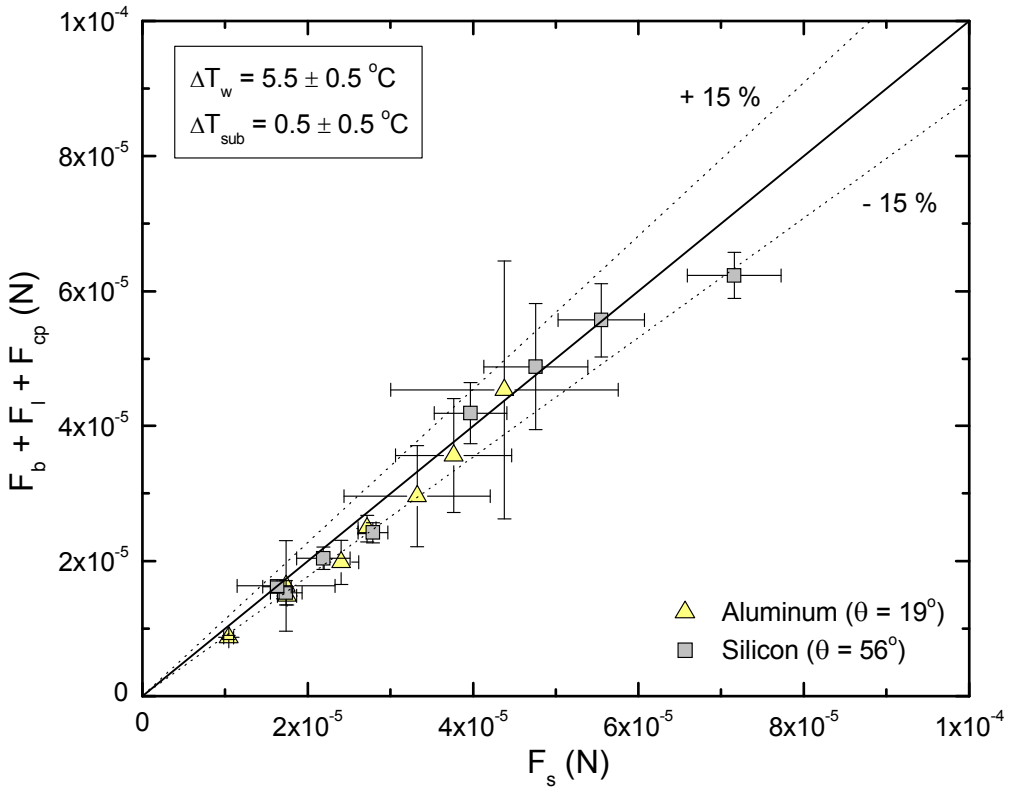

Figure 3.38 Comparison between detaching and attaching forces actual on a bubble, when bubble base diameter is maximum, for horizontal and vertical surfaces – Aluminum and silicon surfaces.

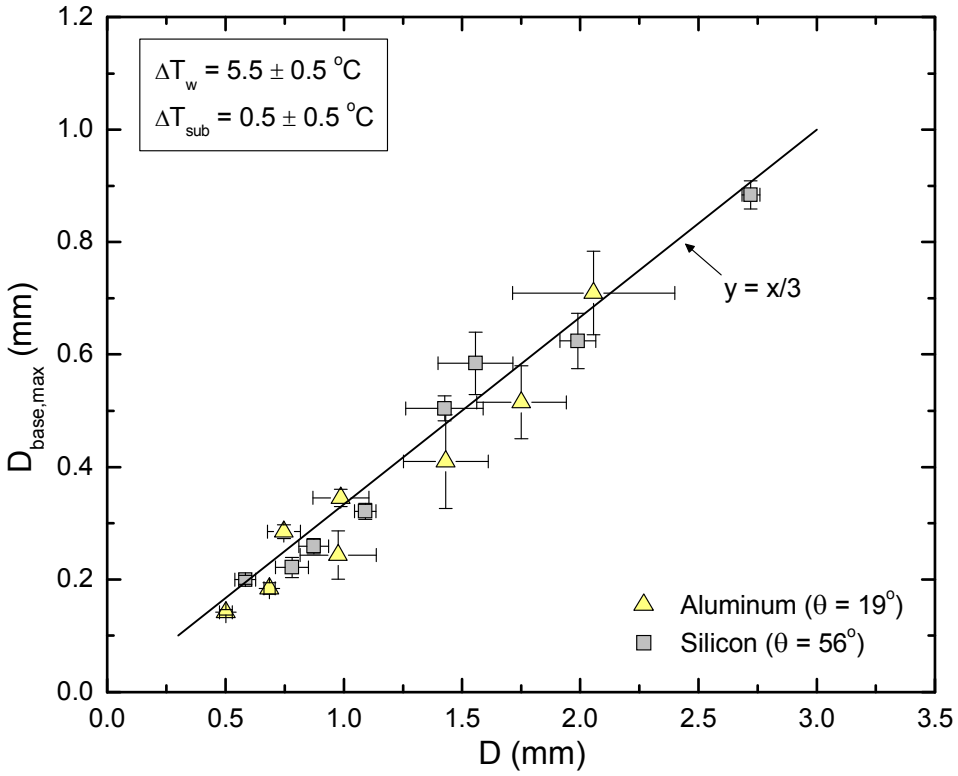

Figure 3.39 Maximum bubble base diameter as a function of bubble diameter, for horizontal and vertical surfaces – Aluminum and silicon surfaces.

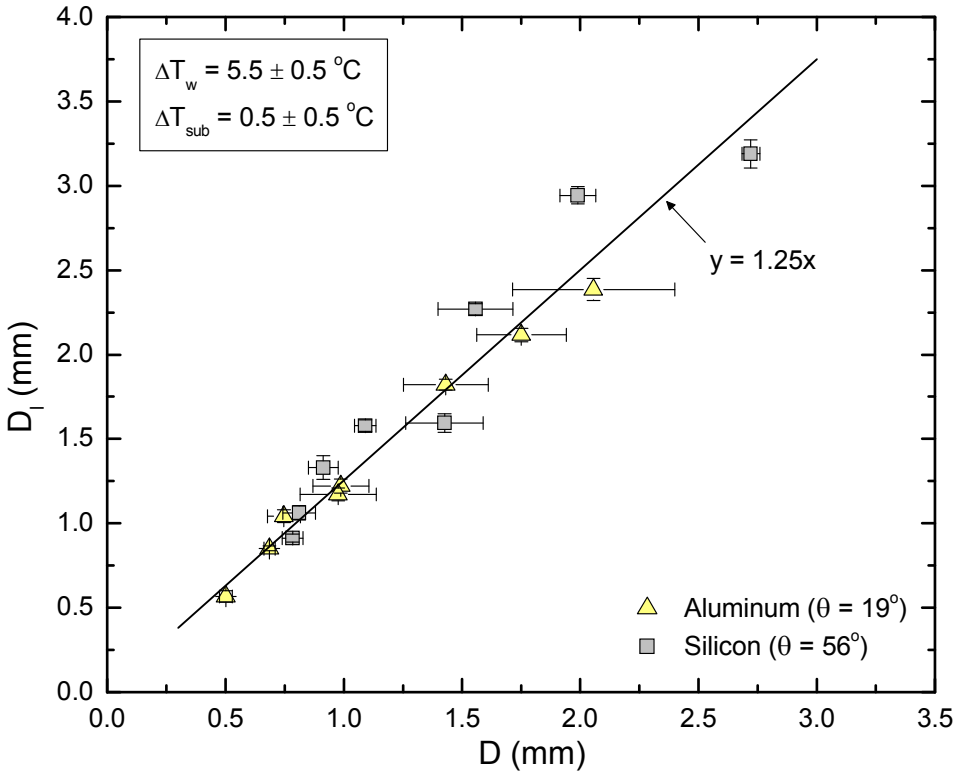

Figure 3.40 Bubble lift off diameter as a function of bubble diameter at D_{base} = $D_{base,max}$ diameter, for horizontal and vertical surfaces – Aluminum and silicon surfaces.

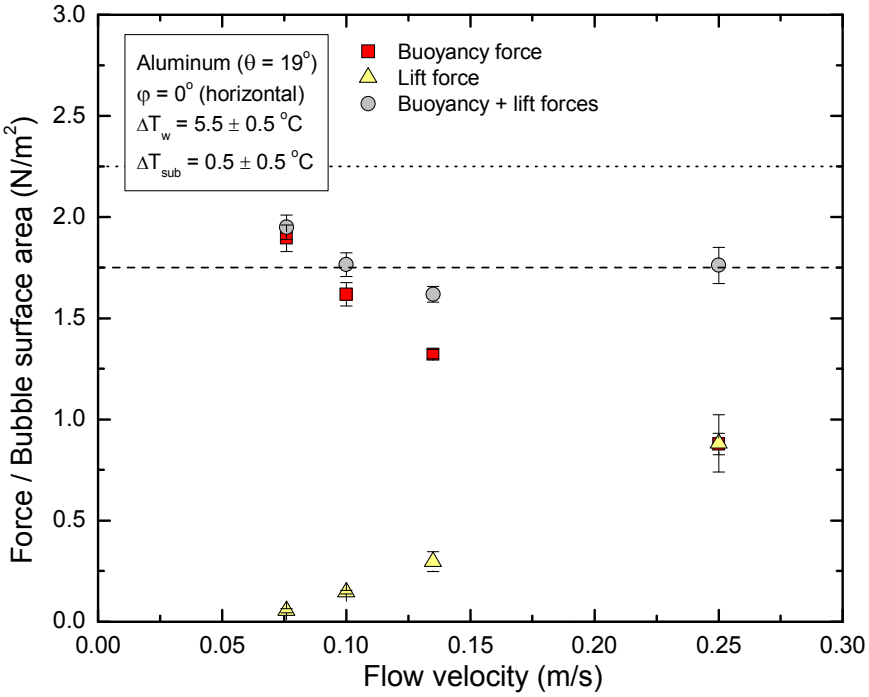

(a)

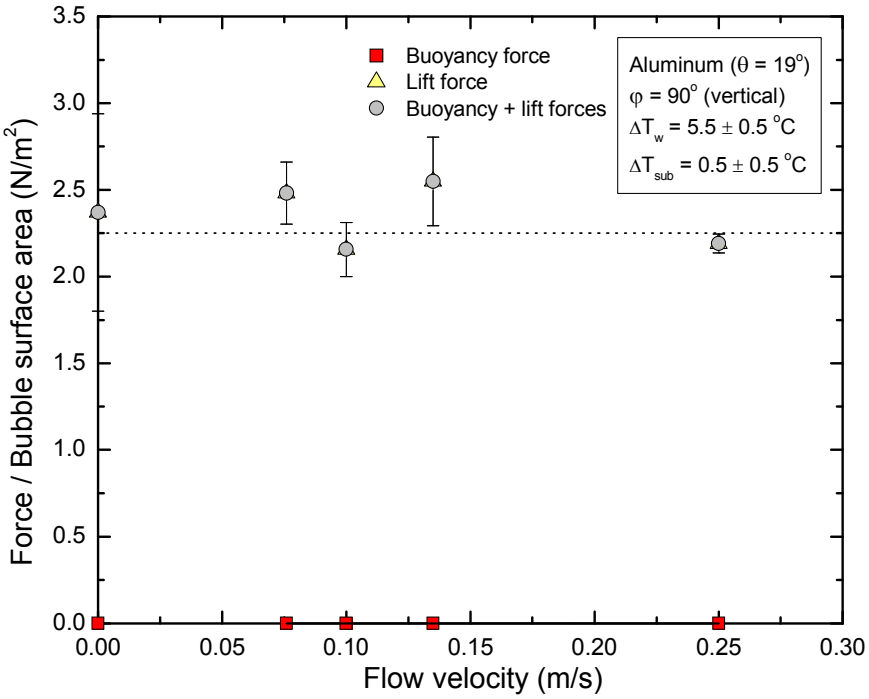

(b)

Figure 3.41 Forces acting on a bubble at lift off as a function of flow velocity, for (a) horizontal surface, and (b) vertical surface – Aluminum surface.

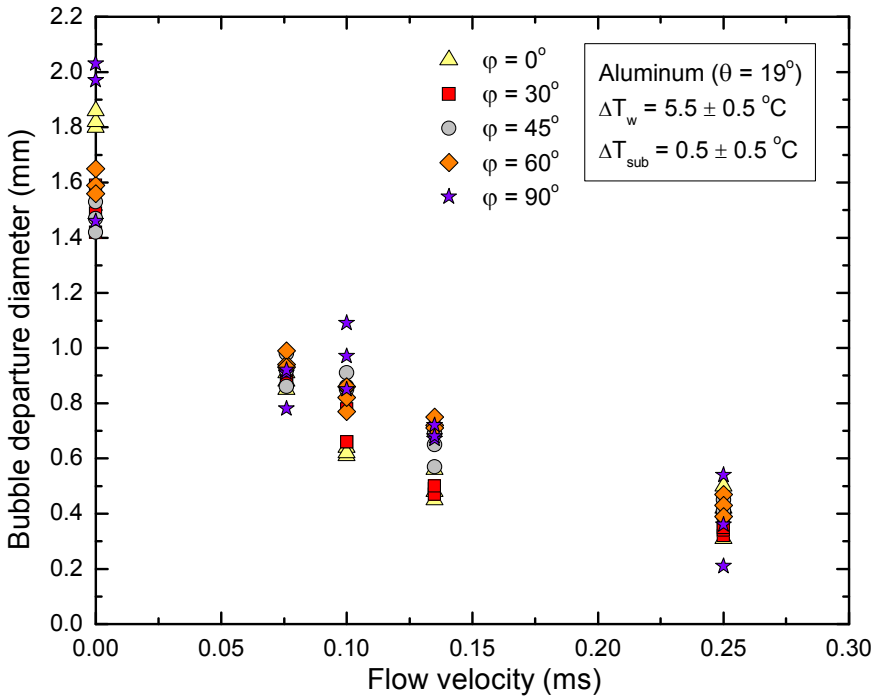

(a)

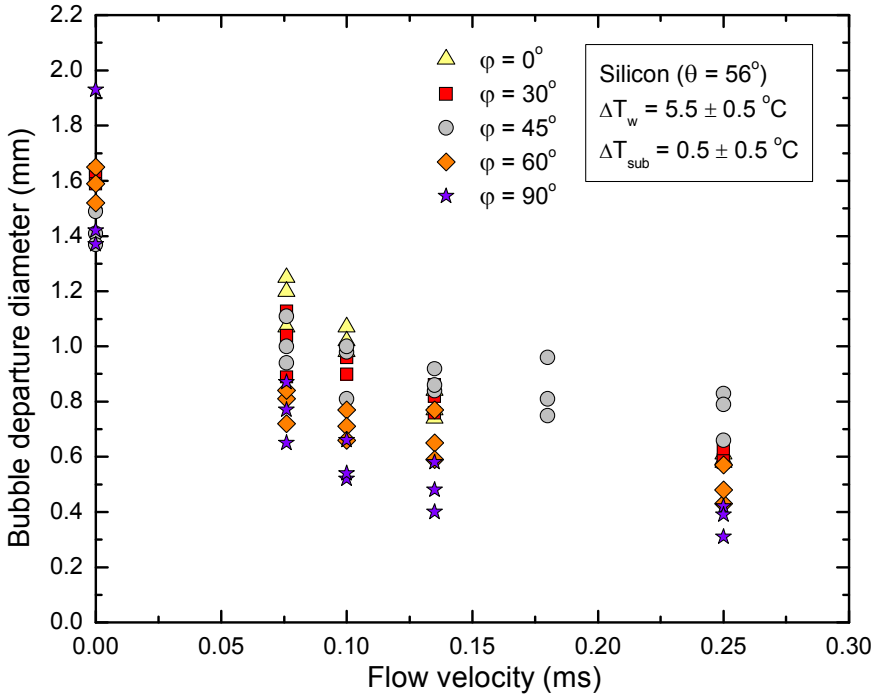

(b)

Figure 3.42 Effect of liquid bulk velocity and orientation on bubble departure diameter – (a) aluminum and (b) silicon surfaces.

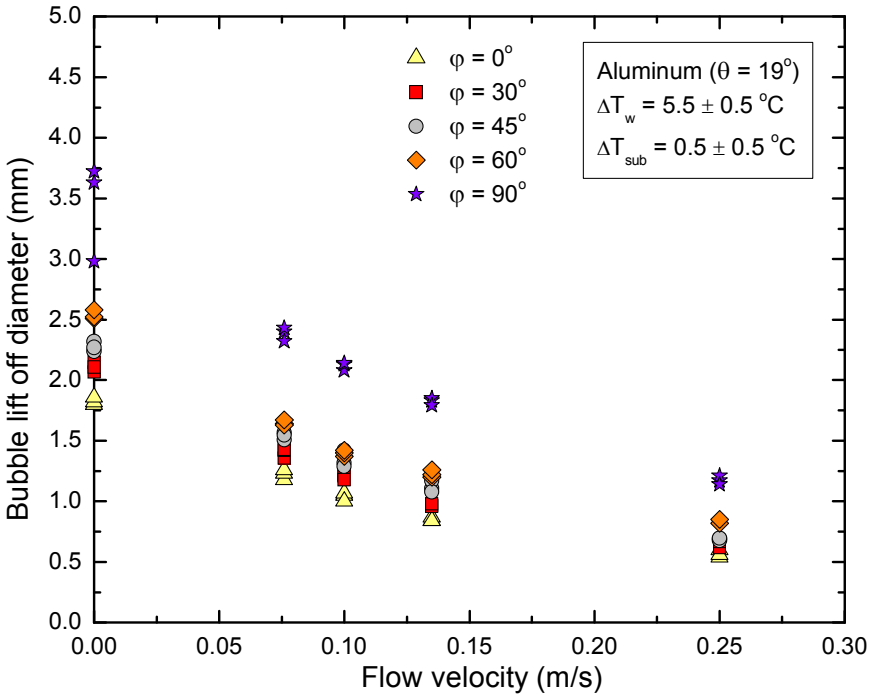

(a)

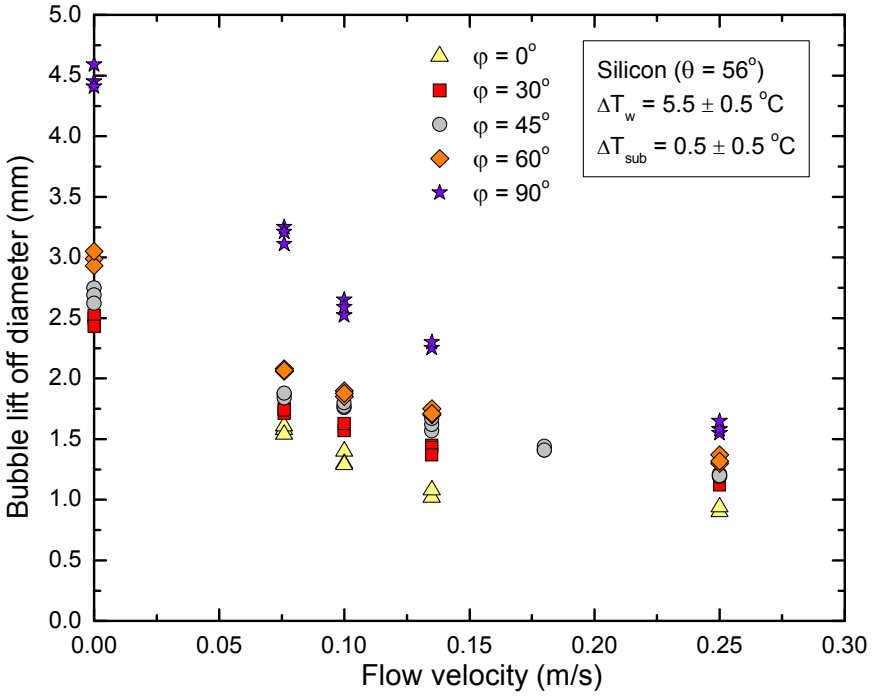

(b)

Figure 3.43 Effect of liquid bulk velocity and orientation on bubble lift off diameter – (a) aluminum and (b) silicon surfaces.

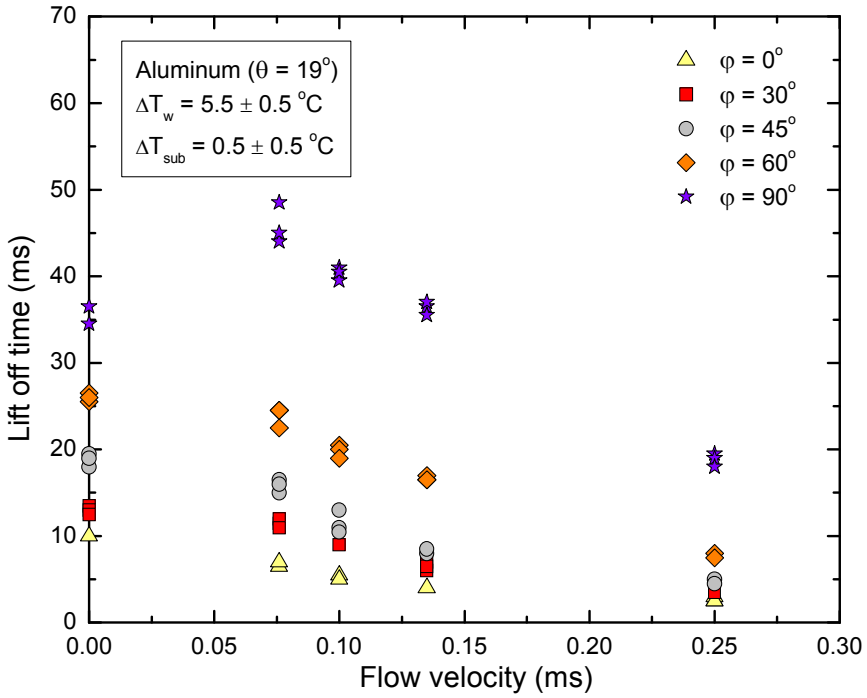

(a)

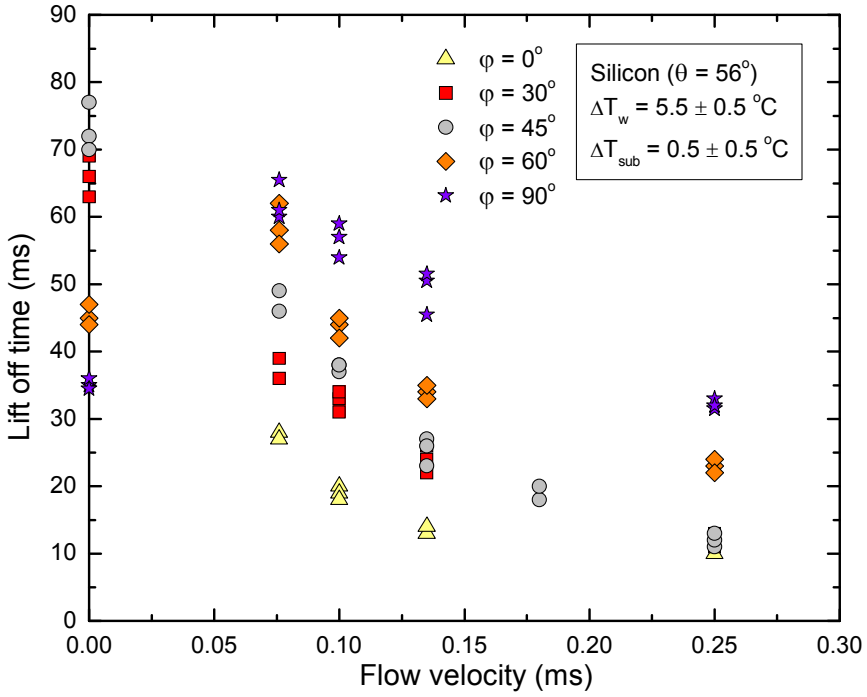

(b)

Figure 3.44 Effect of liquid bulk velocity and orientation on lift off time – (a) aluminum and (b) silicon surfaces.

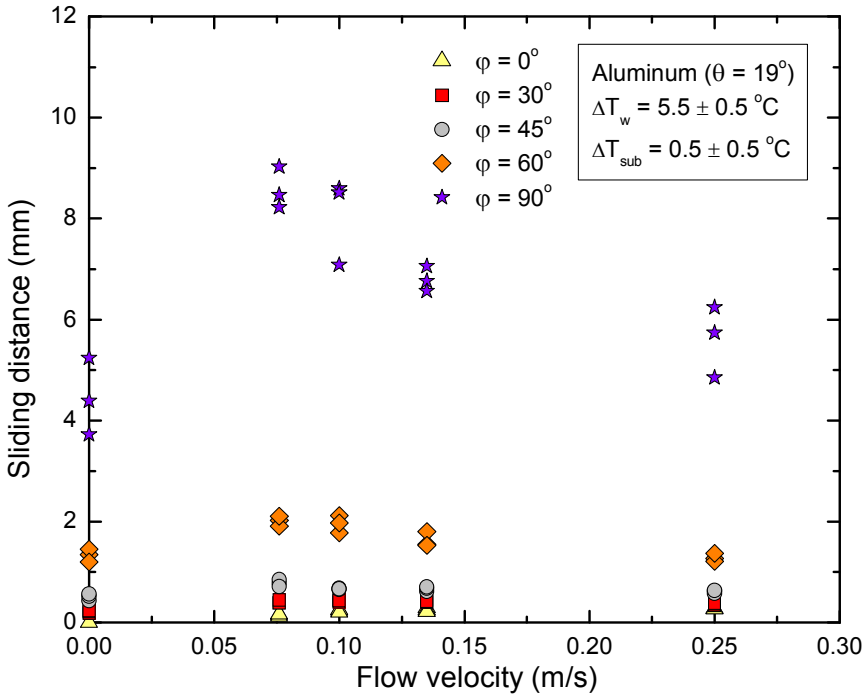

(a)

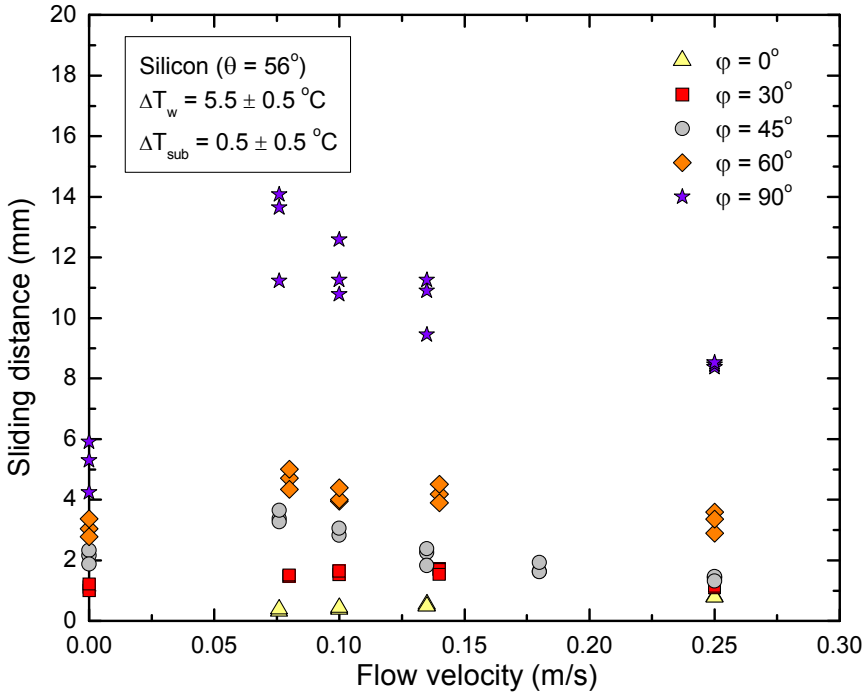

(b)

Figure 3.45 Effect of liquid bulk velocity and orientation on sliding distance – (a) aluminum and (b) silicon surfaces.

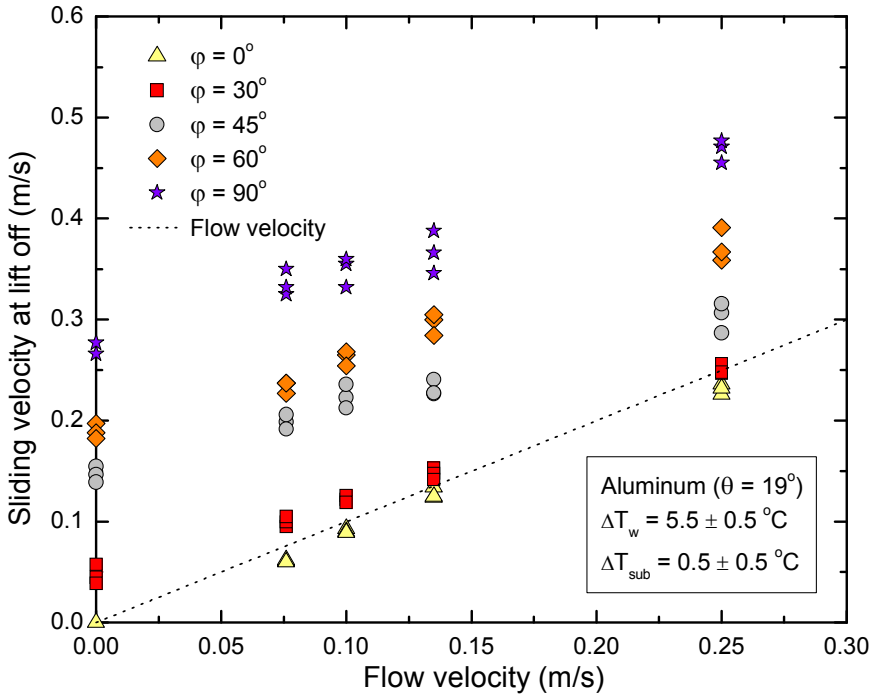

(a)

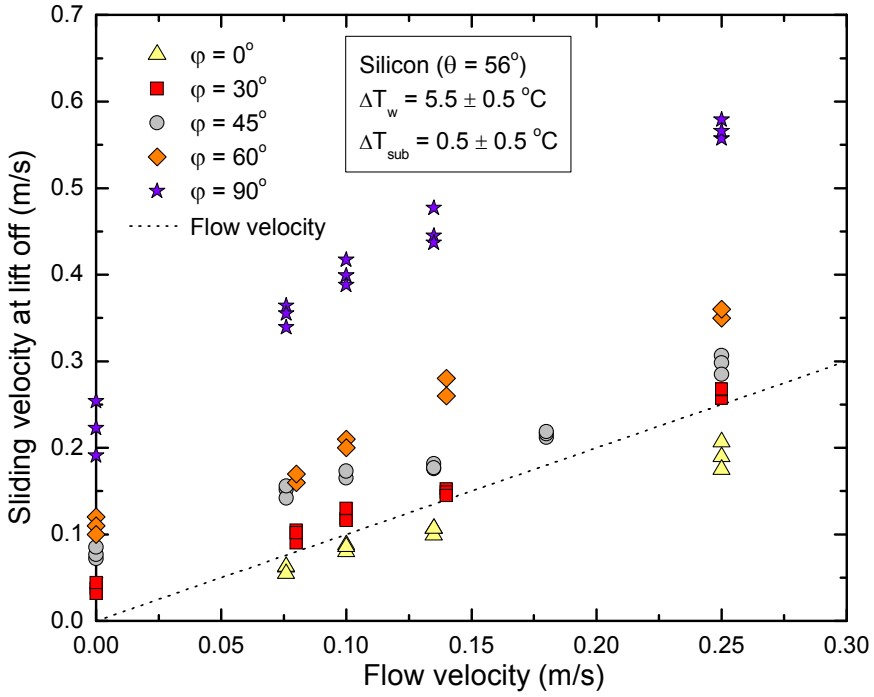

(b)

Figure 3.46 Effect of liquid bulk velocity and orientation on sliding velocity at lift off – (a) aluminum and (b) silicon surfaces.

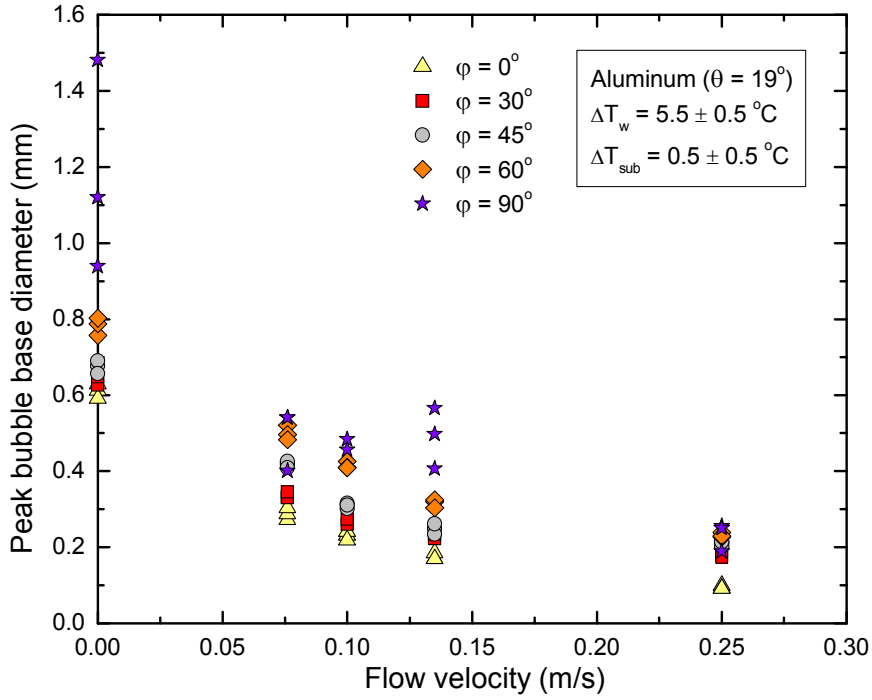

(a)

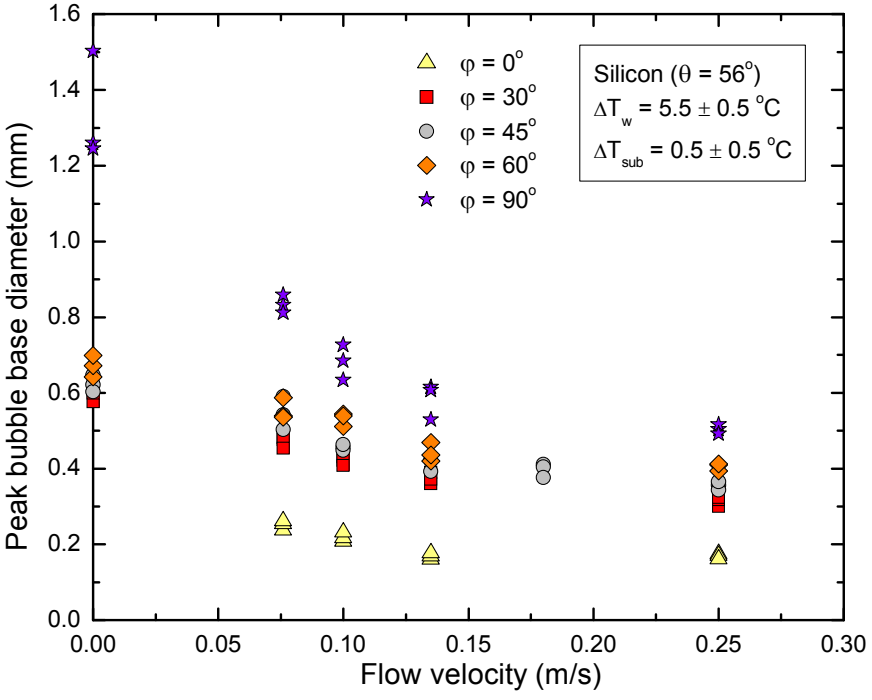

(b)

Figure 3.47 Effect of liquid bulk velocity and orientation on peak bubble base diameter – (a) aluminum and (b) silicon surfaces.

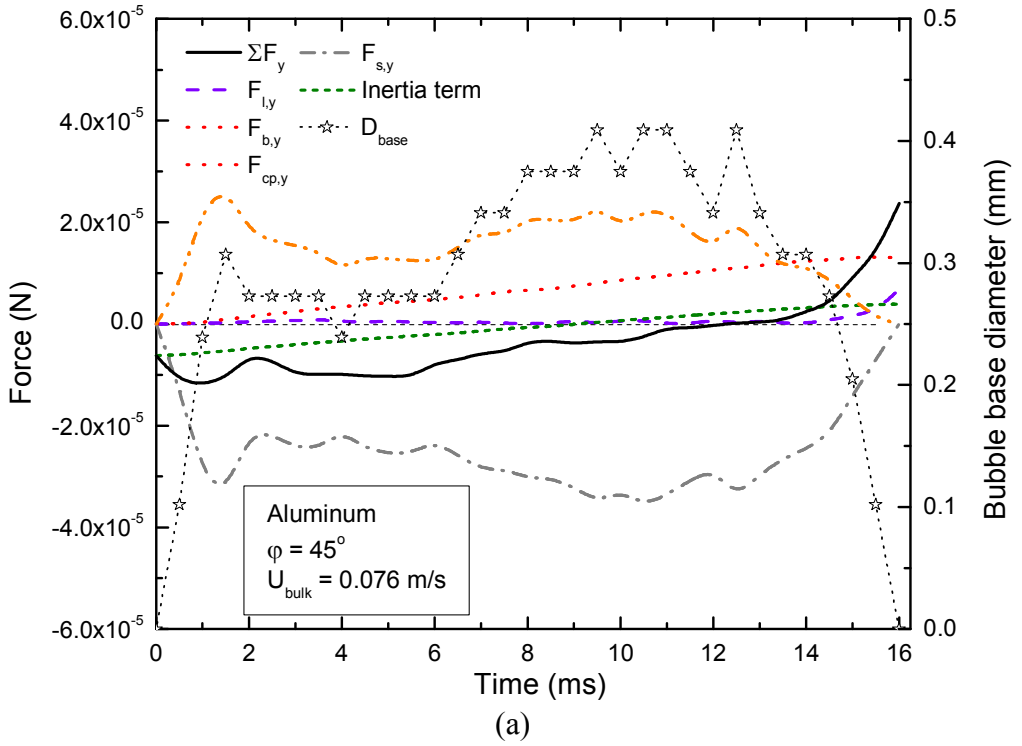

(a)

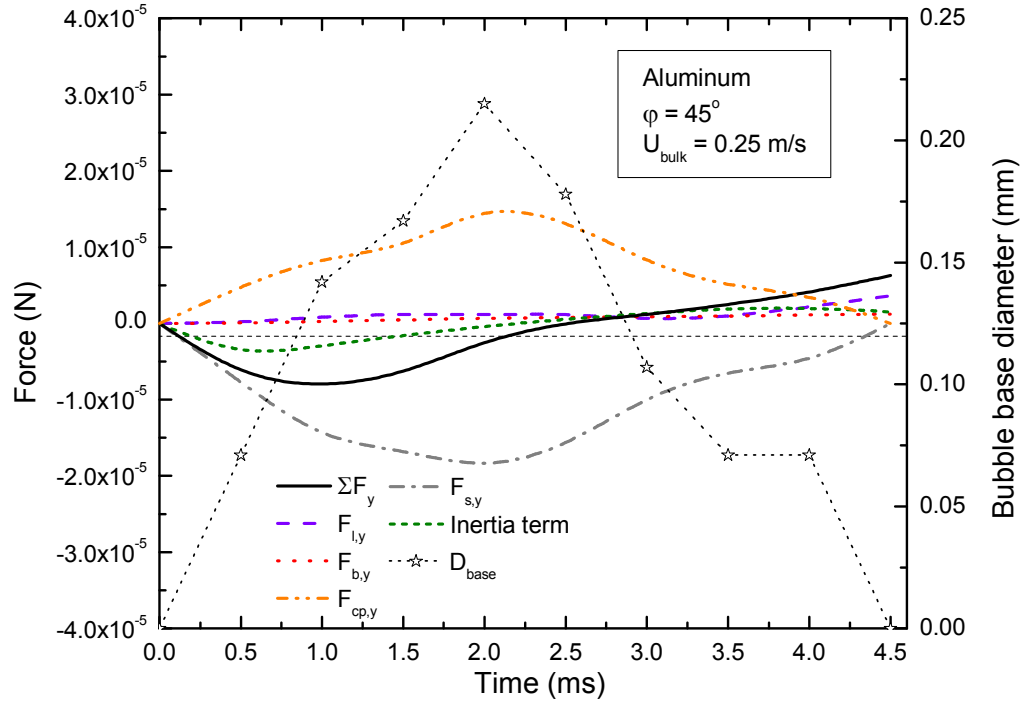

(b)

Figure 3.48 Forces acting on a growing bubble, and bubble base diameter, as a function of time, for 45° inclined surface and (a) U_{bulk} = 0.076 m/s, (b) U_{bulk} = 0.25 m/s – Aluminum surface.

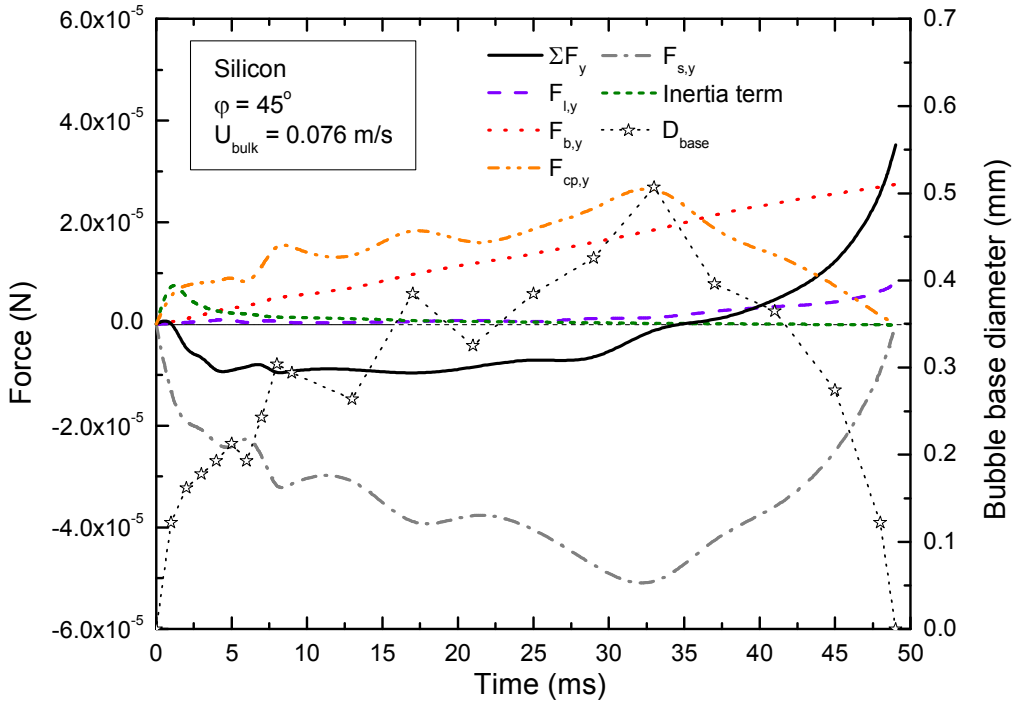

(a)

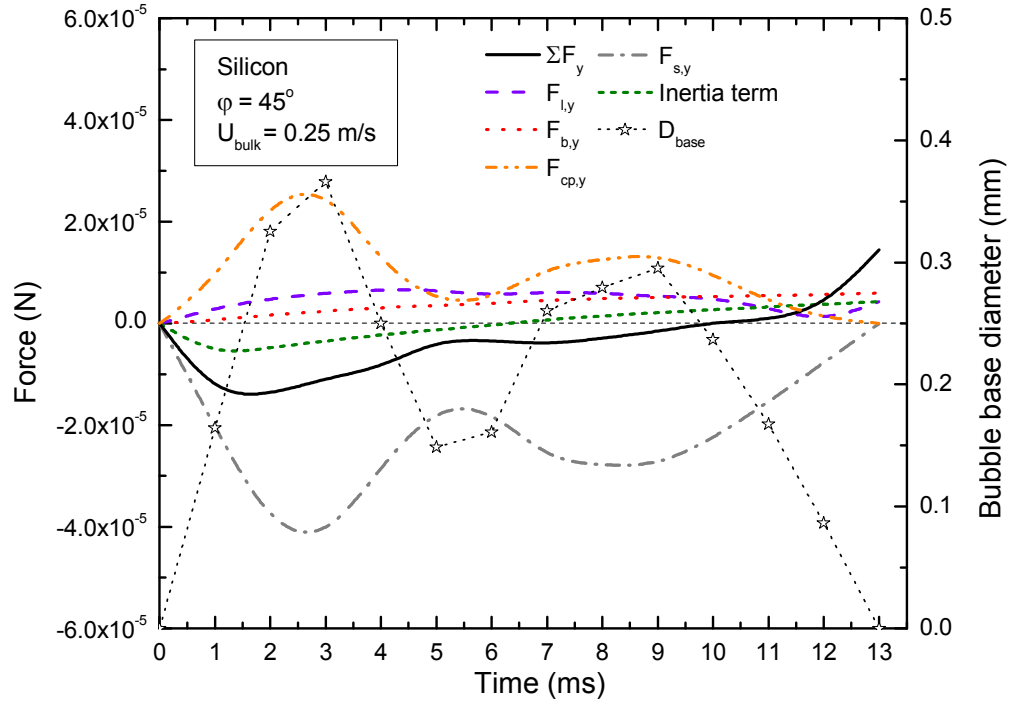

(b)

Figure 3.49 Forces acting on a growing bubble, and bubble base diameter, as a function of time, for 45° inclined surface and (a) U_{bulk} = 0.076 m/s, (b) U_{bulk} = 0.25 m/s – Silicon surface.

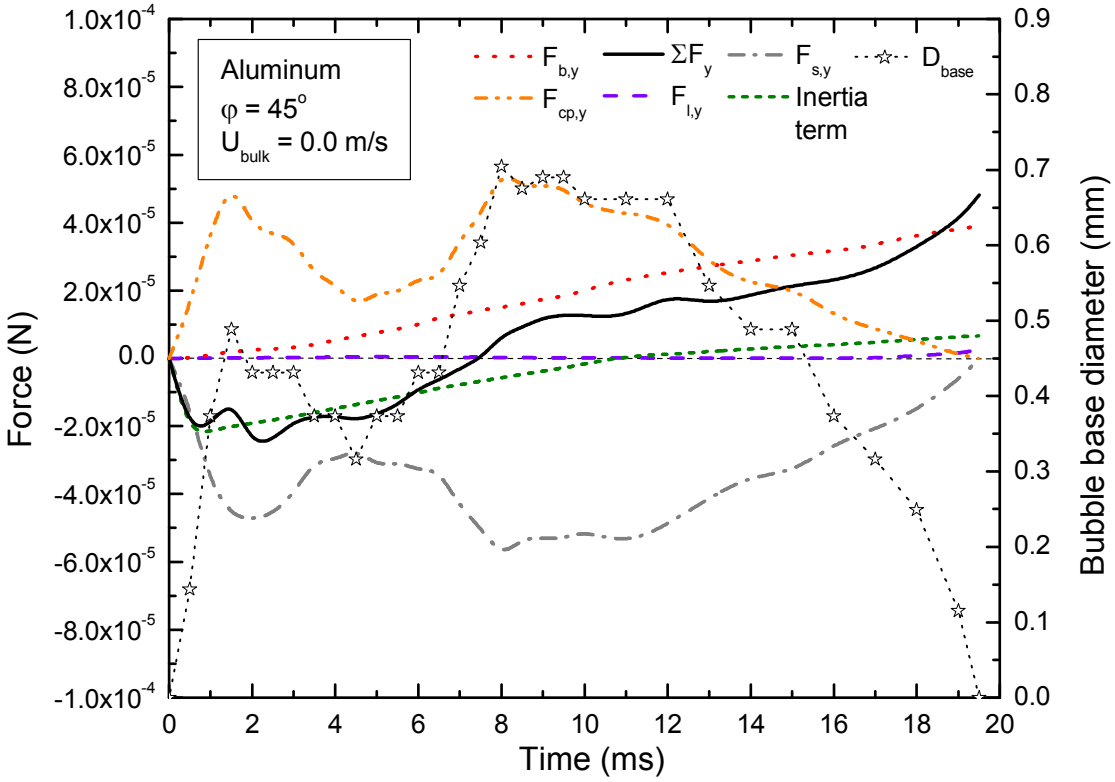

Figure 3.50 Forces acting on a growing bubble, and bubble base diameter, as a function of time, for 45° inclined surface and pool boiling conditions – Aluminum surface.

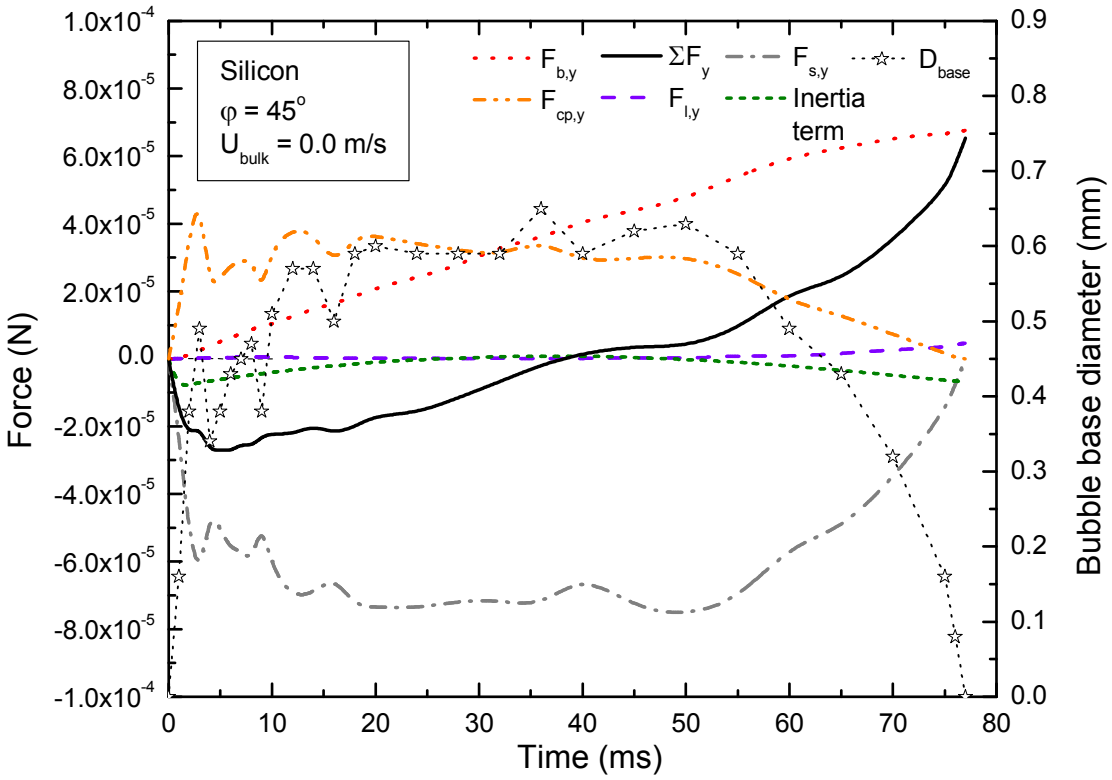

Figure 3.51 Forces acting on a growing bubble, and bubble base diameter, as a function of time, for 45° inclined surface and pool boiling conditions – Silicon surface.

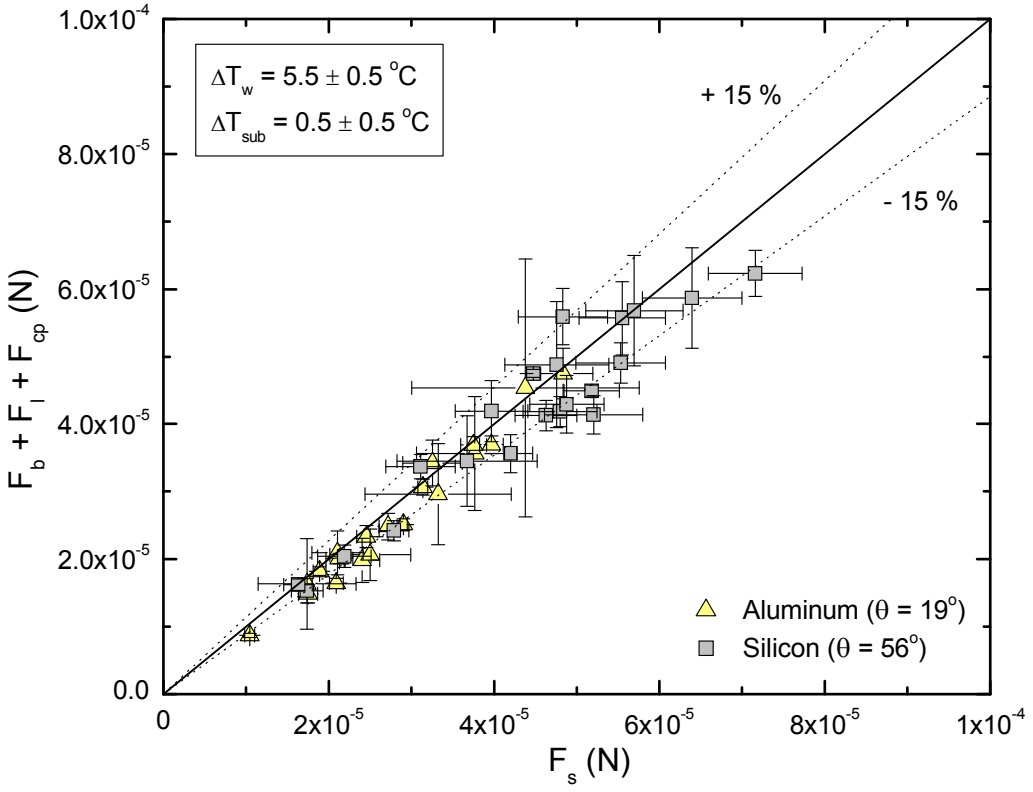

Figure 3.52 Comparison between detaching and attaching forces actual on a bubble, when bubble base diameter is maximum, for horizontal and vertical surfaces – Aluminum and silicon surfaces.

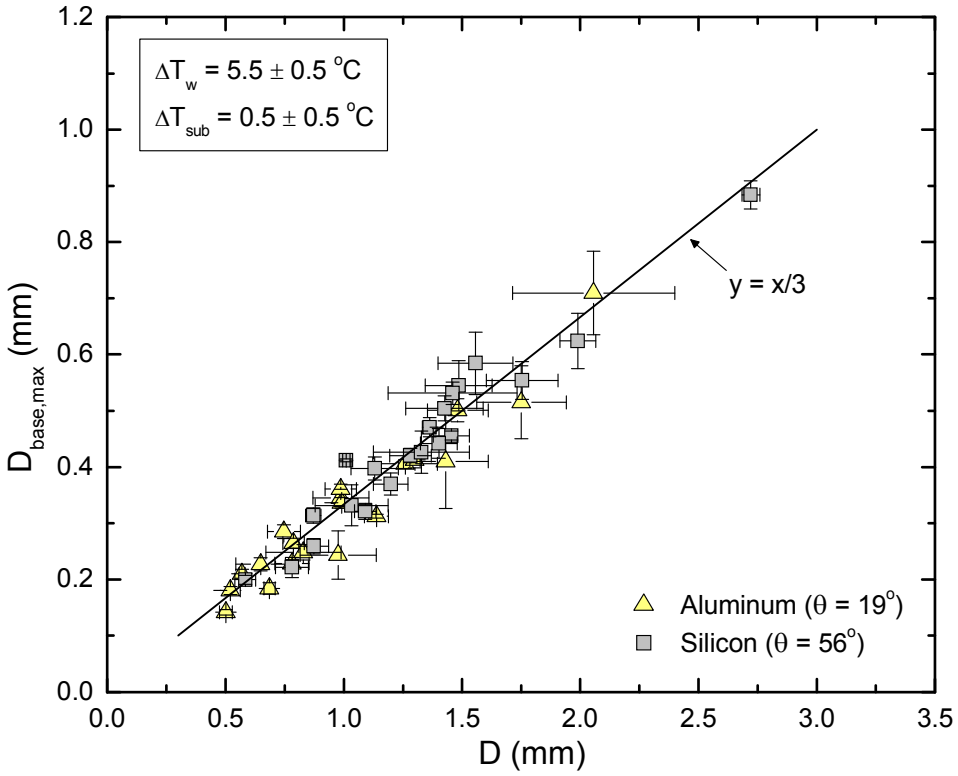

Figure 3.53 Maximum bubble base diameter as a function of bubble diameter, for horizontal and vertical surfaces – Aluminum and silicon surfaces.

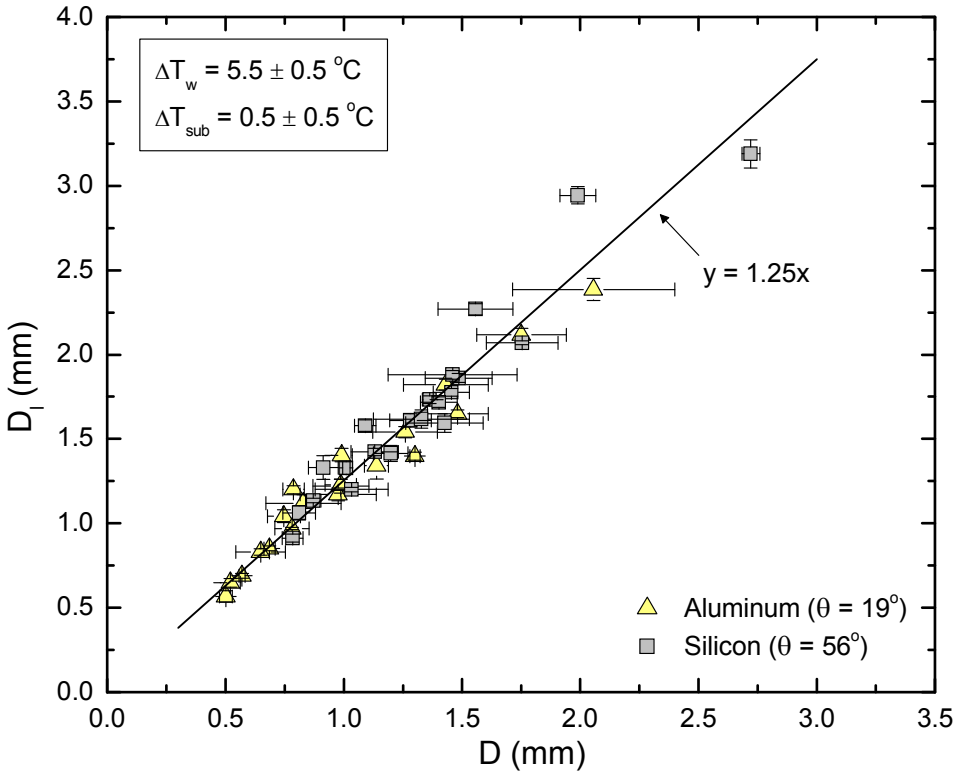

Figure 3.54 Bubble lift off diameter as a function of bubble diameter at D_{base} = $D_{base,max}$ diameter, for horizontal and vertical surfaces – Aluminum and silicon surfaces.

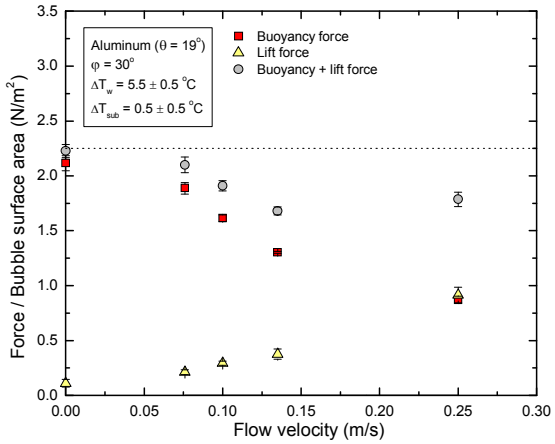

(a)

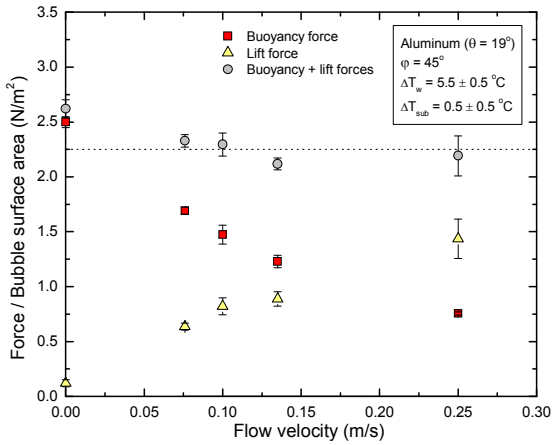

(b)

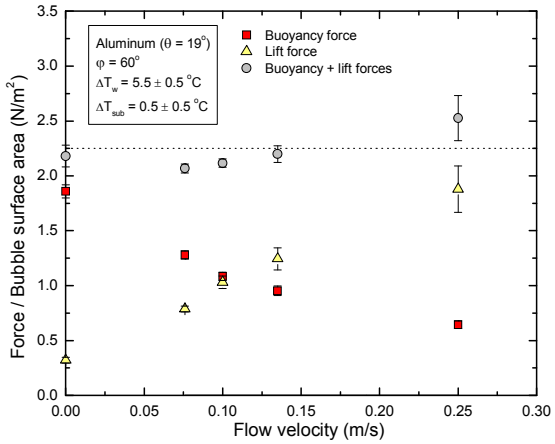

(c)

Figure 3.55 Forces acting on a bubble at lift off as a function of flow velocity, for (a) 30° inclined surface, (b) 45° inclined surface, and (c) 60° inclined surface – Aluminum surface.

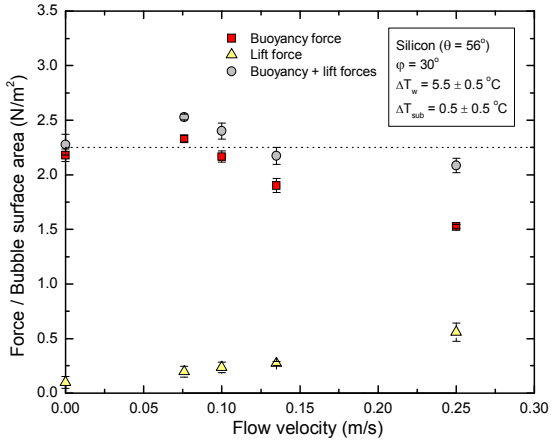

(a)

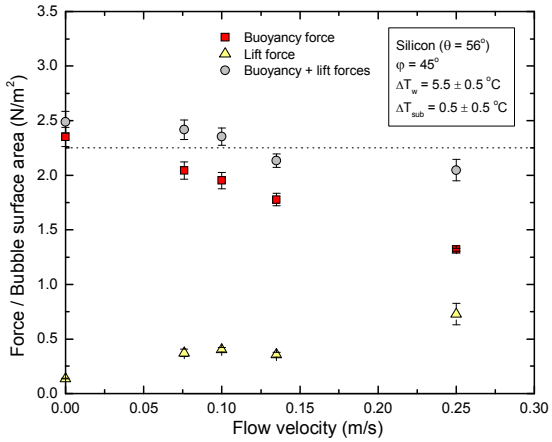

(b)

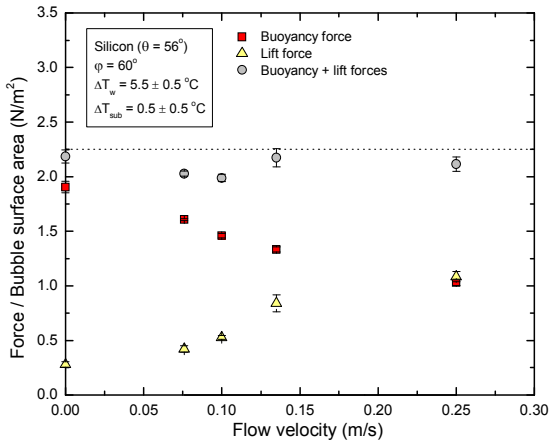

(c)

Figure 3.56 Forces acting on a bubble at lift off as a function of flow velocity, for (a) 30^{o} inclined surface, (b) 45^{o} inclined surface, and (c) 60^{o} inclined surface – Silicon surface.

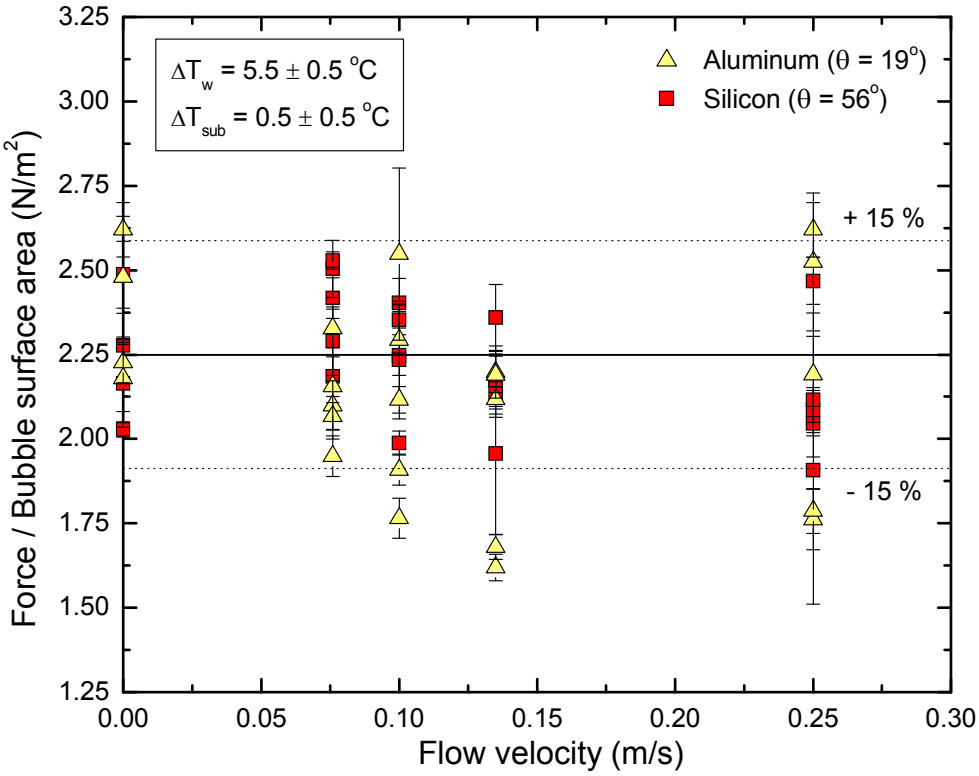

Figure 3.57 Sum of buoyancy and lift forces divided by bubble surface area, as a function of the sum of buoyancy and lift forces, for all orientations, flow velocities and surface materials.

Chapter 4
Results and Discussion – Two-Bubble Lateral Mergers Water Experiments

In order to study the effect of lateral bubble mergers on bubble dynamics during flow nucleate boiling, aluminum and silicon test heaters were assembled, each with two micromachined cavities at the center aligned along the direction of the flow. Heater configurations and components are identical to that for single bubble experiments, and are described in Chapter 2. These cavities, separated by 0.4 mm to 1.2 mm, were used to generate two discreet vapor bubbles. Experiments were run for various flow various velocities, horizontal and vertical inclinations and, as noted earlier, for two surface materials, at near saturated condition ($\Delta T_{sub} \leq 1.0$ K), and almost constant wall superheat ($5.0 \text{ K} \leq \Delta T_w \leq 6.0$ K), using water as test fluid. Measured quantities include bubble growth rate, bubble base diameter, bubble sliding distance (distance a bubble slides between departure from the nucleation site and lift-off from the heater surface) and bubble lift-off diameter (diameter at which the bubble lifts off from the heater surface).

4.1 Experimental results – Silicon test surface

4.1.1 Horizontal surface

This section describes the experiments carried out on a horizontal silicon surface, for a flow velocity varying from 0.076 m/s to 0.25 m/s.

U_{bulk} = 0.076 m/s

A typical ebullition cycle is shown in Fig. 4.1, for bulk liquid velocity of 0.076 m/s, a wall superheat of 5.7 ^{o}C, liquid subcooling of 0.4 ^{o}C, and a distance between the two cavities of 1 mm. It can be seen from Fig. 4.1 that the upstream bubble nucleates 2 ms before the downstream bubble. The two bubbles merge around 17.5 ms, forming a vapor bridge between the bubbles. Surfaces tension forces contract the bubbles, causing the bases to merge completely after 21 ms. The merged bubble lifts off at 23.5 ms. Figure 4.2(a) shows the growth rate for the ebullition cycle presented in Fig. 4.1. It can be seen from Fig. 4.2(a) that the downstream and upstream bubbles grow to diameters of 1.42 mm and 1.31 mm, respectively, before they merge. The merged bubble lifts off diameter is 1.92 mm. Figure 4.2(b) shows the sliding distance for the entire growth cycle. It can be seen that the downstream bubble slides around 0.03 mm before merging with the upstream bubble. The upstream bubble, on the other hand, slides in the opposite direction, as it gets pushed away by the growing downstream bubble. Note that the sliding distances are calculated as the difference between the bubble location and that of the nucleation site of the upstream bubble. The merged bubble lifts off after sliding 0.88 mm from the upstream bubble nucleation site. Finally, the evolution of the bubble base diameter as a function of time is shown in Fig. 4.2(c).

U_{bulk} = 0.1 m/s

Experimental results for 0.1 m/s liquid bulk velocity are presented in Fig. 4.3, for a wall superheat of 5.6 ^{o}C and liquid subcooling of 0.5 ^{o}C, and a distance between the two cavities of 1 mm. It can be seen from Fig. 4.3 that the downstream bubble nucleates 4 ms

after the upstream bubble does. The two bubbles merge around 15 ms, forming a vapor bridge between the bubbles. The bubble bases merge completely after 17 ms. The merged bubble lifts off at 18 ms. The growth rate for the ebullition cycle presented in Fig. 4.3 is shown in Fig. 4.4(a). The downstream bubble diameter reaches 0.90 mm, and the upstream bubble diameter reaches 1.19 mm, before the two bubbles merge. The merged bubble grows to a diameter of 1.61 mm before lift off occurs. The bubble sliding distance for this growth cycle is presented in Figure 4.4(b). The downstream bubble slides around 0.3 mm, and the upstream bubble slides around 0.35 mm, before merging. The merged bubble lifts off after sliding 0.88 mm from the upstream bubble nucleation site. The evolution of the bubble base diameter as a function of time is shown in Fig. 4.4(c).

$U_{bulk} = 0.135$ *m/s*

Figure 4.5 shows results obtained for a higher flow velocity, 0.135 m/s, for a wall superheat of 5.3 ^{o}C, a liquid subcooling of 0.7 ^{o}C, and a distance between the two cavities of 1 mm. The downstream bubble nucleates 6 ms after the upstream one. The bubbles start to merge after 13.5 ms, and their bases merge completely at 14.5 ms. The merged bubble lifts off at 15.5 ms. The growth rate for the ebullition cycle showed in Fig. 4.5 is plotted in Fig. 4.6(a). As can be seen in Fig. 4.6(a), the downstream bubble grows to a diameter of 0.81 mm before it merges with the upstream bubble, which reaches 1.09 mm in diameter. The merged bubble lifts off at a diameter of 1.30 mm. As can be seen in Fig. 4.6(b), the upstream bubble sliding distance is 0.18 mm before it merges with the downstream bubble, which slid for 0.06 mm. The merge bubble lift off occurs 0.87 mm

away from the upstream bubble nucleation site. The evolution of the bubble base diameter as a function of time is shown in Fig. 4.6(c).

U_{bulk} = 0.25 m/s

Figure 4.7 shows results obtained for the highest flow velocity studied for the horizontal silicon surface, 0.25 m/s. Wall superheat is 5.7 ^{o}C, liquid subcooling is 0.4 ^{o}C, and distance between the two cavities is 1 mm. The downstream bubble nucleates 2 ms after the upstream one, and the bubbles merge after 11.5 ms. The bubble bases merge completely at 12.5 ms. The merged bubble lifts off at 13 ms. Figure 4.8(a) shows the growth rate for the same ebullition cycle as in Fig. 4.7. The downstream bubble diameter before merger is 0.69 mm, while the upstream bubble diameter is 1.03 mm. The merged bubble lift off diameter is 1.15 mm. Figure 8(b) shows the bubble sliding for the growth cycle plotted in Fig. 7. The downstream bubble sliding distance before merger is 0.05 mm, and the upstream bubble sliding distance before merger is 0.11 mm. The merged bubble slides 0.70 mm from the nucleation site of the upstream bubble before lift off. The evolution of the bubble base diameter as a function of time is shown in Fig. 4.8(c).

Effect of flow velocity

Bubble lift off diameter, lift off time and sliding distance, are plotted in Fig. 4.9 to highlight the effect of velocity on bubble dynamics on an upward facing horizontal silicon surface, when two-bubble horizontal merger occurs. In Fig. 4.9, experimental results from three different cycles are plotted for each flow velocity. From Figs. 4.9(a) and 4.9(b), it is clear that as velocity increases, both lift off diameter and lift off time

decreases non-linearly. Lift off diameters and times are much smaller than for two-bubble merger in pool boiling conditions, as shown by the data from Mukherjee (2004) (for ΔT_w = 5.0 ^oC, $\Delta T_{sub} \approx 0$ ^oC, $\theta = 54^o$, and x_{cav} = 1.4 mm). Bubble lift off diameter is smaller at higher velocities, due to an increase in lift force with increase in relative velocity. The effect of velocity on sliding distance is unclear: at low velocities (0 m/s to 0.1 m/s), sliding distance increases with increase in velocity while for 0.1 m/s to 0.25 m/s the opposite is seen.

4.1.2 Vertical surface

Experiments described in this section were carried out on a vertical silicon surface, for a flow velocity varying from 0.076 m/s to 0.25 m/s.

U_{bulk} = 0.076 m/s

A typical ebullition cycle is shown in Fig. 4.10, for bulk liquid velocity of 0.076 m/s, a wall superheat of 5.9 ^oC, liquid subcooling of 0.4 ^oC, and a distance between the two cavities of 1.2 mm. It can be seen from Fig. 4.10 that the upstream bubble nucleates 11.5 ms after the downstream bubble. The two bubbles merge around 20.5 ms, and their bases merge completely after 21 ms. The merged bubble lifts off at 33 ms. Figure 4.11(a) shows the growth rate for the ebullition cycle presented in Fig. 4.10. It can be seen from Fig. 4.11(a) that the downstream and upstream bubbles grow to diameters of 2.14 mm and 1.98 mm, respectively, before they merge. The merged bubble lifts off diameter is 3.37 mm. Figure 4.11(b) shows the sliding distance for the entire growth cycle. It can be seen that the downstream bubble slides around 1.96 mm before merging with the

upstream bubble. The upstream bubble, on the other hand, slides for 1.08 mm before the merger. The merged bubble lifts off after sliding 3.62 mm from the upstream bubble nucleation site. Finally, the evolution of the bubble base diameter as a function of time is shown in Fig. 4.11(c).

$U_{bul}k$ = 0.1 m/s

Experimental results for 0.1 m/s liquid bulk velocity are presented in Fig. 4.12, for a wall superheat of 5.8 ^{o}C and liquid subcooling of 0.6 ^{o}C, and a distance between the two cavities of 1.2 mm. It can be seen from Fig. 4.12 that the downstream bubble nucleates 4.5 ms after the upstream bubble does. The two bubbles merge around 14.5 ms, forming a vapor bridge between the bubbles. The bubble bases merge completely after 18.5 ms. The merged bubble lifts off at 26.5 ms. The growth rate for the ebullition cycle presented in Fig. 4.12 is shown in Fig. 4.13(a). The downstream bubble diameter reaches 1.41 mm, and the upstream bubble diameter reaches 1.82 mm, before the two bubbles merge. The merged bubble grows to a diameter of 2.82 mm before lift off occurs. The bubble sliding distance for this growth cycle is presented in Figure 4.13(b). The downstream bubble slides around 0.38 mm, and the upstream bubble slides around 0.17 mm, before merging. The merged bubble lifts off after sliding 3.07 mm from the upstream bubble nucleation site. The evolution of the bubble base diameter as a function of time is shown in Fig. 4.13(c).

U_{bulk} = 0.135 m/s

Figure 4.14 shows results obtained for a higher flow velocity, 0.135 m/s, for a wall superheat of 5.9 ^{o}C, a liquid subcooling of 0.5 ^{o}C, and a distance between the two cavities of 1.2 mm. The downstream bubble nucleates 3.5 ms after the upstream one. The bubbles start to merge after 13.5 ms, and their bases merge completely at 15.5 ms. The merged bubble lifts off at 22 ms. The growth rate for the ebullition cycle showed in Fig. 4.14 is plotted in Fig. 4.15(a). As can be seen in Fig. 4.15(a), the downstream bubble grows to a diameter of 1.35 mm before it merges with the upstream bubble, which reaches 1.51 mm in diameter. The merged bubble lifts off at a diameter of 2.44 mm. As can be seen in Fig. 4.15(b), the upstream bubble sliding distance is 0.11 mm before it merges with the downstream bubble, which slid in the opposing direction, due to the wake of the large bubble that lifted of moments before. The merge bubble lift off occurs 2.14 mm away from the upstream bubble nucleation site. The evolution of the bubble base diameter as a function of time is shown in Fig. 4.15(c).

U_{bulk} = 0.25 m/s

Figure 4.16 shows results obtained for the highest flow velocity studied for the vertical silicon surface, 0.25 m/s. Wall superheat is 5.7 ^{o}C, liquid subcooling is 0.7 ^{o}C, and distance between the two cavities is 1.2 mm. The downstream bubble nucleates 6 ms after the upstream one, and the bubbles merge after 8 ms. The bubble bases merge completely at 10 ms. The merged bubble lifts off at 17 ms. Figure 4.17(a) shows the growth rate for the same ebullition cycle as in Fig. 4.16. The downstream bubble diameter before merger is 0.96 mm, while the upstream bubble diameter is 1.05 mm. The

merged bubble lift off diameter is 1.89 mm. Figure 4.17(b) shows the bubble sliding for the growth cycle plotted in Fig. 4.16. The downstream bubble sliding distance before merger is 0.07 mm, and the upstream bubble sliding distance before merger is 0.34 mm. The merged bubble slides 1.99 mm from the nucleation site of the upstream bubble before lift off. The evolution of the bubble base diameter as a function of time is shown in Fig. 4.17(c).

Effect of flow velocity

Bubble lift off diameter, lift off time and sliding distance, for are plotted in Fig. 4.18 to highlight the effect of velocity on bubble dynamics on a vertical silicon surface, when two-bubble horizontal merger occurs, in upflow conditions. In Fig. 4.18, experimental results from three different cycles are plotted for each flow velocity. From Figs. 4.18(a) and 4.18(b), it is clear that as velocity increases, both lift off diameter and lift off time decreases non-linearly. The effect of velocity on sliding distance (for velocities between 0.076 m/s and 0.25 m/s) is a decrease in sliding distance with increase in velocity, as shown in Fig. 4.18(c).

4.1.3 Effect of orientation

To study the effect of orientation on two-bubble merger bubble dynamics, comparison between bubble lift off diameter, lift off time and sliding distance data for horizontal and vertical heater orientations is shown in the following section.

Bubble lift off diameter

Figure 4.19(a) shows the effect of orientation and velocity on lift off diameter. Lift off diameter increases with both flow velocity and orientation. The absence of a component of gravity normal to the heater surface, results in a smaller direct contribution of buoyancy towards lift off. As a consequence, the bubble needs to grow to a larger size for the lift force to be able to compensate the forces keeping the bubble on the surface. Also, it appears that the effect of orientation on lift off diameter is reduced with increase in flow velocity.

Bubble lift off time

The effect of orientation and velocity on lift off time is presented in Fig. 4.19(b). Lift off time increases with increase in heater orientation from horizontal to vertical. Heater orientation does not have a significant effect on bubble growth rate, and as shown in the previous paragraph, lift off diameter is larger for vertical heater orientation than for horizontal. As a result, the lift off time is larger for the vertical configuration than for the horizontal one.

Bubble sliding distance

Sliding distance increases with orientation, as shown in Fig. 4.19(c), whereas the effect of velocity on sliding distance is unclear, and depends on orientation. For horizontal surface, sliding distance at low velocities (0.076 m/s to 0.1 m/s) increases with increase in velocity, while for 0.1 m/s to 0.25 m/s sliding distance decreases with increase

in velocity. For vertical surface, on the other hand, sliding distance (for velocities between 0.076 m/s and 0.25 m/s) decreases with increase in velocity.

4.2 Experimental results – Aluminum test surface

4.2.1 Horizontal surface

This section describes the experiments carried out on a horizontal aluminum surface, for a flow velocity varying from 0.076 m/s to 0.25 m/s.

$U_{bulk} = 0.076$ *m/s*

A typical ebullition cycle is shown in Fig. 4.20, for bulk liquid velocity of 0.076 m/s, a wall superheat of 5.8 ^{o}C, liquid subcooling of 0.5 ^{o}C, and a distance between the two cavities of 0.6 mm. It can be seen from Fig. 4.20 that the upstream and downstream bubbles nucleate at the same time. The two bubbles merge around 4 ms, forming a vapor bridge between the bubbles. The bubble bases merge completely after 6 ms. The merged bubble lifts off at 10 ms. Figure 4.21(a) shows the growth rate for the ebullition cycle presented in Fig. 4.20. It can be seen from Fig. 4.21(a) that the downstream and upstream bubbles grow to diameters of 1.03 mm and 0.91 mm, respectively, before they merge. The merged bubble lifts off diameter is 1.48 mm. Figure 4.21(b) shows the sliding distance for the entire growth cycle. It can be seen that the downstream bubble slides around 0.20 mm before merging with the upstream bubble. The upstream bubble, on the other hand, slides in the opposite direction, as it get pushed away by the growing downstream bubble, as shown in Fig. 20. The merged bubble lifts off after sliding 0.77

mm from the upstream bubble nucleation site. Finally, the evolution of the bubble base diameter as a function of time is shown in Fig. 4.21(c).

U_{bulk} = 0.1 m/s

Experimental results for 0.1 m/s liquid bulk velocity are presented in Fig. 4.22, for a wall superheat of 5.6 ^{o}C and liquid subcooling of 0.6 ^{o}C, and a distance between the two cavities of 0.6 mm. It can be seen from Fig. 4.22 that the upstream and downstream bubbles nucleate at the same time. Note that due to the small bubble size and the intense backlight, the upstream bubble embryo can hardly be seen. The two bubbles merge around 4 ms, forming a vapor bridge between the bubbles. The bubble bases merge completely after 6.5 ms. The merged bubble lifts off at 9 ms. The growth rate for the ebullition cycle presented in Fig. 4.22 is shown in Fig. 4.23(a). The downstream bubble diameter reaches 0.73 mm, and the upstream bubble diameter reaches 0.94 mm, before the two bubbles merge. The merged bubble grows to a diameter of 1.25 mm before lift off occurs. The bubble sliding distance for this growth cycle is presented in Figure 4.23(b). The downstream bubble slides around 0.16 mm, and the upstream bubble slides around 0.13 mm, before merging. The merged bubble lifts off after sliding 0.51 mm from the upstream bubble nucleation site. The evolution of the bubble base diameter as a function of time is shown in Fig. 4.23(c).

U_{bulk} = 0.135 m/s

Figure 4.24 shows results obtained for a higher flow velocity, 0.135 m/s, for a wall superheat of 5.5 ^{o}C, a liquid subcooling of 0.4 ^{o}C, and a distance between the two cavities

of 0.4 mm. The downstream bubble nucleates 0.5 ms after the upstream one. The bubbles start to merge after 3.5 ms, and their bases merge completely at 4.5 ms. The merged bubble lifts off at 8.5 ms. The growth rate for the ebullition cycle shown in Fig. 4.24 is plotted in Fig. 4.25(a). As can be seen in Fig. 4.25(a), the downstream bubble grows to a diameter of 0.63 mm before it merges with the upstream bubble, which reaches 0.82 mm in diameter. The merged bubble lifts off at a diameter of 1.13 mm. As can be seen in Fig. 4.25(b), the upstream bubble sliding distance is 0.11 mm before it merges with the downstream bubble, which slid for 0.03 mm. The merge bubble lift off occurs 0.43 mm away from the upstream bubble nucleation site. The evolution of the bubble base diameter as a function of time is shown in Fig. 4.25(c).

U_{bulk} = 0.25 m/s

Figure 4.26 shows results obtained for the highest flow velocity studied for the horizontal aluminum surface, 0.25 m/s. Wall superheat is 5.8 ^{o}C, liquid subcooling is 0.6 ^{o}C, and distance between the two cavities is 0.4 mm. The upstream and downstream bubbles nucleate at the same time, and the bubbles merge after 3 ms. The bubble bases merge completely at 4.5 ms. The merged bubble lifts off at 6 ms. Figure 4.27(a) shows the growth rate for the same ebullition cycle as in Fig. 4.26. The downstream bubble diameter before merger is 0.54 mm, while the upstream bubble diameter is 0.62 mm. The merged bubble lift off diameter is 0.90 mm. Figure 4.27(b) shows the bubble sliding for the growth cycle plotted in Fig. 4.26. The downstream bubble sliding distance before merger is 0.15 mm, and the upstream bubble sliding distance before merger is 0.06 mm. The merged bubble slides 0.53 mm from the nucleation site of the upstream bubble

before lift off. The evolution of the bubble base diameter as a function of time is shown in Fig. 4.27(c).

Effect of flow velocity

Bubble lift off diameter, lift off time and sliding distance, are plotted in Fig. 4.28 to highlight the effect of velocity on bubble dynamics on an upward facing horizontal aluminum surface, when two-bubble horizontal merger occurs. In Fig. 4.28, experimental results from three different cycles are plotted for each flow velocity. From Figs. 4.28(a) and 4.28(b), it is clear that as velocity increases, both lift off diameter and lift off time decreases non-linearly. As can be seen in Fig. 4.28(c), the overall trend is a decrease in sliding distance with increase in flow velocity (for 0.076 m/s to 0.25 m/s), although very little change in sliding distance is observed between 0.1 m/s and 0.135 m/s flow velocities.

4.2.2 Vertical surface

Experiments described in this section were carried out on a vertical aluminum surface, for a flow velocity varying from 0.076 m/s to 0.25 m/s.

U_{bulk} = 0.076 m/s

A typical ebullition cycle is shown in Fig. 4.29, for bulk liquid velocity of 0.076 m/s, a wall superheat of 5.7 ^{o}C, liquid subcooling of 0.5 ^{o}C, and a distance between the two cavities of 1.2 mm. It can be seen from Fig. 4.29 that the upstream bubble nucleates 0.5 ms before the downstream bubble. The two bubbles merge around 9.5 ms, and their bases

merge completely after 13 ms. The merged bubble lifts off at 23 ms. Figure 4.30(a) shows the growth rate for the ebullition cycle presented in Fig. 4.29. It can be seen from Fig. 4.30(a) that the downstream and upstream bubbles grow to diameters of 1.75 mm and 1.57 mm, respectively, before they merge. The merged bubble lifts off diameter is 2.65 mm. Figure 4.30(b) shows the sliding distance for the entire growth cycle. It can be seen that the downstream bubble slides around 0.2 mm before merging with the upstream bubble. The upstream bubble, on the other hand, does not leave its nucleation site, probably because it is blocked by the downstream bubble. The merged bubble lifts off after sliding 1.92 mm from the upstream bubble nucleation site. Finally, the evolution of the bubble base diameter as a function of time is shown in Fig. 4.30(c).

U_{bulk} = 0.1 m/s

Experimental results for 0.1 m/s liquid bulk velocity are presented in Fig. 4.31, for a wall superheat of 5.5 ^{o}C and liquid subcooling of 0.4 ^{o}C, and a distance between the two cavities of 1.2 mm. It can be seen from Fig. 4.31 that the downstream bubble nucleates 0.5 ms after the upstream bubble does. The two bubbles merge around 8.5 ms, forming a vapor bridge between the bubbles. The bubble bases merge completely after 13 ms. The merged bubble lifts off at 18 ms. The growth rate for the ebullition cycle presented in Fig. 4.31 is shown in Fig. 4.32(a). The downstream bubble diameter reaches 1.55 mm, and the upstream bubble diameter reaches 1.54 mm, before the two bubbles merge. The merged bubble grows to a diameter of 2.36 mm before lift off occurs. The bubble sliding distance for this growth cycle is presented in Figure 4.32(b). The downstream bubble slides around 0.45 mm, and the upstream bubble slides around 0.18 mm, before merging. The

merged bubble lifts off after sliding 1.90 mm from the upstream bubble nucleation site. The evolution of the bubble base diameter as a function of time is shown in Fig. 4.32(c).

U_{bulk} = 0.135 m/s

Figure 4.33 shows results obtained for a higher flow velocity, 0.135 m/s, for a wall superheat of 5.7 ^{o}C, a liquid subcooling of 0.6 ^{o}C, and a distance between the two cavities of 1.2 mm. The downstream bubble nucleates 3.5 ms after the upstream one. The bubbles start to merge after 8.5 ms, and their bases merge completely at 11 ms. The merged bubble lifts off at 14 ms. The growth rate for the ebullition cycle showed in Fig. 4.33 is plotted in Fig. 4.34(a). As can be seen in Fig. 4.34(a), the downstream bubble grows to a diameter of 0.95 mm before it merges with the upstream bubble, which reaches 1.47 mm in diameter. The merged bubble lifts off at a diameter of 1.96 mm. As can be seen in Fig. 4.34(b), the upstream bubble sliding distance is 0.16 mm before it merges with the downstream bubble, which slid 0.08 mm. The merge bubble lift off occurs 1.35 mm away from the upstream bubble nucleation site. The evolution of the bubble base diameter as a function of time is shown in Fig. 4.34(c).

U_{bulk} = 0.25 m/s

Figure 4.35 shows results obtained for the highest flow velocity studied for the vertical aluminum surface, 0.25 m/s. Wall superheat is 5.6 ^{o}C, liquid subcooling is 0.6 ^{o}C, and distance between the two cavities is 1.2 mm. The upstream and downstream bubbles nucleate at the same time, and the bubbles merge after 5.5 ms. The bubble bases merge completely at 7.5 ms. The merged bubble lifts off at 12 ms. Figure 4.36(a) shows the

growth rate for the same ebullition cycle as in Fig. 4.35. The downstream bubble diameter before merger is 1.17 mm, while the upstream bubble diameter is 1.06 mm. The merged bubble lift off diameter is 1.73 mm. Figure 4.36(b) shows the bubble sliding for the growth cycle plotted in Fig. 4.36. The downstream bubble sliding distance before merger is 0.52 mm. The upstream bubble, on the other hand, does not leave its nucleation site, probably because it is blocked by the larger downstream bubble. The merged bubble slides 2.09 mm from the nucleation site of the upstream bubble before lift off. The evolution of the bubble base diameter as a function of time is shown in Fig. 4.36(c).

Effect of flow velocity

Bubble lift off diameter, lift off time and sliding distance, for are plotted in Fig. 4.37 to highlight the effect of velocity on bubble dynamics on a vertical aluminum surface, when two-bubble horizontal merger occurs, in upflow conditions. In Fig. 37, experimental results from three different cycles are plotted for each flow velocity. From Figs. 4.37(a) and 4.37(b), it is clear that as velocity increases, both lift off diameter and lift off time decreases non-linearly, as shown in Chapter 3 for single bubble conditions. The effect of velocity on sliding distance is unclear: sliding distance at low velocities (0.076 m/s to 0.1 m/s) increases with increase in velocity, while for 0.1 m/s to 0.25 m/s sliding distance decreases with increase in velocity. Moreover, very little change in sliding distance is observed between 0.076 m/s and 0.1 m/s flow velocities.

4.2.3 Effect of orientation

To study the effect of orientation on two-bubble merger bubble dynamics, comparison between bubble lift off diameter, lift off time and sliding distance data for horizontal and vertical aluminum heater orientations is shown in the following section.

Bubble lift off diameter

Figure 4.38(a) shows the effect of orientation and velocity on lift off diameter. Lift off diameter increases with both flow velocity and orientation. Note that it appears that the effect of orientation on lift off diameter is reduced with increase in flow velocity.

Bubble lift off time

The effect of orientation and velocity on lift off time is presented in Fig. 4.38(b). Lift off time increases with increase in heater orientation from horizontal to vertical. Heater orientation does not have a significant effect on bubble growth rate, and as shown in the previous paragraph, lift off diameter is larger for vertical heater orientation than for horizontal. As a result, the lift off time is larger for the vertical configuration than for the horizontal one. Also, it appears that the effect of orientation on lift off time is reduced with increase in flow velocity.

Bubble sliding distance

Sliding distance increases with orientation, as shown in Fig. 4.38(c), whereas the effect of velocity on sliding distance is unclear, and depends on orientation. For horizontal surface, sliding distance (for velocities between 0.076 m/s and 0.25 m/s)

decreases with increase in velocity. For vertical surface, on the other hand, sliding distance at low velocities (0.076 m/s to 0.1 m/s) increases with increase in velocity, while for 0.1 m/s to 0.25 m/s sliding distance decreases with increase in velocity.

4.2.4 Effect of heater material

To study the effect of heater material on two-bubble merger bubble dynamics, comparison between bubble lift off diameter, lift off time and sliding distance data for aluminum ($\theta = 19^o$) and silicon ($\theta = 56^o$) heaters, for both horizontal and vertical heater orientations, is shown in the following section.

4.2.4.1 Horizontal surfaces

Bubble lift off diameter

Figure 4.39(a) shows the effect of surface material on lift off diameter. Contact angle appears to have a slight effect on the trend of the curves, and the effect of contact angle on lift off diameter seems to decrease with increase in flow velocity. Lift off diameter decreases with increase in flow velocity, irrespective of heater material. What changes with contact angle is the magnitude of lift off diameter. For similar conditions, lift off diameter is much smaller for a lower contact angle.

Bubble lift off time

Lift off times for silicon and aluminum are shown in Fig. 4.39(b). Contact angle appears to have an effect on the trend of lift off time for velocities between 0.076 m/s and 0.1 m/s: the effect of contact angle on lift off time appears to decrease with increase in

velocity. For velocities between 0.1 m/s and 0.25 m/s, the trend is the same for lift off time for both materials, but the values are different. For all velocities, the lift off times for aluminum are much smaller than that for silicon. Growth rate is not affected dramatically by contact angle, which means that smaller lift off diameters result in shorter growth periods.

Bubble sliding distance

The effects flow velocity and contact angle on sliding distance are shown in Fig. 4.39(c). The effect of contact angle on the trend is unclear. For aluminum surface, sliding distance (for velocities between 0.076 m/s and 0.25 m/s) decreases with increase in velocity. For silicon surface, on the other hand, sliding distance at low velocities (0.076 m/s to 0.1 m/s) increases with increase in velocity, while for 0.1 m/s to 0.25 m/s sliding distance decreases with increase in velocity. Again, the difference is in the magnitude of the sliding distance. For low contact angle, the growth period is much shorter than for larger contact angle and similar parameters. This in turn leads to a shorter sliding distance, since sliding time is reduced. While very little difference is seen for the lowest flow velocity (0.076 m/s), this effect appears to decrease with increase in flow velocity (for flow velocities between 0.1 m/s and 0.25 m/s). It must be noted that uncertainty is largest for sliding distance measurements, and that these results should therefore be taken with caution.

4.2.4.2 Vertical surfaces

Bubble lift off diameter

Figure 4.40(a) shows the effect of surface material on lift off diameter, for vertical surfaces. Contact angle appears to have an effect on the trend of the curves: the effect of contact angle on lift off diameter seems to decrease with increase in velocity. It can be seen from Fig. 4.40(a) that the effect of contact angle on bubble lift off diameter is largest at low flow velocities. Lift off diameter decreases with increase in flow velocity, irrespective of heater material. However, contact angle affects the magnitude of lift off diameter. For similar flow conditions, lift off diameter is smaller for a lower contact angle. Note that for the largest flow velocity, 0.25 m/s, there is almost no effect of contact angle on lift off diameter.

Bubble lift off time

Lift off times for silicon and aluminum, for vertical heaters, are shown in Fig. 4.40(b). The trend is the same for lift off time for both materials, but the magnitudes of the values are different. For all velocities, the lift off times for aluminum are much smaller than that for silicon. Growth rate is not affected dramatically by contact angle, which means that smaller lift off diameters result in shorter growth periods.

Bubble sliding distance

The effects flow velocity and contact angle on sliding distance are shown in Fig. 4.40(c). The effect of contact angle on the trend is unclear. For aluminum surface, sliding distance at low velocities (0.076 m/s to 0.1 m/s) increases with increase in velocity, while

for 0.1 m/s to 0.25 m/s sliding distance decreases with increase in velocity. For silicon surface, on the other hand, sliding distance (for velocities between 0.076 m/s and 0.25 m/s) decreases with increase in velocity. Again, the magnitude of the sliding distance is different for different contact angle. For low contact angle, the growth period is much shorter than for larger contact angle and similar parameters. This in turn leads to a shorter sliding distance, since sliding time is reduced.

4.3 Chapter conclusions

In this Chapter, two-bubble lateral in-line merger experiments were run for various flow velocities, orientations and surface materials. The effect of these parameters on some key characteristics of the bubble growth, such as bubble lift off diameter, lift off time and sliding distance, were investigated. The main conclusions that can be drawn from theses results are as follows:

- Irrespective of orientation, contact angle, and flow velocities, a vapor bridge is formed between the bubbles when they start to merge, with water trapped underneath.
- For all cases, after bubble merger is initiated, surfaces tension forces contract the bubbles, causing the bases to merge completely.
- Irrespective of orientation and contact angle, lift off diameter and time decrease with increase in bulk liquid velocity.
- For given conditions, bubble lift off diameter increases when the gravity component normal to the heater is decreased. The effect gravity on lift off diameter decreases with increase in flow velocity. Most importantly, for vertical

surfaces, at high flow velocities, the effect of contact angle on lift off diameter is almost negligible.

- While the effect of velocity on bubble sliding distance is unclear and depends on the conditions, for most cases sliding distance increases with decrease in the magnitude of the component of gravity normal to the heater, and with increase in contact angle.

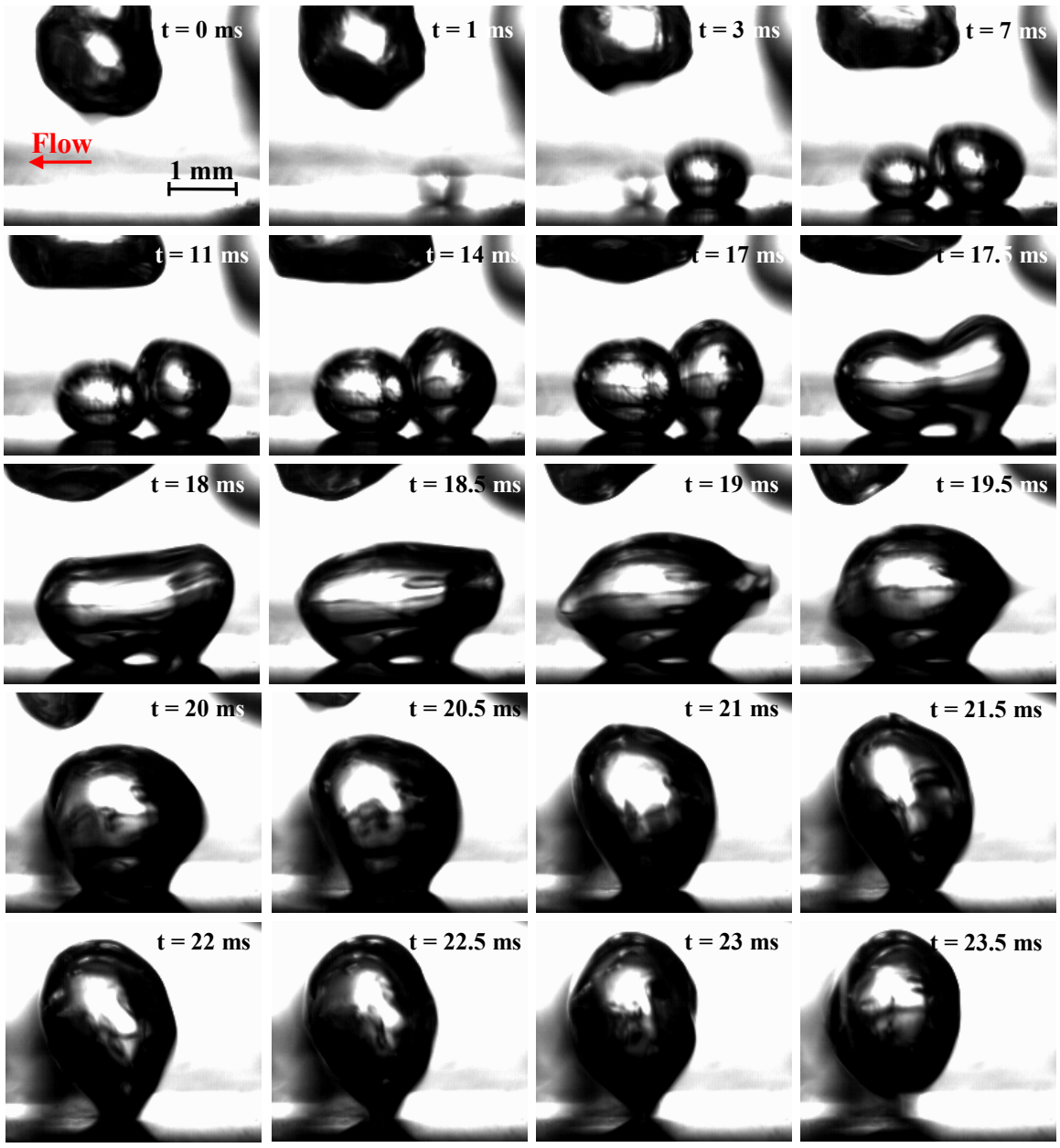

Figure 4.1 Two-bubble merger growth cycle, for horizontal silicon surface, U_{bulk} = 0.076 m/s, ΔT_w = 5.7 ^oC, ΔT_{sub} = 0.4 ^oC and x_{cav} = 1 mm.

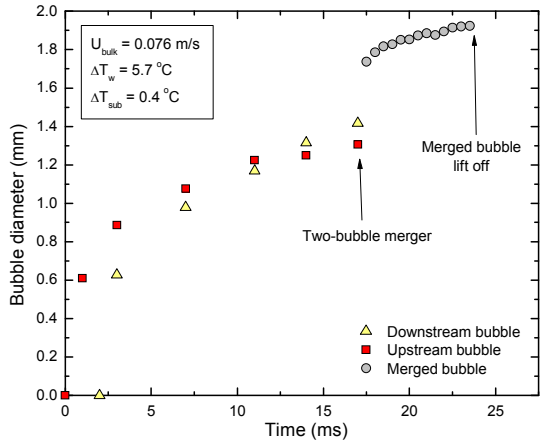

(a)

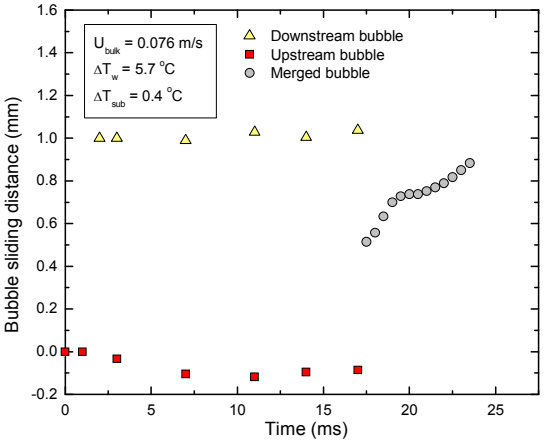

(b)

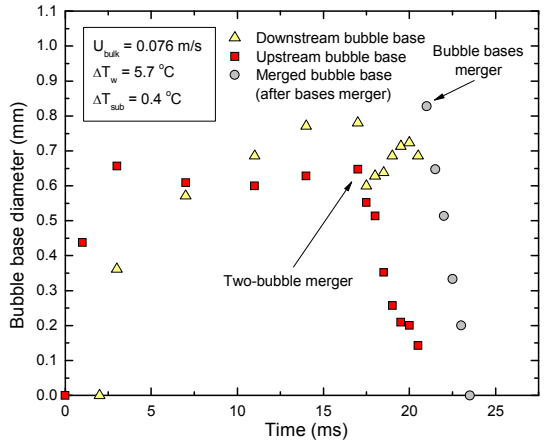

(c)

Figure 4.2 (a) Growth rate, (b) sliding distance, and (c) base diameter, during two-bubble merger, for horizontal silicon surface, U_{bulk} = 0.076 m/s, ΔT_w = 5.7 °C, ΔT_{sub} = 0.4 °C and x_{cav} = 1 mm.

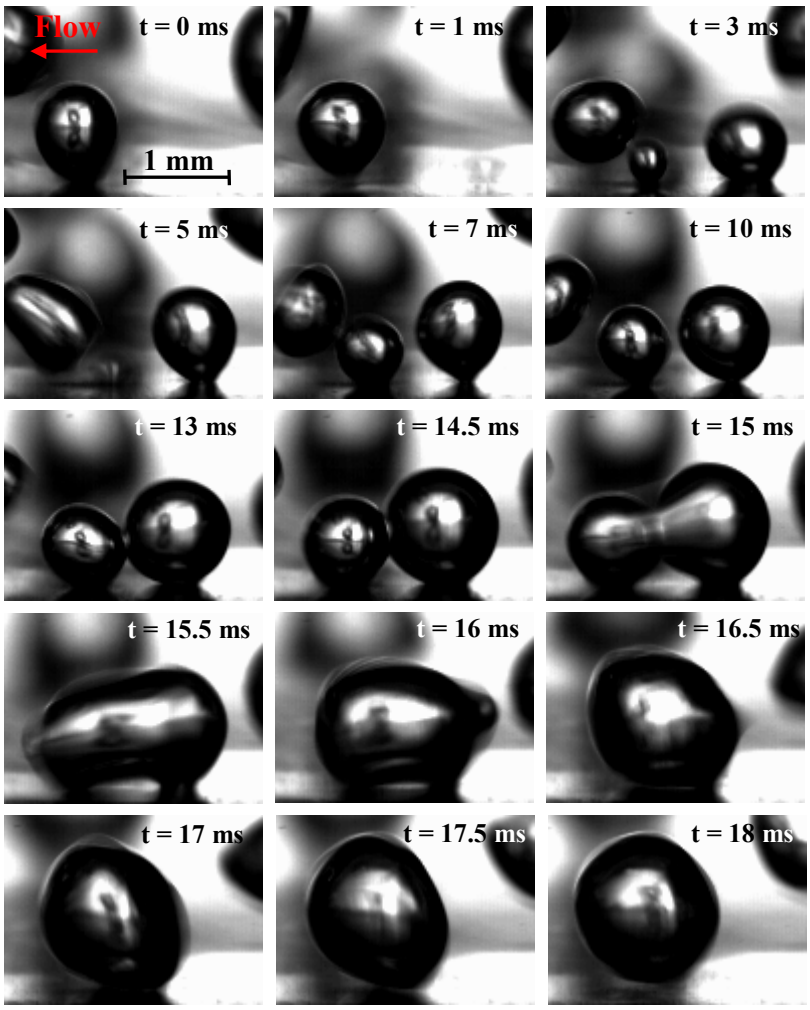

Figure 4.3 Two-bubble merger growth cycle, for horizontal silicon surface, U_{bulk} = 0.1 m/s, ΔT_w = 5.6 ^oC, ΔT_{sub} = 0.5 ^oC and x_{cav} = 1 mm.

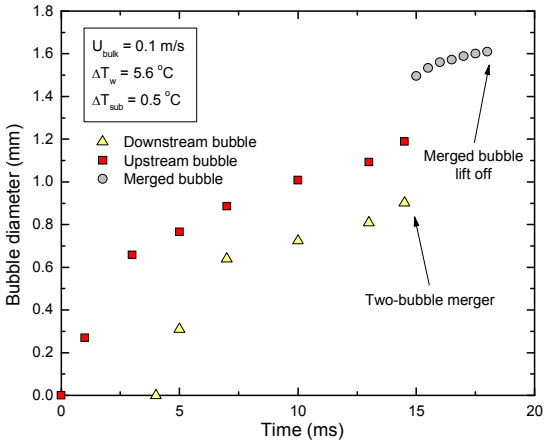

(a)

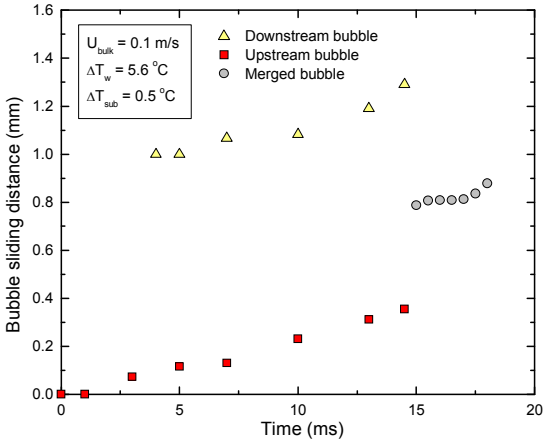

(b)

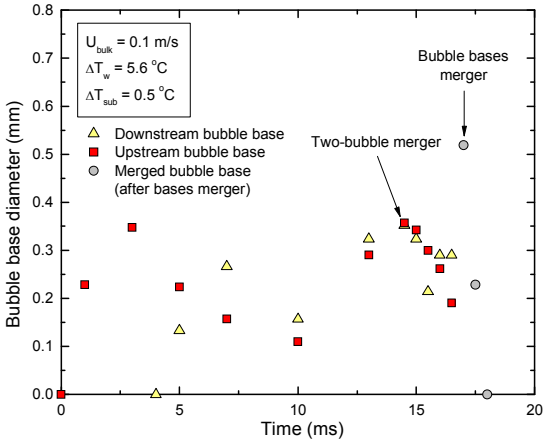

(c)

Figure 4.4 (a) Growth rate, (b) sliding distance, and (c) base diameter, for horizontal silicon surface, U_{bulk} = 0.1 m/s, ΔT_w = 5.6 °C, ΔT_{sub} = 0.5 °C and x_{cav} = 1 mm.

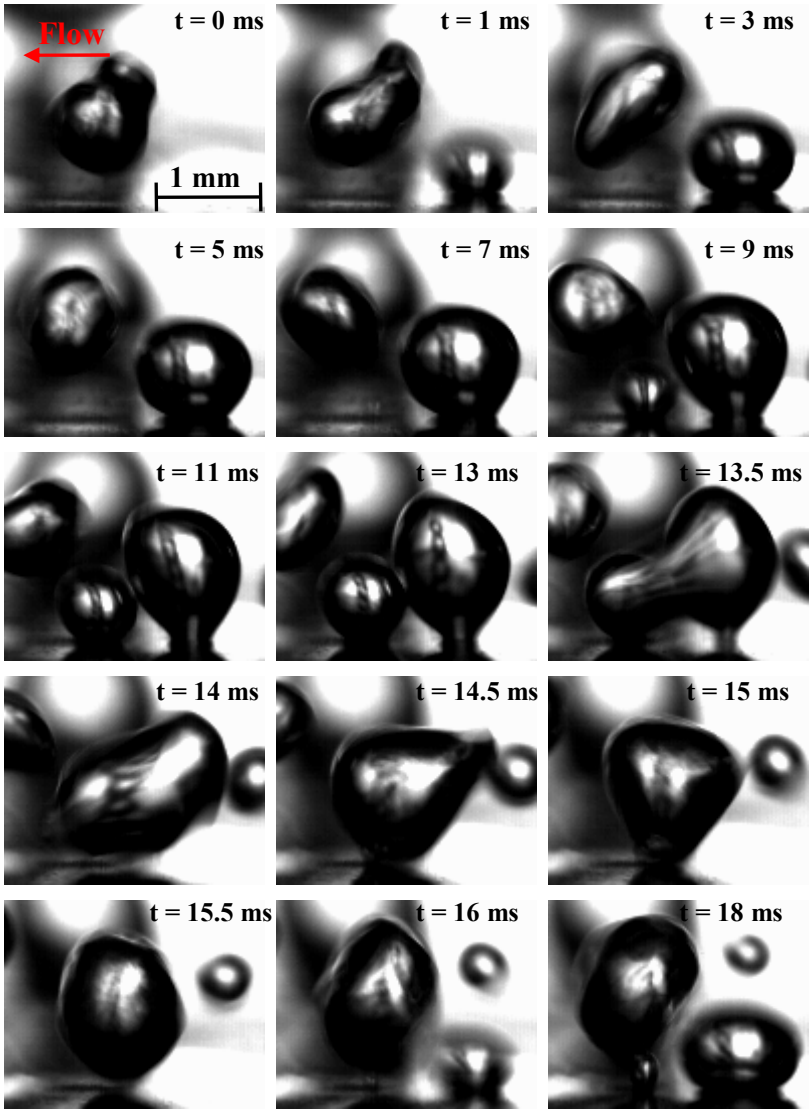

Figure 4.5 Two-bubble merger growth cycle, for horizontal silicon surface, U_{bulk} = 0.135 m/s, ΔT_w = 5.3 ^oC, ΔT_{sub} = 0.7 ^oC and x_{cav} = 1 mm.

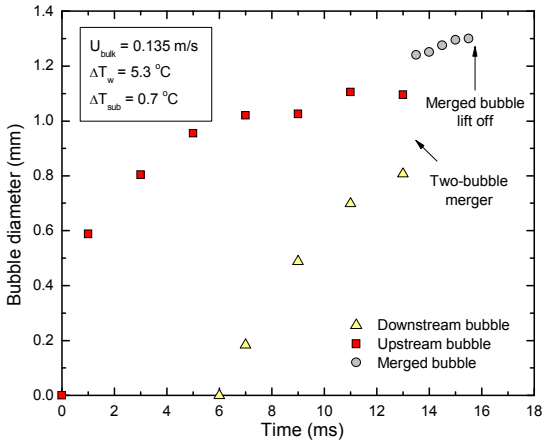

(a)

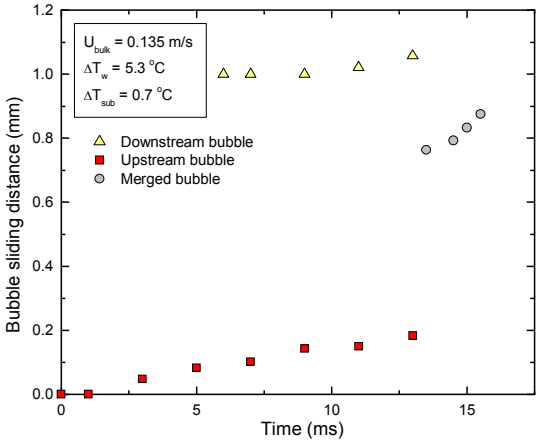

(b)

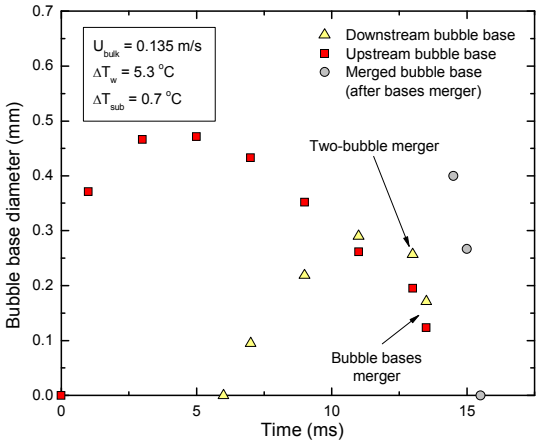

(c)

Figure 4.6 (a) Growth rate, (b) sliding distance, and (c) base diameter, for horizontal silicon surface, U_{bulk} = 0.135 m/s, ΔT_w = 5.3 °C, ΔT_{sub} = 0.7 °C and x_{cav} = 1 mm.

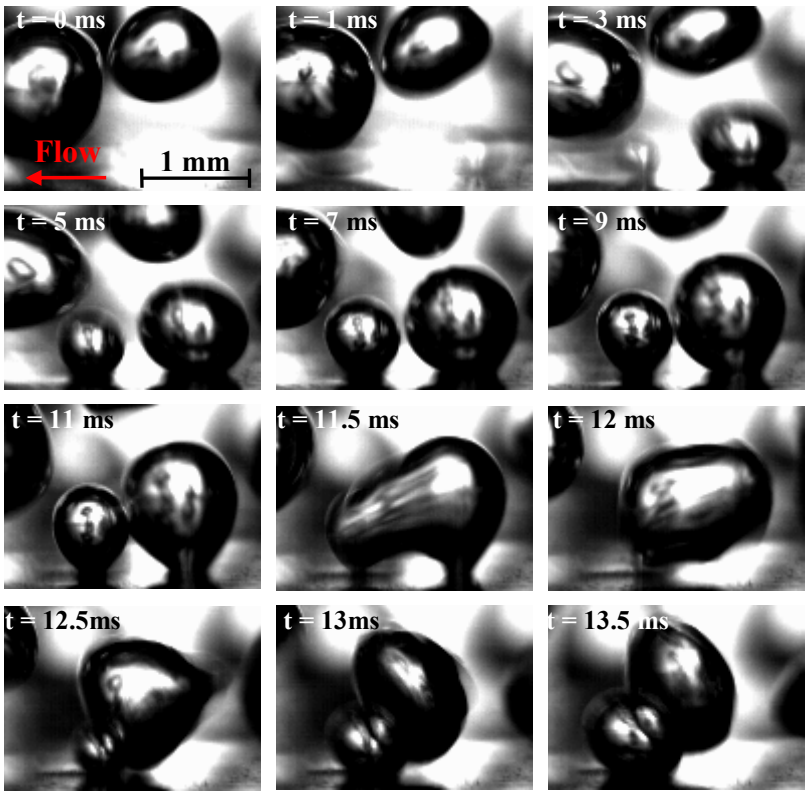

Figure 4.7 Two-bubble merger growth cycle, for horizontal silicon surface, U_{bulk} = 0.25 m/s, ΔT_w = 5.7 ^oC, ΔT_{sub} = 0.4 ^oC and x_{cav} = 1 mm.

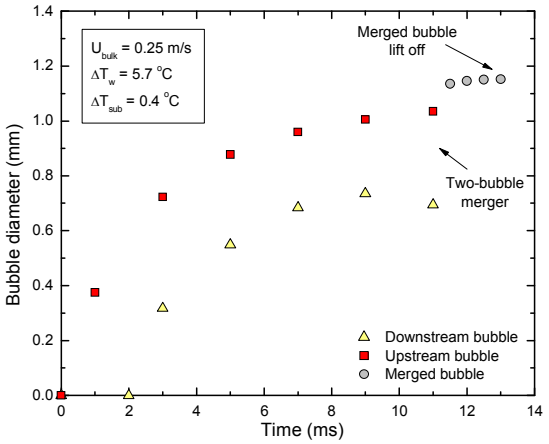

(a)

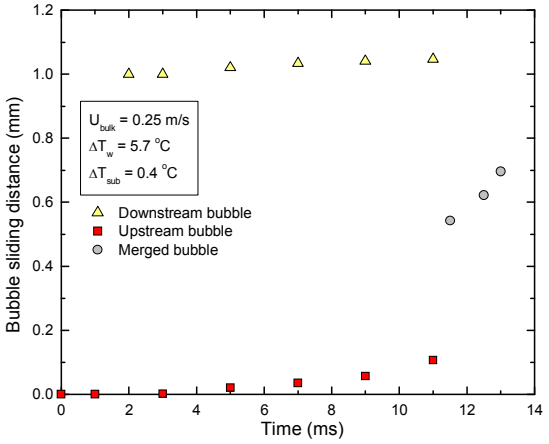

(b)

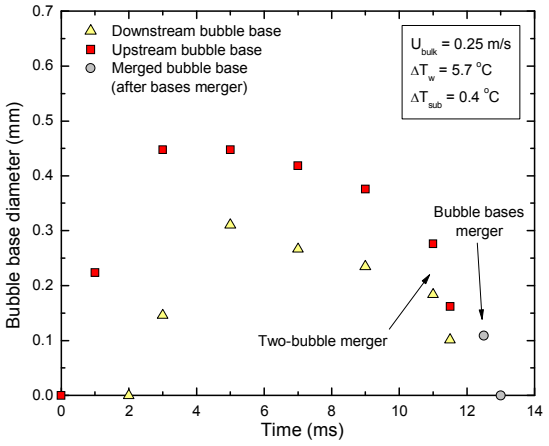

(c)

Figure 4.8 (a) Growth rate, (b) sliding distance, and (c) base diameter, for horizontal silicon surface, U_{bulk} = 0.25 m/s, ΔT_w = 5.7 °C, ΔT_{sub} = 0.4 °C and x_{cav} = 1 mm.

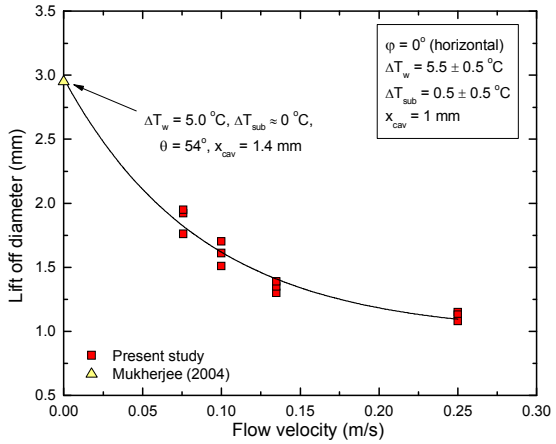

(a)

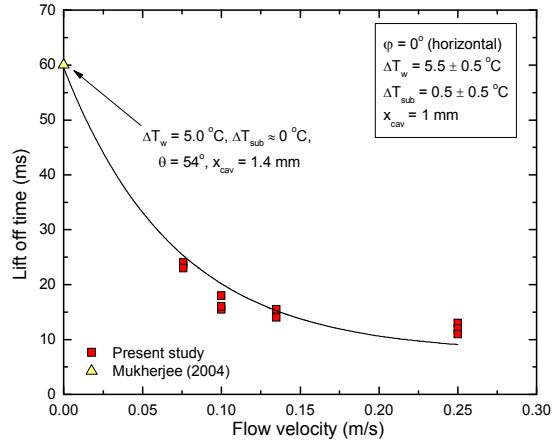

(b)

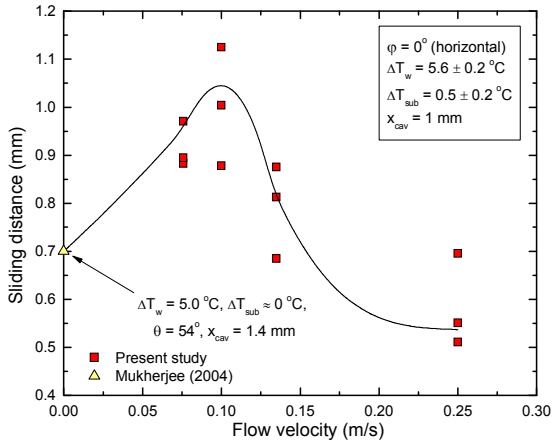

(c)

Figure 4.9 Effect of liquid bulk velocity on (a) lift off diameter, (b) lift off times, and (c) sliding distance – Horizontal silicon surface.

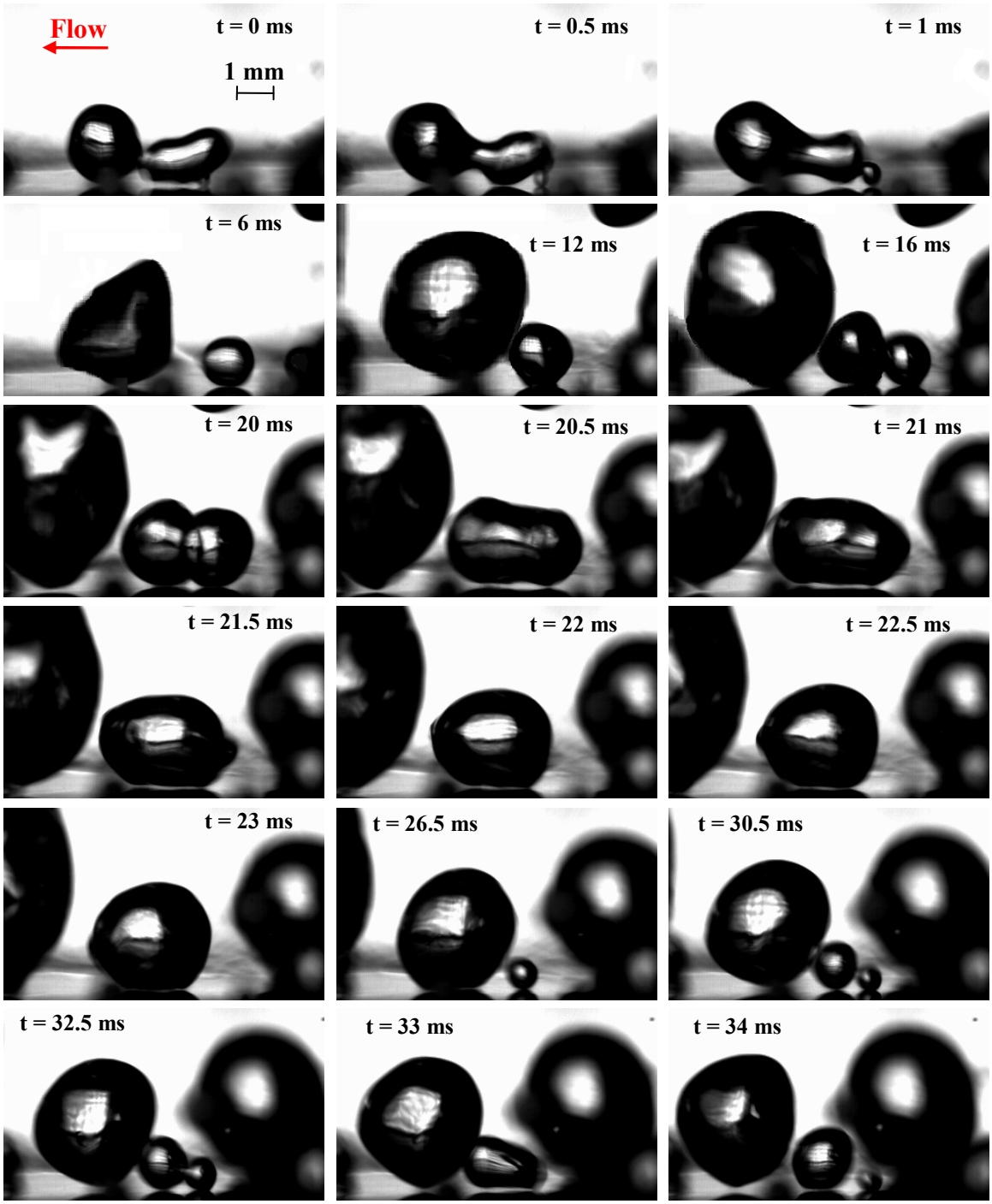

Figure 4.10 Two-bubble merger growth cycle, for vertical silicon surface, U_{bulk} = 0.076 m/s, ΔT_w = 5.9 ^oC, ΔT_{sub} = 0.4 ^oC and x_{cav} = 1.2 mm.

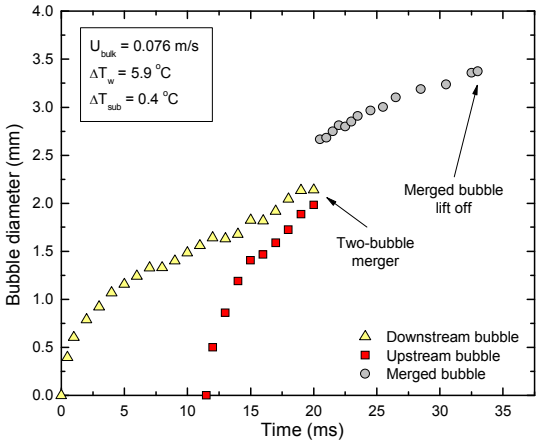

(a)

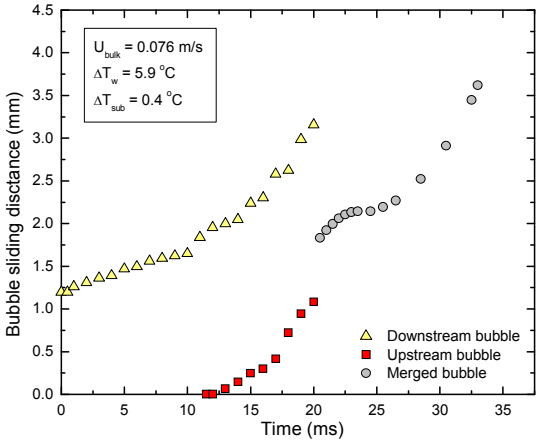

(b)

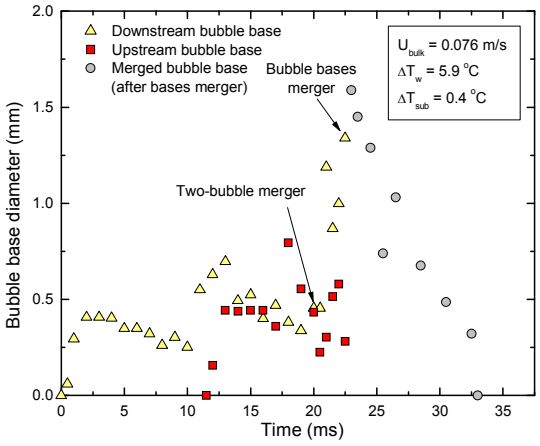

(c)

Figure 4.11 (a) Growth rate, (b) sliding distance, and (c) base diameter, for vertical silicon surface, U_{bulk} = 0.076 m/s, ΔT_w = 5.9 °C, ΔT_{sub} = 0.4 °C and x_{cav} = 1.2 mm.

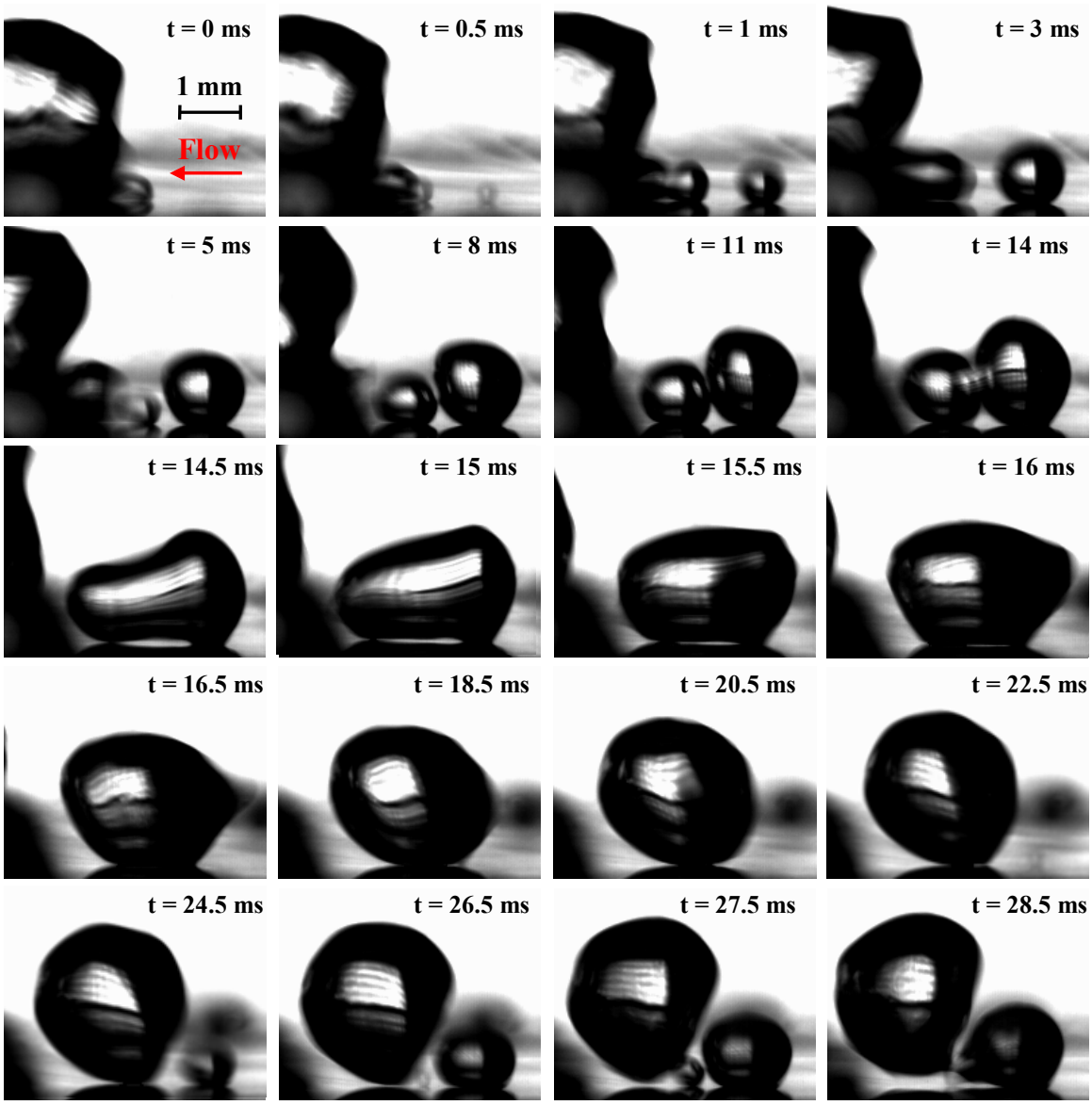

Figure 4.12 Two-bubble merger growth cycle, for vertical silicon surface, U_{bulk} = 0.1 m/s, ΔT_w = 5.8 ^oC, ΔT_{sub} = 0.6 ^oC and x_{cav} = 1.2 mm.

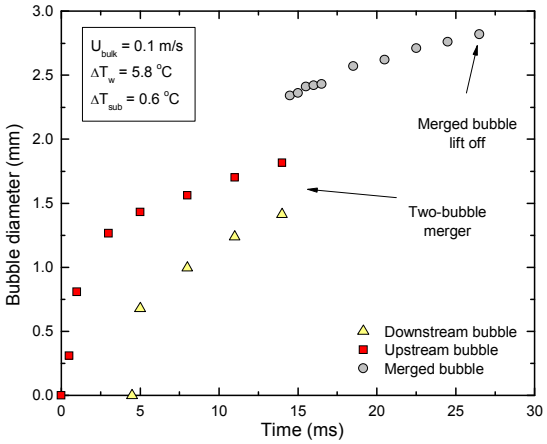

(a)

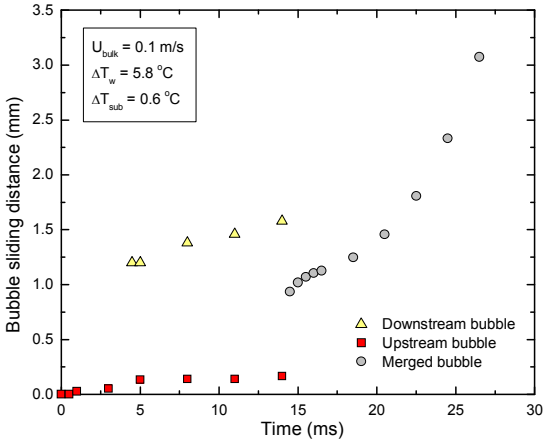

(b)

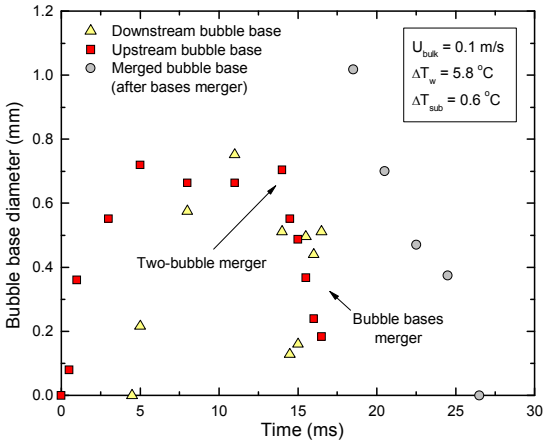

(c)

Figure 4.13 (a) Growth rate, (b) sliding distance, and (c) base diameter, for vertical silicon surface, U_{bulk} = 0.1 m/s, ΔT_w = 5.8 °C, ΔT_{sub} = 0.6 °C and x_{cav} = 1.2 mm.

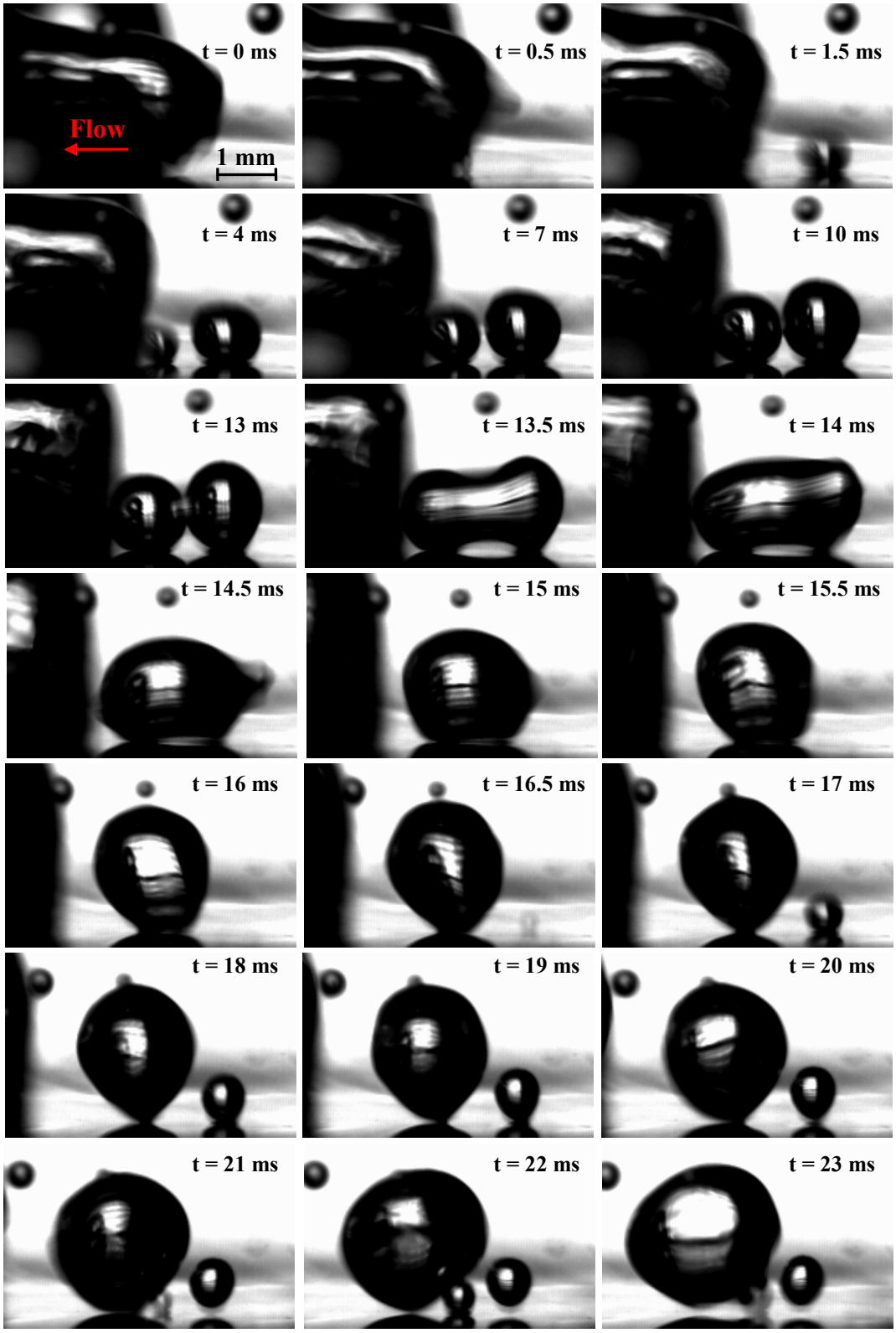

Figure 4.14 Two-bubble merger growth cycle, for vertical silicon surface, U_{bulk} = 0.135 m/s, ΔT_w = 5.9 ^oC, ΔT_{sub} = 0.5 ^oC and x_{cav} = 1.2 mm.

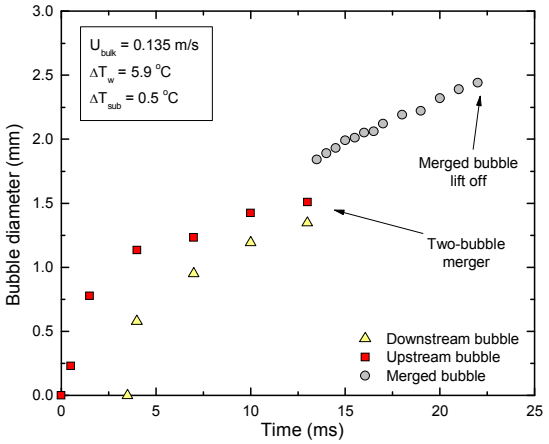

(a)

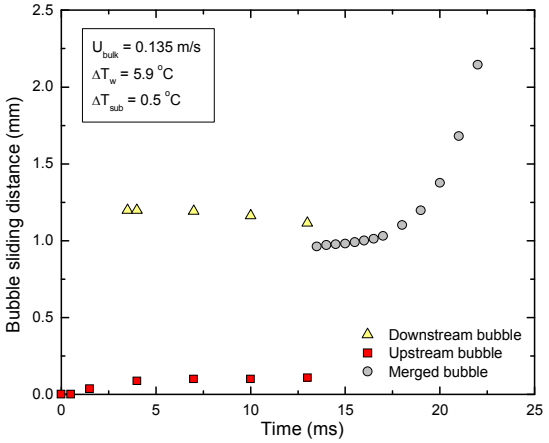

(b)

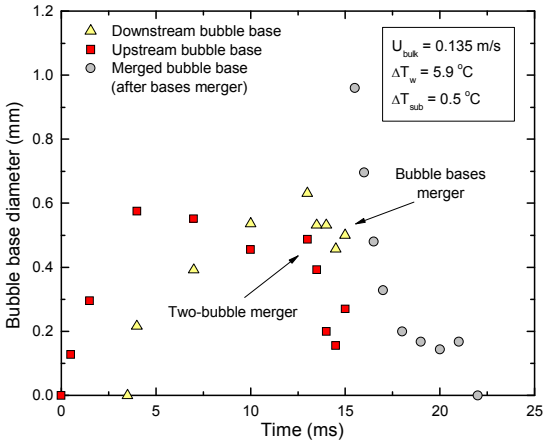

(c)

Figure 4.15 (a) Growth rate, (b) sliding distance, and (c) base diameter, for vertical silicon surface, U_{bulk} = 0.135 m/s, ΔT_w = 5.9 °C, ΔT_{sub} = 0.5 °C and x_{cav} = 1.2 mm.

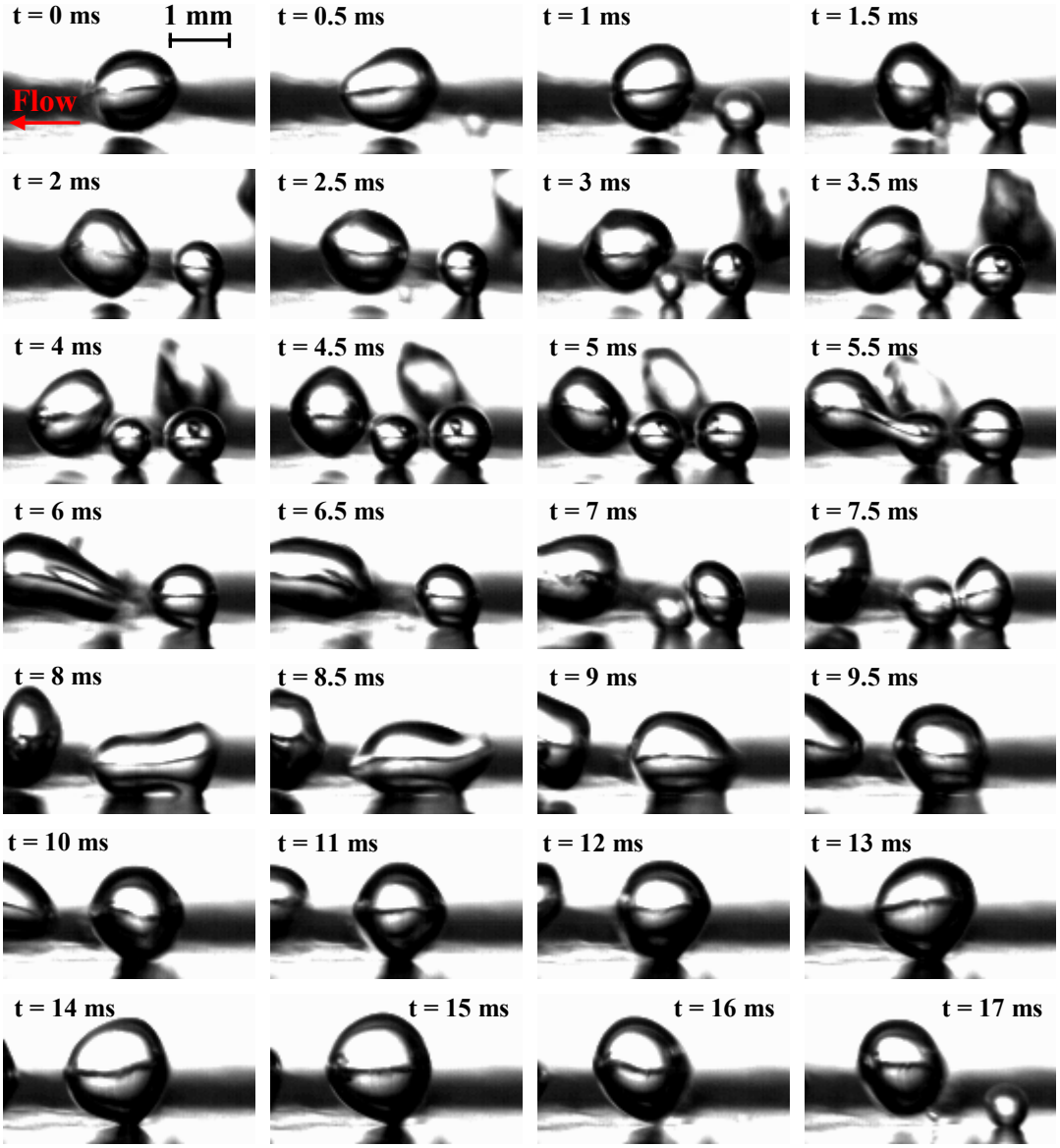

Figure 4.16 Two-bubble merger growth cycle, for vertical silicon surface, U_{bulk} = 0.25 m/s, ΔT_w = 5.7 ^oC, ΔT_{sub} = 0.7 ^oC and x_{cav} = 1.2 mm.

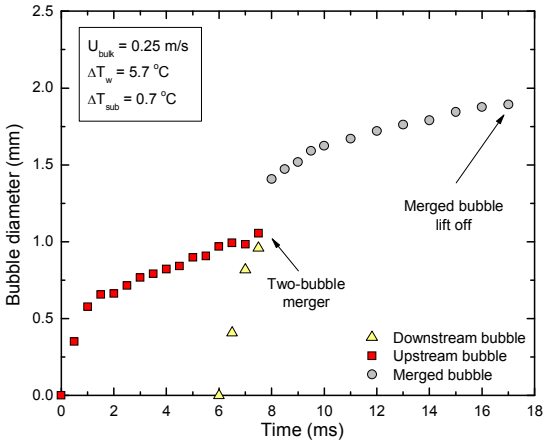

(a)

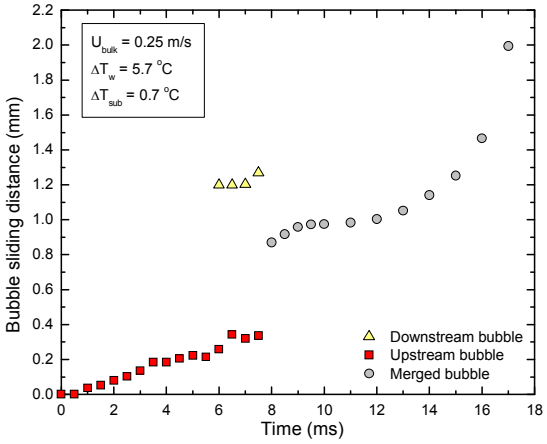

(b)

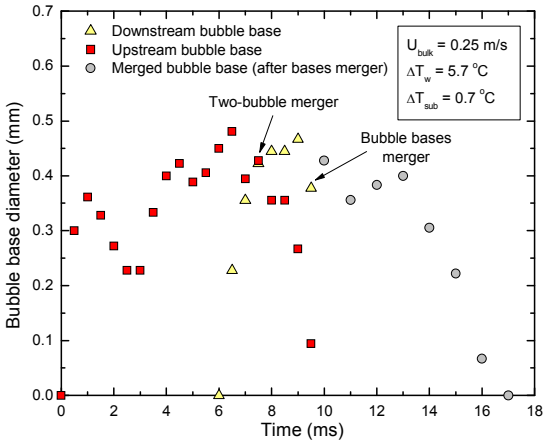

(c)

Figure 4.17 (a) Growth rate, (b) sliding distance, and (c) base diameter, for vertical silicon surface, U_{bulk} = 0.25 m/s, ΔT_w = 5.7 °C, ΔT_{sub} = 0.7 °C and x_{cav} = 1.2 mm.

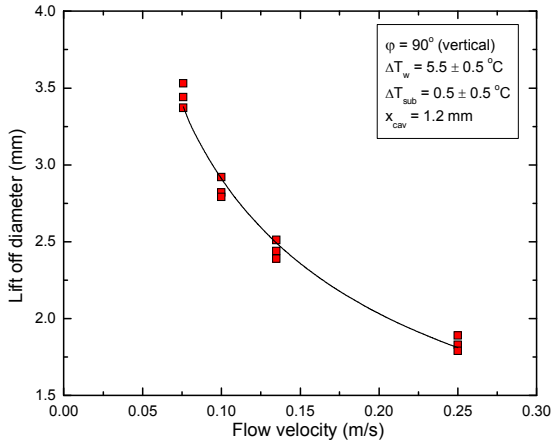

(a)

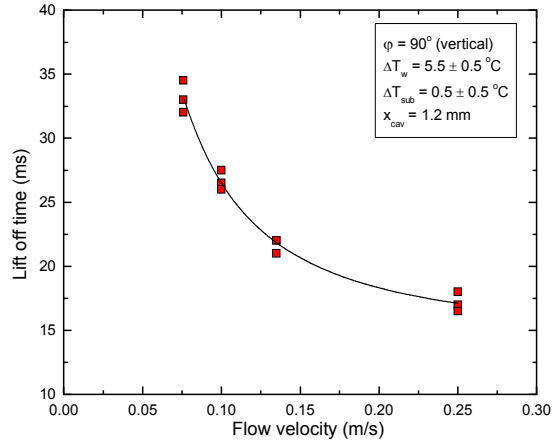

(b)

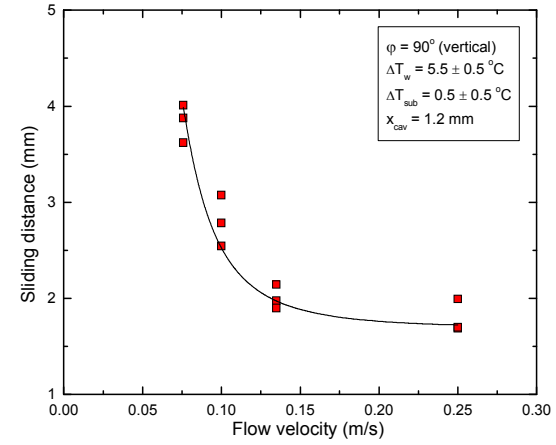

(c)

Figure 4.18 Effect of liquid bulk velocity on (a) lift off diameter, (b) lift off times, and (c) sliding distance – Vertical silicon surface.

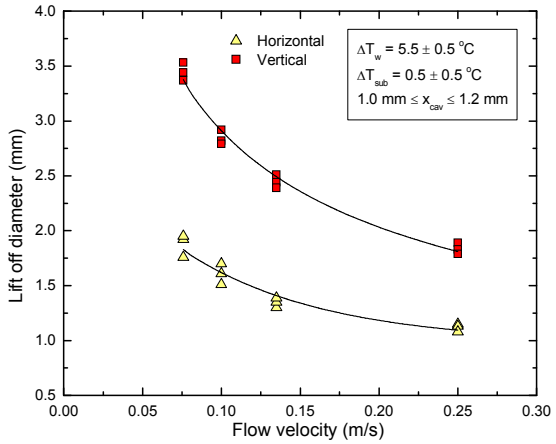

(a)

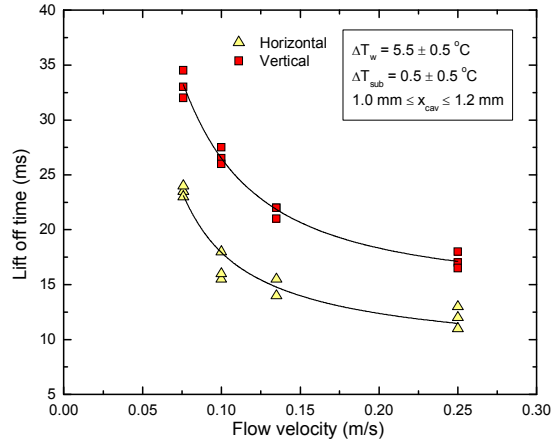

(b)

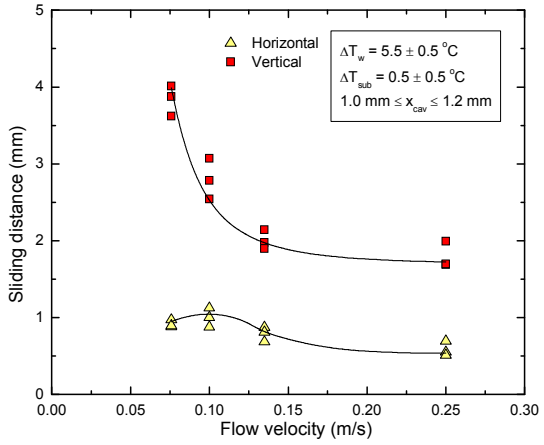

(c)

Figure 4.19 Effect of liquid bulk velocity and heater orientation on (a) lift off diameter, (b) lift off times, and (c) sliding distance – Silicon surface.

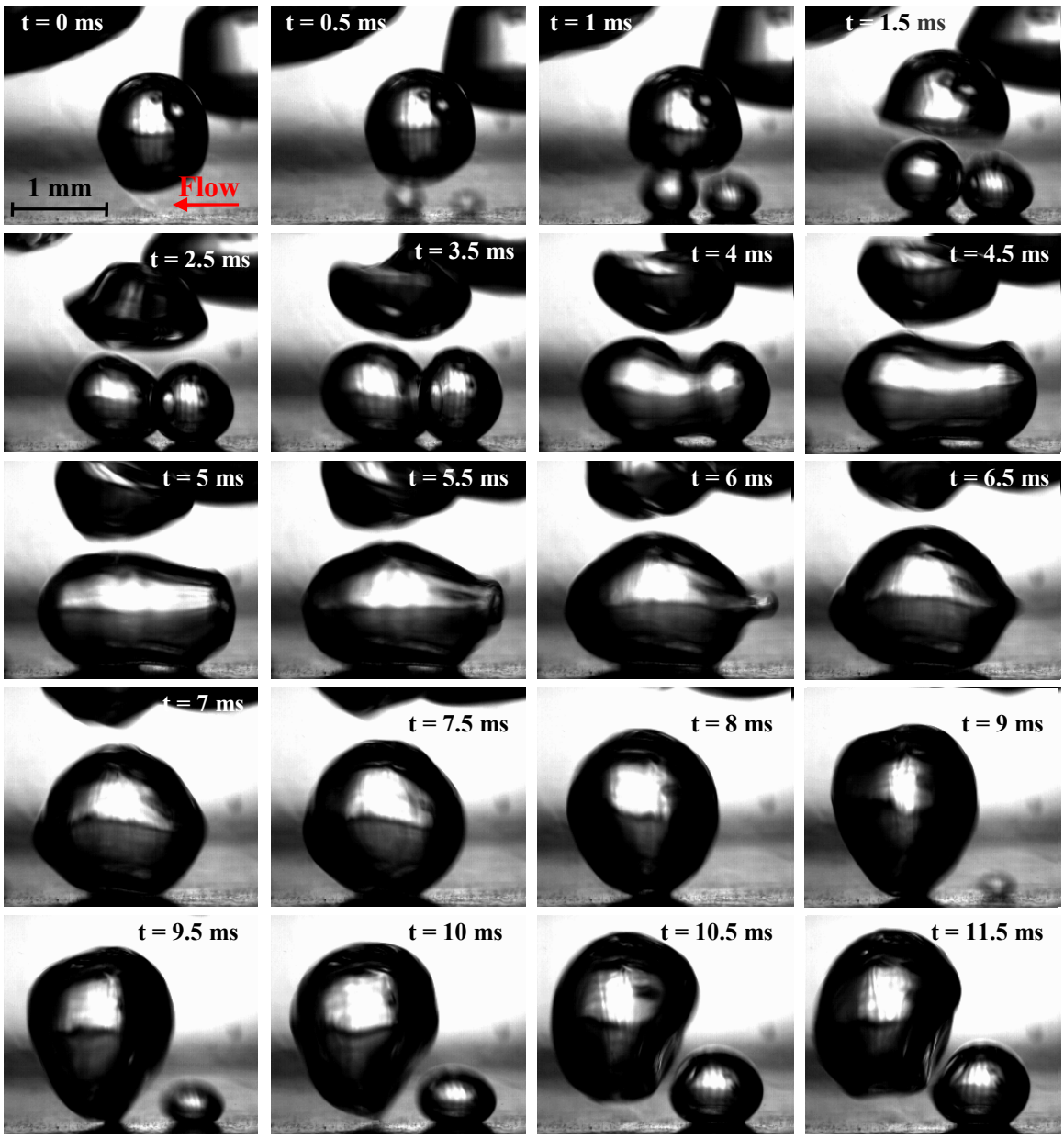

Figure 4.20 Two-bubble merger growth cycle, for horizontal aluminum surface, U_{bulk} = 0.076 m/s, ΔT_w = 5.8 ^oC, ΔT_{sub} = 0.5 ^oC and x_{cav} = 0.6 mm.

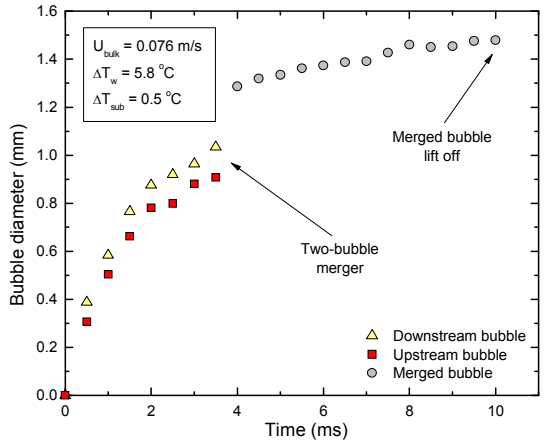

(a)

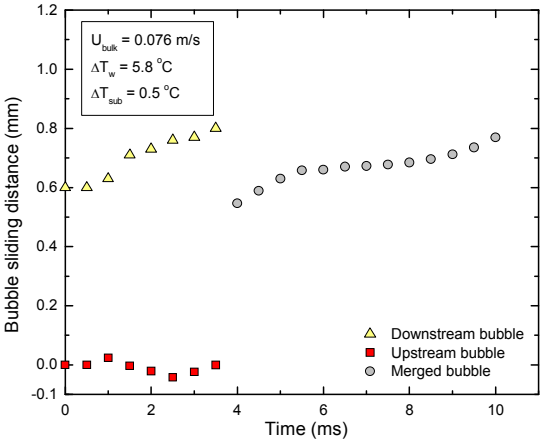

(b)

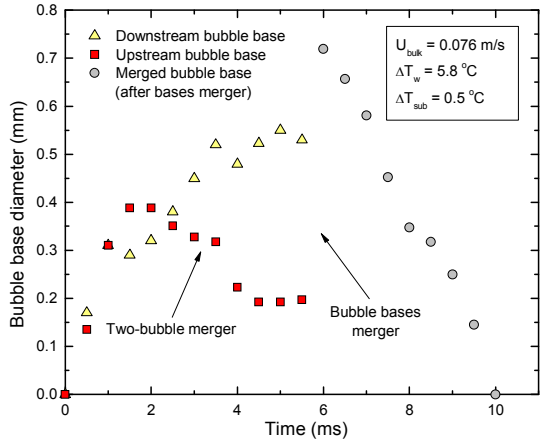

(c)

Figure 4.21 (a) Growth rate, (b) sliding distance, and (c) base diameter, for horizontal aluminum surface, U_{bulk} = 0.076 m/s, ΔT_w = 5.8 °C, ΔT_{sub} = 0.5 °C and x_{cav} = 0.6 mm.

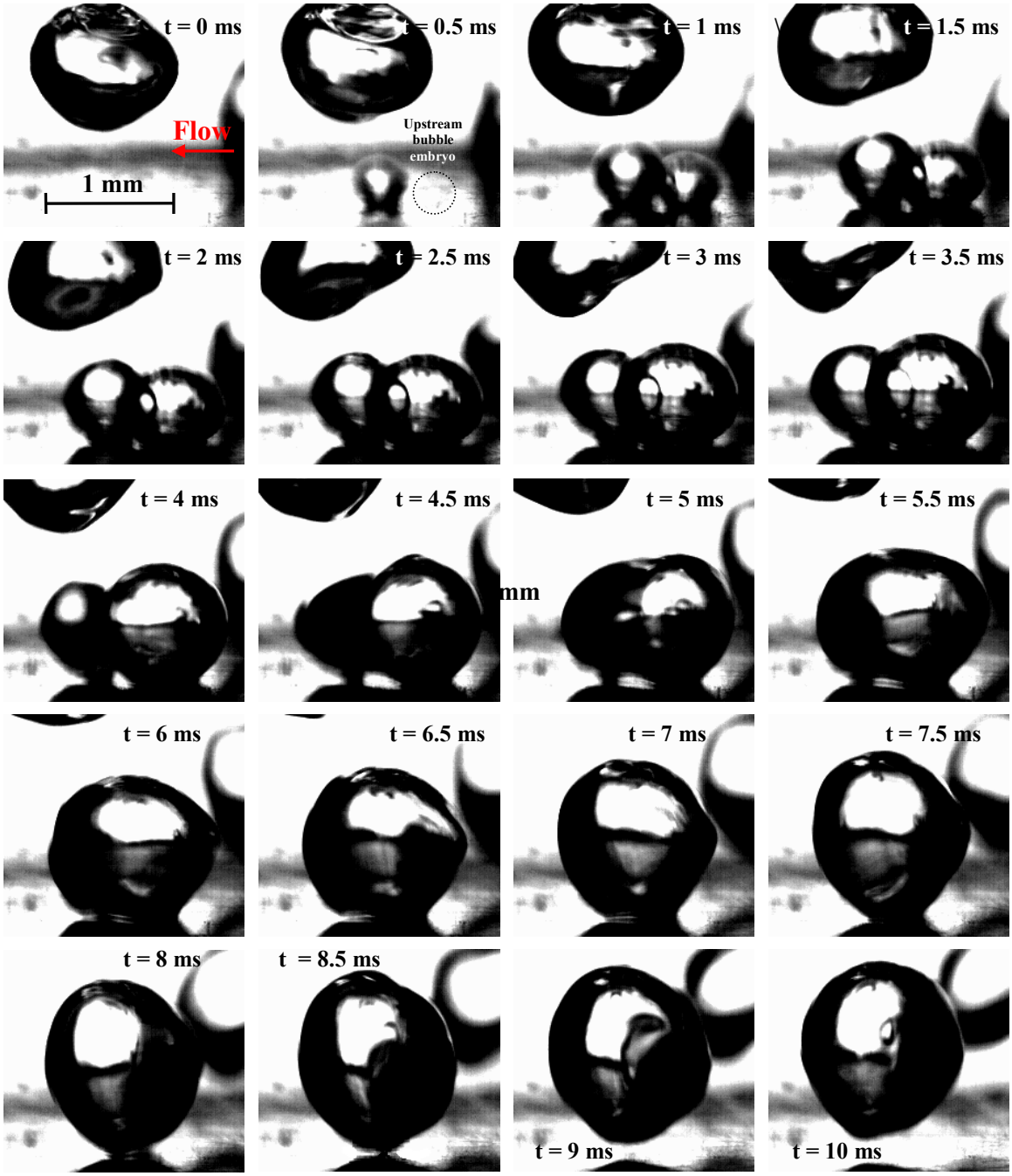

Figure 4.22 Two-bubble merger growth cycle, for horizontal aluminum surface, U_{bulk} = 0.1 m/s, ΔT_w = 5.6 °C, ΔT_{sub} = 0.6 °C and x_{cav} = 0.6 mm.

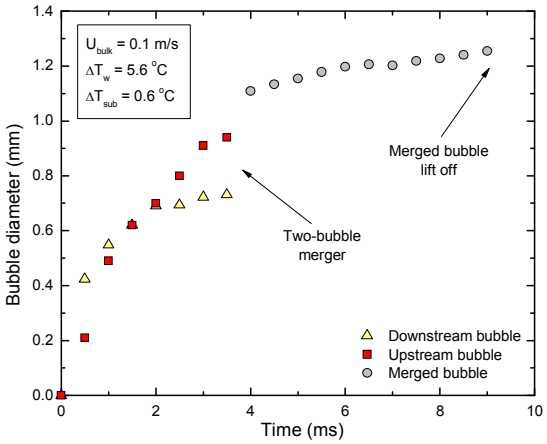

(a)

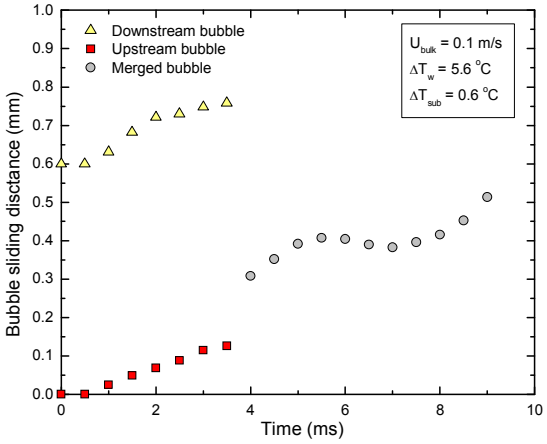

(b)

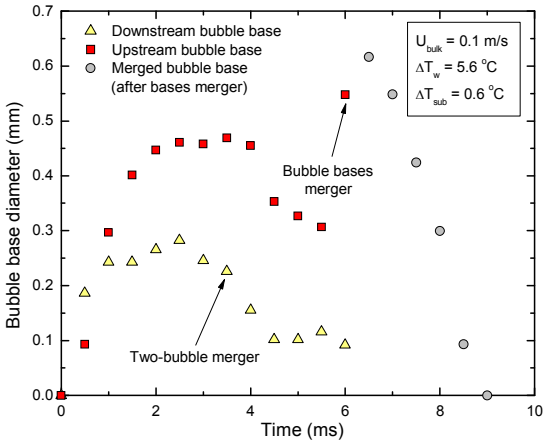

(c)

Figure 4.23 (a) Growth rate, (b) sliding distance, and (c) base diameter, for horizontal aluminum surface, U_{bulk} = 0.1 m/s, ΔT_w = 5.6 °C, ΔT_{sub} = 0.6 °C and x_{cav} = 0.6 mm.

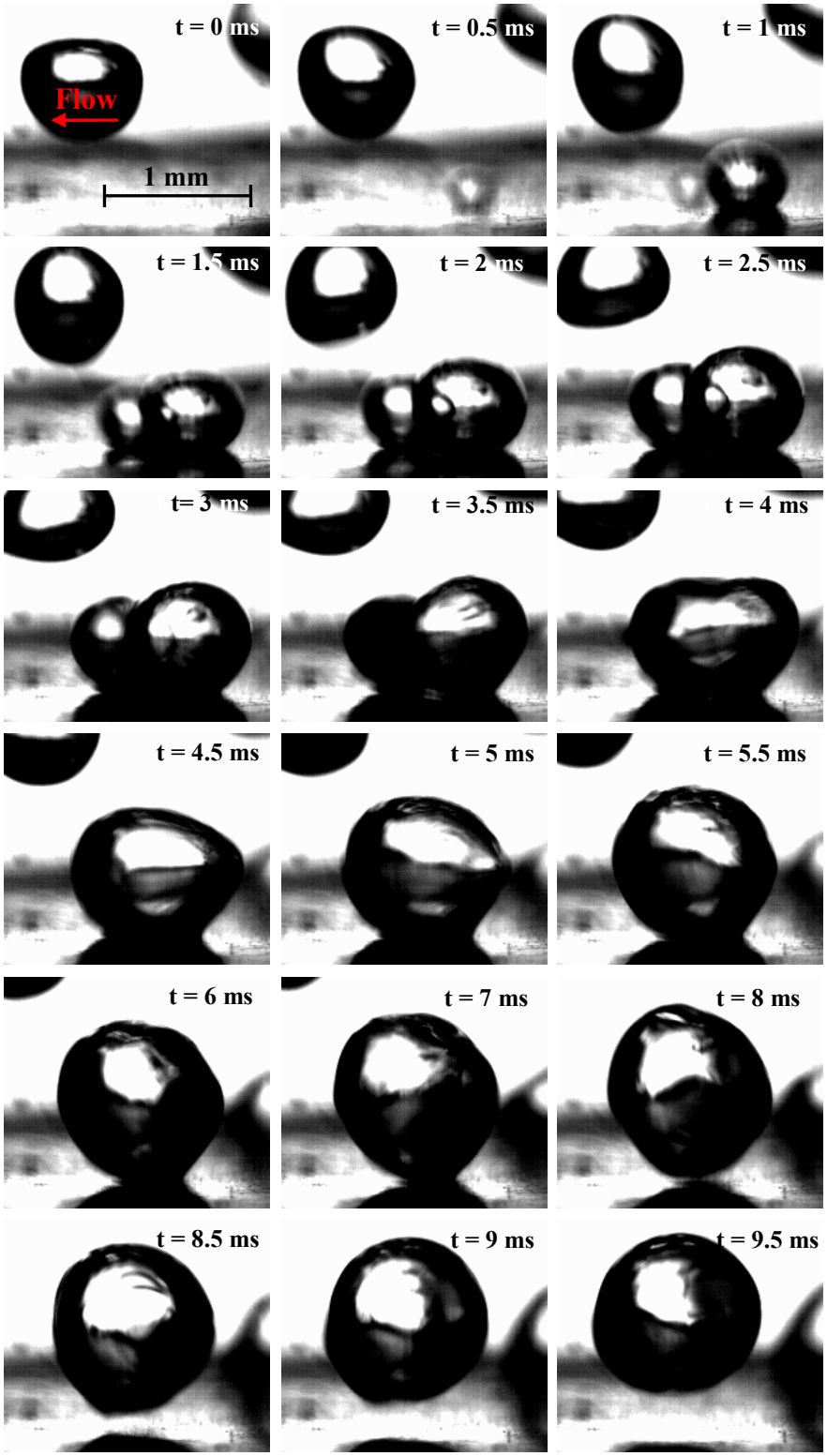

Figure 4.24 Two-bubble merger growth cycle, for horizontal aluminum surface, U_{bulk} = 0.135 m/s, ΔT_w = 5.5 ^oC, ΔT_{sub} = 0.4 ^oC and x_{cav} = 0.4 mm.

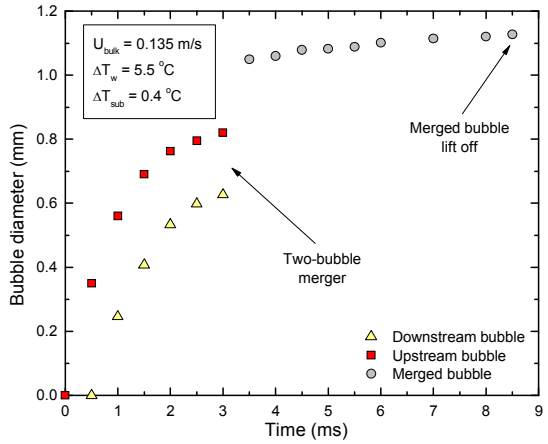

(a)

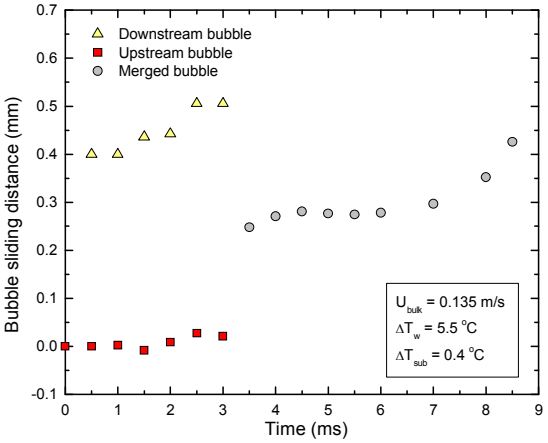

(b)

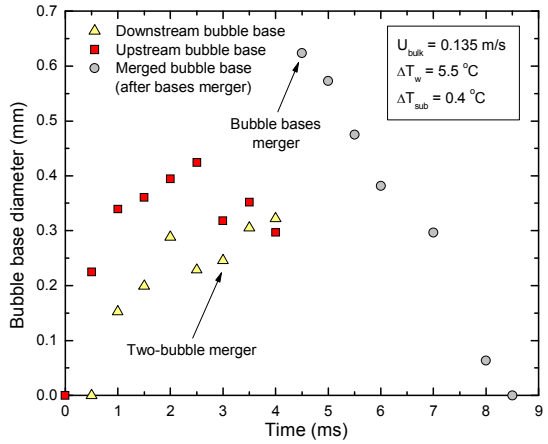

(c)

Figure 4.25 (a) Growth rate, (b) sliding distance, and (c) base diameter, for horizontal aluminum surface, U_{bulk} = 0.135 m/s, ΔT_w = 5.5 °C, ΔT_{sub} = 0.4 °C and x_{cav} = 0.4 mm.

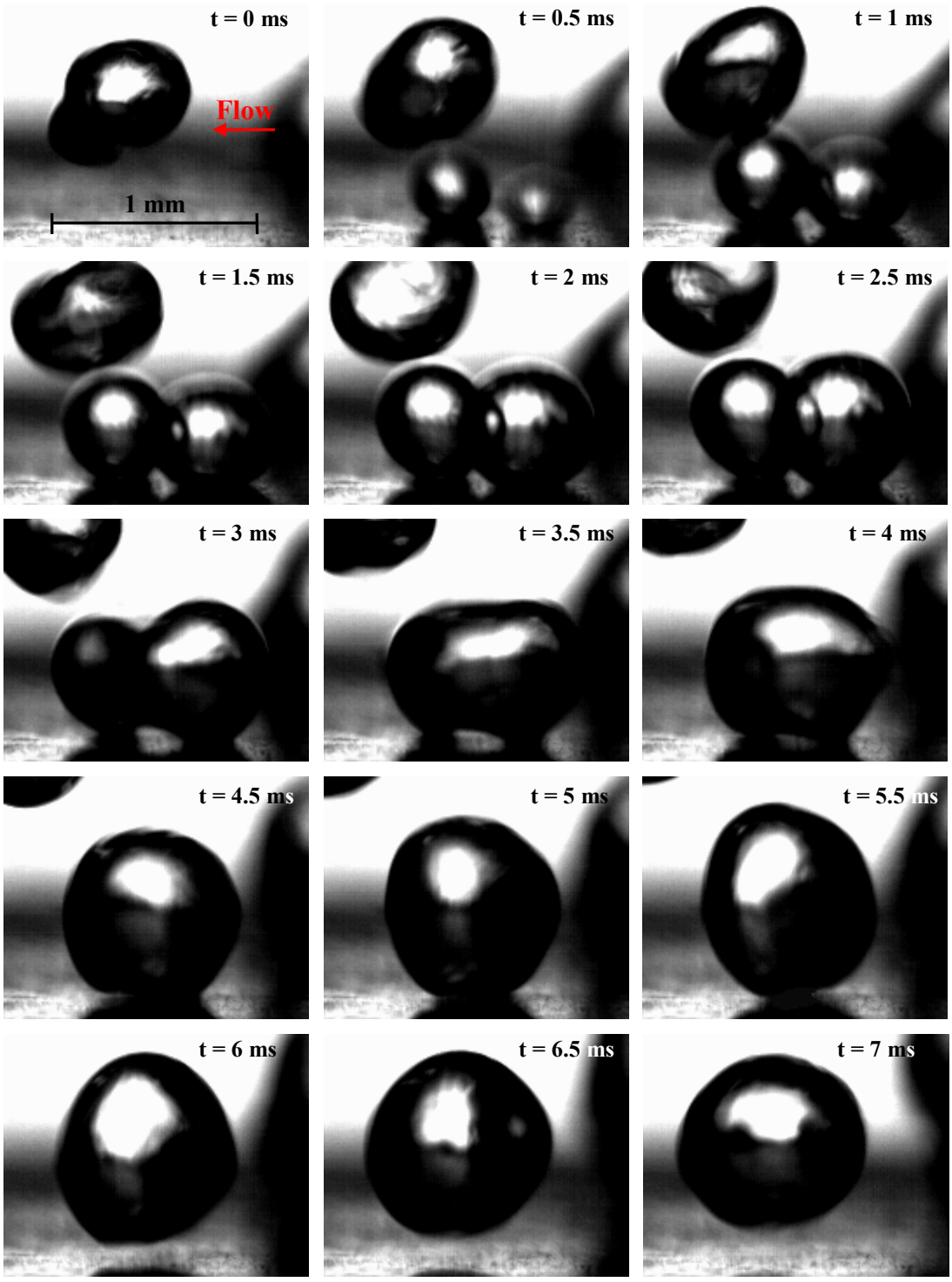

Figure 4.26 Two-bubble merger growth cycle, for horizontal aluminum surface, U_{bulk} = 0.25 m/s, ΔT_w = 5.8 ^oC, ΔT_{sub} = 0.6 ^oC and x_{cav} = 0.4 mm.

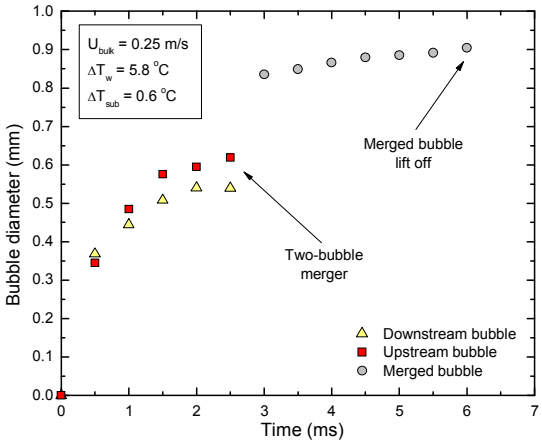

(a)

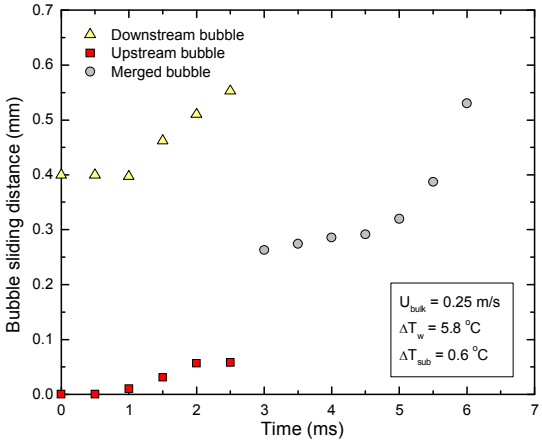

(b)

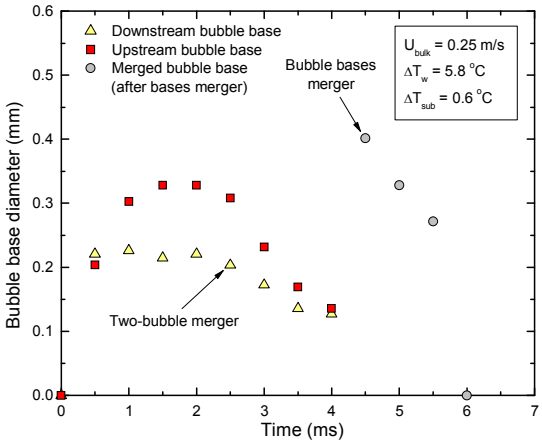

(c)

Figure 4.27 (a) Growth rate, (b) sliding distance, and (c) base diameter, for horizontal aluminum surface, U_{bulk} = 0.25 m/s, ΔT_w = 5.8 °C, ΔT_{sub} = 0.6 °C and x_{cav} = 0.4 mm.

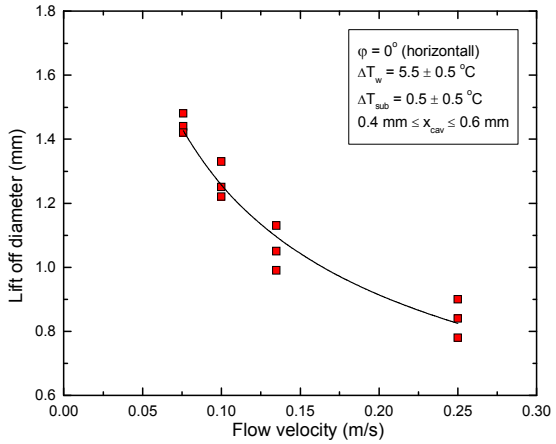

(a)

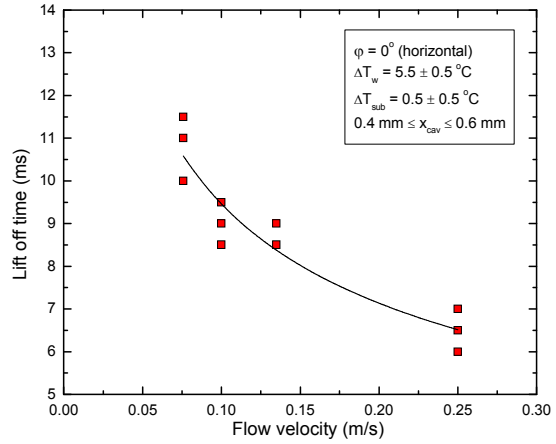

(b)

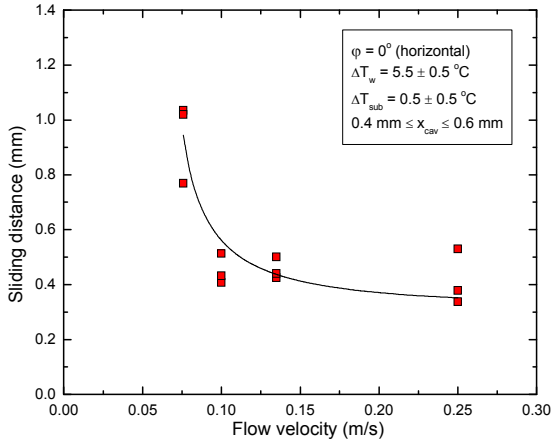

(c)

Figure 4.28 Effect of liquid bulk velocity on (a) lift off diameter, (b) lift off times, and (c) sliding distance – Horizontal aluminum surface.

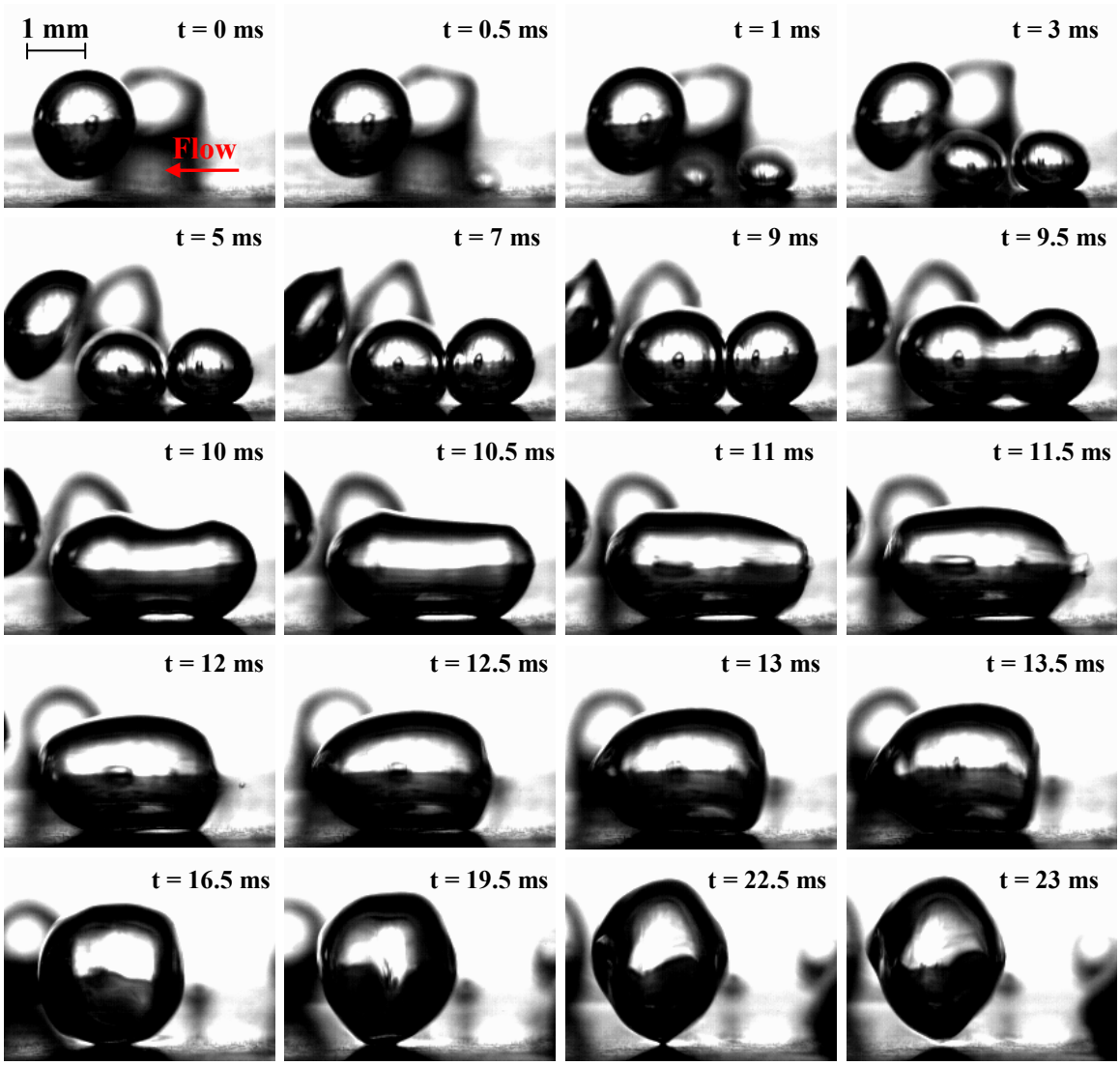

Figure 4.29 Two-bubble merger growth cycle, for vertical aluminum surface, U_{bulk} = 0.076 m/s, ΔT_w = 5.7 ^oC, ΔT_{sub} = 0.5 ^oC and x_{cav} = 1.2 mm.

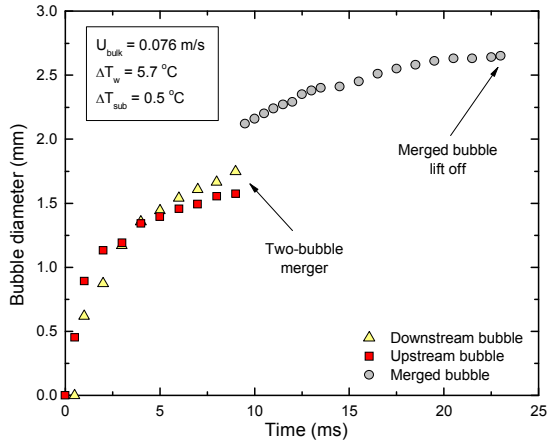

(a)

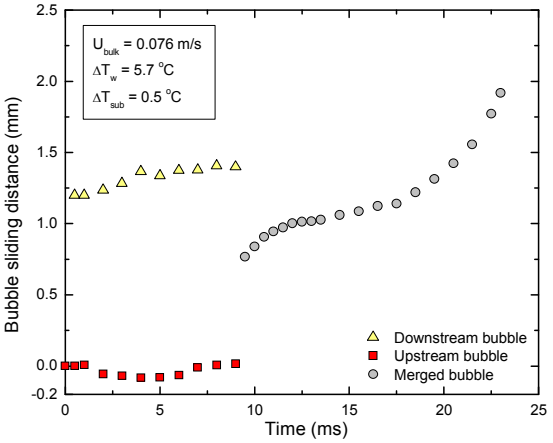

(b)

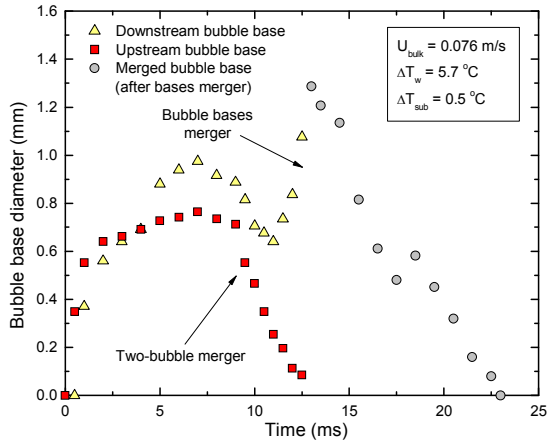

(c)

Figure 4.30 (a) Growth rate, (b) sliding distance, and (c) base diameter, for vertical aluminum surface, U_{bulk} = 0.076 m/s, ΔT_w = 5.7 °C, ΔT_{sub} = 0.5 °C and x_{cav} = 1.2 mm.

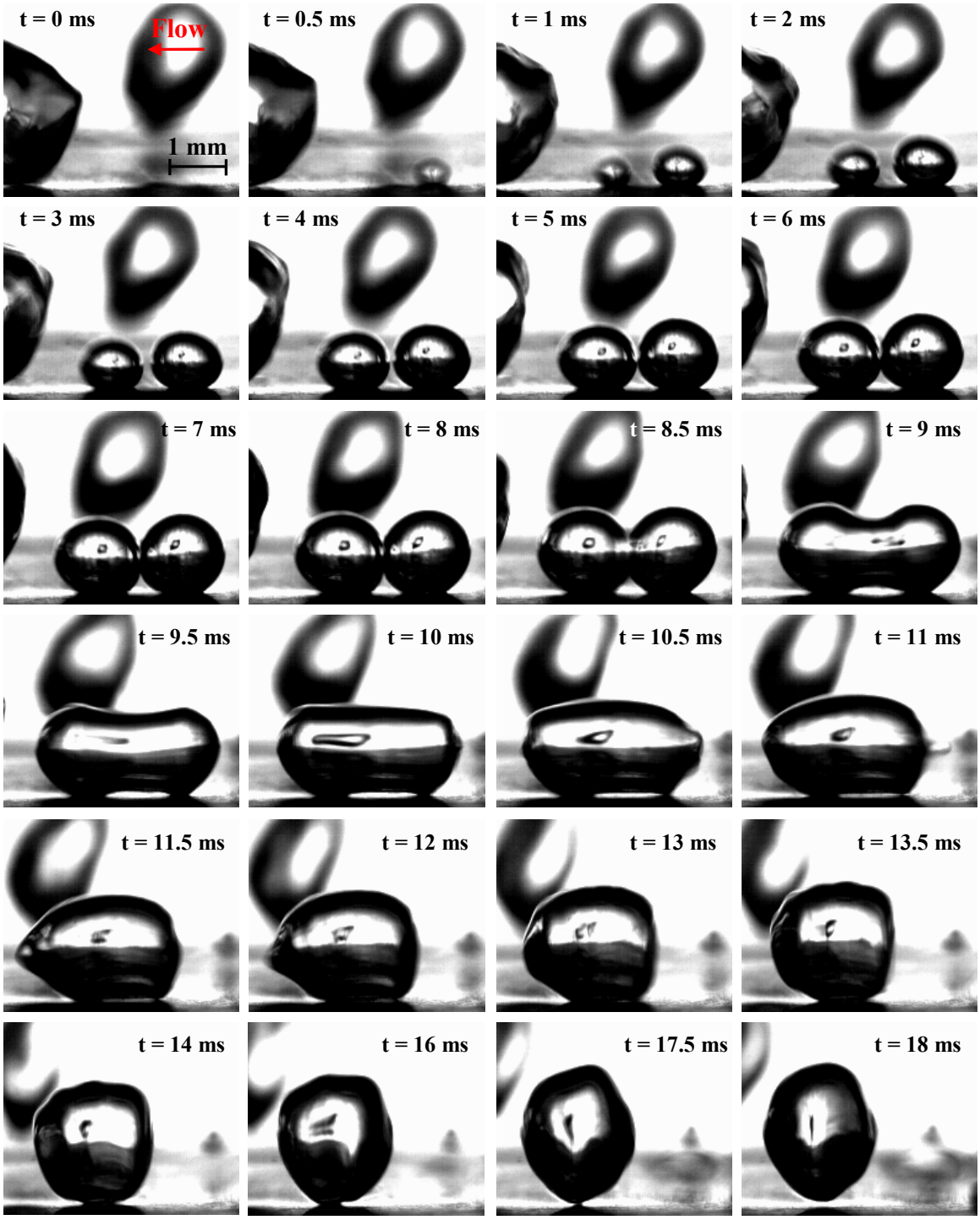

Figure 4.31 Two-bubble merger growth cycle, for vertical aluminum surface, U_{bulk} = 0.1 m/s, ΔT_w = 5.5 ^oC, ΔT_{sub} = 0.4 ^oC and x_{cav} = 1.2 mm.

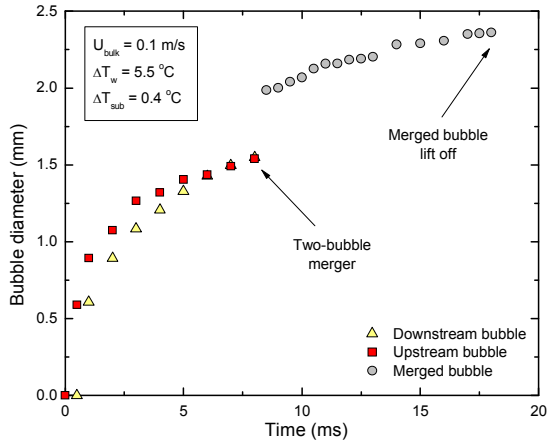

(a)

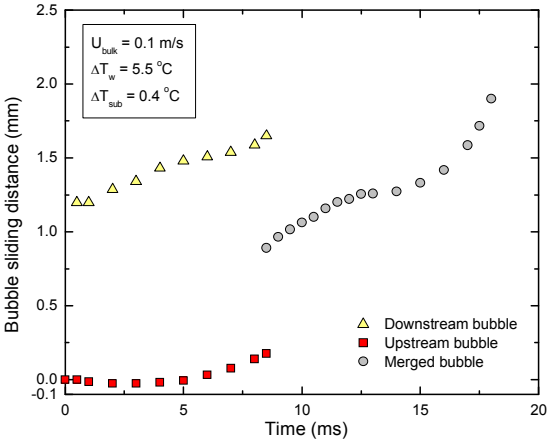

(b)

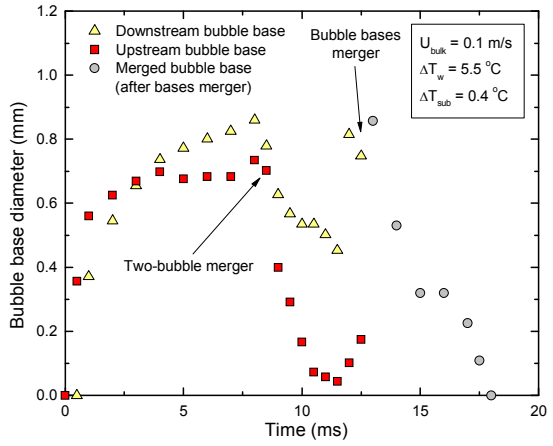

(c)

Figure 4.32 (a) Growth rate, (b) sliding distance, and (c) base diameter, for vertical aluminum surface, U_{bulk} = 0.1 m/s, ΔT_w = 5.5 °C, ΔT_{sub} = 0.4 °C and x_{cav} = 1.2 mm.

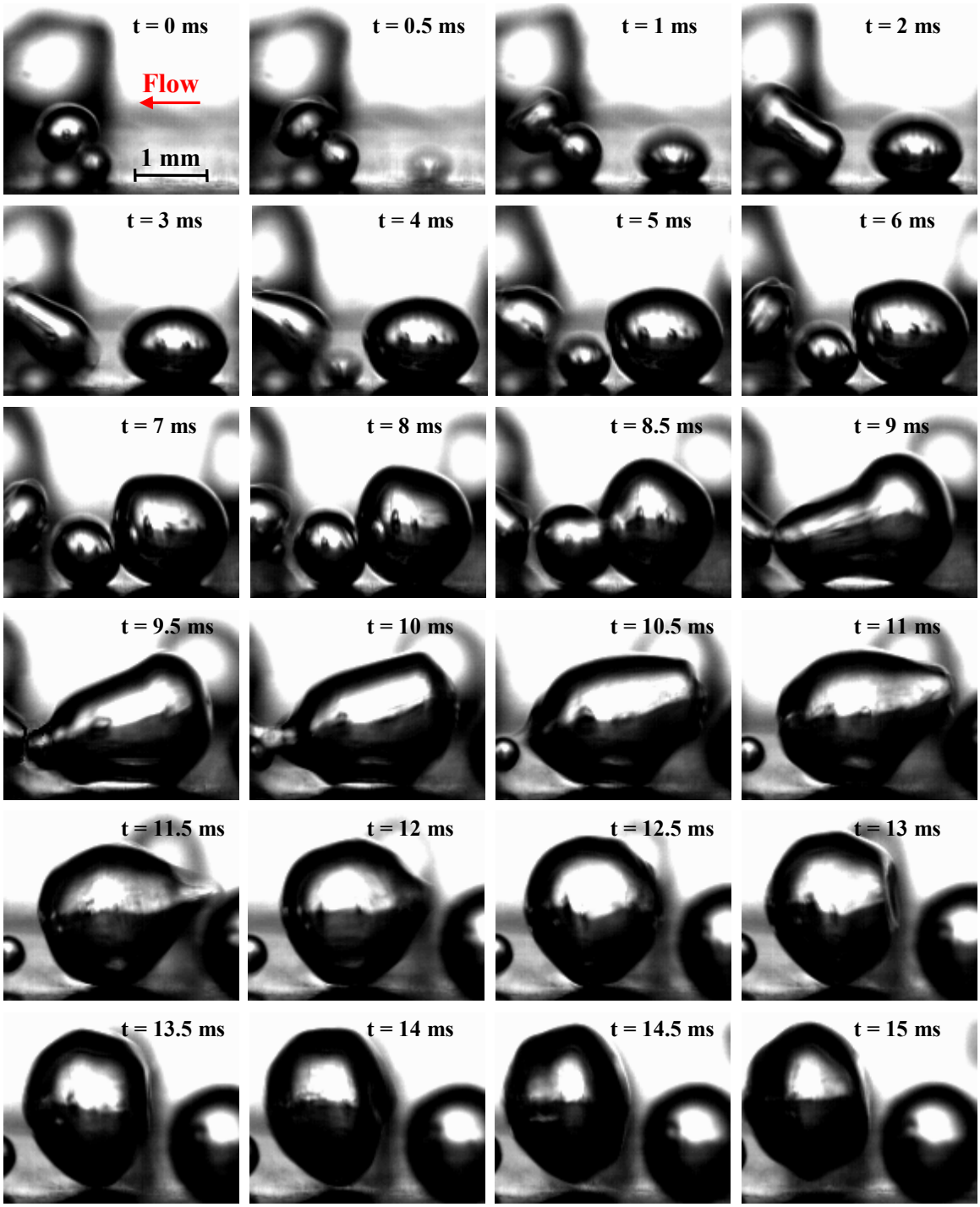

Figure 4.33 Two-bubble merger growth cycle, for vertical aluminum surface, U_{bulk} = 0.135 m/s, ΔT_w = 5.7 °C, ΔT_{sub} = 0.6 °C and x_{cav} = 1.2 mm.

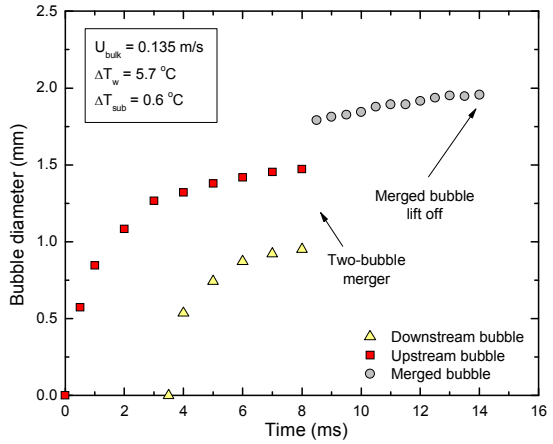

(a)

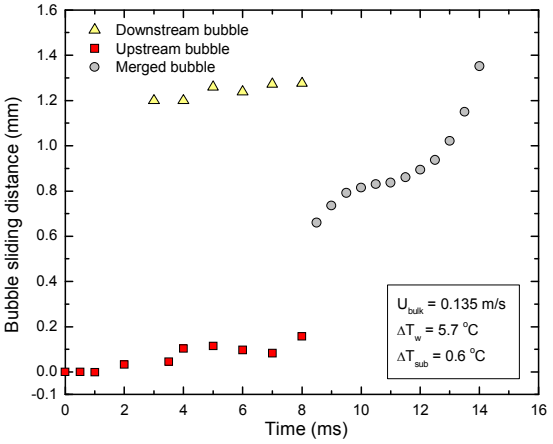

(b)

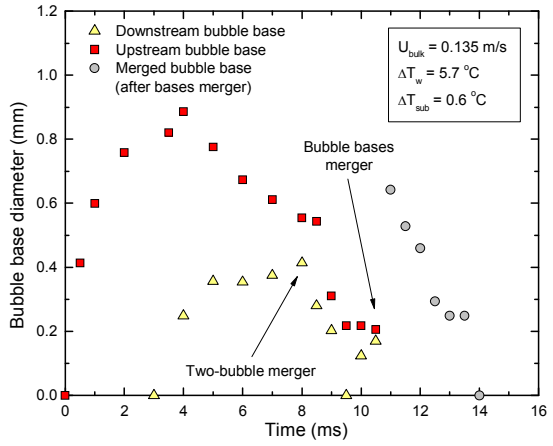

(c)

Figure 4.34 (a) Growth rate, (b) sliding distance, and (c) base diameter, for vertical aluminum surface, U_{bulk} = 0.135 m/s, ΔT_w = 5.7 °C, ΔT_{sub} = 0.6 °C and x_{cav} = 1.2 mm.

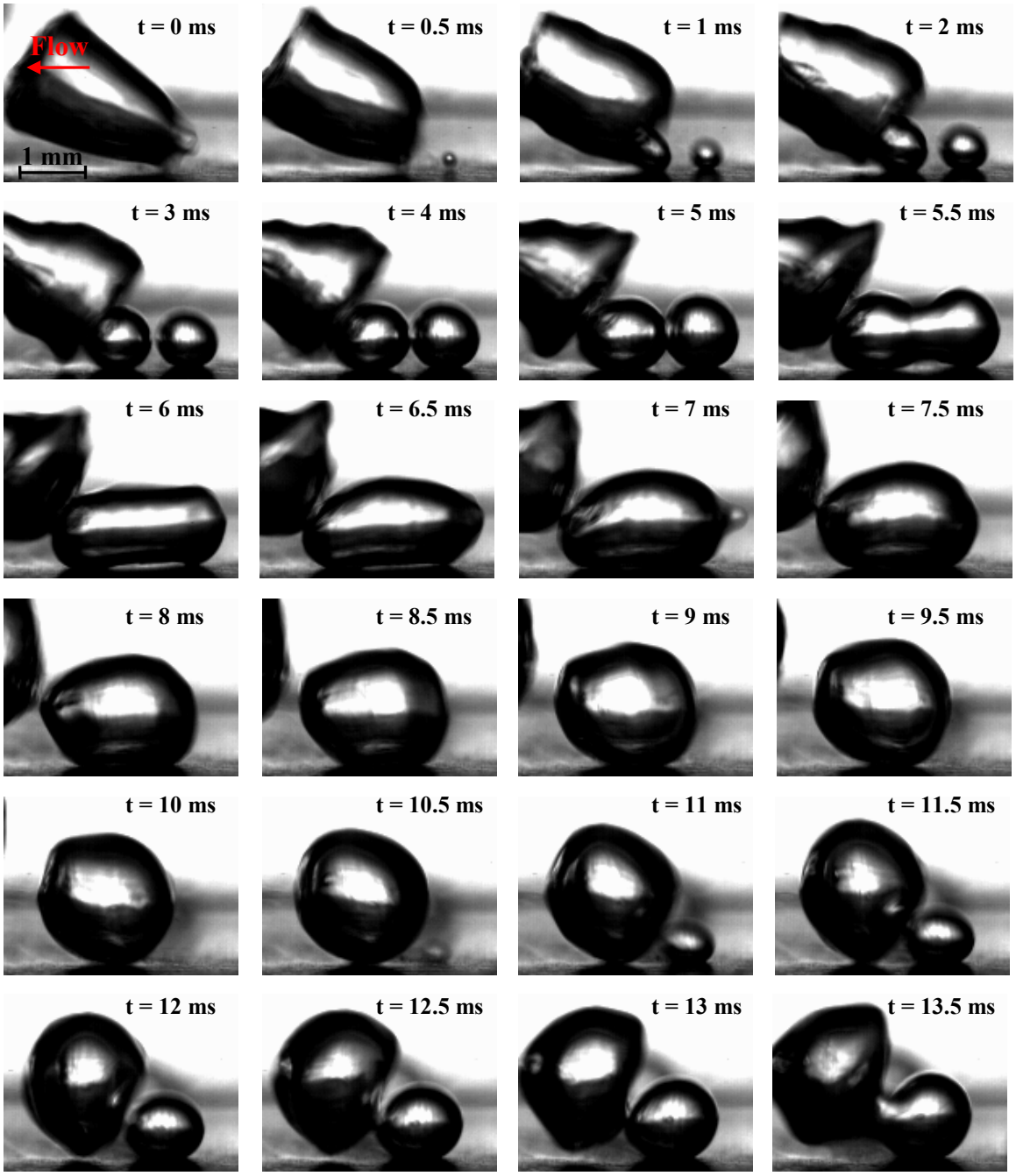

Figure 4.35 Two-bubble merger growth cycle, for vertical aluminum surface, U_{bulk} = 0.25 m/s, ΔT_w = 5.6 ^oC, ΔT_{sub} = 0.6 ^oC and x_{cav} = 1.2 mm.

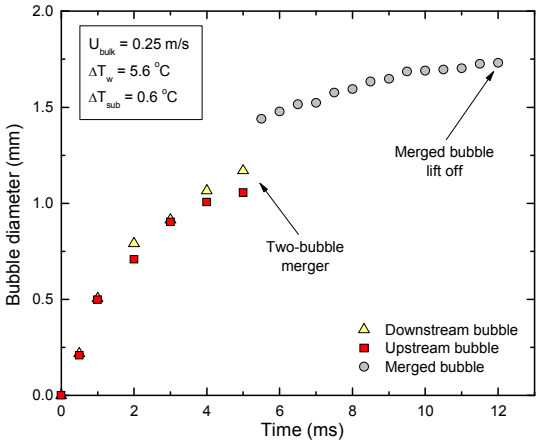

(a)

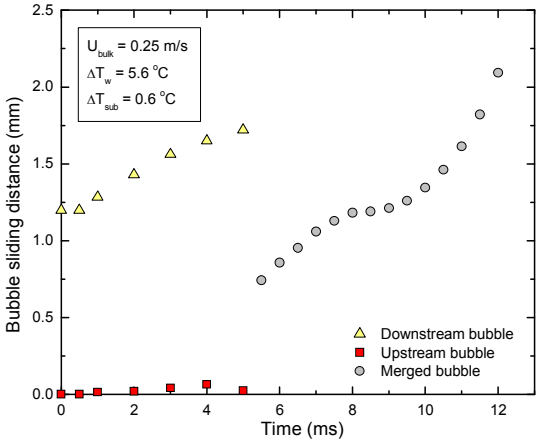

(b)

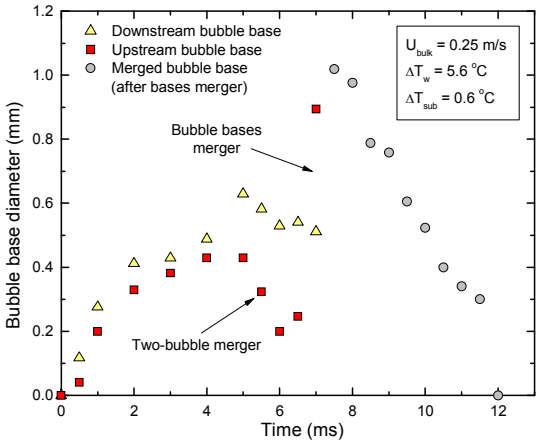

(c)

Figure 4.36 (a) Growth rate, (b) sliding distance, and (c) base diameter, for vertical aluminum surface, U_{bulk} = 0.25 m/s, ΔT_w = 5.6 °C, ΔT_{sub} = 0.6 °C and x_{cav} = 1.2 mm.

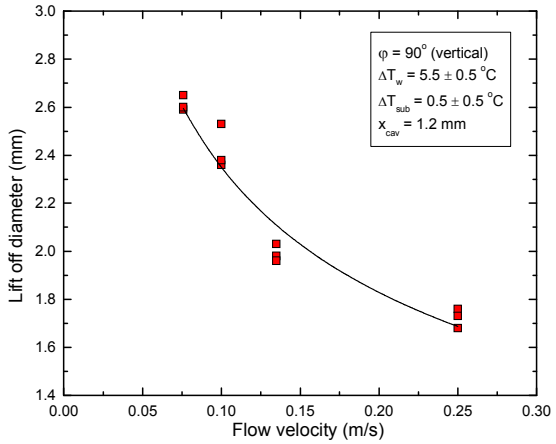

(a)

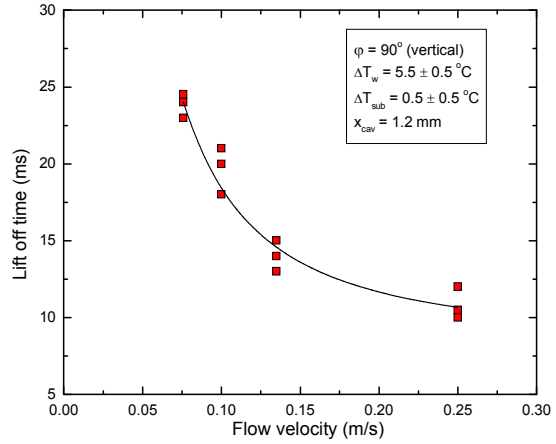

(b)

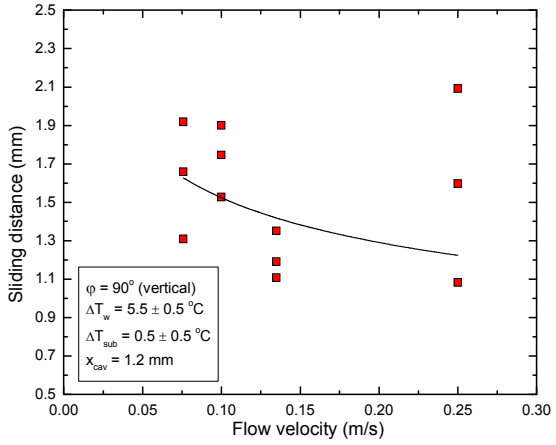

(c)

Figure 4.37 Effect of liquid bulk velocity on (a) lift off diameter, (b) lift off times, and (c) sliding distance – Vertical aluminum surface.

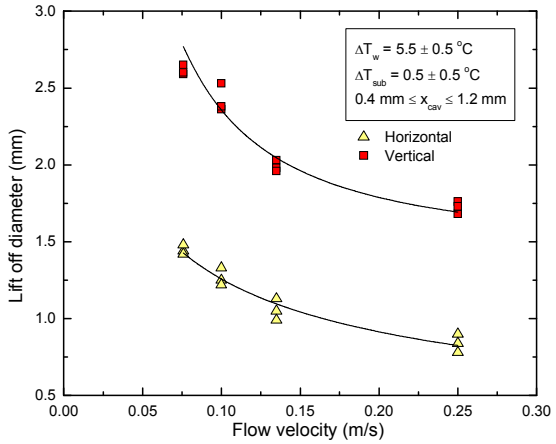

(a)

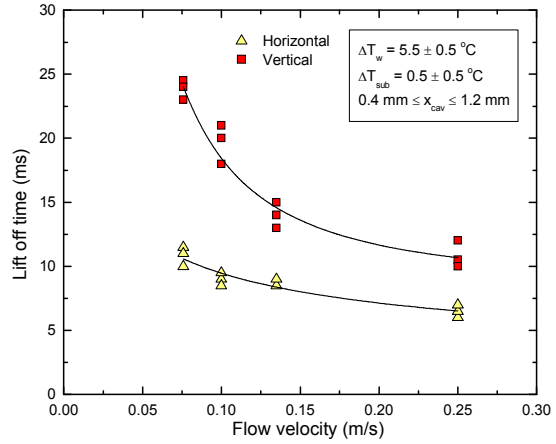

(b)

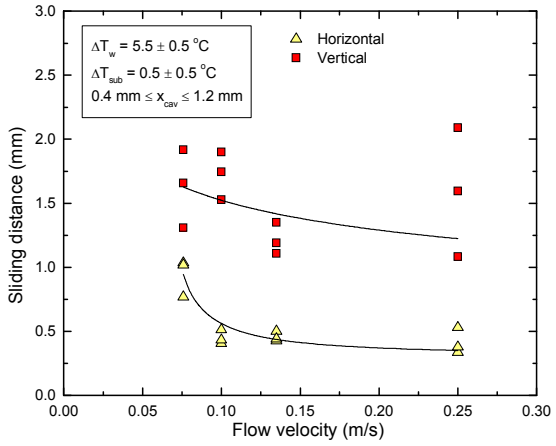

(c)

Figure 4.38 Effect of liquid bulk velocity and heater orientation on (a) lift off diameter, (b) lift off times, and (c) sliding distance – Aluminum surface.

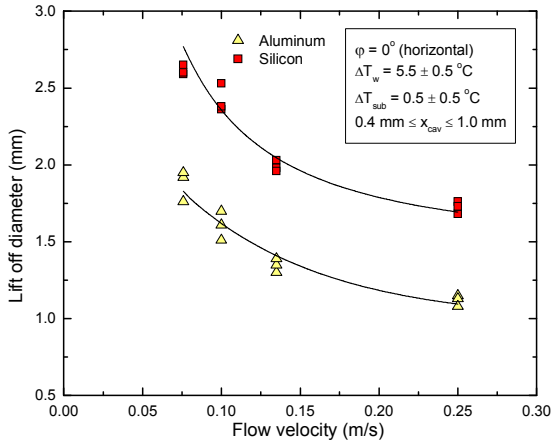

(a)

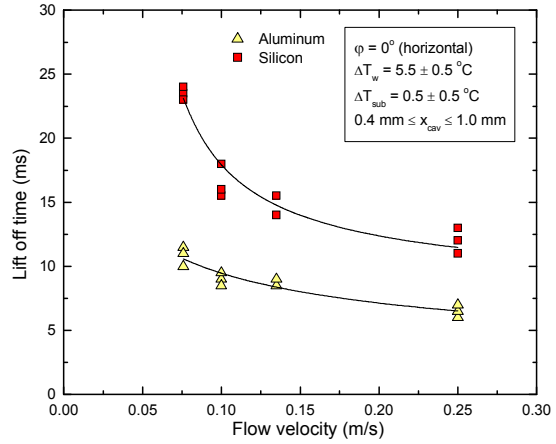

(b)

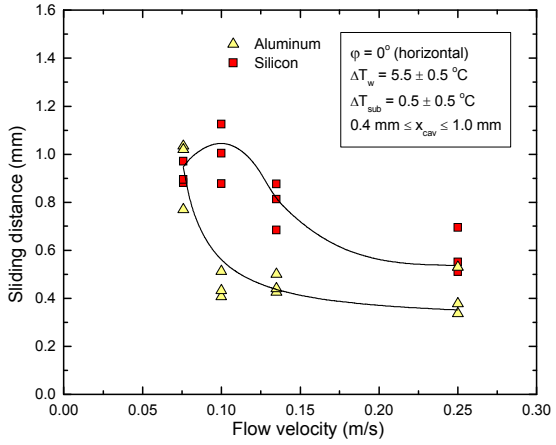

(c)

Figure 4.39 Effect of liquid bulk velocity and heater material on (a) lift off diameter, (b) lift off times, and (c) sliding distance – Horizontal surface.

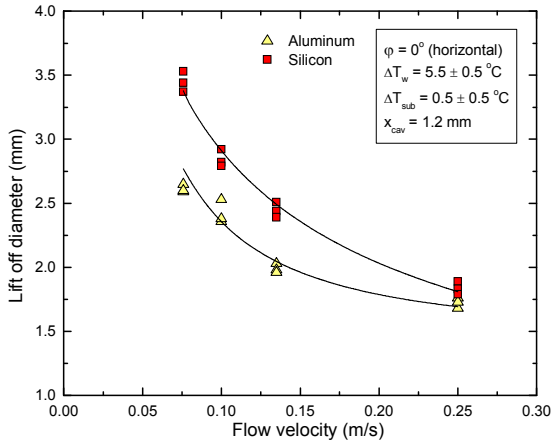

(a)

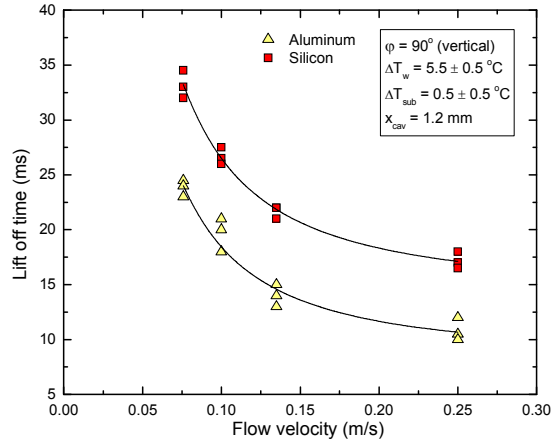

(b)

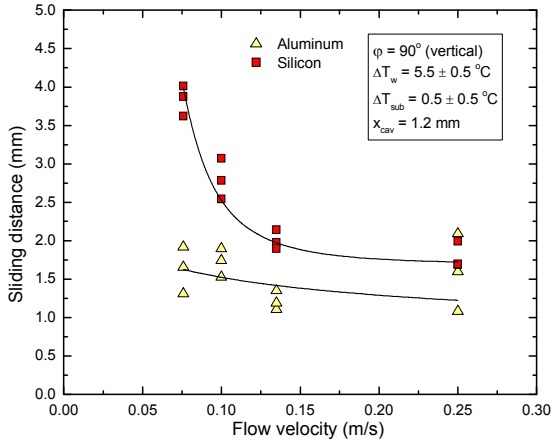

(c)

Figure 4.40 Effect of liquid bulk velocity and heater orientation on (a) lift off diameter, (b) lift off times, and (c) sliding distance – Vertical surface.

Chapter 5
Comparison between Single Bubble and Two-Bubble Lateral Mergers Water Experiments – Effect on Bubble Dynamics and Heat Transfer

In flow boiling, as in pool boiling, transition from partial nucleate boiling to fully developed nucleate boiling in accompanied by an increase in the number of active nucleation sites, which in turns leads to the apparition of lateral bubble merger. To investigate the effects of lateral bubble merger on bubble dynamics and heat transfer in flow boiling, single bubble (refer to Chapter 3) and two-bubble merger (refer to Chapter 4) data are compared. The results of these comparisons are presented in this Chapter.

5.1 Effect of two-bubble merger on bubble growth and lift off

5.1.1 Horizontal surface

In this section, comparison between bubble growth rate, bubble lift off diameter and tine data for single bubble and two-bubble merger is shown, horizontal silicon and aluminum surfaces.

5.1.1.1 Silicon surface

Figure 5.1 shows the comparison between single bubble and two-bubble lateral merger growth rate, lift off diameter, and lift off time data, for horizontal silicon surface. Lift off diameter and lift off time data from Mukherjee (2004) for pool boiling conditions is also shown in Figs. 5.1(e) and 5.1(f). As can be seen from Figs. 5.1(a-b), for given conditions, bubble growth rate for both upstream and downstream bubbles for the two-

bubble merger cases, before merger occurs, are very similar to that for single bubbles. This is an expected result, as both wall superheat and liquid subcooling are almost identical for each experiment. Also plotted in Figs. 5.1(a-b) is the equivalent diameter of the combined upstream and downstream bubbles, before merger. In order to determine this equivalent diameter, both bubbles volume are added, and an equivalent bubble diameter is obtained based on the total volume, assuming the merged bubble is a perfect sphere. For two-bubble merger conditions, the overall growth rate before and after merger follows the same trend, as shown in Figs. 5.1(a-b). For given conditions, immediately after the merger starts, the diameter of the merged bubble is superior to the single bubble lift off diameter. Also, as can be seen in Figs. 5.1(a-b) and in Fig. 5.1(e), for velocities between 0.076 m/s and 0.25 m/s, two-bubble merger lift off diameter is systematically larger than that of single bubble. Flow velocity does not appear to have an effect on the magnitude of the diameter difference, for flow velocities between 0.076 m/s and 0.25 m/s. For pool boiling conditions, according to the data from Mukherjee (2004), the lift off diameter is identical for both cases. Finally, from Figs. 5.1(a-d) and 5.1(f), it can be seen that for 0.076 m/s and 0.1 m/s flow velocities, lift off time is larger for single bubbles than for merged bubbles. This relationship is expected, as bubble merger results in a sudden, discrete increase in bubble growth rate, therefore reducing the time required for the bubble to reach its lift off diameter. However, for flow velocities of 0.135 m/s and 0.25 m/s, lift off time is larger for single bubbles than for merged bubbles. As can be seen in Figs. 5.1(c) and 5.1(d), due to the large cavity spacing relative to single bubble lift off diameter, the two bubbles merger occurs approximately at the same time as lift off time

for single bubbles. After merger, the bubbles keep growing before lifting off from the heater surface.

The comparison between single bubble and two-bubble merger sliding distance data is shown in Fig. 5.2. For single bubble, sliding distance increases quasi-linearly with increase in flow velocity. For two-bubble merger and low flow velocities (0.076 m/s $\leq U_{bulk} \leq$ 0.1 m/s), sliding distance increases with increase in flow velocity; for larger flow velocities (0.1 m/s $\leq U_{bulk} \leq$ 0.25 m/s), sliding distance decreases with increase in flow velocity. Also, sliding distance is larger for two-bubble merger than that for single bubble for 0.076 m/s $\leq U_{bulk} \leq$ 0.135 m/s, and smaller for U_{bulk} = 0.25 m/s.

In order to explain why lift off diameter is larger for merged bubbles than for single bubbles, for given conditions, sliding velocity relative to the flow velocity data are plotted in Fig. 5.3 and bubble base diameter data are plotted in Fig. 5.4. In both figures, data are plotted as a function of the reduced time t^*, defined as $t^* = t / t_l$, where t_l is the lift off time. Single bubble data are plotted for bubbles departed from their nucleation sites, and two-bubble data are plotted for merged bubbles.

As can be seen in Fig. 5.3, bubble relative velocity at $t^* = 1$ for merged bubbles is comparable (in absolute value) to that for single bubbles. Therefore, sliding velocity cannot explain the differences in lift off diameter observed, as the contribution from lift force should be similar for both cases. However, at given relative velocity, merged bubbles are larger than single bubbles, therefore they experience a smaller rate of sheer γ_r than single bubbles. As a result, merged bubbles need to grow to a larger to generate enough lift for lift off to occur. Note that in Figs. 5.3(a) and 5.3(b), for merged bubbles relative velocity decreases after merger, reaches a minimum, and increases as bubble

bases finally merge. This signifies that after merger, bubble sliding velocity decreases, reaches a minimum, and then increases after the bases merge. This is a direct consequence of the smaller downstream bubble being absorbed by the larger upstream, since the inertia of the merger process slows the merged bubble sliding motion. Once the bubble bases merge, the bubble gets elongated in the vertical direction, which coupled with the drag force in the direction parallel to the heater surface, increases bubble sliding velocity before lift off, which becomes larger than that of the flow at the instant before lift off, for U_{bulk} = 0.076 m/s and 0.1 m/s. As noted earlier, sliding distance for two-bubble merger is greatly affected by cavity spacing. Merger causes the upstream bubble to move towards the downstream bubble, increasing the sliding distance. However, as shown in Fig. 5.3 as the bubble bases start to merge, bubble sliding velocity decreases, therefore reducing the overall sliding distance of the merged bubble, compared to that of a single bubble. Also note than in some cases, merged bubble sliding velocity is larger than that of the flow. This is due to the large inertia of the merger processes, which increases the bubble sliding velocity.

From Fig. 5.4, it can be seen that for all cases, merged bubble base diameter is larger than that for single bubble. Also, merged bubble base diameter peaks much later in the growth cycle than single bubble base diameter, and this peak coincides with the merger of the bubble bases. As a consequence of the larger bubble base diameter observed for merged bubbles, lift off diameter for those cases is much larger, as buoyancy and lift forces need to be larger to compensate for larger surface tension force keeping the bubble attached to the heater wall. Comparison between Figs. 5.3(a) and 5.3(b), and Figs. 5.4(a) and 5.4(b), shows that merged bubble diameter is larger for the smallest relative

velocities, therefore for the smallest bubble sliding velocities. In the direction parallel to the heater wall, surface tension, which is proportional to bubble base diameter, opposes the bubble sliding motion. As a consequence, a larger base diameter leads to a lower sliding velocity.

5.1.1.2 Aluminum surface

Figure 5.5 shows the comparison between single bubble and two-bubble lateral merger growth rate, lift off diameter, and lift off time data, for horizontal aluminum surface. As can be seen from Figs. 5.5(a-b), for given conditions, bubble growth rate for both upstream and downstream bubbles for the two-bubble merger cases, before merger occurs, are very similar to that for single bubbles. This is an expected result, as both wall superheat and liquid subcooling are almost identical for each experiment. For two-bubble merger conditions, the overall growth rate before (based on the equivalent diameter of the combined upstream and downstream bubbles) and after merger follows the same trend, as shown in Figs. 5.5(a-b). For given conditions, immediately after the merger starts, the diameter of the merged bubble is superior to the single bubble lift off diameter. Also, as can be seen in Figs. 5.5(a-b) and in Fig. 5.5(e), for velocities between 0.076 m/s and 0.25 m/s, two-bubble merger lift off diameter is systematically larger than that of single bubble. Flow velocity does not appear to have an effect on the magnitude of the diameter difference, for flow velocities between 0.076 m/s and 0.135 m/s, and for velocities between 0.135 m/s and 0.25 m/s, increase in flow velocities leads to a larger increase in lift off diameter difference between single bubble and two-bubble merger cases. From Figs. 5.5(a-d) and 5.5(f), it can be seen that for all flow velocities, lift off time is larger

for merged bubbles than for single bubbles. This is a surprising result, as bubble merger results in a sudden, discrete increase in bubble growth rate, and should therefore reduce the time required for the bubble to reach its lift off diameter.

The comparison between single bubble and two-bubble merger sliding distance data is shown in Fig. 5.6. For single bubble, sliding distance increases quasi-linearly with increase in flow velocity, 0.076 m/s $\leq U_{bulk} \leq$ 0.135 m/s, and decrease with increase in flow velocity for 0.135 m/s $\leq U_{bulk} \leq$ 0.25 m/s. For two-bubble merger, sliding distance decreases with increase in flow velocity, for 0.076 m/s $\leq U_{bulk} \leq$ 0.25 m/s. As can be seen in Fig. 5.6, sliding distance is larger for two-bubble merger than that for single bubble, for 0.076 m/s $\leq U_{bulk} \leq$ 0.25 m/s.

In order to explain why lift off diameter is larger for merged bubbles than for single bubbles, for given conditions, sliding velocity relative to the flow velocity data are plotted in Fig. 5.7 and bubble base diameter data are plotted in Fig. 5.8. Similarly to that for horizontal surface, data are plotted as a function of the reduced time t^*. Also, single bubble data are plotted for bubbles departed from their nucleation sites, and two-bubble data are plotted for merged bubbles.

Similarly to what was observed in the previous section for horizontal aluminum surface, Fig. 5.7 shows that bubble relative velocity at $t^* = 1$ for merged bubbles is comparable (in absolute value) to that for single bubbles. Most importantly, at given relative velocity, merged bubbles are larger than single bubbles, therefore they experience a smaller rate of sheer γ_r than single bubbles. As a result, merged bubbles need to grow to a larger to generate enough lift for lift off to occur. As observed in Figs. 5.3(a) and 5.3(b) for silicon surfaces, Fig. 5.7 shows that for all aluminum surface cases,

merged bubbles relative velocity decreases after merger, reaches a minimum, and increases as bubble bases finally merge. Note than in some cases, merged bubble sliding velocity is larger than that of the flow. This is due to the large inertia of the merger processes, which increases the bubble sliding velocity.

From Fig. 5.8, it can be seen that for all cases, merged bubble base diameter is larger than that for single bubble. Also, merged bubble base diameter peaks much later in the growth cycle than single bubble base diameter, and this peak coincides with the merger of the bubble bases. As a consequence of the larger bubble base diameter observed for merged bubbles, lift off diameter for those cases is much larger, as buoyancy and lift forces need to be larger to compensate for larger surface tension force keeping the bubble attached to the heater wall. An additional consequence of the merger process is to increase lift off time, as seen in Fig. 5.5. Bubble base diameter peaks later (when the bases merge) in the growth cycle for merged bubble than for single bubble, which has for effect to delay bubble lift off. Also, as can be seen from Fig. 5.8, and from the data plotted in Chapter 4 for horizontal aluminum surfaces, an average of 2 ms separate bubble merger and merger of the bases. The combined effect of this two factors, coupled with the fact that single bubble lift off times for horizontal aluminum surfaces are very short, result in larger lift off times for merged bubbles than for single bubbles.

5.1.2 Vertical surface

In this section, comparison between bubble growth rate, bubble lift off diameter and tine data for single bubble and two-bubble merger is shown, for vertical silicon and aluminum surfaces.

5.1.2.1 Silicon surface

Figure 5.9 shows the comparison between single bubble and two-bubble lateral merger growth rate, lift off diameter, and lift off time data, for vertical silicon surface. As can be seen from Figs. 5.9(a-b), for given conditions, bubble growth rate for both upstream and downstream bubbles for the two-bubble merger cases, before merger occurs, are very similar to that for single bubbles. For two-bubble merger conditions, when both upstream and downstream bubbles nucleate around the same time, as in Figs. 5.9(b) and 5.9(c), the overall growth rate before and after merger follows the same trend. When the downstream bubble nucleates and merges quickly with the upstream one, as shown in Figs. 5.9(a) and 5.9(d), growth rate is much higher instants before and after merger, and decreases as the merged bubble slides on the heater surface. As opposed to what was shown for horizontal silicon and aluminum surfaces in the previous section, for given conditions, after merger, the diameter of the merged bubble is smaller than the single bubble lift off diameter. Therefore, as expected based on the single bubble data, the merged bubble continues to slide and grow until it reaches lift off diameter. However, as can be seen in Figs. 5.9(a-b) and in Fig. 5.9(e), for velocities between 0.076 m/s and 0.25 m/s, two-bubble merger lift off diameter is systematically larger than that of single bubble, and flow velocity does not appear to have an effect on the magnitude of the diameter difference. Finally, from Figs. 5.9(a-d) and 5.9(f), it can be seen that for all flow velocities, lift off time is much larger for single bubbles than for merged bubbles, despite the fact that lift off diameter is larger for merged bubbles than for single bubbles. This relationship is expected, as bubble merger results in a sudden, discrete increase in bubble

growth rate, therefore reducing the time required for the bubble to reach its lift off diameter.

The comparison between single bubble and two-bubble merger sliding distance data is shown in Fig. 5.10. For both single and merged bubbles, sliding distance decreases non-linearly with increase in flow velocity. Also, sliding distance is more important for single bubble than for merged bubbles, in part because of the larger lift off time for single bubble than for merged bubble.

Sliding velocity relative to the flow velocity data are plotted in Fig. 5.11 and bubble base diameter data are plotted in Fig. 5.12, as a function of the reduced time t^*. Single bubble data are plotted for bubbles departed from their nucleation sites, and two-bubble data are plotted for merged bubbles.

As can be seen in Fig. 5.11, bubble relative velocity at $t^* = 1$ for merged bubbles is comparable or smaller (in absolute value) to that for single bubbles. These differences could have an effect on the lift off diameter, as lift force is proportional to the relative velocity. Most importantly, at given relative velocity, merged bubbles are larger than single bubbles, therefore they experience a smaller rate of sheer γ_r than single bubbles. As a result, merged bubbles need to grow to a larger to generate enough lift for lift off to occur. Note that in Figs. 5.11, merged bubbles relative velocity decreases after merger, reaches a minimum, and increases as bubble bases finally merge. This signifies that after merger, bubble sliding velocity decreases, reaches a minimum, and then increases after the bases merge. Once the bubble bases merge, the bubble gets elongated in the vertical direction, which coupled with the drag and buoyancy forces in the direction parallel to the heater surface, increases bubble sliding velocity before lift off, which becomes larger

than that of the flow at the instant before lift off, for 0.076 m/s ≤ U_{bulk} ≤ 0.135 m/s. A similar behavior is observed for single bubbles, as velocity before lift off is systematically larger than that of the flow For U_{bulk} = 0.25 m/s, on the other hand, sliding velocity is smaller than that of the flow. The inertia of the bubble merger process is large enough to slow the bubble down, and counteract the effects drag and buoyancy forces have on bubble sliding velocity.

From Fig. 5.12, it can be seen that for all cases, merged bubble base diameter is systematically larger than that for single bubble. As a consequence of the larger bubble base diameter observed for merged bubbles, lift off diameter for those cases is much larger, as lift force needs to be larger to compensate for larger surface tension force keeping the bubble attached to the heater wall.

5.1.2.2 Aluminum surface

Figure 5.13 shows the comparison between single bubble and two-bubble lateral merger growth rate, lift off diameter, and lift off time data, for vertical aluminum surface. As can be seen from Figs. 5.13(a-b), for given conditions, both upstream and downstream bubbles growth rates, for the two-bubble merger cases before merger occurs, and single bubble growth rate are very similar. For two-bubble merger conditions, the overall growth rate before and after merger follows the same trend. As can be seen in Figs. 5.13(a-c), for 0.076 m/s ≤ U_{bulk} ≤ 0.135 m/s, after merger, the diameter of the merged bubble is smaller than the single bubble lift off diameter, similarly to what was observed for vertical silicon surface. This behavior differs from that for horizontal silicon and aluminum surfaces, as presented earlier in this Chapter. Therefore, as expected based on

the single bubble data, the merged bubble continues to slide and grow until it reaches lift off diameter. For U_{bulk} = 0.25 m/s, on the other hand, diameter of the merged bubble after merger occurs is larger than single bubble lift off diameter. As can be seen in Figs. 5.13(a-b) and in Fig. 5.13(e), for velocities between 0.076 m/s and 0.25 m/s, two-bubble merger lift off diameter is systematically larger than that of single bubble. For flow velocities between 0.076 m/s and 0.135 m/s, flow velocity does not appear to have an effect on the magnitude of the diameter difference. For flow velocities between 0.135 m/s and 0.25 m/s, on the other hand, difference in lift off diameter increases with increase in flow velocity. This behavior is possibly due to the fact that the single bubble lift of diameter for U_{bulk} = 0.25 m/s is very close to the distance separating the cavities. As a result, bubble merger increases dramatically bubble diameter, which becomes much larger than the single bubble lift off diameter. Finally, from Figs. 5.13(a-d) and 5.13(f), it can be seen that for all flow velocities, lift off time is much larger for single bubbles than for merged bubbles. As for horizontal silicon surface, even though lift off diameter is larger for merged bubbles than for single bubbles, bubble merger results in a sudden increase in bubble diameter, therefore reducing the time required for the bubble to reach its lift off diameter.

Figure 5.14 shows the comparison between single bubble and two-bubble merger sliding distance data. For single bubbles, sliding distance decreases non-linearly with increase in flow velocity, as for merged bubbles for flow velocities between 0.1 m/s and 0.25 m/s. However, for flow velocities between 0.076 m/s and 0.1 m/s, merged bubble sliding distance increases with increase in flow velocity. Most importantly, Fig. 5.14

shows that sliding distance is more important for single bubble than for merged bubbles, in part because of the larger lift off time for single bubble than for merged bubble.

Sliding velocity relative to the flow velocity data are plotted in Fig. 5.15 and bubble base diameter data are plotted in Fig. 5.15, as a function of the reduced time t^*, for both single and merged bubbles. Single bubble data are plotted for bubbles departed from their nucleation sites, and two-bubble data are plotted for merged bubbles.

As can be seen in Fig. 5.15, bubble relative velocity at $t^* = 1$ for merged bubbles is comparable (in absolute value) to that for single bubbles. Most importantly, at given relative velocity, merged bubbles are larger than single bubbles, therefore they experience a smaller rate of sheer γ_r than single bubbles. As a result, merged bubbles need to grow to a larger to generate enough lift for lift off to occur. Note that in Figs. 5.15, merged bubbles relative velocity decreases after merger, reaches a minimum, and increases as bubble bases finally merge. For both single (all flow velocities) and merged bubbles (all flow velocities), sliding velocity before lift off becomes larger than that of the flow.

From Fig. 5.16, it can be seen that for all cases, merged bubble base diameter is systematically larger than that for single bubble. As a consequence of the larger bubble base diameter observed for merged bubbles, lift off diameter for those cases is much larger, as lift force needs to be larger to compensate for larger surface tension force keeping the bubble attached to the heater wall.

5.2 Two-bubble merger lift of diameter modeling

Figure 5.17 shows the comparison between $F_b + F_s + F_{cp}$ and F_s, at the instant where bubble lift off is initiated (i.e. when bubble base diameter is maximum), for merged bubbles. As can be seen in Fig. 3.48, the detaching forces acting on the bubble are equal to the attaching forces, regardless of orientation ($\varphi = 0^o$ and 90^o) and contact angle ($\theta = 19^o$ and 56^o). Also, as seen in Figs. 5.18 and 5.19, $D_{base,max} = D / 2.25$ and $D_l = 1.11 \times D$, regardless of orientation and contact angles. Therefore, Eqs. (3.18) and (3.19) could be used as a base to develop a model that could predict merged bubble lift off diameter, provided modifications are made to account for the change of D_l and $D_{base,max}$ dependence on D..

Figure 5.20 shows the forces acting on a merged bubble at lift off, as a function of flow velocity, for horizontal (Fig. 5.20(a)), and vertical (Fig. 5.20(b)) aluminum surfaces. Similarly, Fig. 5.21 shows the forces acting on a bubble at lift off, as a function of flow velocity, for horizontal (Fig. 5.21(a)), and vertical (Fig. 5.21(b)) silicon surfaces. As in Chapter 3 for single bubbles, these forces are presented in reduced form, in which F_b, F_l and $F_b + F_l$ are divided by the bubble surface area at lift off A_l.

Figures 5.20(a) and 5.21(a) show that for horizontal surfaces, the contribution of buoyancy force to lift off decreases with increase in flow velocity, while the contribution of lift force to lift off increases with increase in flow velocity, irrespective of orientation and contact angle. Also, comparison between Figs. 5.20(a) and 5.21(a) show that for given condition, the relative contribution of lift force to bubble lift off is larger for horizontal aluminum surface than for horizontal silicon surface. Similar results were obtained in Chapter 3 for single bubbles. As for single bubbles, Figs. 5.20 and 5.21 also

show that for merged bubbles, irrespective of orientation, flow velocity, and heater material, $(F_b + F_l) / A_l$ is constant, and equal to 2.25 N/m^2.

As a result, regardless of orientation, contact angle and flow velocity, $(F_b + F_l) / A_l$ = 2.25 N/m^2, as shown in Fig. 5.22. In Fig. 5.22, the sum of buoyancy and lift forces divided by bubble surface area is plotted as a function of flow velocity, for all orientations, flow velocities, surface materials, and for single and merged bubbles.

5.3 Chapter conclusions

In this Chapter, the effect of two-bubble lateral in-line merger on bubble dynamics, vapor removal rate and heat transfer where analyzed and compared to that for discrete bubbles. Some of the key results from this analysis are:

- Irrespective of orientation and contact angle, lift off and bubble base diameters are larger for merged bubbles than for single bubbles, and sliding distance is smaller for merged bubbles than for single bubbles.
- The increase in bubble lift off diameter is a consequence of larger bubble base diameter for merged bubble. Larger lift and buoyancy forces are required to compensate for greater surface tension attaching the bubble to the surface, which leads to larger lift off diameter.
- For horizontal aluminum surface (0.076 m/s $\leq U_{bulk} \leq$ 0.25 m/s), and for horizontal silicon surface (U_{bulk} = 0.25 m/s), lift off time is larger for merged bubble than for single bubbles. Due to cavity spacing, bubbles merge instants before they reach single bubble lift off diameter (and as a consequence single bubble lift off time). The merger process results in increase in base diameter,

delaying bubble lift off until the merger is complete, and merged bubble lift off diameter is reached. For all other cases, lift of time is smaller for merged bubble, as bubble merger results in a sudden, discrete increase in bubble growth rate, therefore reducing the time required for the bubble to reach its lift off diameter.

- Bubble lift off is initiated at the instant when the sum of these forces becomes positive in the y-direction (normal to the heater). It coincides to the moment when the bubble base starts to shrink. It is found that at this instant, $D_{base} = D / 2.25$.
- Based on this force balance an expression for bubble diameter is developed. From this expression, one can determine the bubble lift off diameter, using the following relationship: $D_l = 1.11 \times D$ (at $D_{base} = D_{base,max}$), for two contact angles (19^o and 56^o), $\varphi = 0^o$ and 90^o, and $0.076 \text{ m/s} \leq U_{bulk} \leq 0.25 \text{ m/s}$.
- When lift off occurs, buoyancy and lift forces are the only forces acting on the bubble, and regardless of orientation, contact angle and flow velocity, the ratio $(F_b + F_l) / A_l = 2.25 \text{ N/m}^2$, where A_l is the bubble surface area at lift off.
- For single and merged bubbles, when lift off occurs, buoyancy and lift forces are the only forces acting on the bubble, and regardless of orientation, contact angle and flow velocity, and $(F_b + F_l) / A_l = 2.25 \text{ N/m}^2$, where A_l is the bubble surface area at lift off.

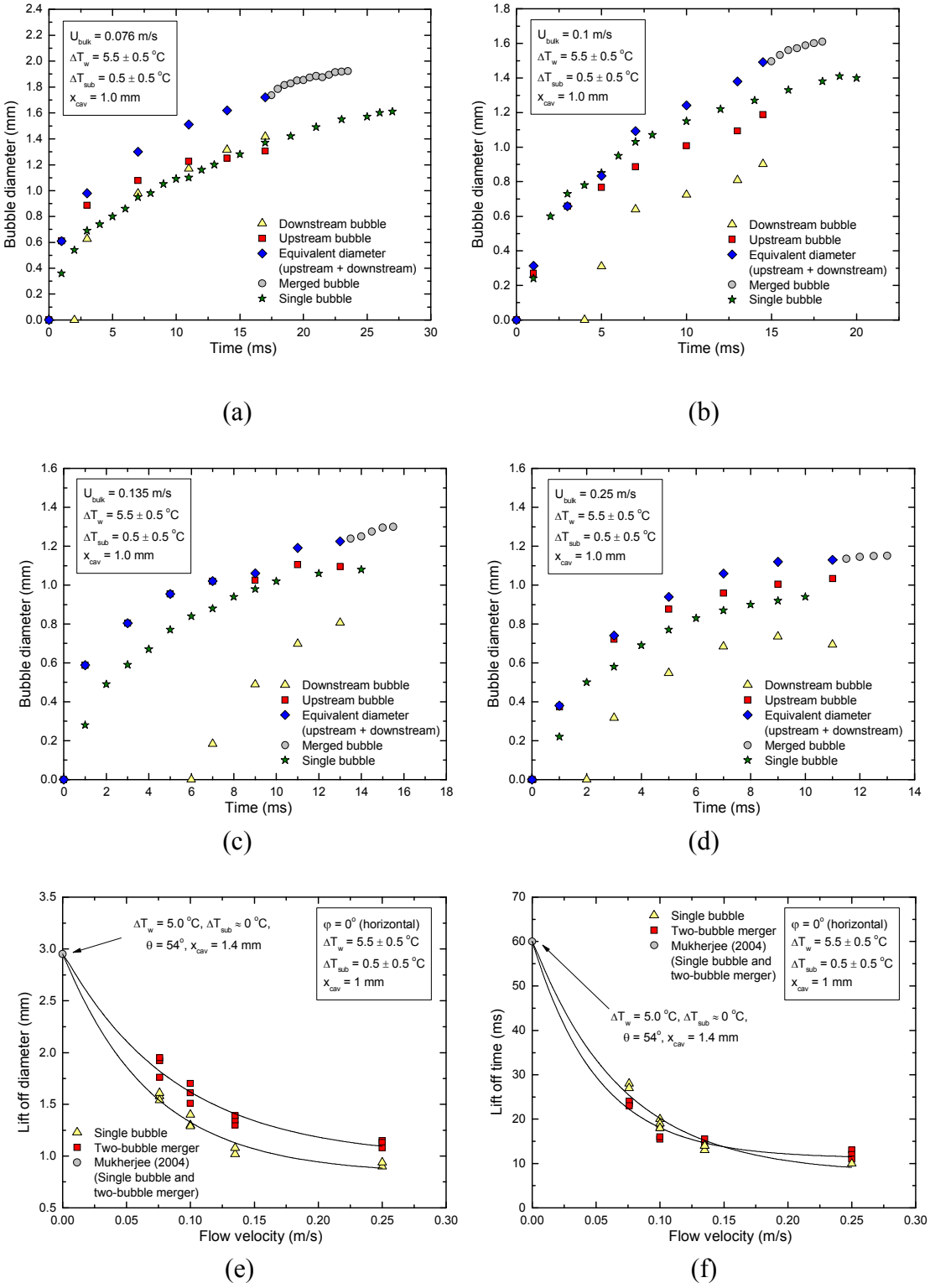

Figure 5.1 Comparison between single bubble and two-bubble lateral merger data for (a-d) growth rate, (e) lift off diameter, and (f) lift off time, for horizontal silicon surface, 0 m/s ≤ U_{bulk} ≤ 0.25 m/s, ΔT_w = 5.5 ± 0.5 °C, ΔT_{sub} = 0.5 ± 0.5 °C, and x_{cav} = 1.0 mm and 1.4 mm.

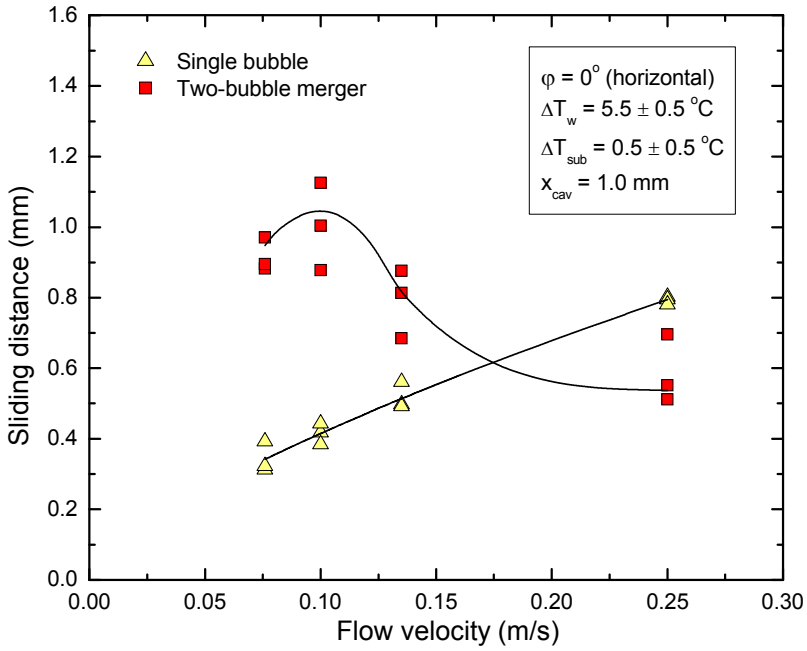

Figure 5.2 Comparison between single bubble and two-bubble lateral merger sliding distance data, for horizontal silicon surface, 0.076 m/s ≤ U_{bulk} ≤ 0.25 m/s, ΔT_w = 5.5 ± 0.5 °C, ΔT_{sub} = 0.5 ± 0.5 °C, and x_{cav} = 1.0 mm.

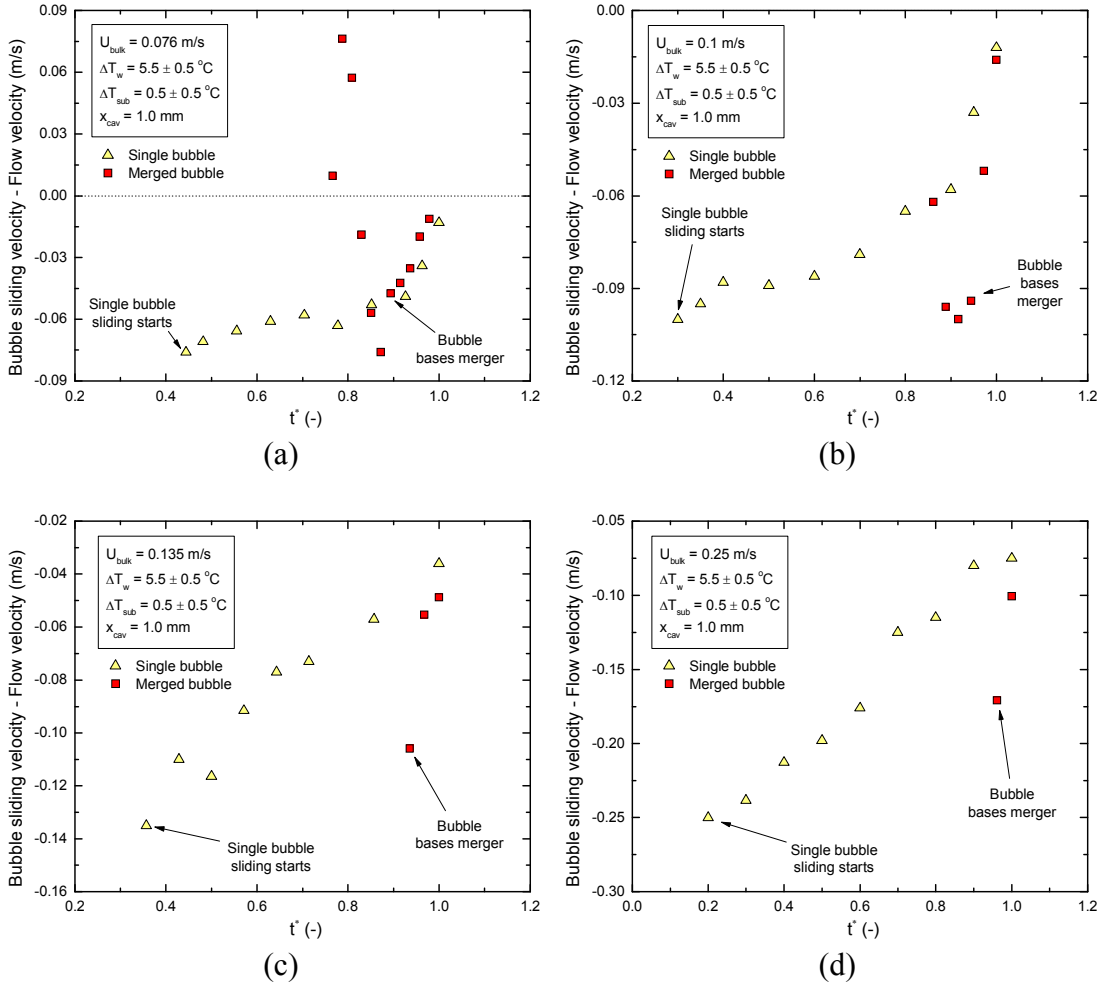

Figure 5.3 Comparison between single bubble and two-bubble lateral merger relative velocity data, for horizontal silicon surface, 0.076 m/s ≤ U_{bulk} ≤ 0.25 m/s, $\Delta T_w = 5.5 \pm 0.5\ ^oC$, $\Delta T_{sub} = 0.5 \pm 0.5\ ^oC$, and $x_{cav} = 1.0$ mm.

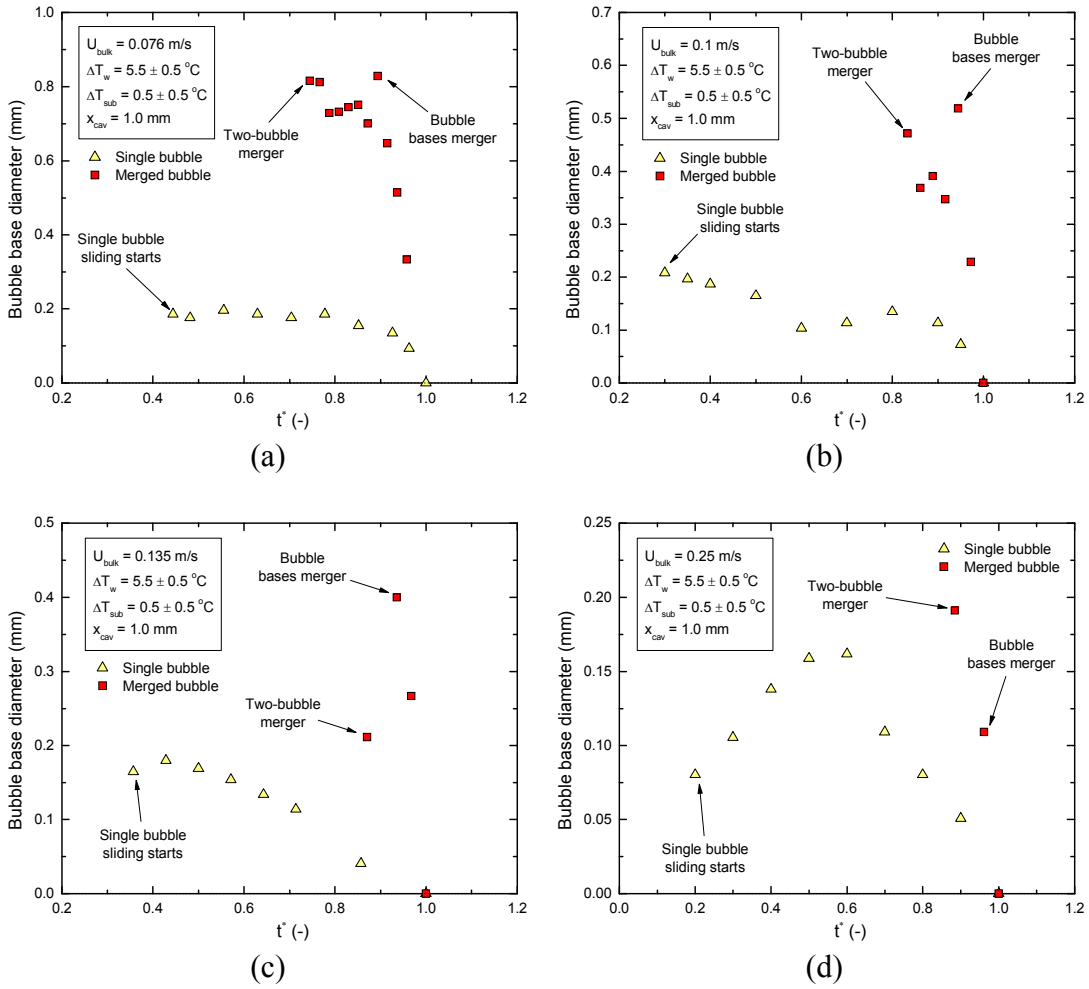

Figure 5.4 Comparison between single bubble and two-bubble lateral merger bubble base diameter, for horizontal silicon surface, 0.076 m/s ≤ U_{bulk} ≤ 0.25 m/s, $\Delta T_w = 5.5 \pm 0.5\ ^oC$, $\Delta T_{sub} = 0.5 \pm 0.5\ ^oC$, and $x_{cav} = 1.0$ mm.

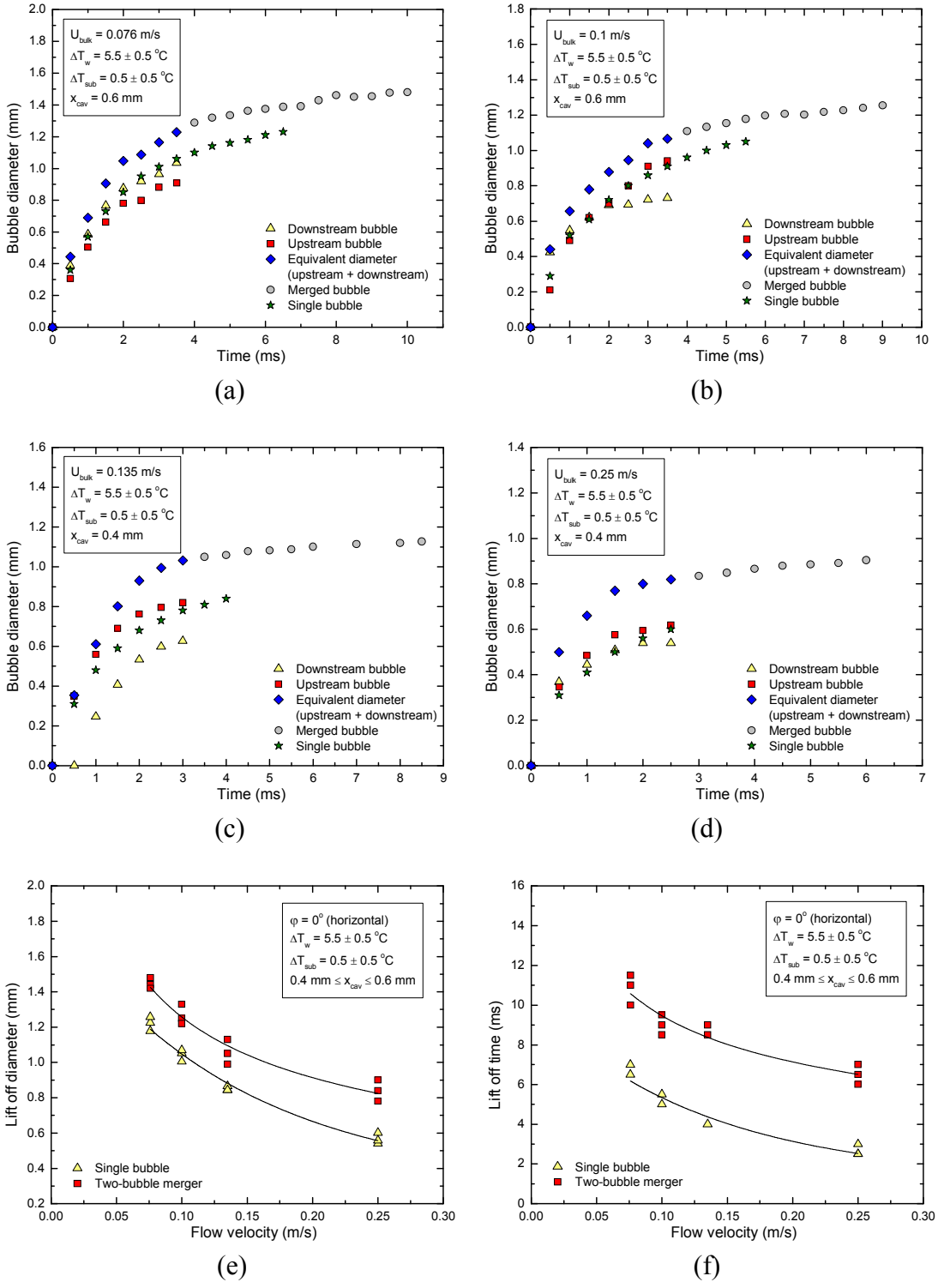

Figure 5.5 Comparison between single bubble and two-bubble lateral merger data for (a-d) growth rate, (e) lift off diameter, and (f) lift off time, for horizontal aluminum surface, 0 m/s ≤ U_{bulk} ≤ 0.25 m/s, ΔT_w = 5.5 ± 0.5 °C, ΔT_{sub} = 0.5 ± 0.5 °C, and 0.4 mm ≤ x_{cav} ≤ 0.6 mm.

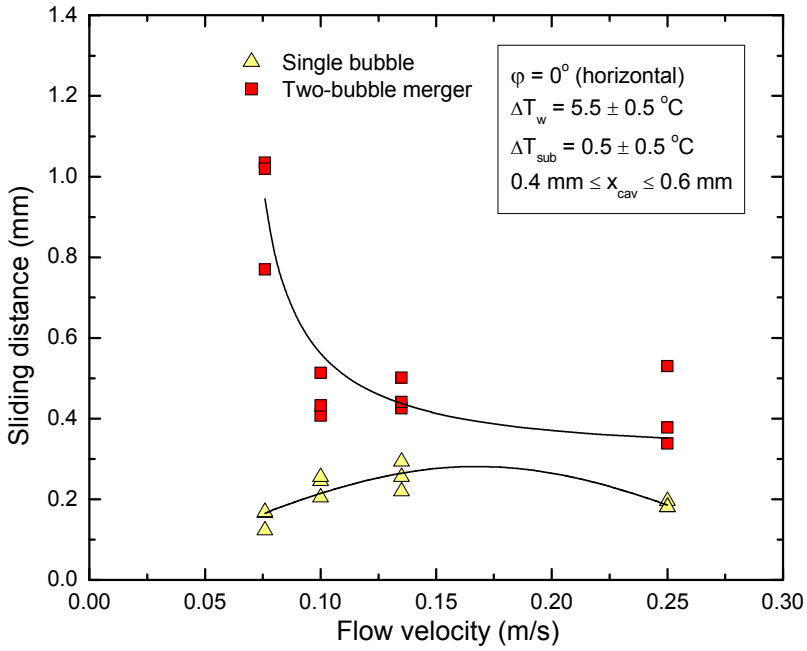

Figure 5.6 Comparison between single bubble and two-bubble lateral merger sliding distance data, for horizontal aluminum, 0.076 m/s ≤ U_{bulk} ≤ 0.25 m/s, ΔT_w = 5.5 ± 0.5 °C, ΔT_{sub} = 0.5 ± 0.5 °C, and x_{cav} = 1.0 mm.

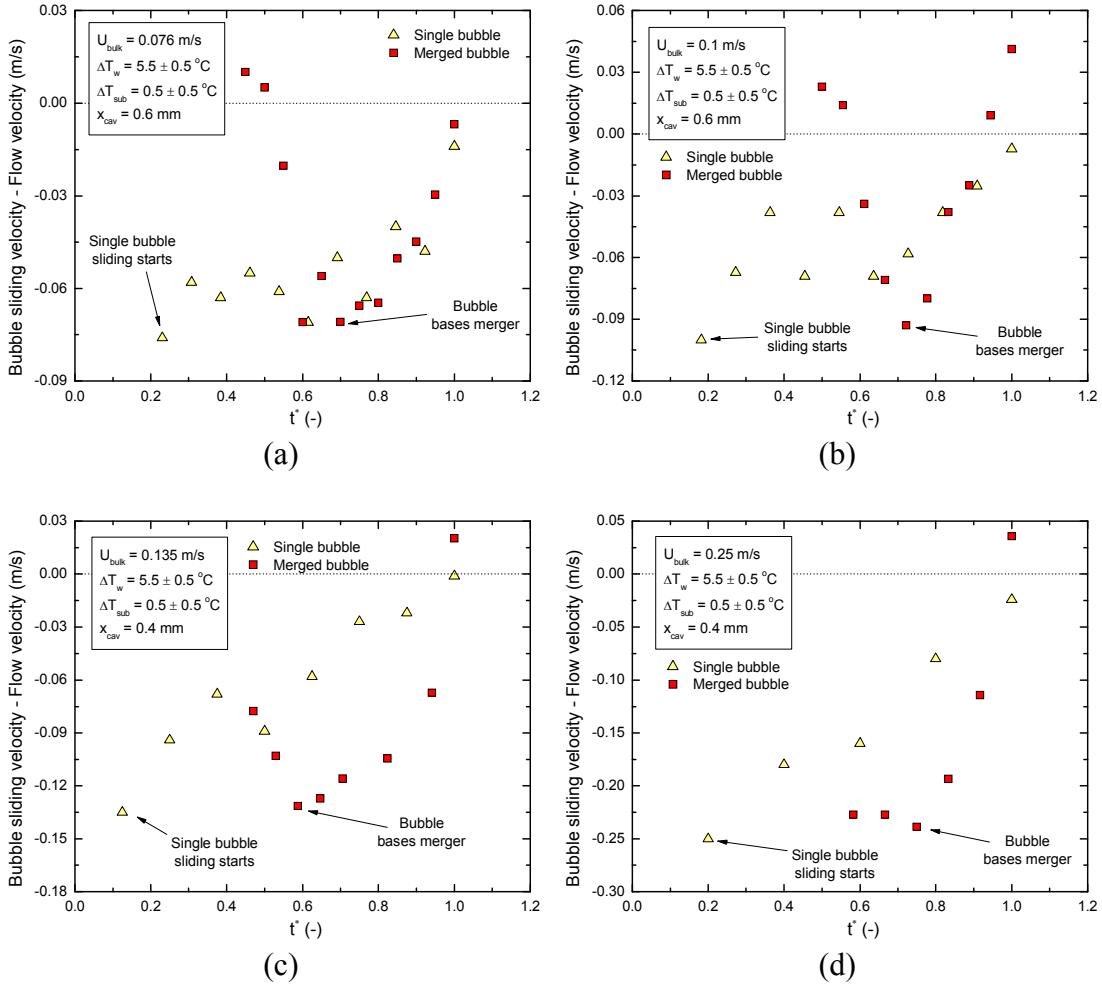

Figure 5.7 Comparison between single bubble and two-bubble lateral merger relative velocity data, for horizontal aluminum surface, 0.076 m/s ≤ U_{bulk} ≤ 0.25 m/s, ΔT_w = 5.5 ± 0.5 °C, ΔT_{sub} = 0.5 ± 0.5 °C, and 0.4 mm ≤ x_{cav} ≤ 0.6 mm.

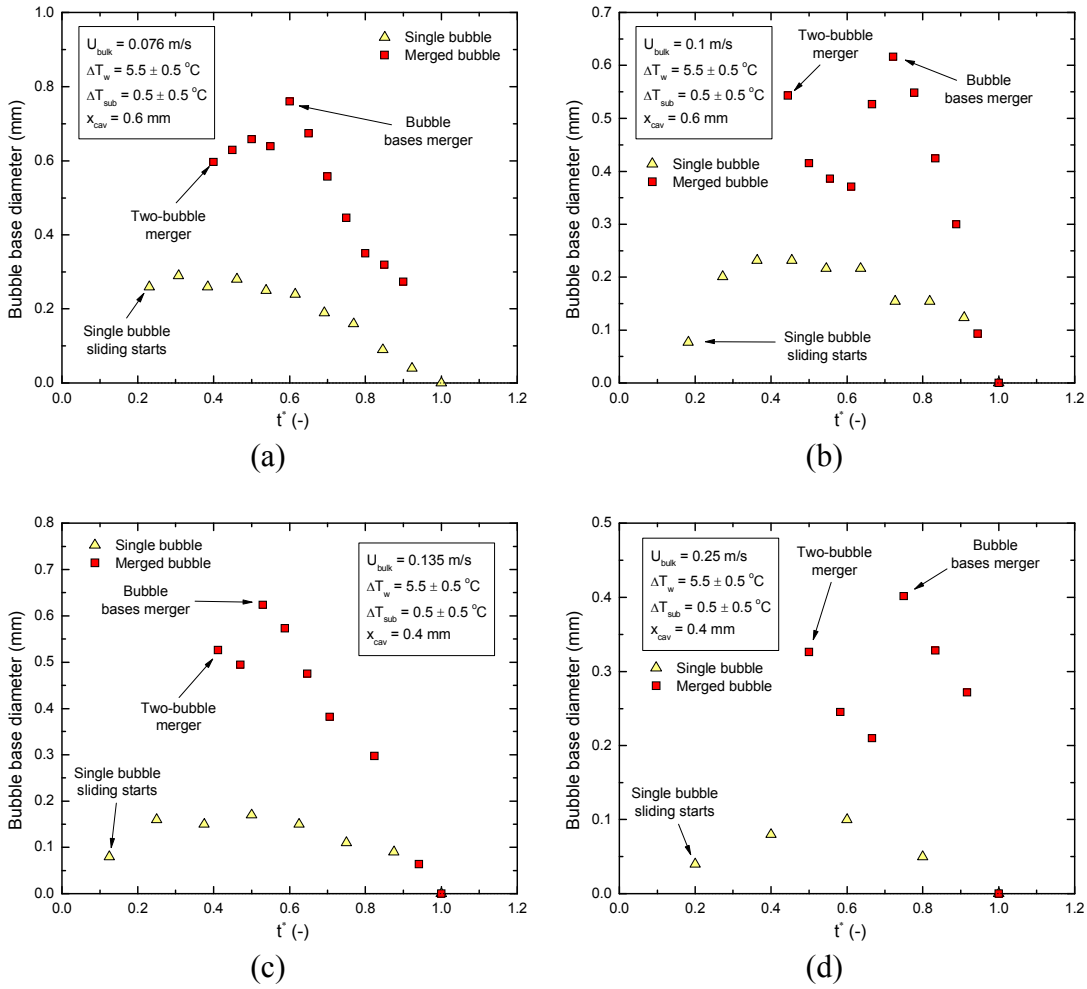

Figure 5.8 Comparison between single bubble and two-bubble lateral merger bubble base diameter, for horizontal aluminum surface, 0.076 m/s ≤ U_{bulk} ≤ 0.25 m/s, ΔT_w = 5.5 ± 0.5 °C, ΔT_{sub} = 0.5 ± 0.5 °C, and 0.4 mm ≤ x_{cav} ≤ 0.6 mm.

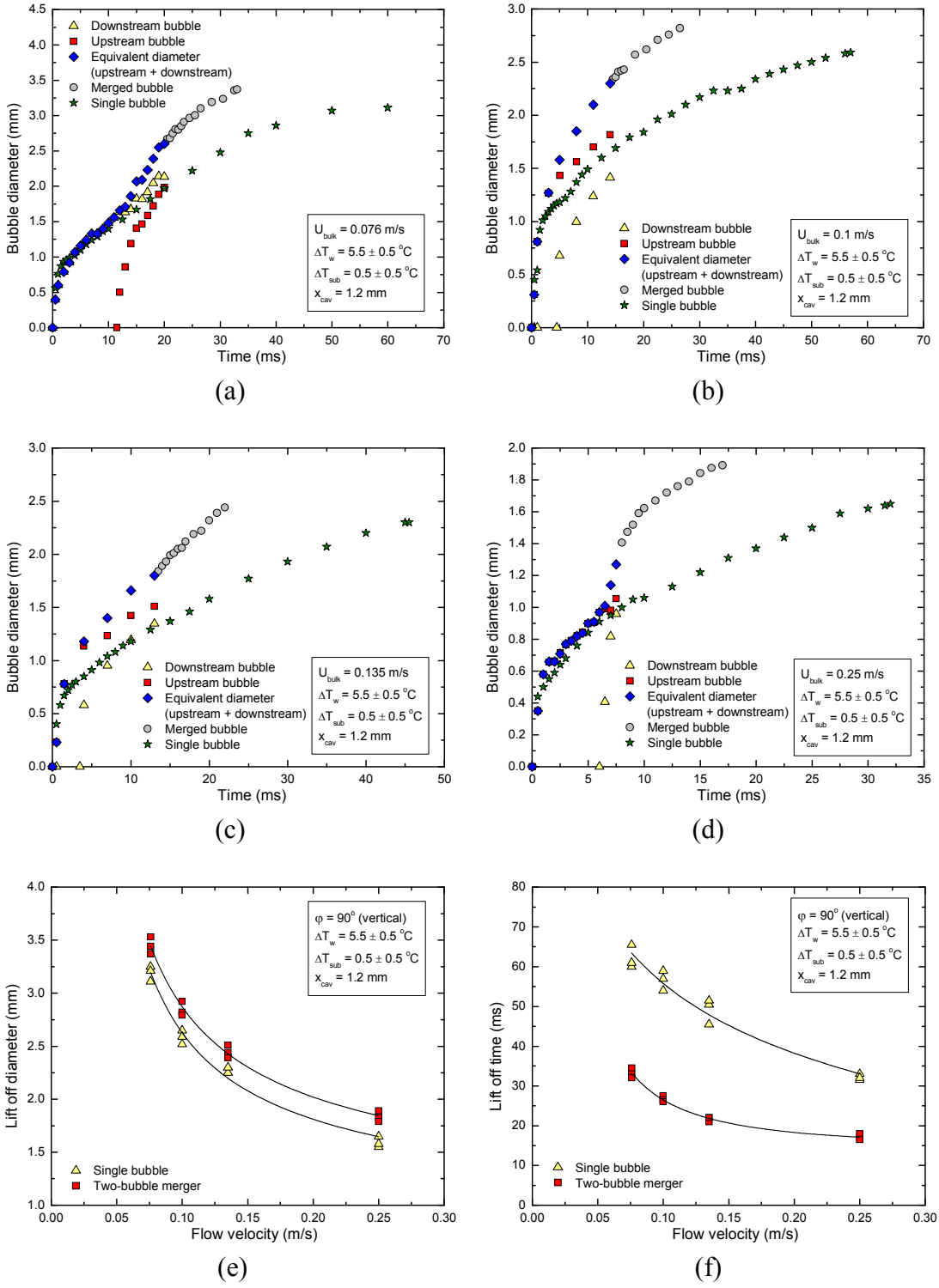

Figure 5.9 Comparison between single bubble and two-bubble lateral merger data for (a-d) growth rate, (e) lift off diameter, and (f) lift off time, for vertical silicon surface, 0.076 m/s ≤ U_{bulk} ≤ 0.25 m/s, $\Delta T_w = 5.5 \pm 0.5$ °C, $\Delta T_{sub} = 0.5 \pm 0.5$ °C, and x_{cav} = 1.2 mm.

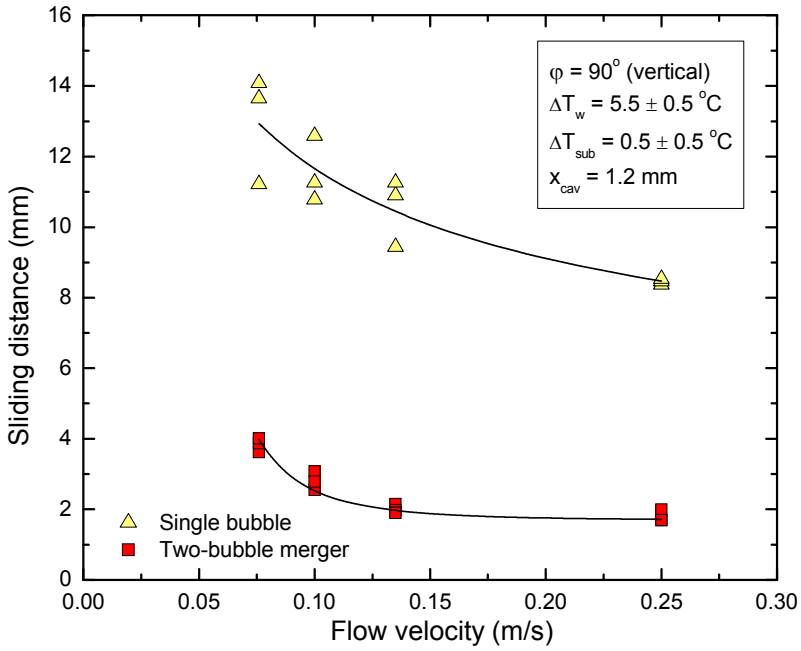

Figure 5.10 Comparison between single bubble and two-bubble lateral merger sliding distance data, for vertical silicon surface, 0.076 m/s ≤ U_{bulk} ≤ 0.25 m/s, ΔT_w = 5.5 ± 0.5 °C, ΔT_{sub} = 0.5 ± 0.5 °C, and x_{cav} = 1.2 mm.

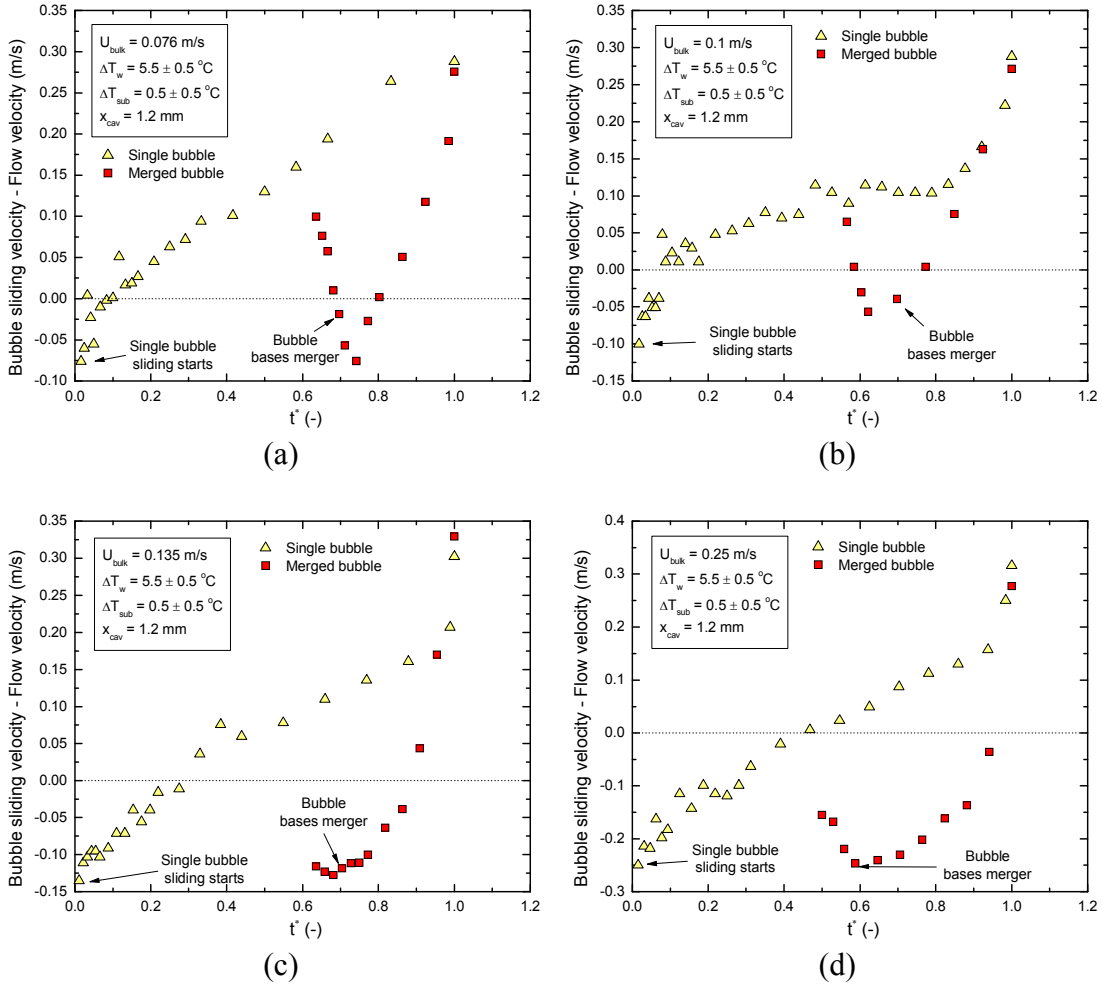

Figure 5.11 Comparison between single bubble and two-bubble lateral merger relative velocity data, for vertical silicon surface, 0.076 m/s ≤ U_{bulk} ≤ 0.25 m/s, ΔT_w = 5.5 ± 0.5 °C, ΔT_{sub} = 0.5 ± 0.5 °C, and x_{cav} = 1.2 mm.

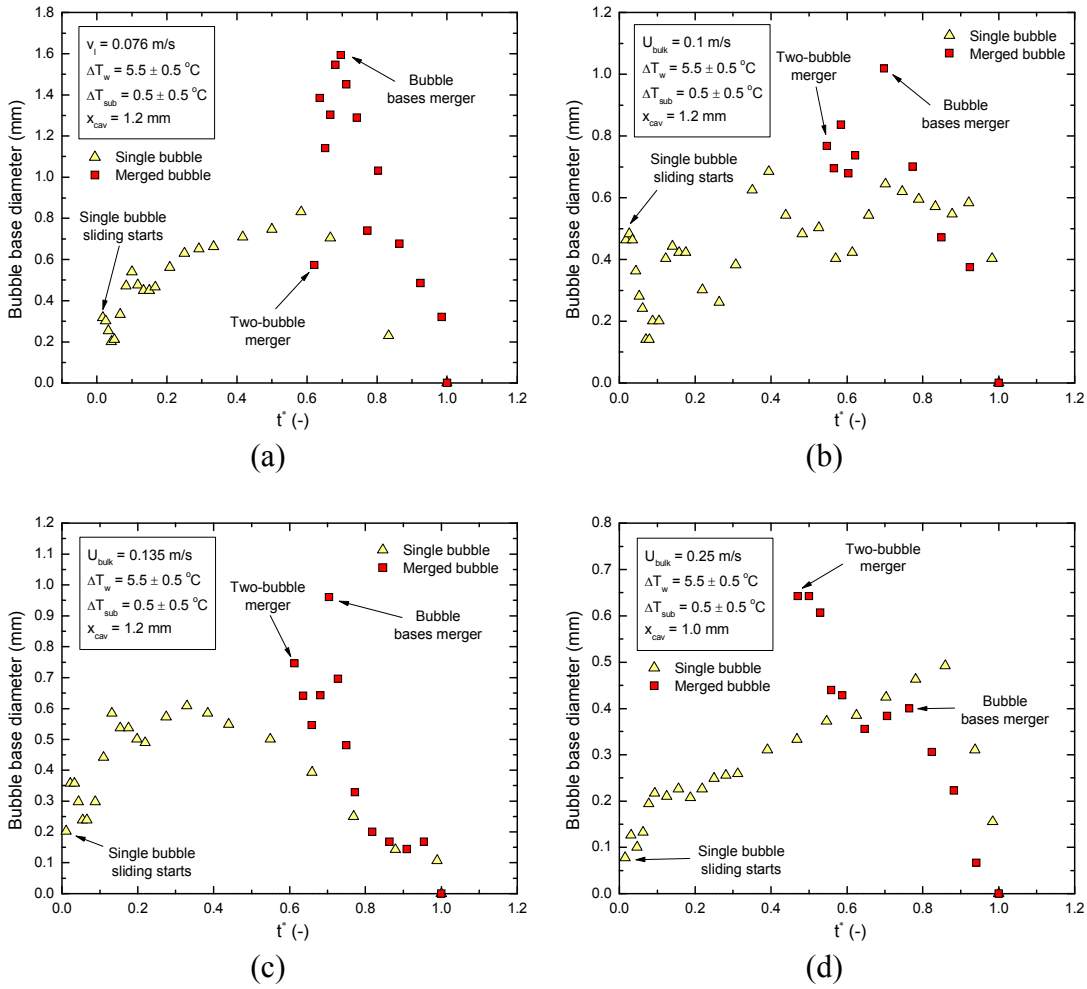

Figure 5.12 Comparison between single bubble and two-bubble lateral merger bubble base diameter, for vertical silicon surface, 0.076 m/s ≤ U_{bulk} ≤ 0.25 m/s, ΔT_w = 5.5 ± 0.5 °C, ΔT_{sub} = 0.5 ± 0.5 °C, and x_{cav} = 1.2 mm.

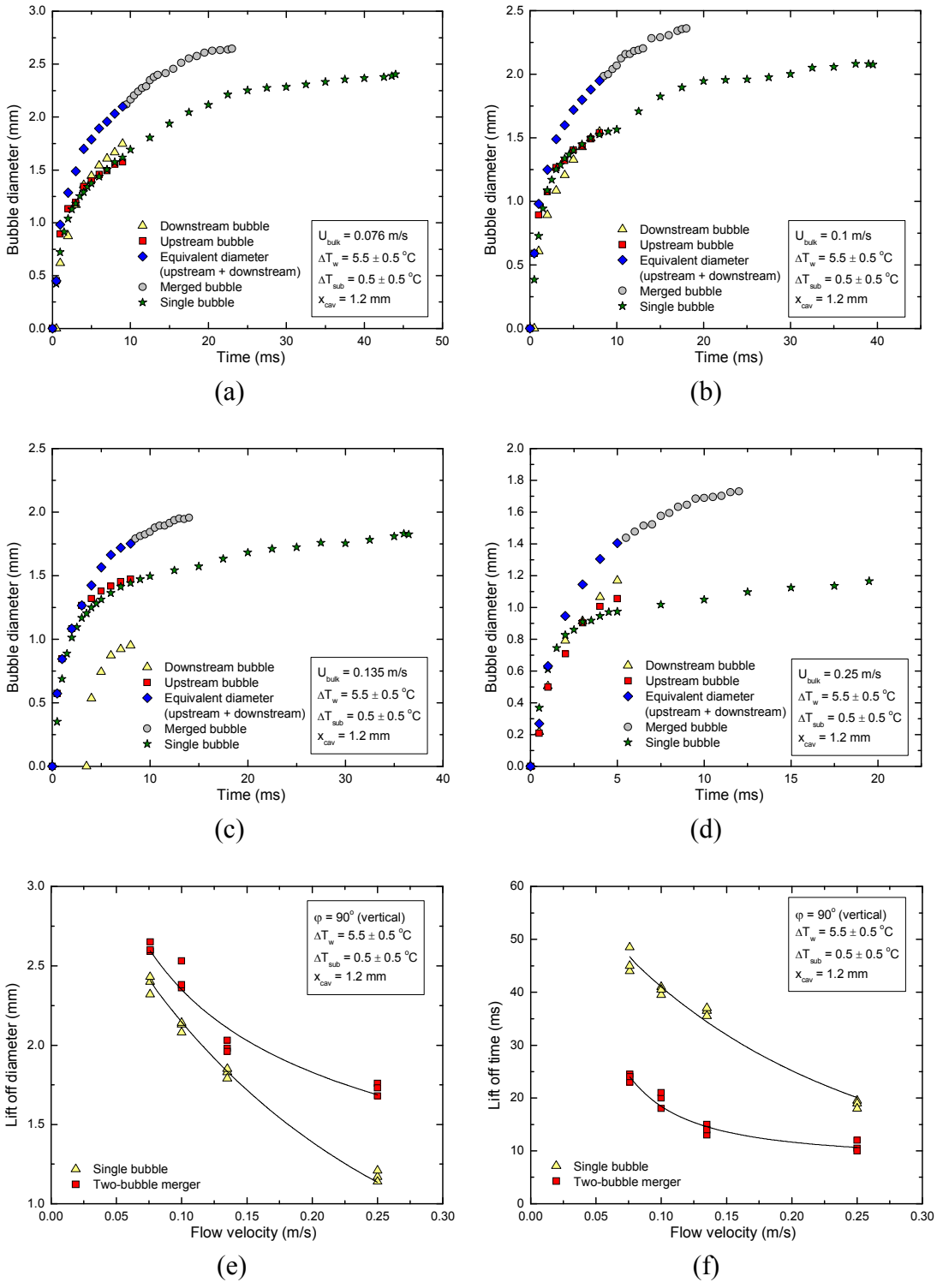

Figure 5.13 Comparison between single bubble and two-bubble lateral merger data for (a-d) growth rate, (e) lift off diameter, and (f) lift off time, for vertical aluminum surface, 0.076 m/s ≤ U_{bulk} ≤ 0.25 m/s, $\Delta T_w = 5.5 \pm 0.5\ ^oC$, $\Delta T_{sub} = 0.5 \pm 0.5\ ^oC$, and x_{cav} = 1.2 mm.

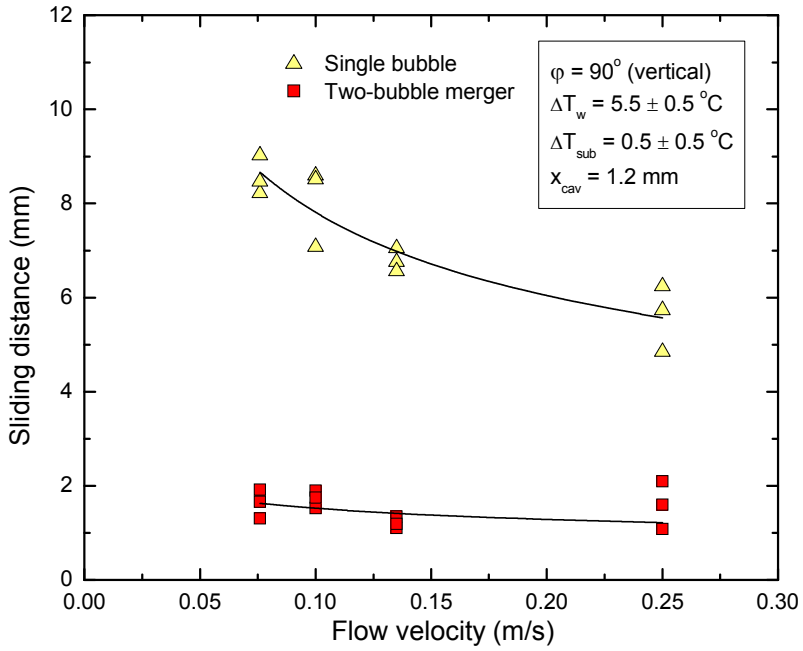

Figure 5.14 Comparison between single bubble and two-bubble lateral merger sliding distance data, for vertical aluminum surface, 0.076 m/s ≤ U_{bulk} ≤ 0.25 m/s, ΔT_w = 5.5 ± 0.5 °C, ΔT_{sub} = 0.5 ± 0.5 °C, and x_{cav} = 1.2 mm.

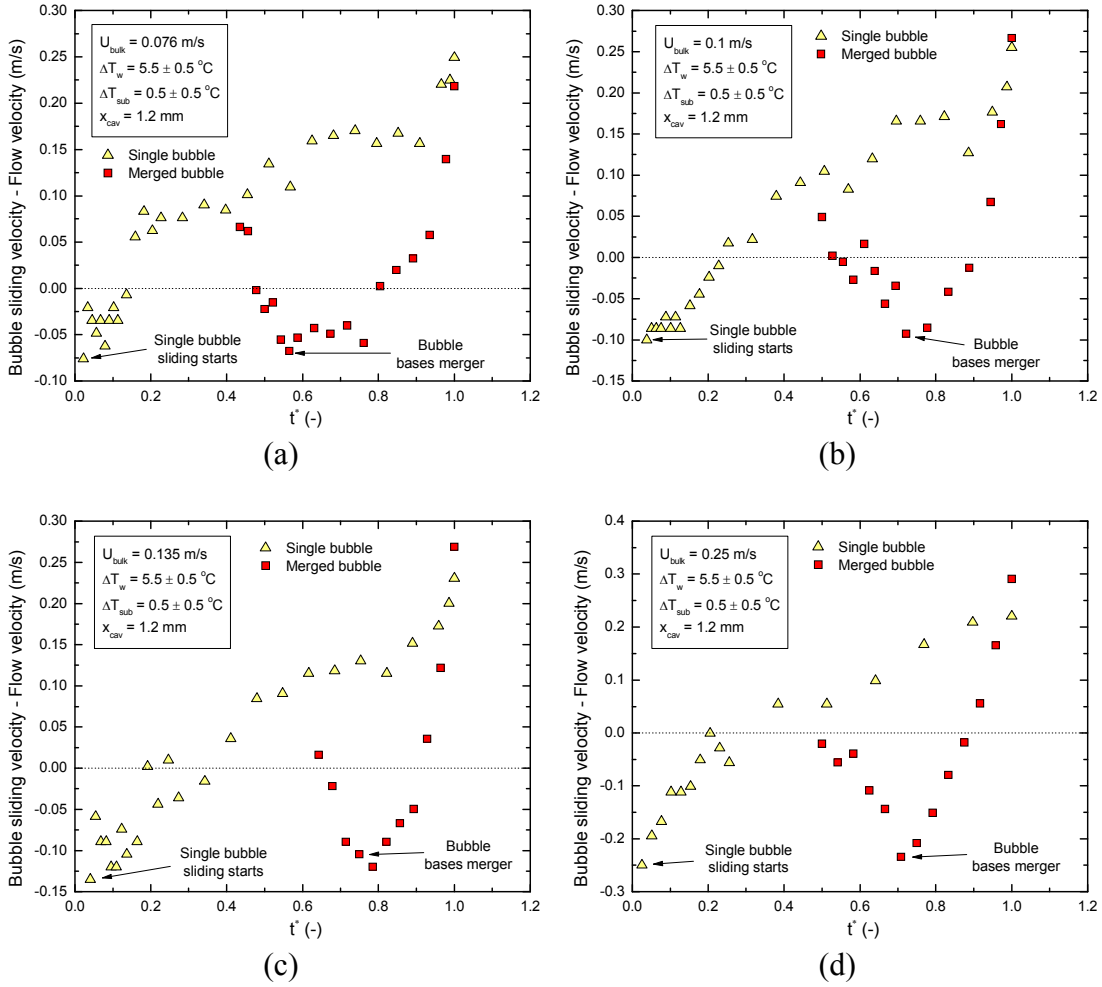

Figure 5.15 Comparison between single bubble and two-bubble lateral merger relative velocity data, for vertical aluminum surface, 0.076 m/s ≤ U_{bulk} ≤ 0.25 m/s, $\Delta T_w = 5.5 \pm 0.5\ ^oC$, $\Delta T_{sub} = 0.5 \pm 0.5\ ^oC$, and $x_{cav} = 1.2$ mm.

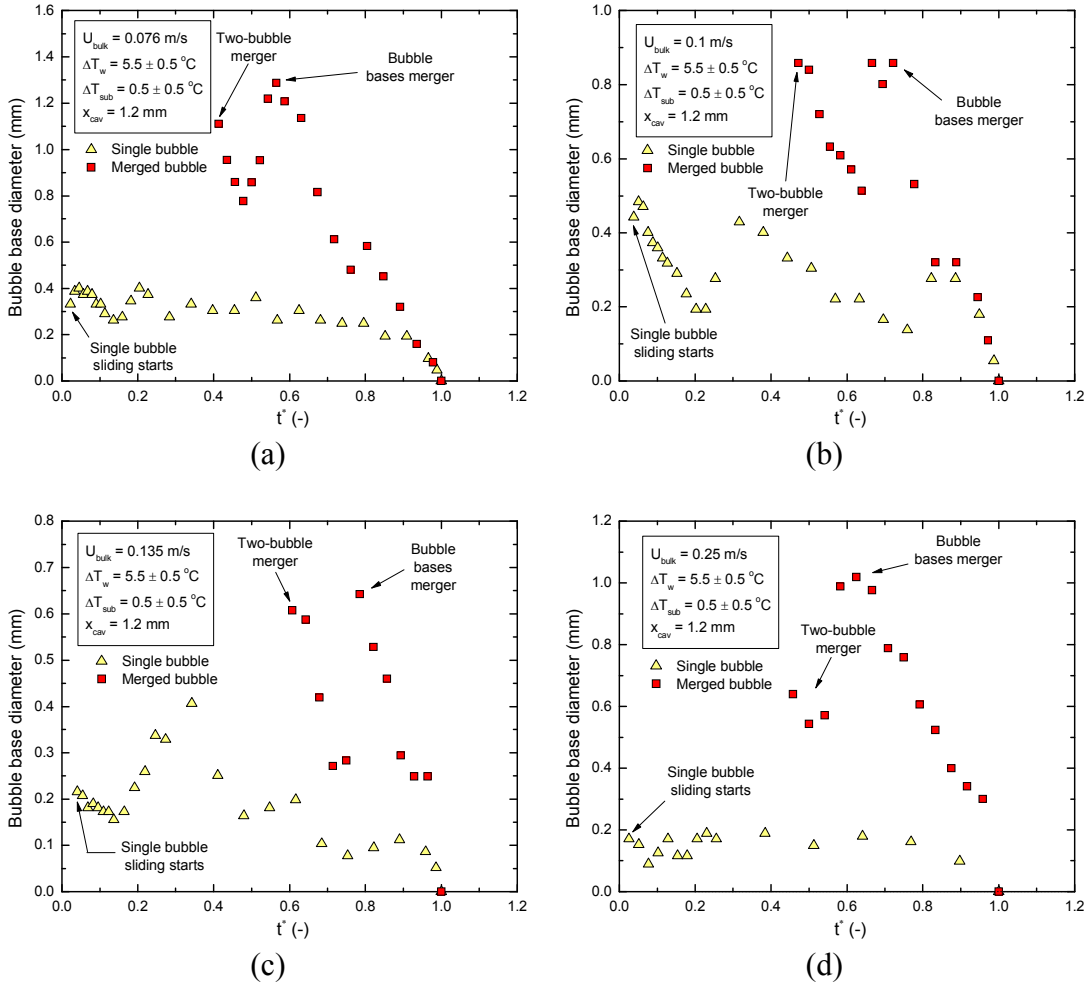

Figure 5.16 Comparison between single bubble and two-bubble lateral merger bubble base diameter, for vertical aluminum surface, 0.076 m/s ≤ U_{bulk} ≤ 0.25 m/s, $\Delta T_w = 5.5 \pm 0.5\ ^oC$, $\Delta T_{sub} = 0.5 \pm 0.5\ ^oC$, and $x_{cav} = 1.2$ mm.

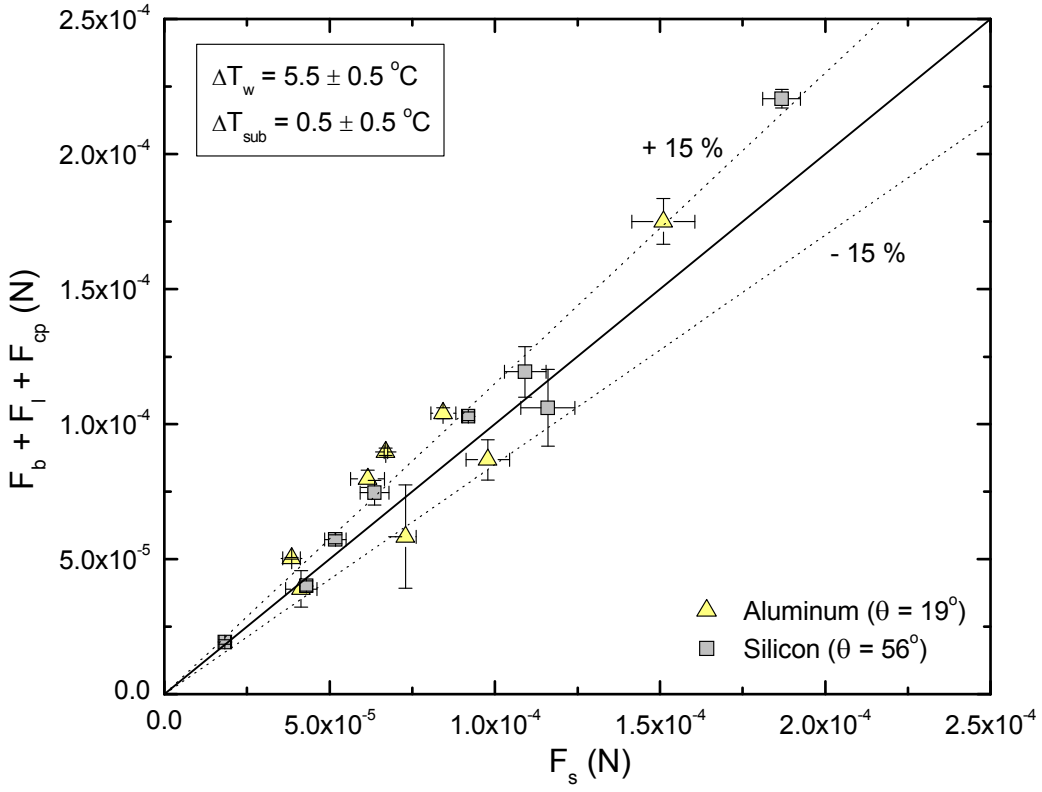

Figure 5.17 Comparison between detaching and attaching forces actual on a merged bubble, when bubble base diameter is maximum, for horizontal and vertical surfaces – Aluminum and silicon surfaces.

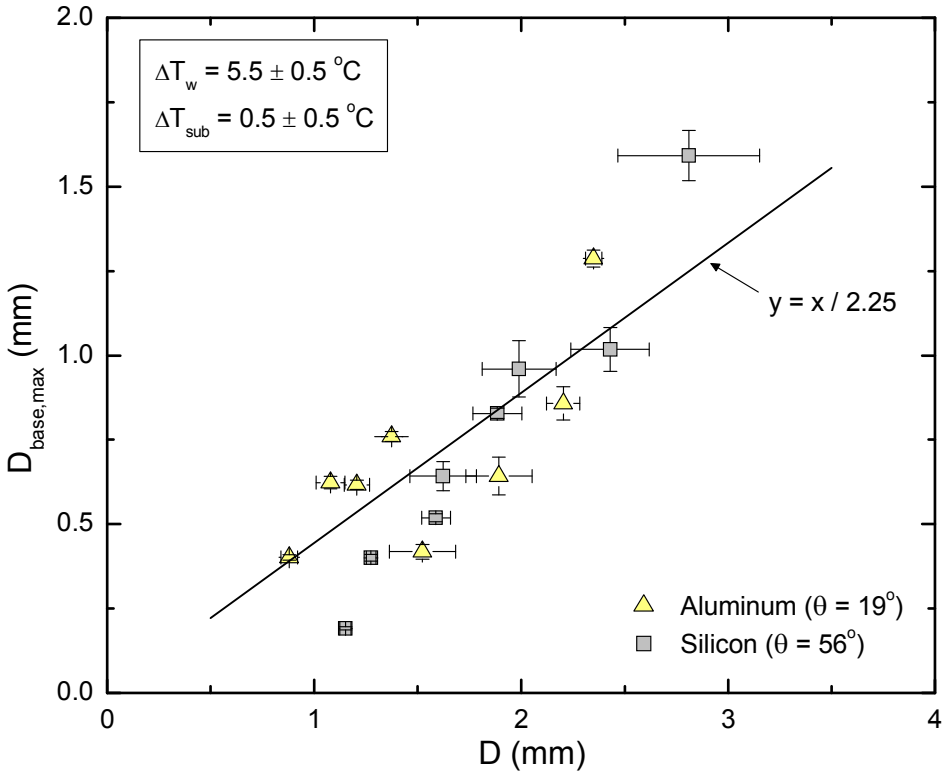

Figure 5.18 Maximum merged bubble base diameter as a function of merged bubble diameter, for horizontal and vertical surfaces – Aluminum and silicon surfaces.

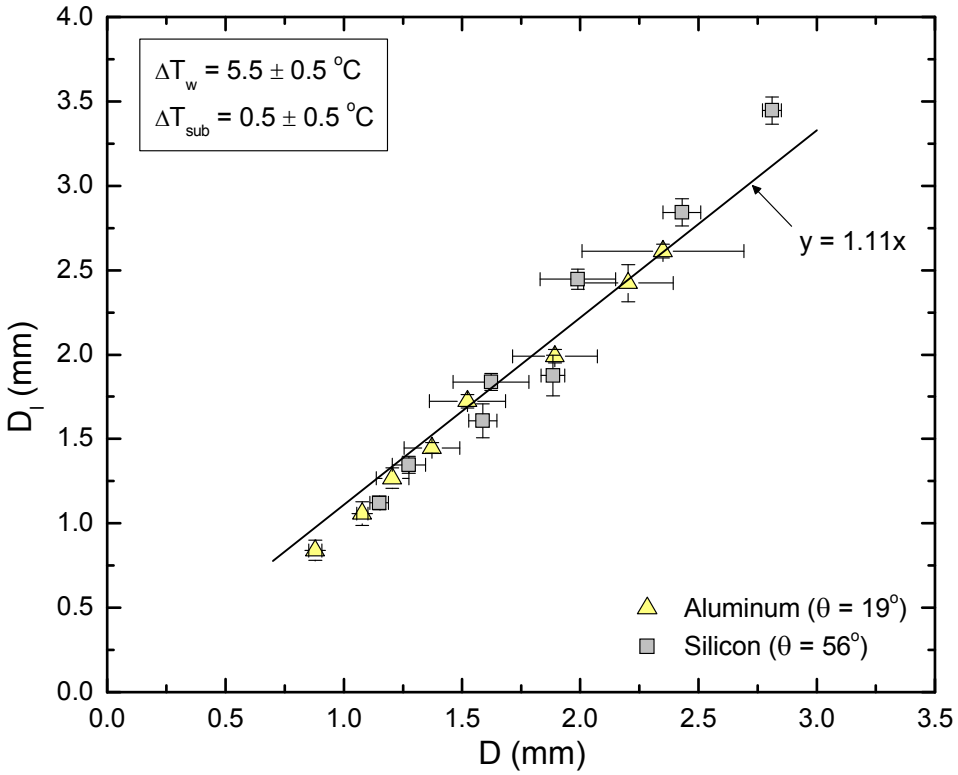

Figure 5.19 Merged bubble lift off diameter as a function of merged bubble diameter at $D_{base} = D_{base,max}$ diameter, for horizontal and vertical surfaces – Aluminum and silicon surfaces.

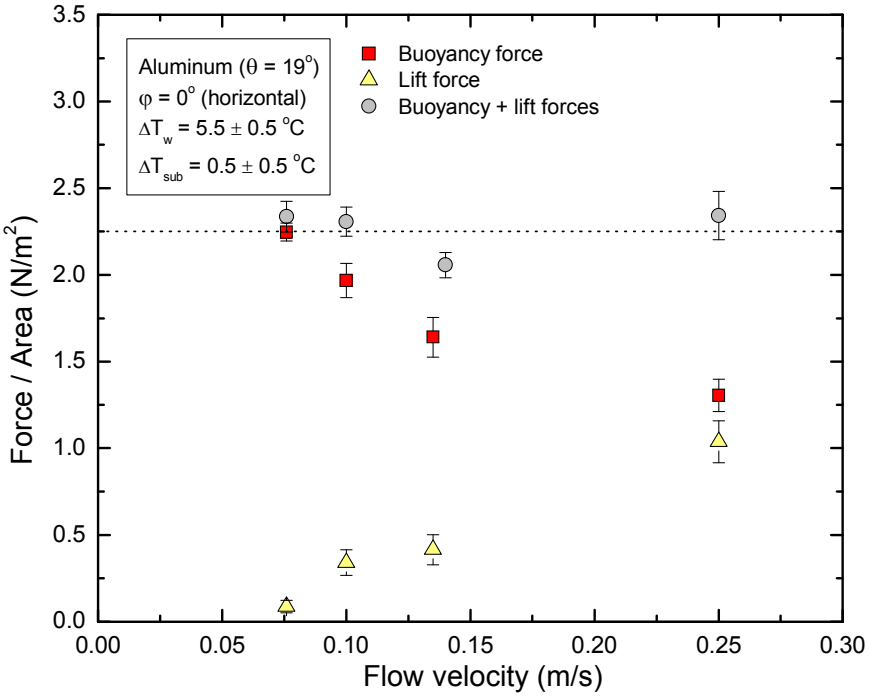

(a)

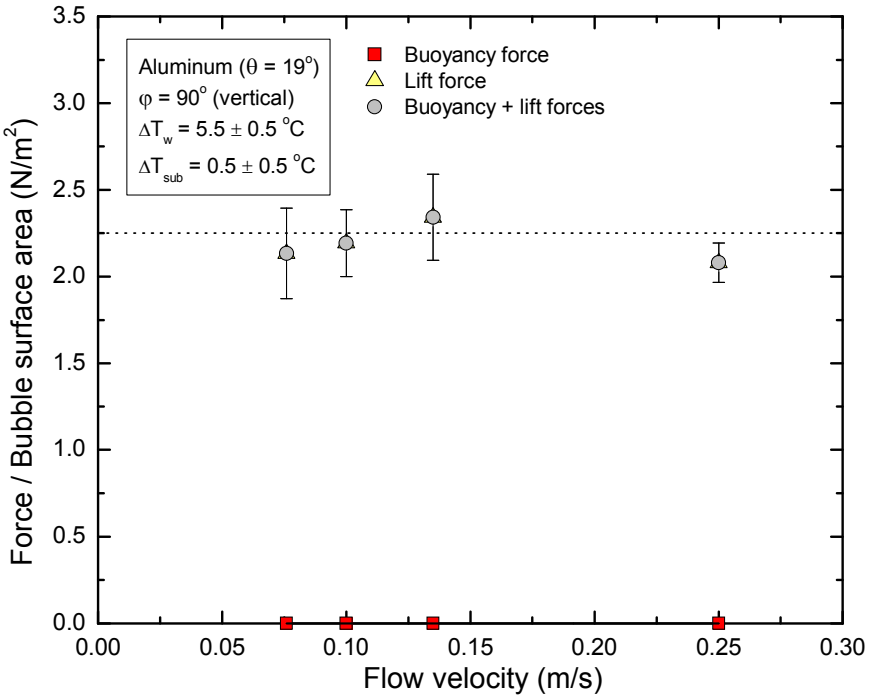

(b)

Figure 5.20 Forces acting on a merged bubble at lift off as a function of flow velocity, for (a) horizontal surface, and (b) vertical surface – Aluminum surface.

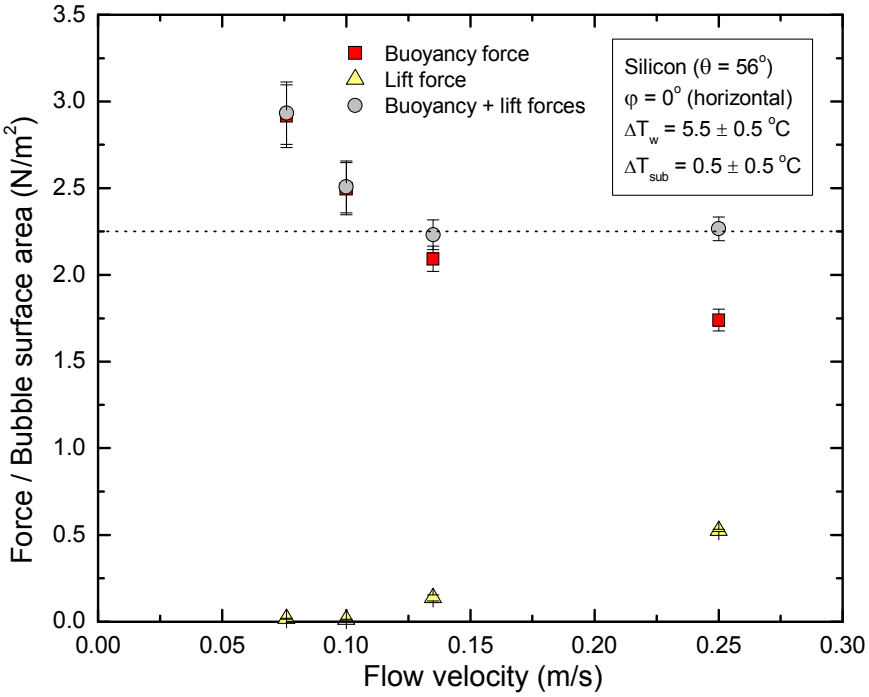

(a)

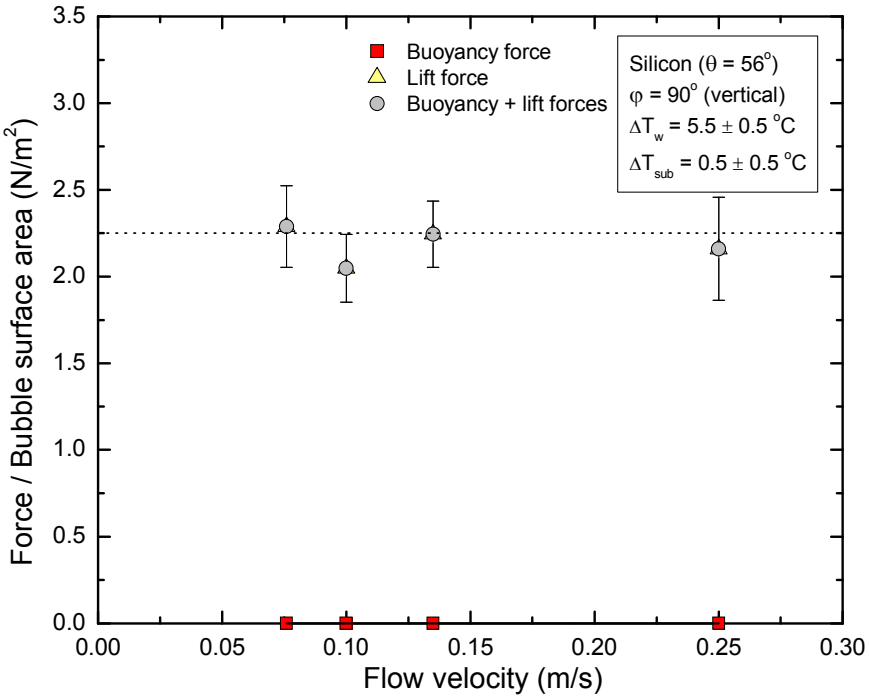

(b)

Figure 5.21 Forces acting on a merged bubble at lift off as a function of flow velocity, for (a) horizontal surface, and (b) vertical surface – Silicon surface.

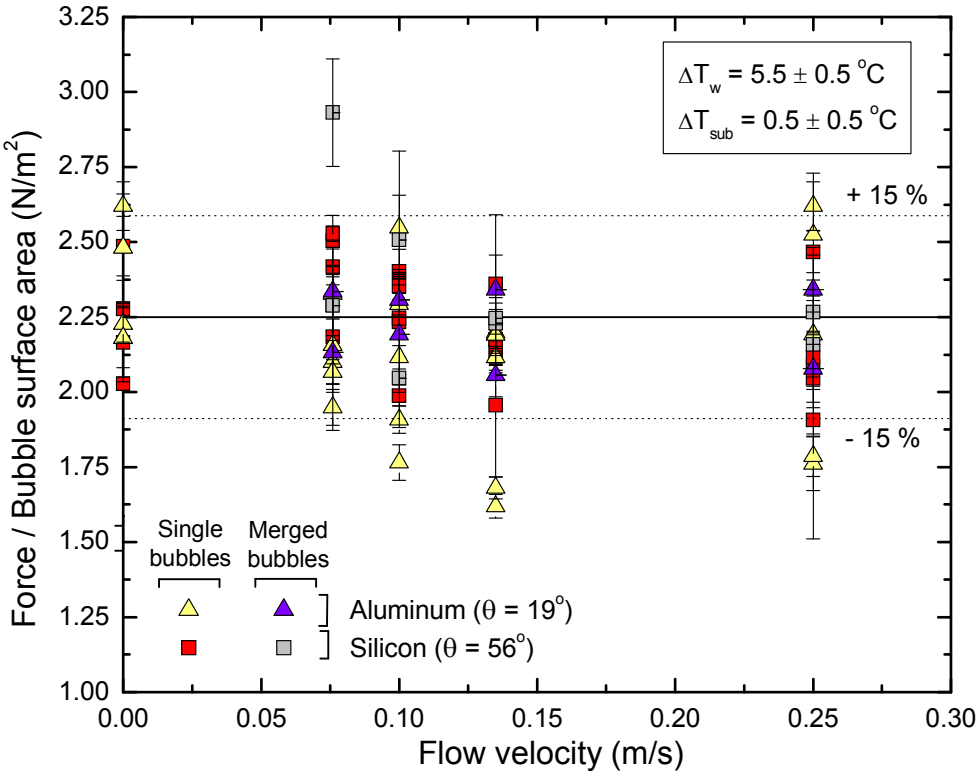

Figure 5.22 Sum of buoyancy and lift forces divided by bubble surface area, as a function of flow velocity, for all orientations, flow velocities and surface materials – Single and merged bubbles.

Chapter 6
Conclusions

The dynamics of a single bubble and two-bubble lateral inline merger under different levels of bulk liquid velocity, surface orientation, contact angle, surface material and cavity spacing were studied in this work. A simple force balance model was developed to predict single bubble lift off diameter. Comparison between single bubble and two-bubble merger were conducted, and the effects of bubble coalescence on bubble dynamics were analyzed. The key conclusions of this study are:

Bubble dynamics

- For single and merged bubbles, irrespective of orientation and contact angle, lift off diameter decreases with increase in bulk liquid velocity. Decrease in contact angle leads to decrease in lift off diameter.
- For single and merged bubbles, and given conditions, bubble lift off diameter increases when the gravity component normal to the heater is decreased. The effect gravity on lift off diameter is reduced at high liquid bulk velocities.
- For given conditions, bubble lift off diameter for merged bubbles is larger than for single bubbles, due to an increase in bubble base diameter for merged bubbles. Larger lift and buoyancy forces are required to compensate for greater surface tension attaching the bubble to the surface, which leads to larger lift off diameter.

- For single and merged bubbles, bubble sliding distance increases with decrease in the magnitude of the component of gravity normal to the heater. For given conditions, sliding distance decreases with decrease in contact angle.

Bubble force balance and lift off diameter modeling

- The validity of a simple force balance model to predict bubble lift off was demonstrated. These forces are the lift force (F_l), the buoyancy force (F_b), the surface tension force (F_s), the contact pressure force (F_{cp}), and the inertia of both the vapor and the liquid displaced by the growing bubble.
- For horizontal heater, regardless of flow velocity, the contribution of lift force to bubble lift off is minimal. Buoyancy and contact pressure forces are the forces driving lift off.
- For vertical heater, lift and contact pressure forces are dominant. Buoyancy does not affect directly bubble lift off, since it only acts parallel to the heater wall. It does affect lift off through sliding velocity, since buoyancy allows for the bubble velocity to increase far beyond that of the flow, creating lift.
- In microgravity conditions, the bubble sliding velocity may never become larger than flow velocity, due to the negligible contribution of buoyancy. Therefore the velocity gradient would be very small and the viscous sheer stress should be the dominating factor in the lift force required for the bubble to lift off.
- Bubble lift off is initiated at the instant when the sum of these forces becomes positive in the y-direction (normal to the heater). It coincides with the moment when the bubble base starts to shrink. It is found that at this instant, $D_{base} = D / 3$

for single bubbles and D_{base} = D / 2.25. These relationships are valid for two contact angles (19^o and 56^o), $0^o \leq \varphi \leq 90^o$, and 0 m/s $\leq U_{bulk} \leq$ 0.25 m/s.

- Based on this force balance an expression for bubble diameter is developed. From this expression, one can determine the bubble lift off diameter, using the following relationship: for single bubbles, D_l = 1.25 x D (at $D_{base} = D_{base,max}$), and for merged bubbles, D_l = 1.11 x D (at $D_{base} = D_{base,max}$). These relationships are valid for two contact angles (19^o and 56^o), $0^o \leq \varphi \leq 90^o$, and 0 m/s $\leq U_{bulk} \leq$ 0.25 m/s.
- When lift off occurs, buoyancy and lift forces are the only forces acting on the bubble, and regardless of orientation, contact angle and flow velocity, the ratio $(F_b + F_l) / A_l = 2.25$ N/m^2, where A_l is the bubble surface area at lift off. Based on this result, a simple bubble lift off diameter expression, applicable for two contact angles (19^o and 56^o), $0^o \leq \varphi \leq 90^o$, and 0 m/s $\leq U_{bulk} \leq$ 0.25 m/s, was developed.

APPENDIX A
SINGLE BUBBLE EXPERIMENTAL RESULTS – SILICON SURFACE

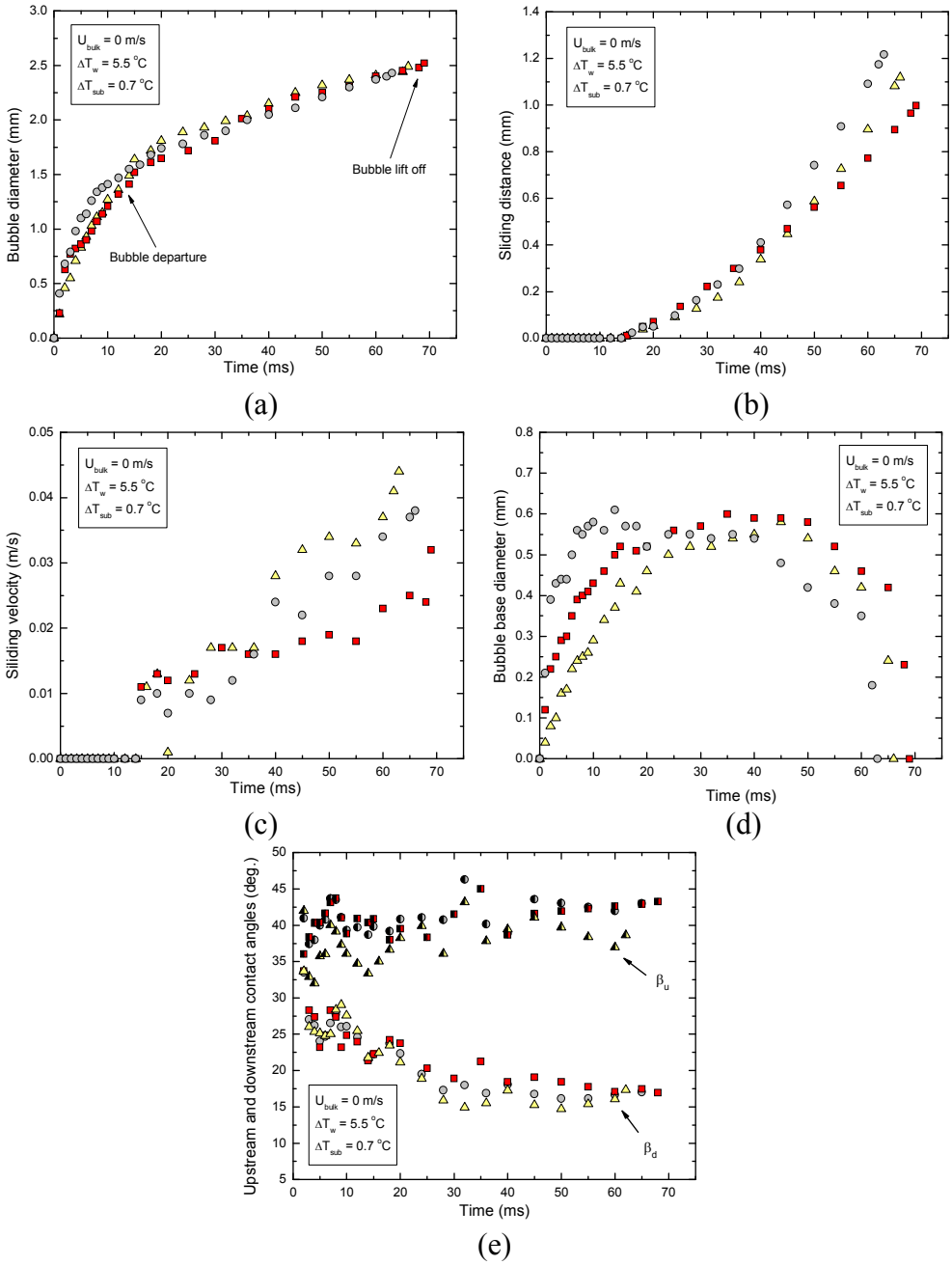

Measured quantities for 30^{o} inclined silicon surface: (a) bubble diameter, (b) sliding distance, (c) sliding velocity, (d) bubble base diameter and (e) upstream and downstream contact angles, for U_{bulk} = 0 m/s, ΔT_w = 5.5 ^{o}C, and ΔT_{sub} = 0.7 ^{o}C.

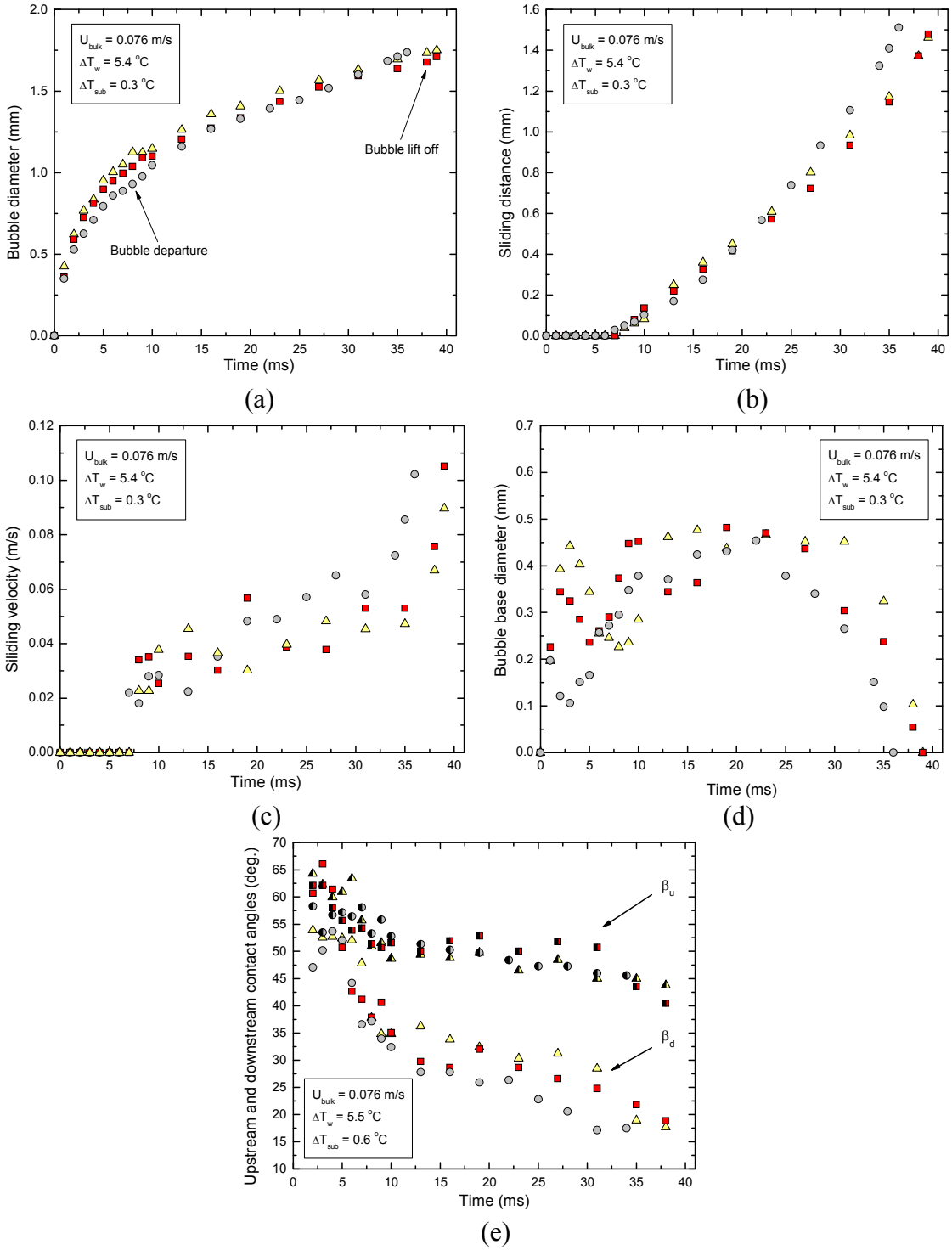

Measured quantities for 30^{o} inclined silicon surface: (a) bubble diameter, (b) sliding distance, (c) sliding velocity, (d) bubble base diameter and (e) upstream and downstream contact angles, for U_{bulk} = 0.076 m/s, ΔT_w = 5.4 ^{o}C, and ΔT_{sub} = 0.3 ^{o}C.

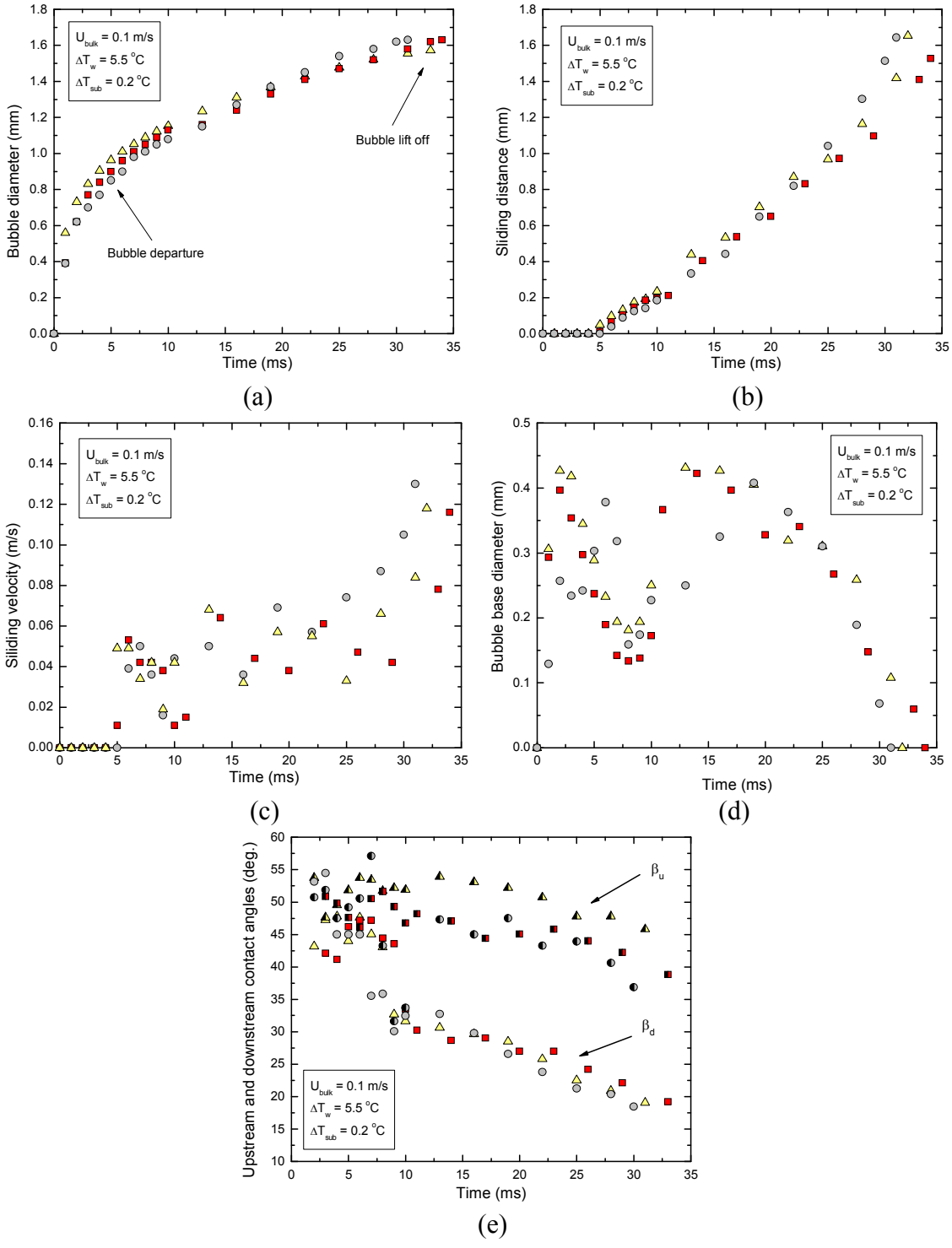

Measured quantities for 30^{o} inclined silicon surface: (a) bubble diameter, (b) sliding distance, (c) sliding velocity, (d) bubble base diameter and (e) upstream and downstream contact angles, for U_{bulk} = 0.1 m/s, ΔT_w = 5.5 ^{o}C, and ΔT_{sub} = 0.2 ^{o}C.

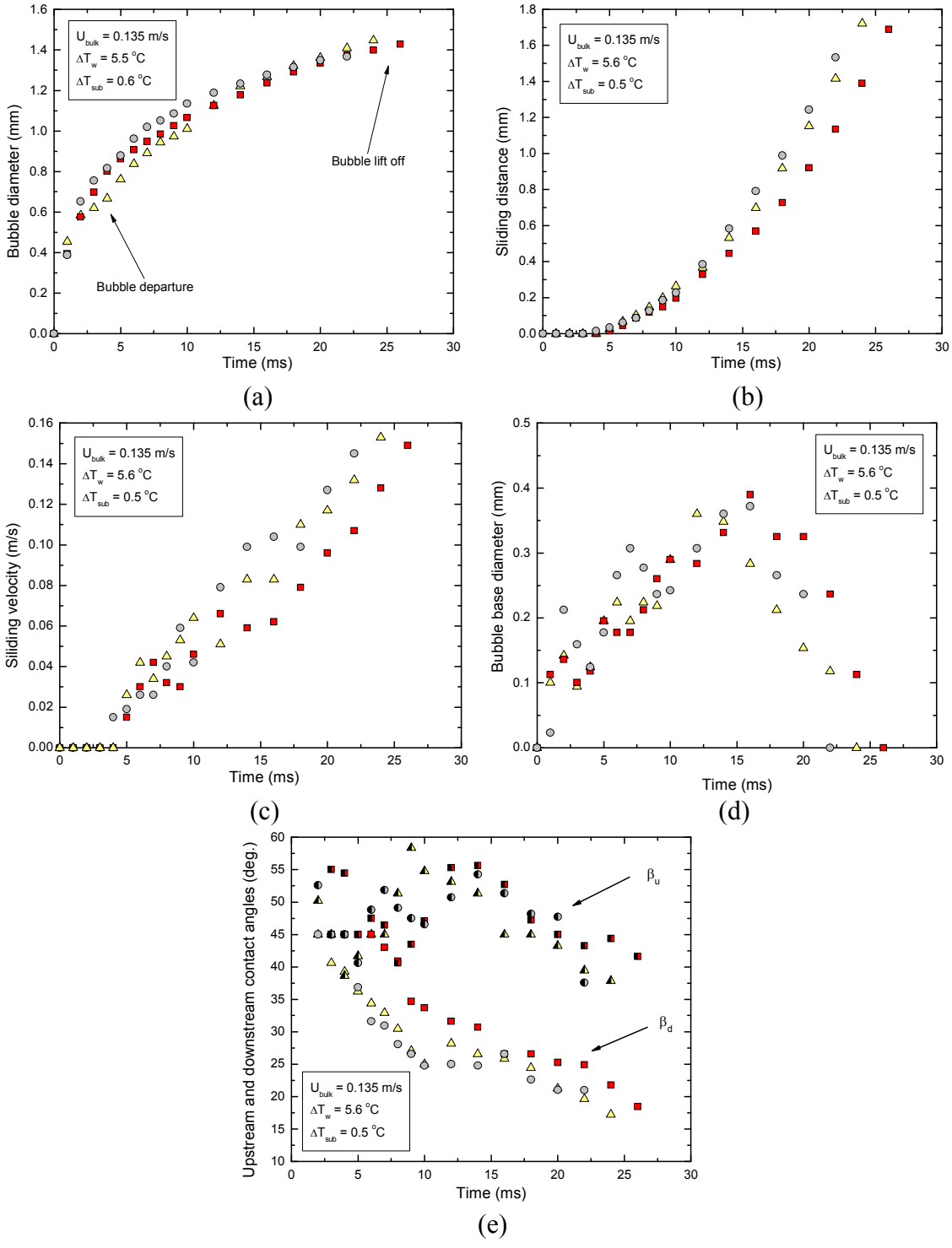

Measured quantities for 30^{o} inclined silicon surface: (a) bubble diameter, (b) sliding distance, (c) sliding velocity, (d) bubble base diameter and (e) upstream and downstream contact angles, for U_{bulk} = 0.135 m/s, ΔT_w = 5.6 ^{o}C, and ΔT_{sub} = 0.5 ^{o}C.

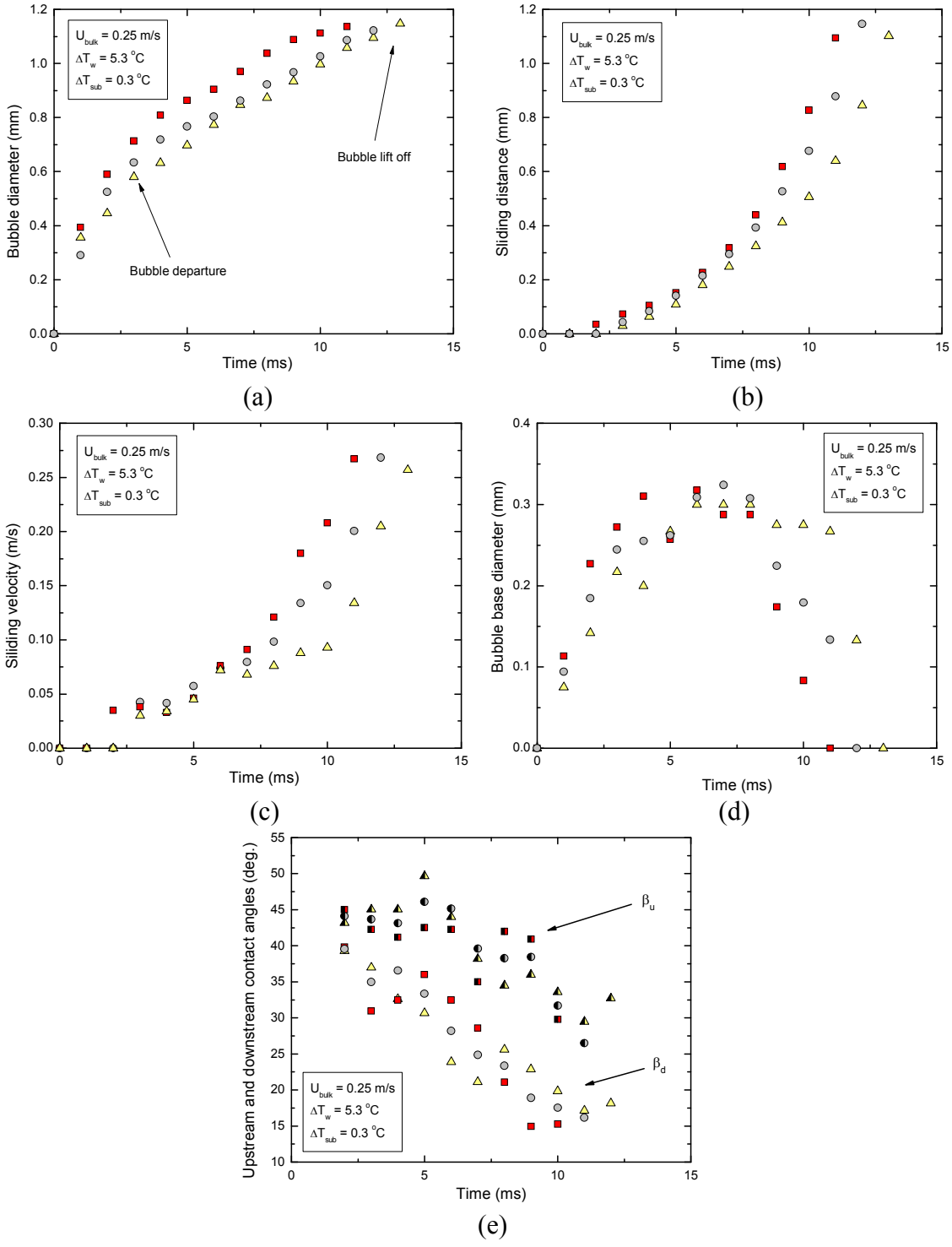

Measured quantities for 30^o inclined silicon surface: (a) bubble diameter, (b) sliding distance, (c) sliding velocity, (d) bubble base diameter and (e) upstream and downstream contact angles, for U_{bulk} = 0.25 m/s, ΔT_w = 5.3 ^{o}C, and ΔT_{sub} = 0.3 ^{o}C.

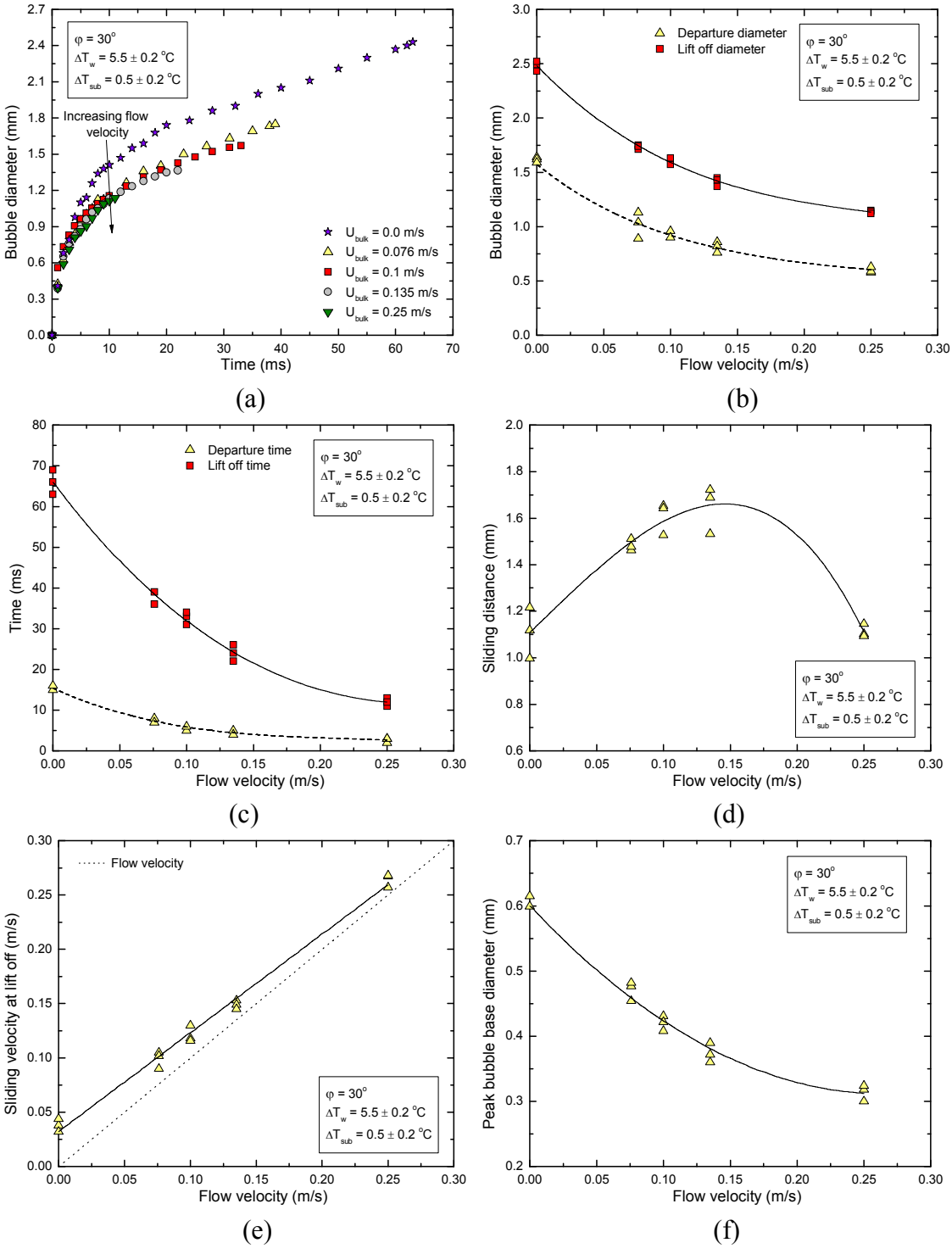

Effect of liquid bulk velocity on (a) variation of bubble diameter with time, (b) bubble departure and lift off diameters, (c) departure and lift off times, (d) sliding distance, (e) sliding velocity at lift off and (f) peak bubble base diameter – 30° inclined silicon surface.

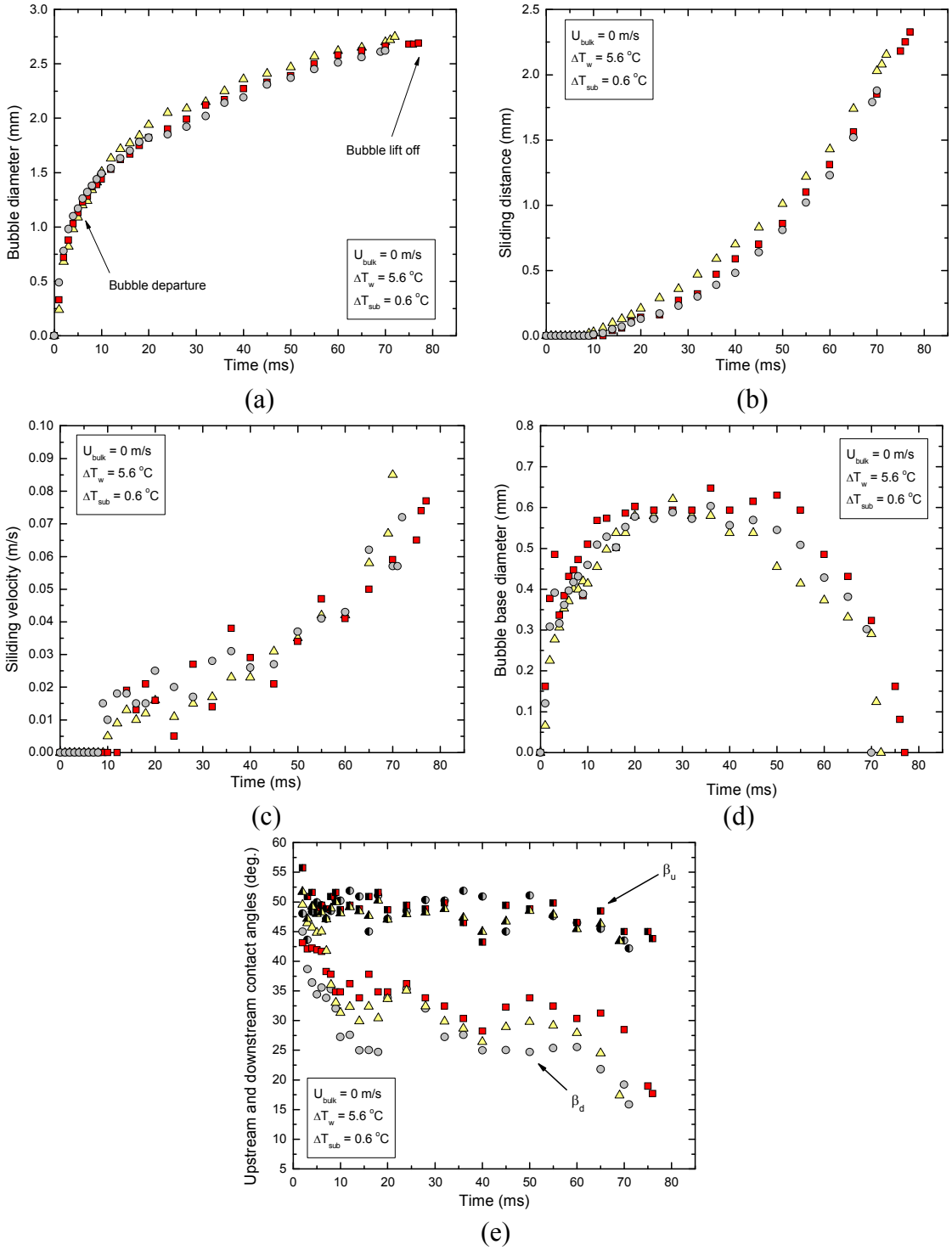

Measured quantities for 45^o inclined silicon surface: (a) bubble diameter, (b) sliding distance, (c) sliding velocity, (d) bubble base diameter and (e) upstream and downstream contact angles, for U_{bulk} = 0 m/s, ΔT_w = 5.6 ^{o}C, and ΔT_{sub} = 0.6 ^{o}C.

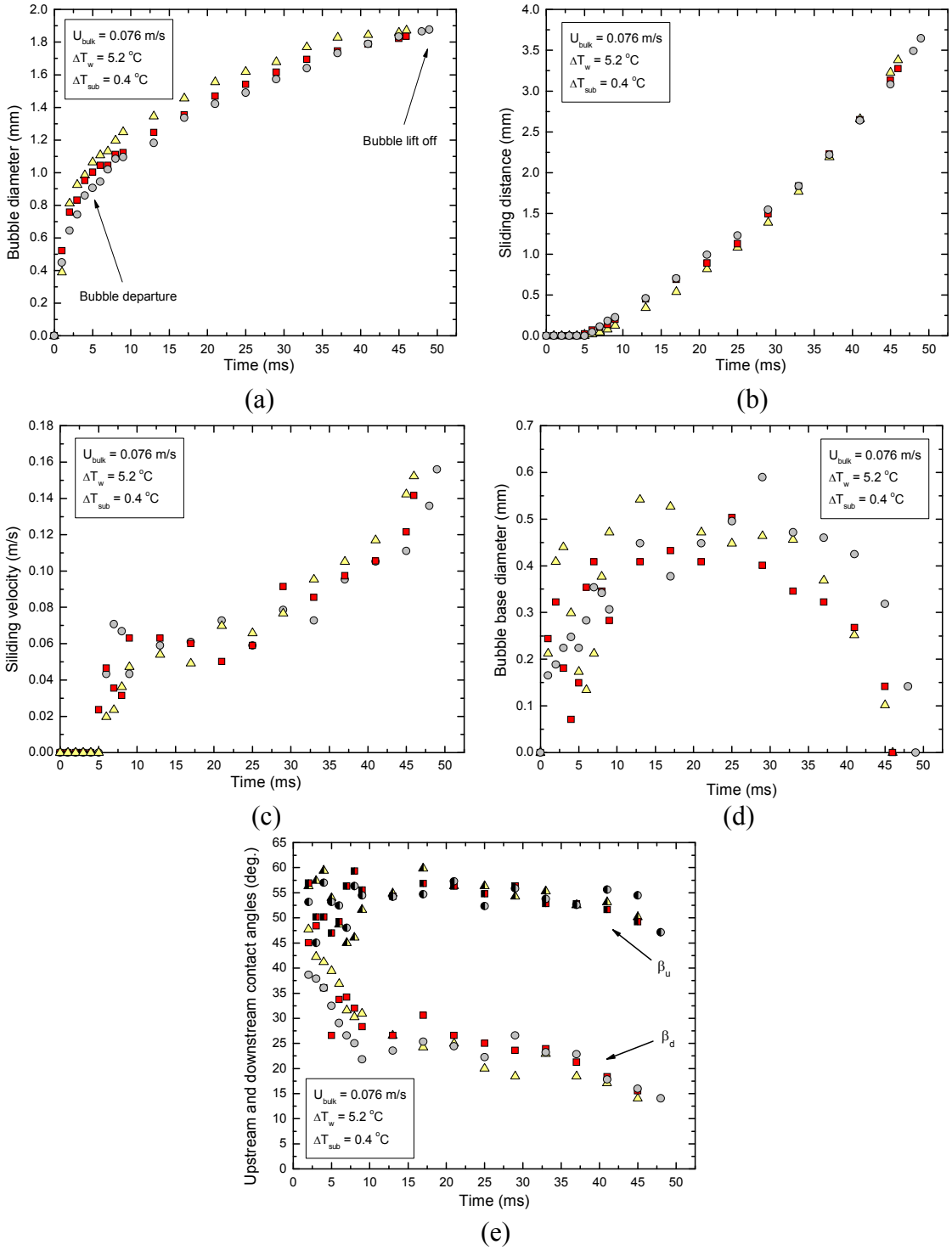

Measured quantities for 45° inclined silicon surface: (a) bubble diameter, (b) sliding distance, (c) sliding velocity, (d) bubble base diameter and (e) upstream and downstream contact angles, for U_{bulk} = 0.076 m/s, ΔT_w = 5.2 °C, and ΔT_{sub} = 0.4 °C.

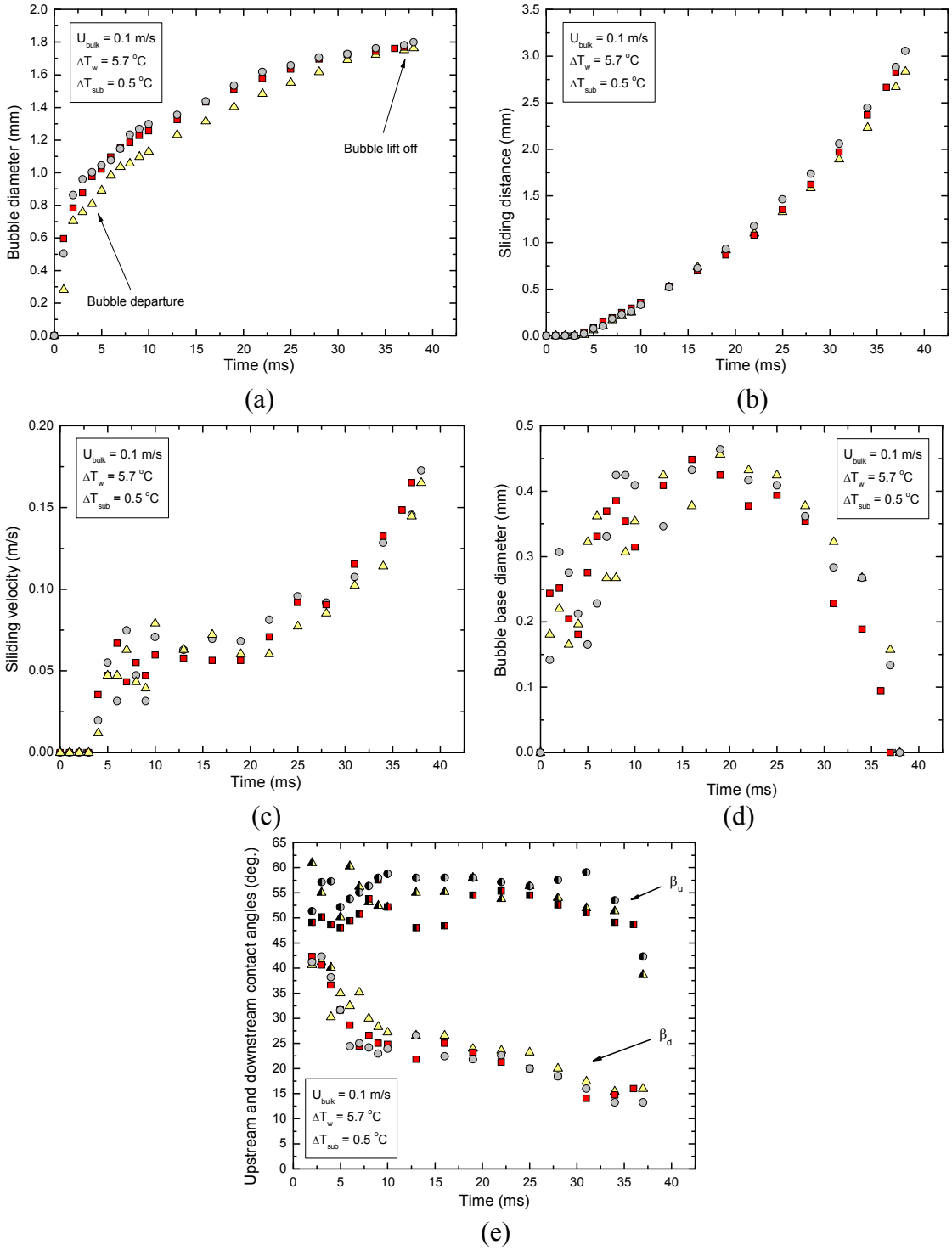

Measured quantities for 45^o inclined silicon surface: (a) bubble diameter, (b) sliding distance, (c) sliding velocity, (d) bubble base diameter and (e) upstream and downstream contact angles, for U_{bulk} = 0.1 m/s, ΔT_w = 5.7 ^{o}C, and ΔT_{sub} = 0.5 ^{o}C.

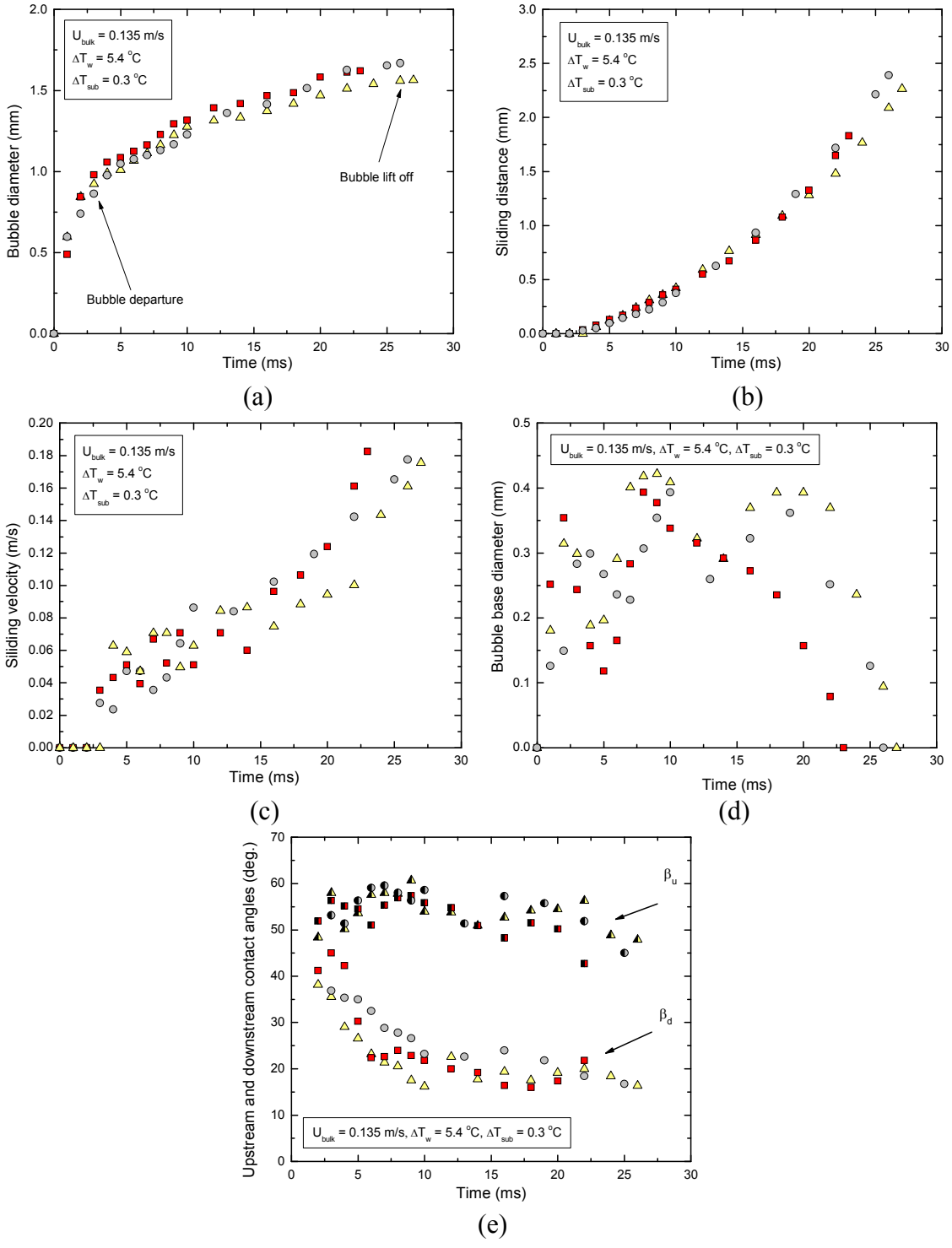

Measured quantities for 45° inclined silicon surface: (a) bubble diameter, (b) sliding distance, (c) sliding velocity, (d) bubble base diameter and (e) upstream and downstream contact angles, for U_{bulk} = 0.135 m/s, ΔT_w = 5.4 °C, and ΔT_{sub} = 0.3 °C.

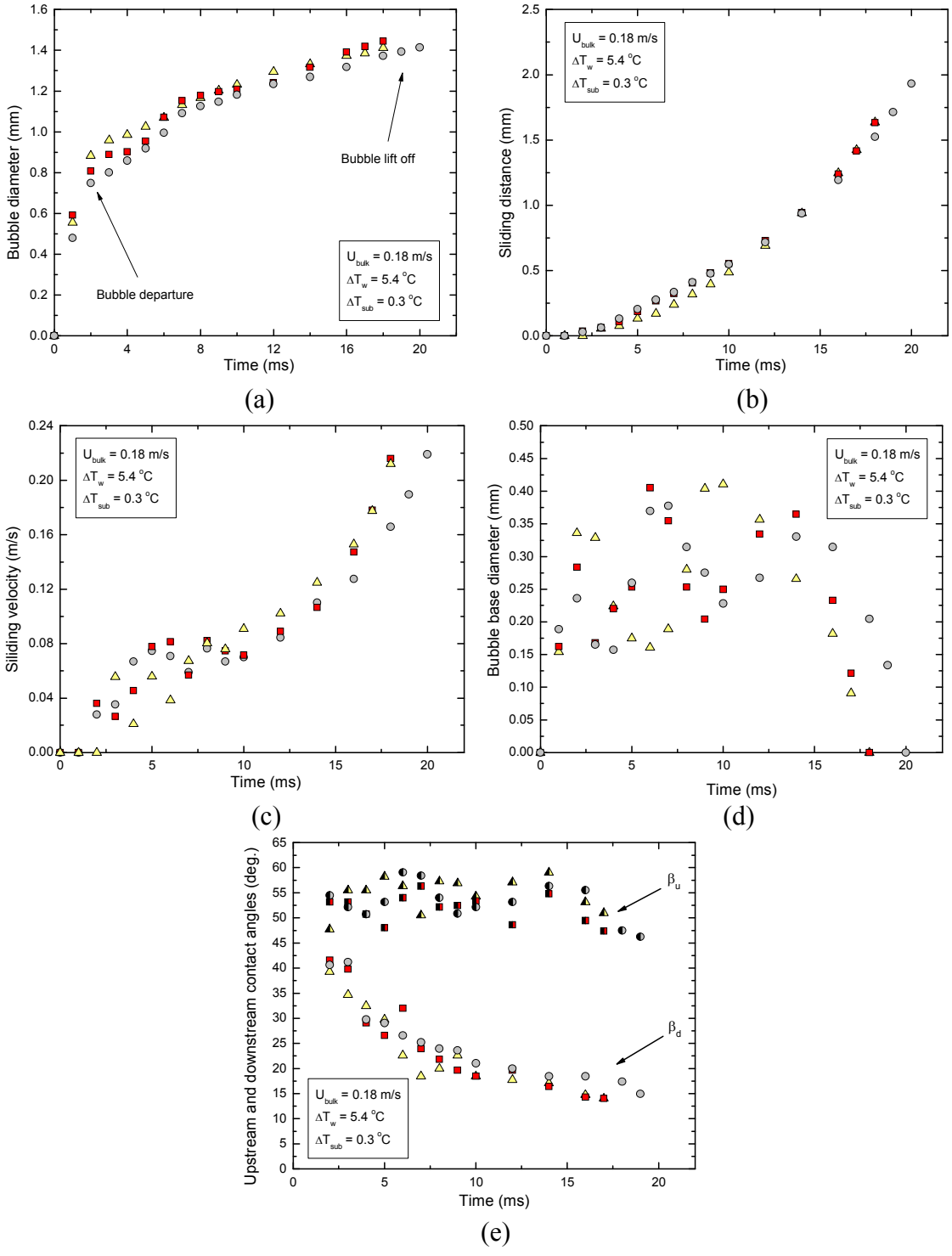

Measured quantities for 45^{o} inclined silicon surface: (a) bubble diameter, (b) sliding distance, (c) sliding velocity, (d) bubble base diameter and (e) upstream and downstream contact angles, for U_{bulk} = 0.18 m/s, ΔT_w = 5.4 ^{o}C, and ΔT_{sub} = 0.3 ^{o}C.

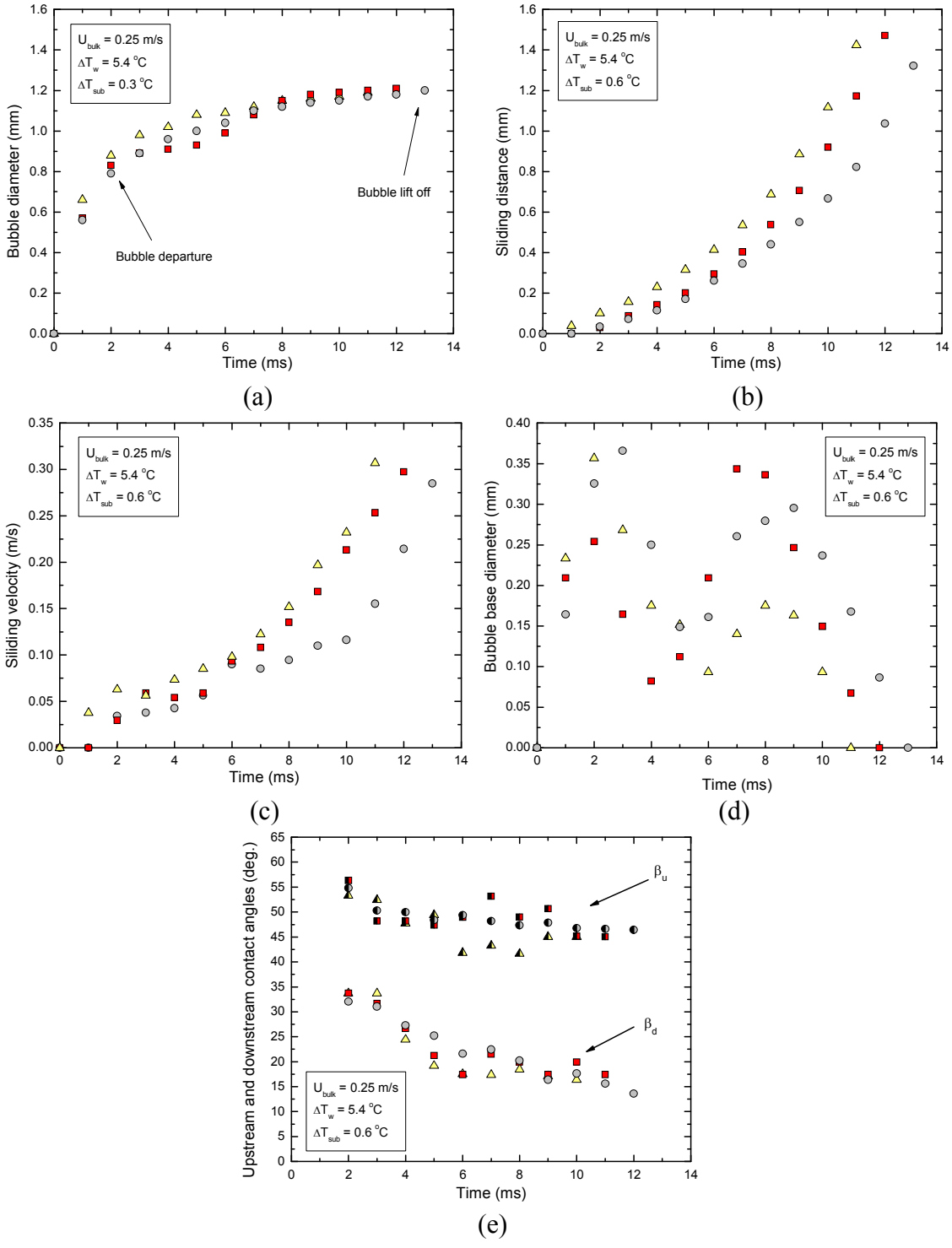

Measured quantities for 45^{o} inclined silicon surface: (a) bubble diameter, (b) sliding distance, (c) sliding velocity, (d) bubble base diameter and (e) upstream and downstream contact angles, for U_{bulk} = 0.25 m/s, ΔT_w = 5.4 ^{o}C, and ΔT_{sub} = 0.6 ^{o}C.

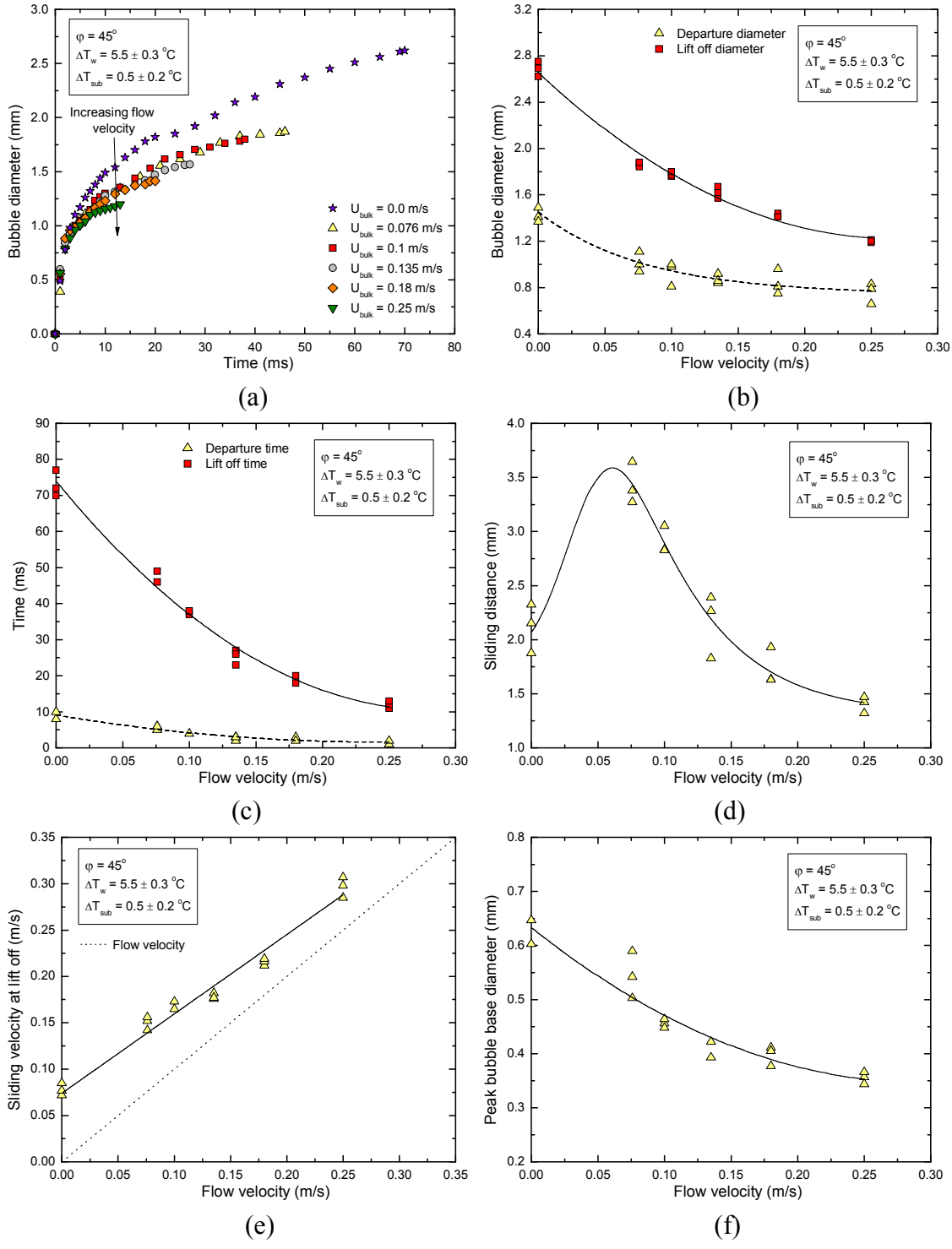

Effect of liquid bulk velocity on (a) variation of bubble diameter with time, (b) bubble departure and lift off diameters, (c) departure and lift off times, (d) sliding distance, (e) sliding velocity at lift off and (f) peak bubble base diameter – 45^{o} inclined silicon surface.

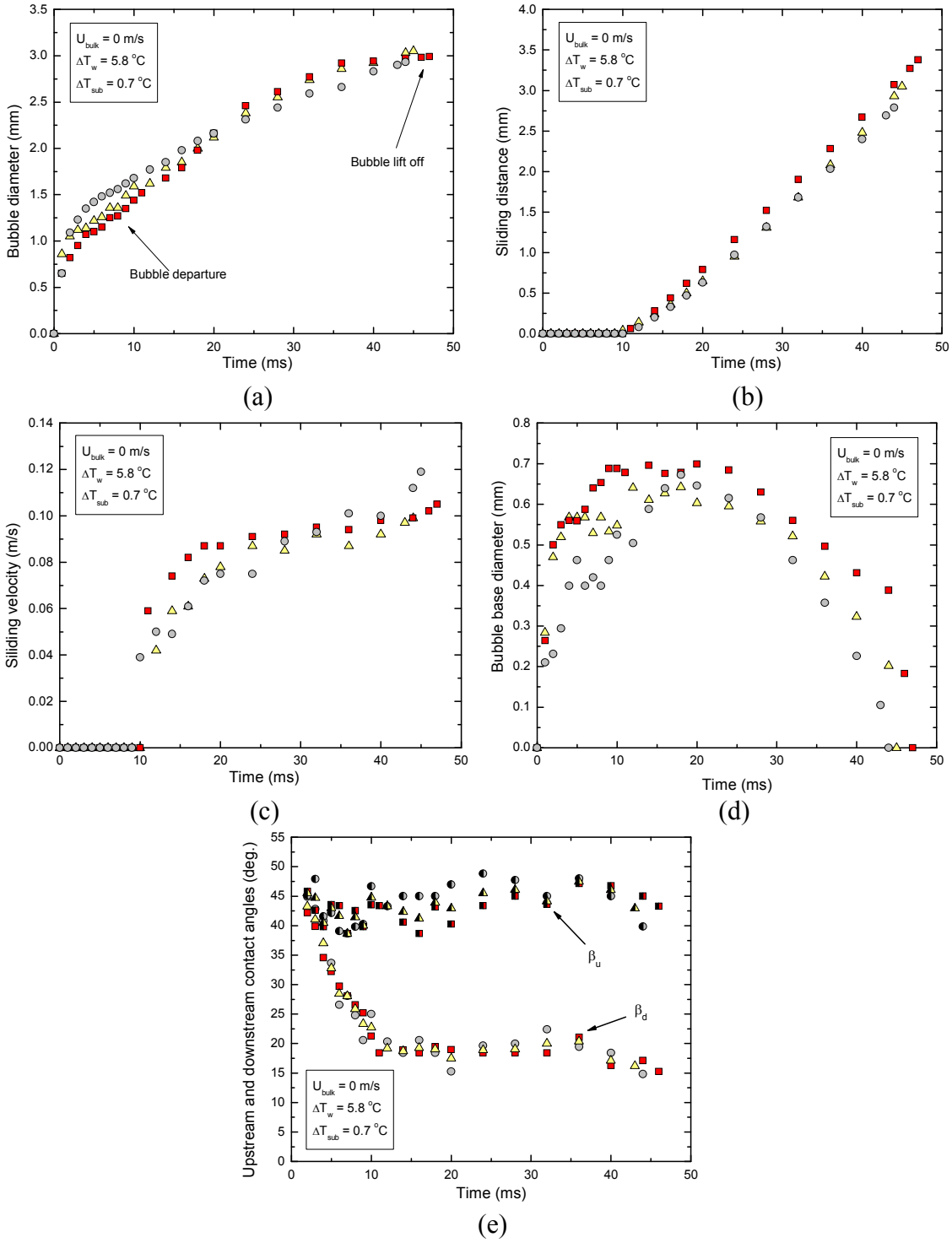

Measured quantities for 60^o inclined silicon surface: (a) bubble diameter, (b) sliding distance, (c) sliding velocity, (d) bubble base diameter and (e) upstream and downstream contact angles, for U_{bulk} = 0 m/s, ΔT_w = 5.8 ^{o}C, and ΔT_{sub} = 0.7 ^{o}C.

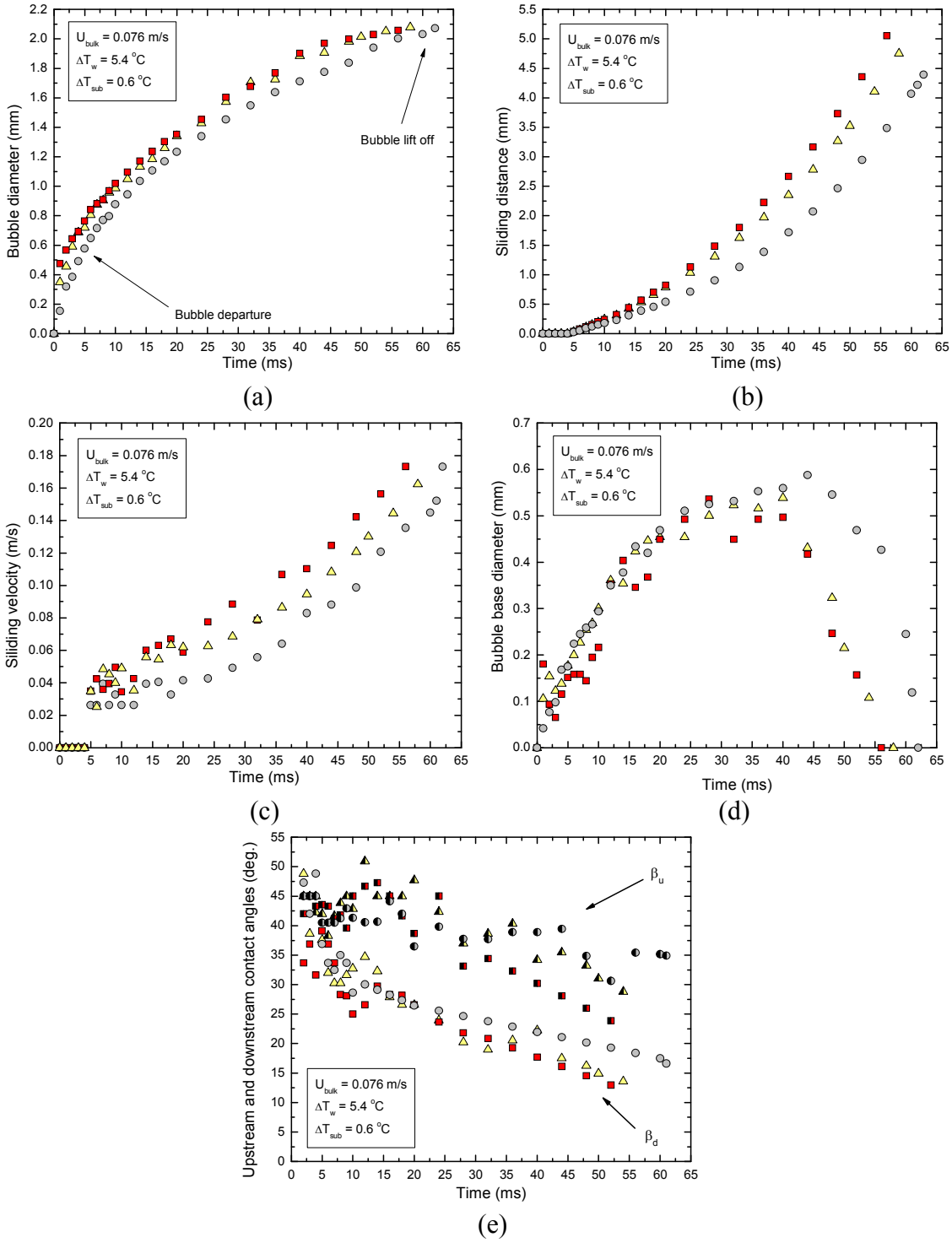

Measured quantities for 60^o inclined silicon surface: (a) bubble diameter, (b) sliding distance, (c) sliding velocity, (d) bubble base diameter and (e) upstream and downstream contact angles, for U_{bulk} = 0.076 m/s, ΔT_w = 5.4 ^{o}C, and ΔT_{sub} = 0.6 ^{o}C.

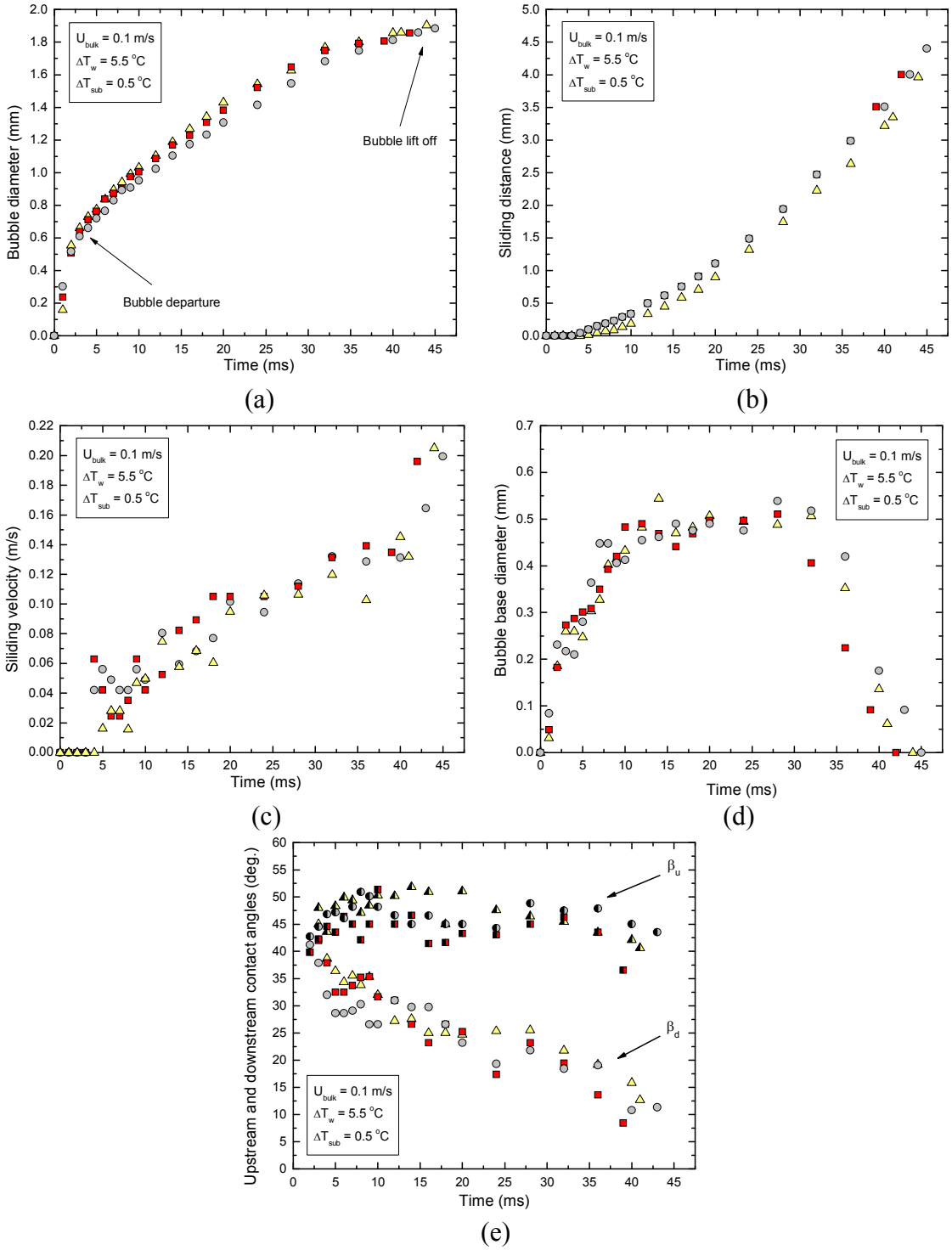

Measured quantities for 60° inclined silicon surface: (a) bubble diameter, (b) sliding distance, (c) sliding velocity, (d) bubble base diameter and (e) upstream and downstream contact angles, for U_{bulk} = 0.1 m/s, ΔT_w = 5.5 °C, and ΔT_{sub} = 0.5 °C.

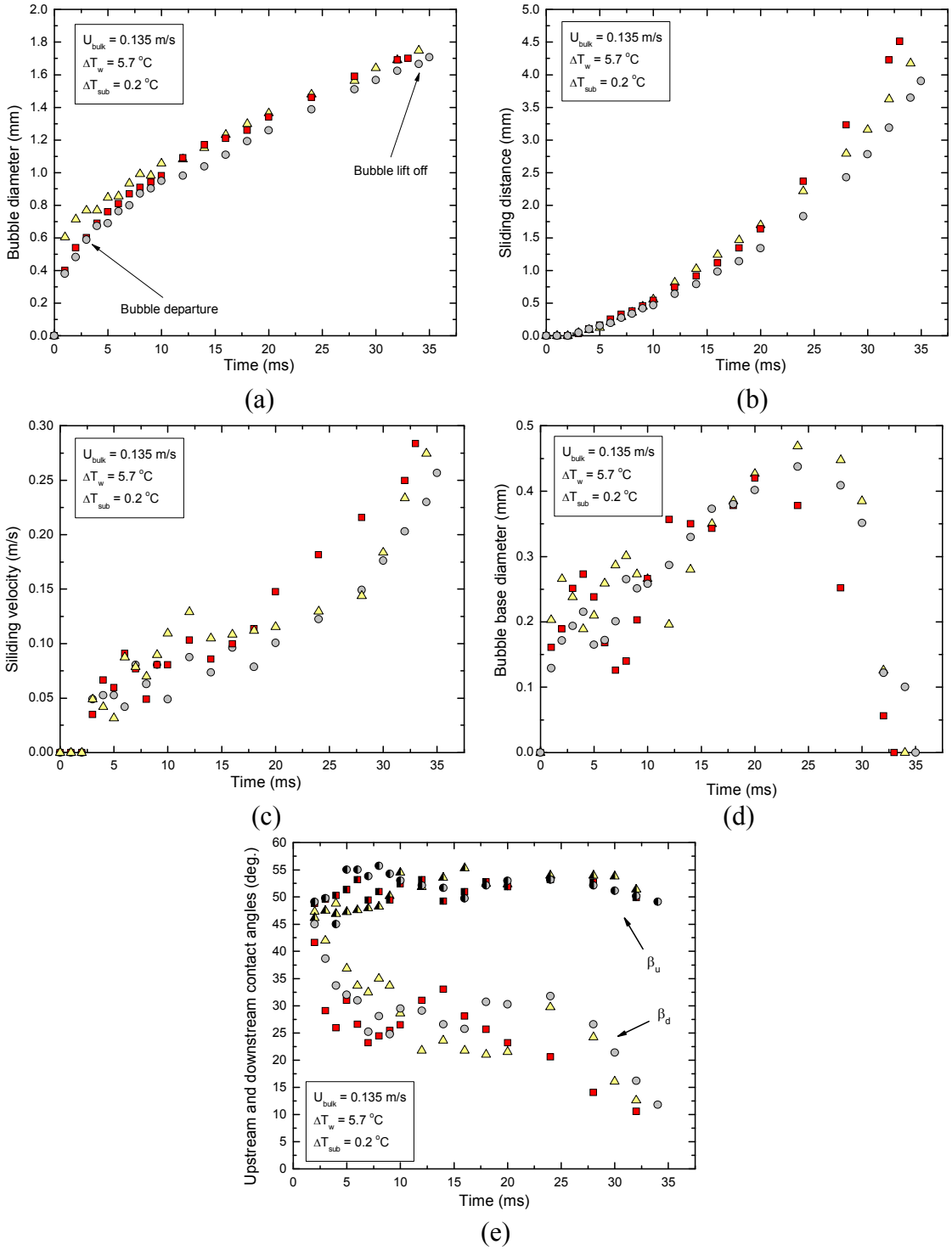

Measured quantities for 60^o inclined silicon surface: (a) bubble diameter, (b) sliding distance, (c) sliding velocity, (d) bubble base diameter and (e) upstream and downstream contact angles, for U_{bulk} = 0.135 m/s, ΔT_w = 5.7 ^{o}C, and ΔT_{sub} = 0.2 ^{o}C.

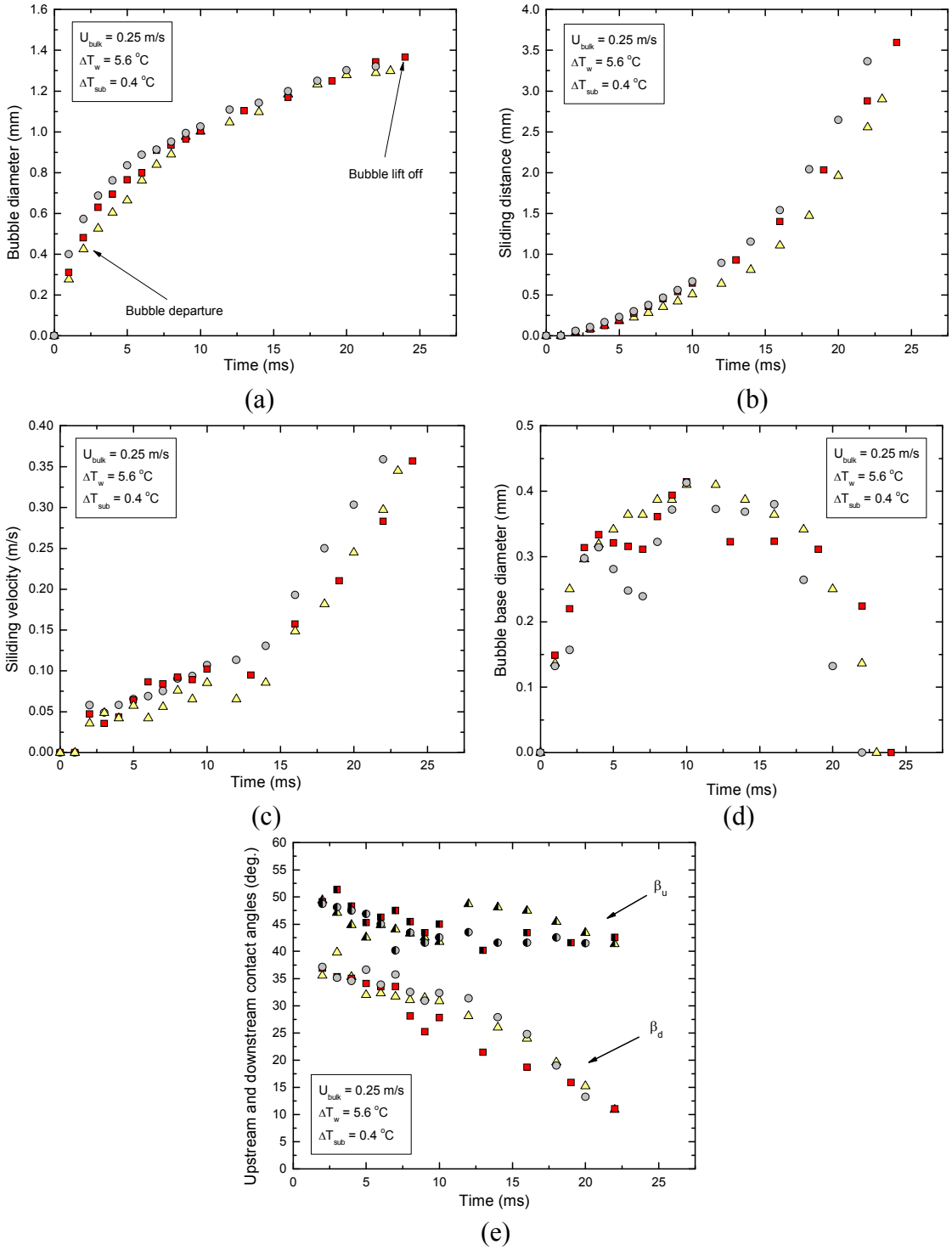

Measured quantities for 60^o inclined silicon surface: (a) bubble diameter, (b) sliding distance, (c) sliding velocity, (d) bubble base diameter and (e) upstream and downstream contact angles, for U_{bulk} = 0.25 m/s, ΔT_w = 5.6 ^{o}C, and ΔT_{sub} = 0.4 ^{o}C.

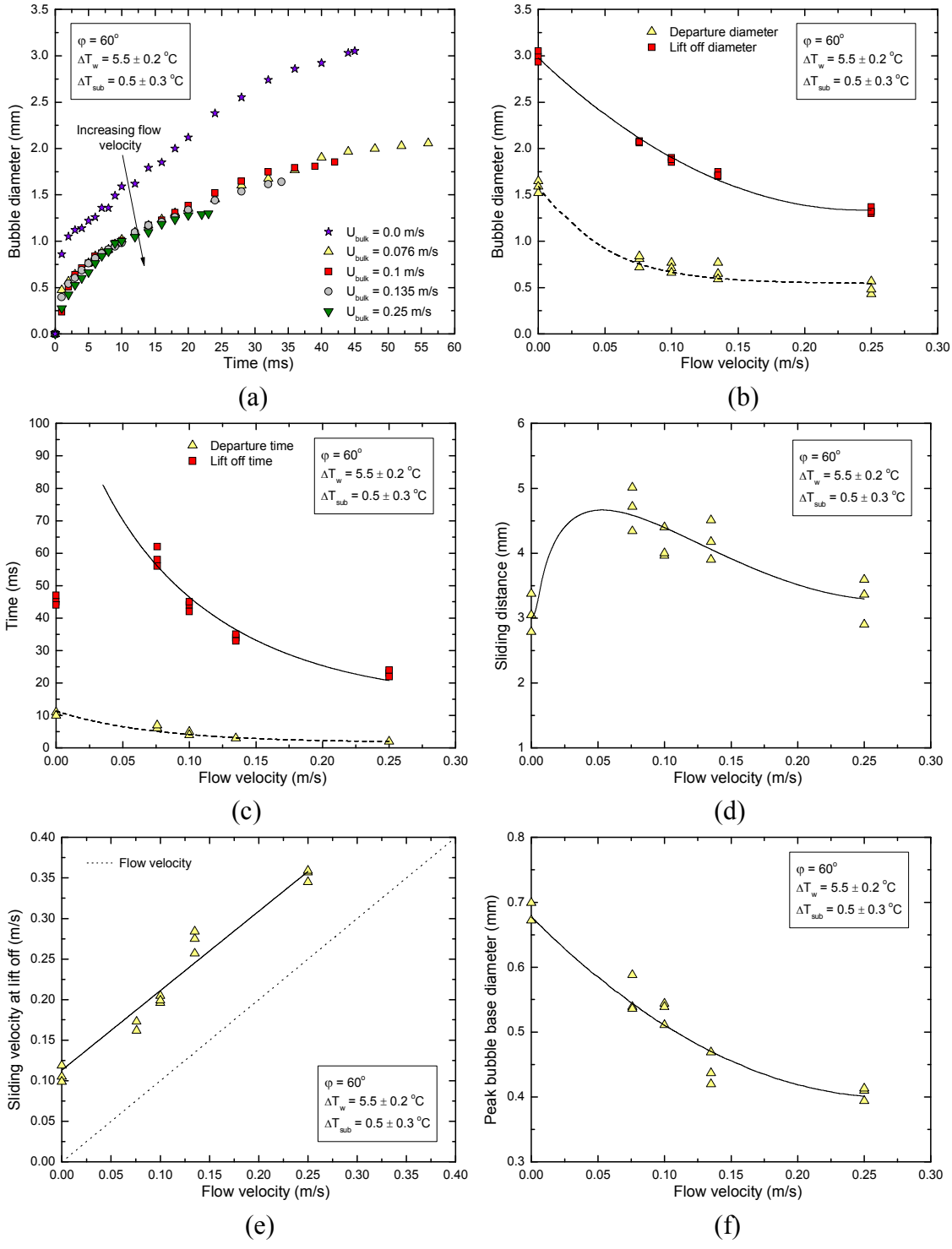

Effect of liquid bulk velocity on (a) variation of bubble diameter with time, (b) bubble departure and lift off diameters, (c) departure and lift off times, (d) sliding distance, (e) sliding velocity at lift off and (f) peak bubble base diameter – 60^{o} inclined silicon surface.

APPENDIX B
SINGLE BUBBLE EXPERIMENTAL RESULTS – ALUMINUM SURFACE

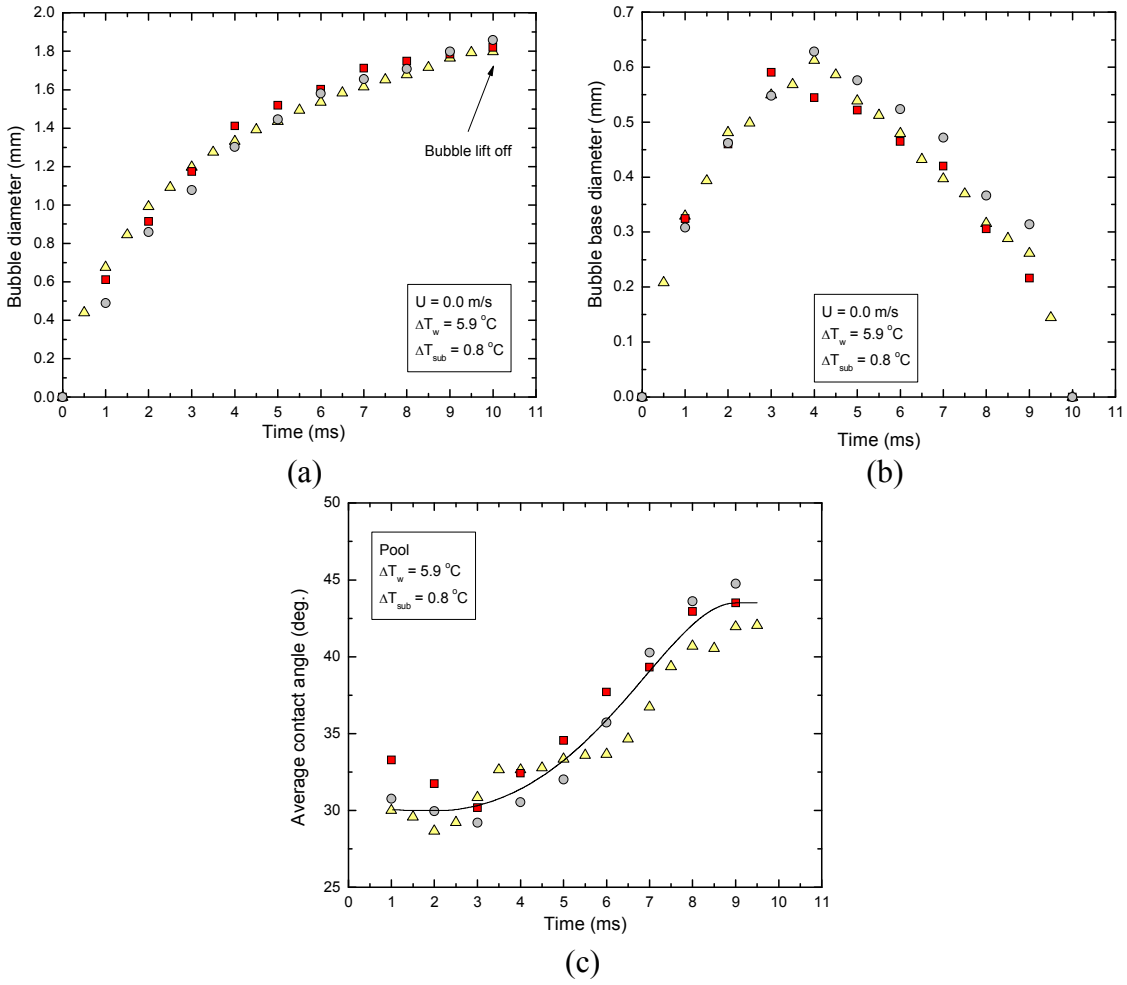

Measured quantities for horizontal aluminum surface: (a) bubble diameter, (b) bubble base diameter and (c) average contact angle, Pool, $\Delta T_w = 5.9\ ^oC$, and $\Delta T_{sub} = 0.8\ ^oC$.

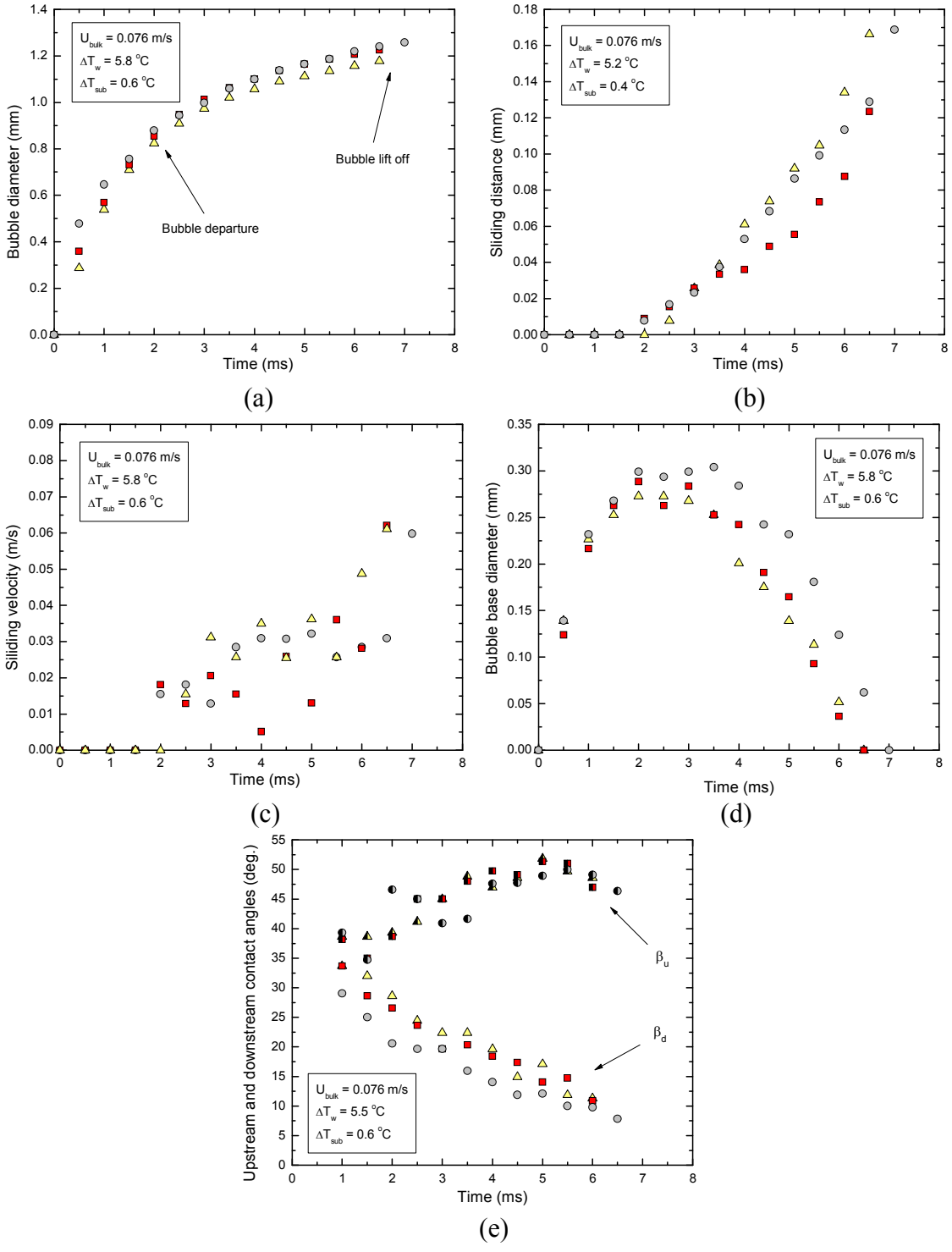

Measured quantities for horizontal aluminum surface: (a) bubble diameter, (b) sliding distance, (c) sliding velocity, (d) bubble base diameter and (e) upstream and downstream contact angles, for U_{bulk} = 0.076 m/s, ΔT_w = 5.8 °C, and ΔT_{sub} = 0.6 °C.

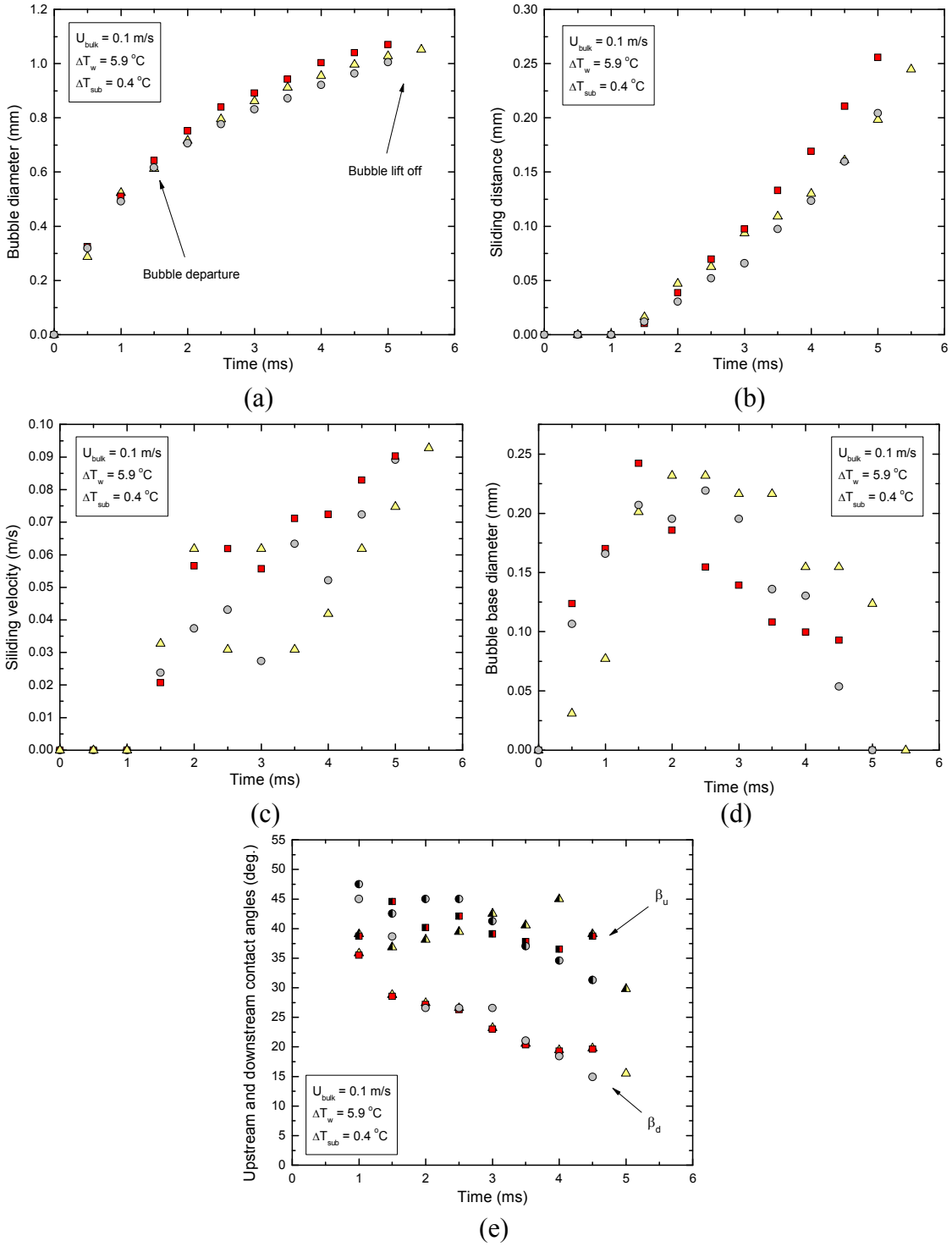

Measured quantities for horizontal aluminum surface: (a) bubble diameter, (b) sliding distance, (c) sliding velocity, (d) bubble base diameter and (e) upstream and downstream contact angles, for U_{bulk} = 0.1 m/s, ΔT_w = 5.9 °C, and ΔT_{sub} = 0.4 °C.

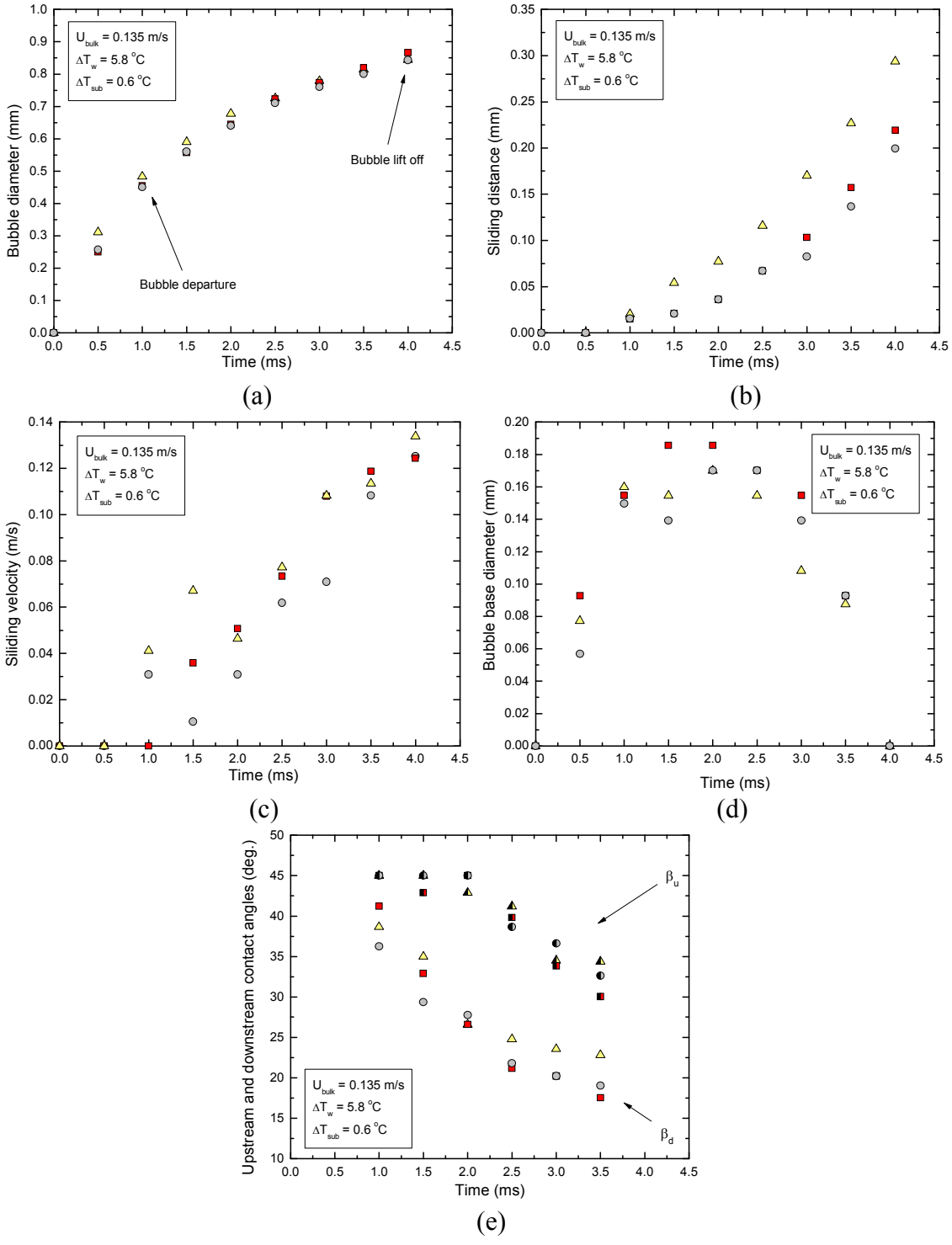

Measured quantities for horizontal aluminum surface: (a) bubble diameter, (b) sliding distance, (c) sliding velocity, (d) bubble base diameter and (e) upstream and downstream contact angles, for U_{bulk} = 0.135 m/s, ΔT_w = 5.8 °C, and ΔT_{sub} = 0.6 °C.

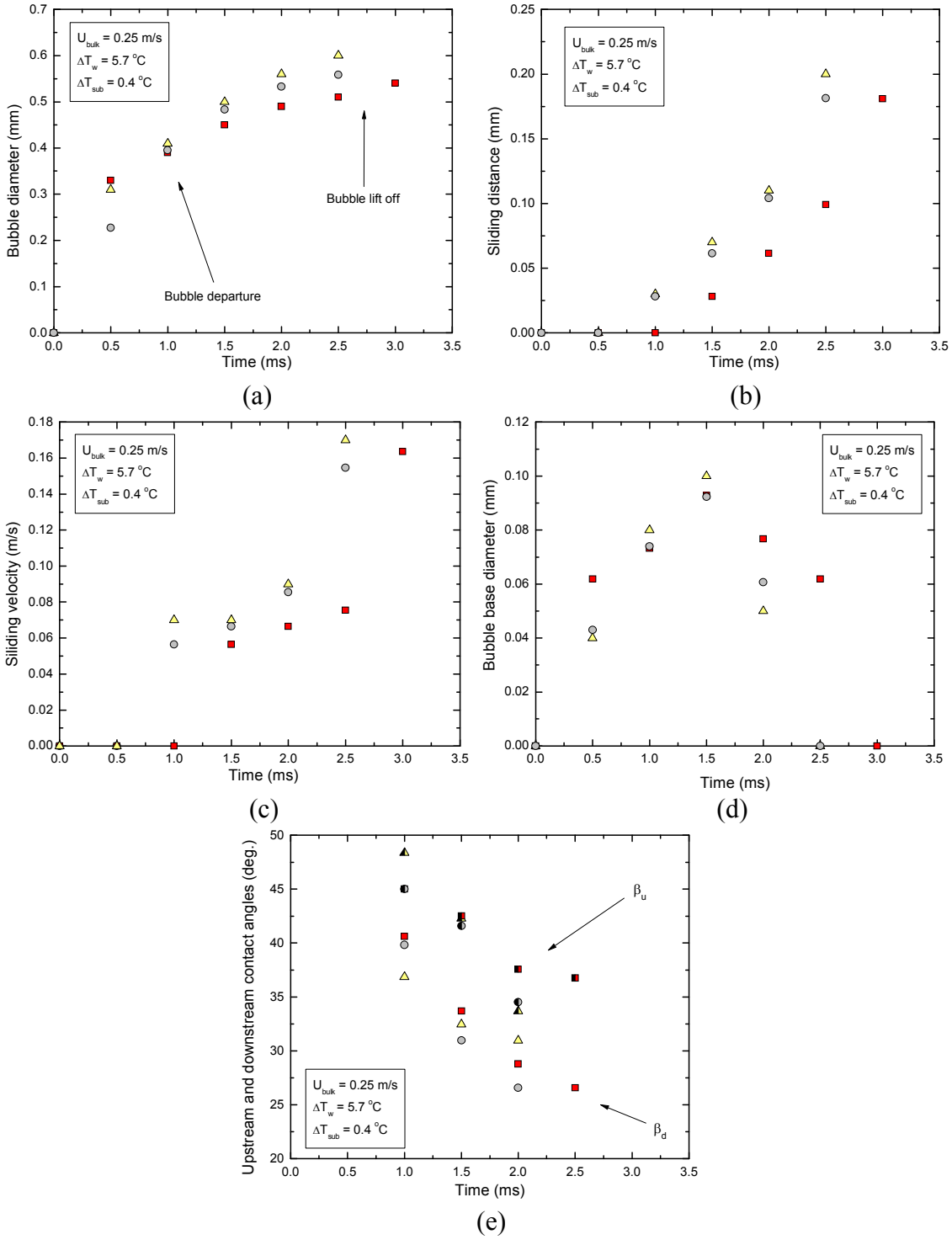

Measured quantities for horizontal aluminum surface: (a) bubble diameter, (b) sliding distance, (c) sliding velocity, (d) bubble base diameter and (e) upstream and downstream contact angles, for U_{bulk} = 0.25 m/s, ΔT_w = 5.7 °C, and ΔT_{sub} = 0.4 °C.

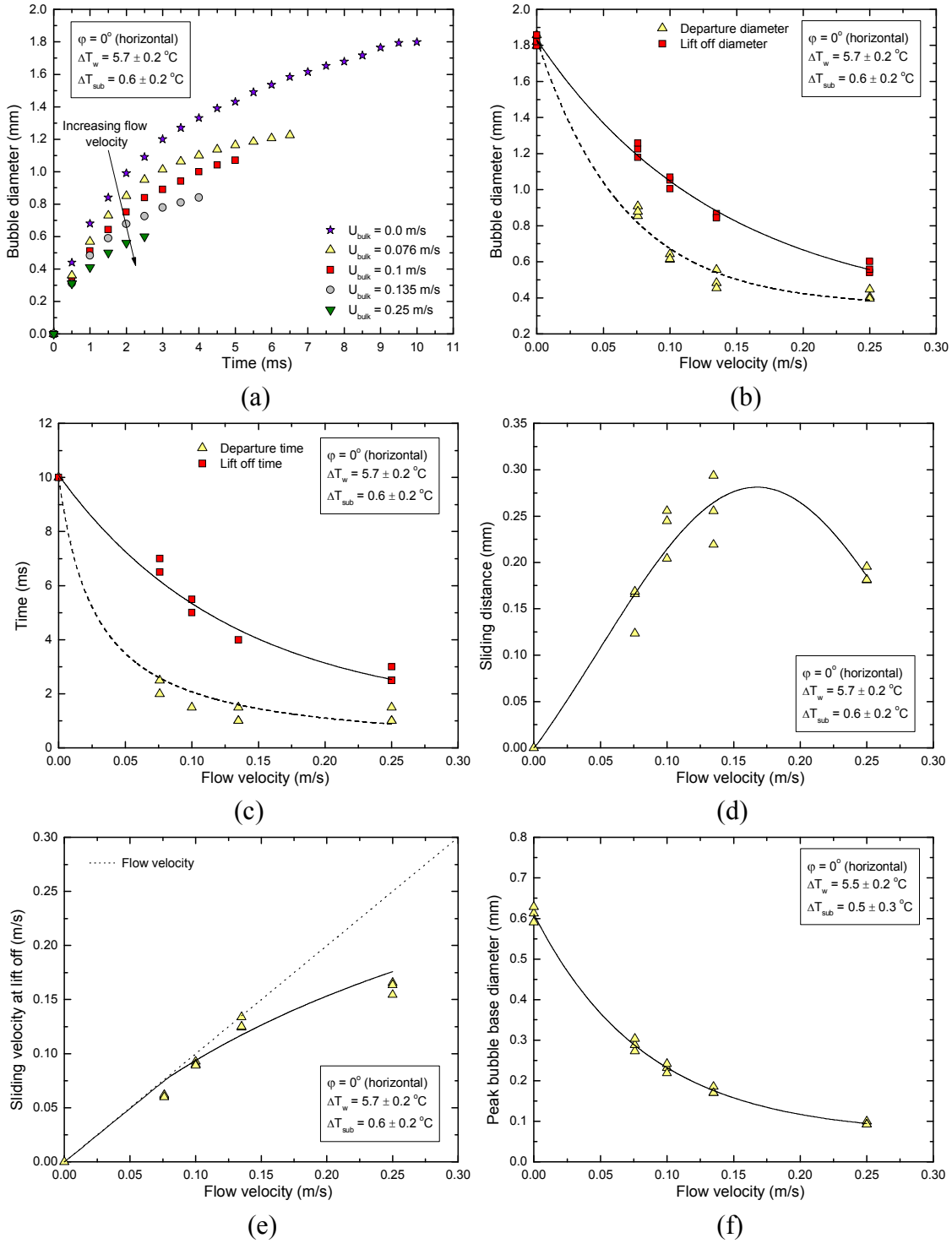

Effect of liquid bulk velocity on (a) variation of bubble diameter with time, (b) bubble departure and lift off diameters, (c) departure and lift off times, (d) sliding distance, (e) sliding velocity at lift off and (f) peak bubble base diameter – Horizontal aluminum surface.

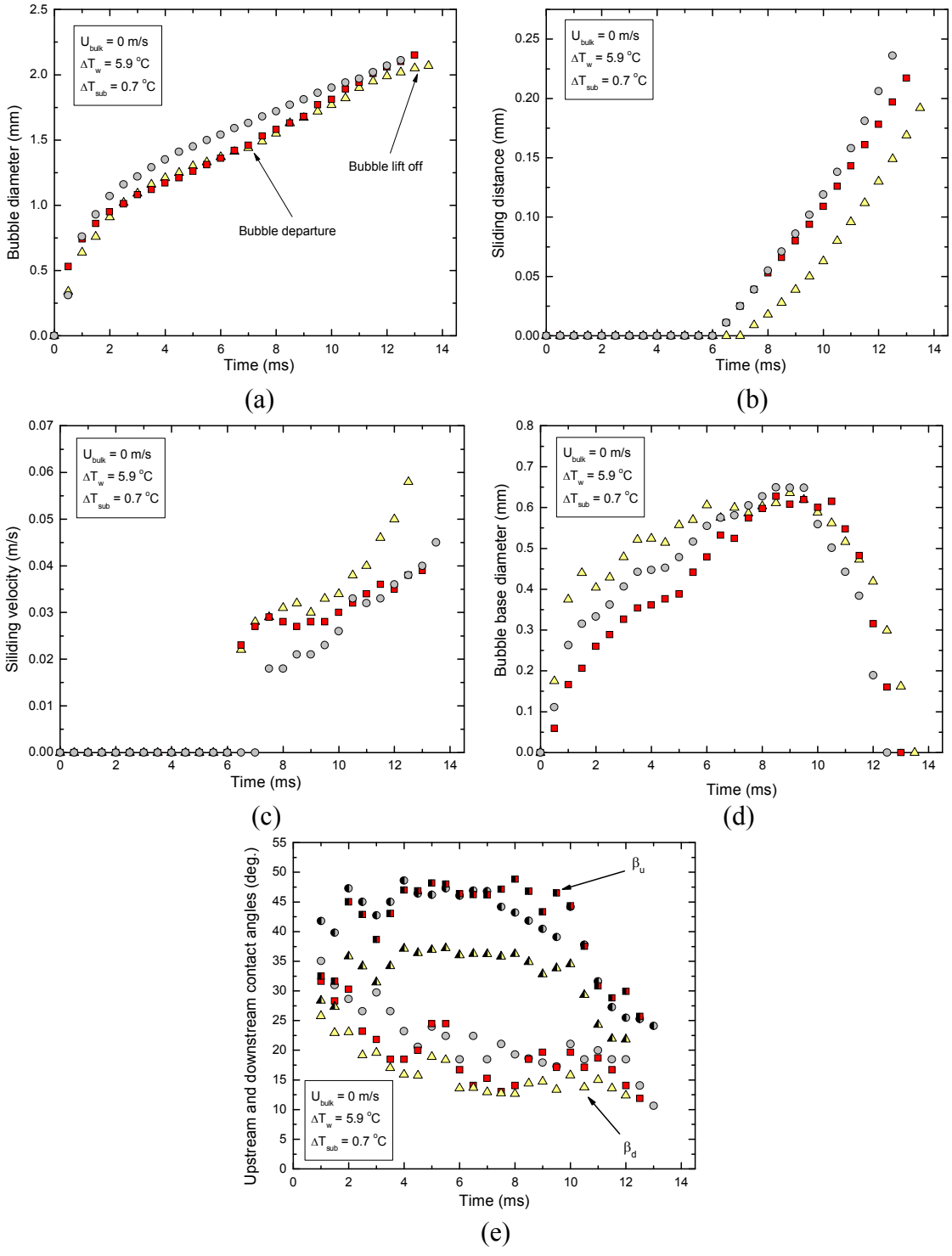

Measured quantities for 30^o inclined aluminum surface: (a) bubble diameter, (b) sliding distance, (c) sliding velocity, (d) bubble base diameter and (e) upstream and downstream contact angles, for U_{bulk} = 0 m/s, ΔT_w = 5.9 ^{o}C, and ΔT_{sub} = 0.7 ^{o}C.

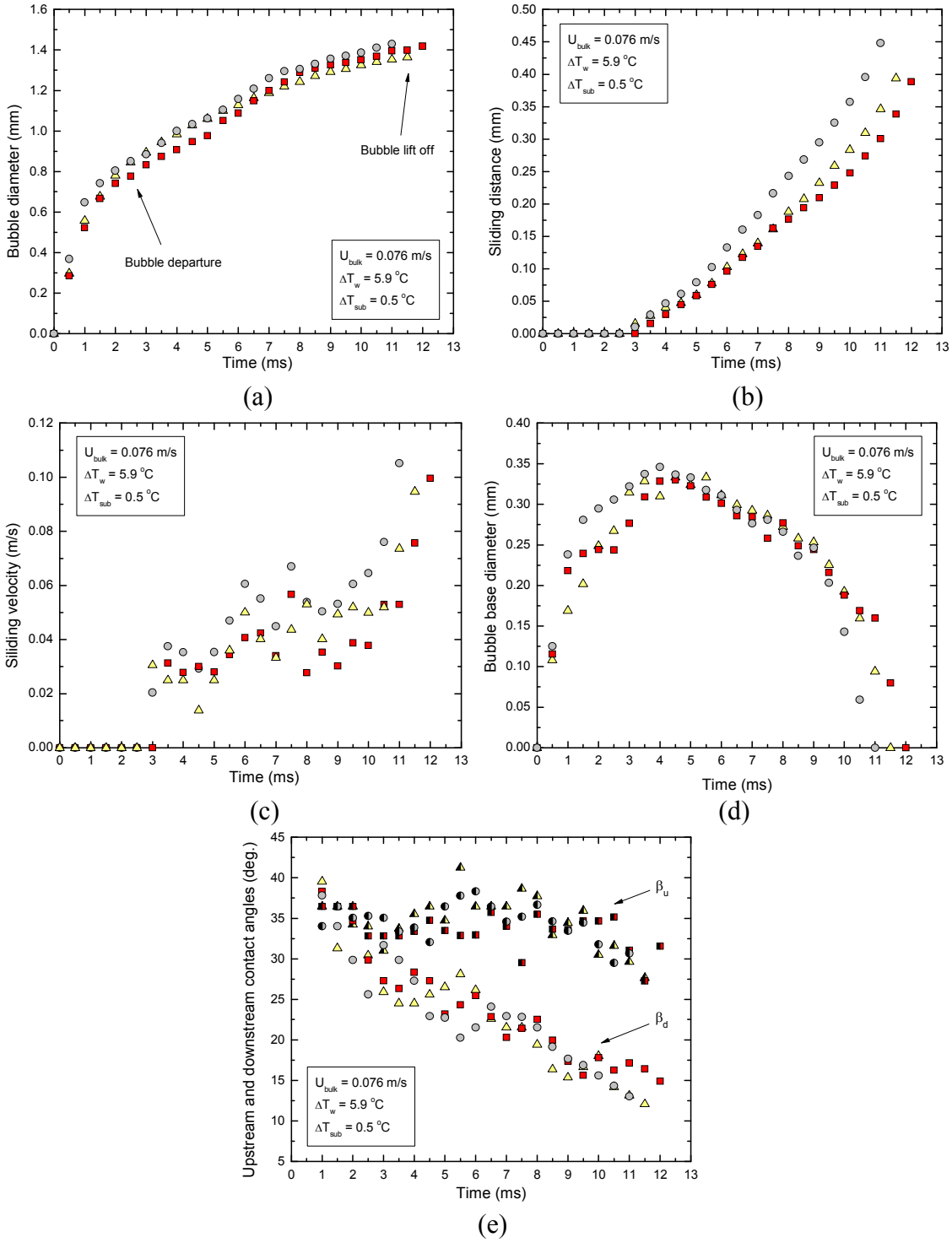

Measured quantities for 30^{o} inclined aluminum surface: (a) bubble diameter, (b) sliding distance, (c) sliding velocity, (d) bubble base diameter and (e) upstream and downstream contact angles, for U_{bulk} = 0.076 m/s, ΔT_w = 5.9 ^{o}C, and ΔT_{sub} = 0.5 ^{o}C.

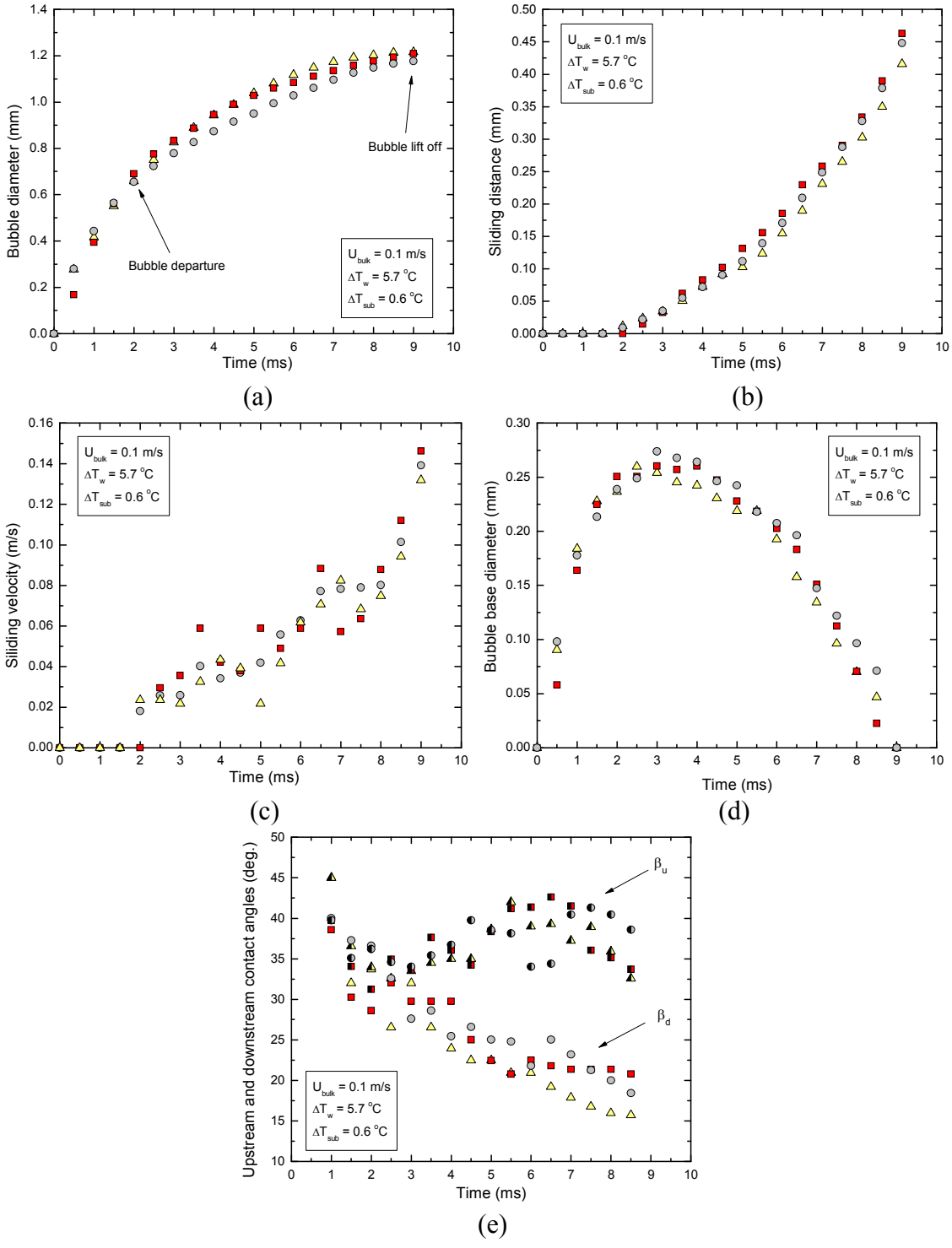

Measured quantities for 30^{o} inclined aluminum surface aluminum surface: (a) bubble diameter, (b) sliding distance, (c) sliding velocity, (d) bubble base diameter and (e) upstream and downstream contact angles, for U_{bulk} = 0.01 m/s, ΔT_w = 5.7 ^{o}C, and ΔT_{sub} = 0.6 ^{o}C.

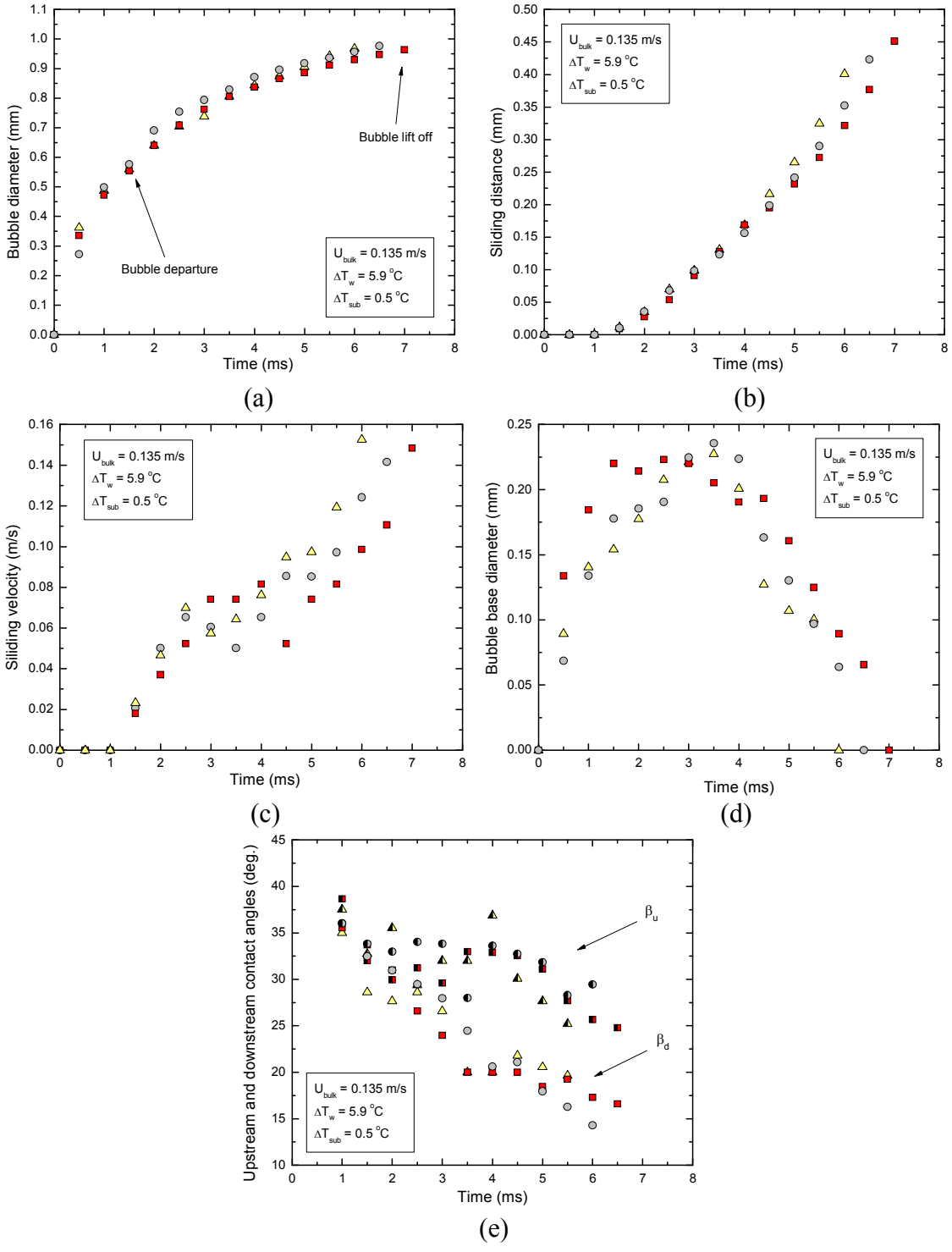

Measured quantities for 30^{o} inclined aluminum surface aluminum surface: (a) bubble diameter, (b) sliding distance, (c) sliding velocity, (d) bubble base diameter and (e) upstream and downstream contact angles, for U_{bulk} = 0.135 m/s, ΔT_w = 5.9 ^{o}C, and ΔT_{sub} = 0.5 ^{o}C.

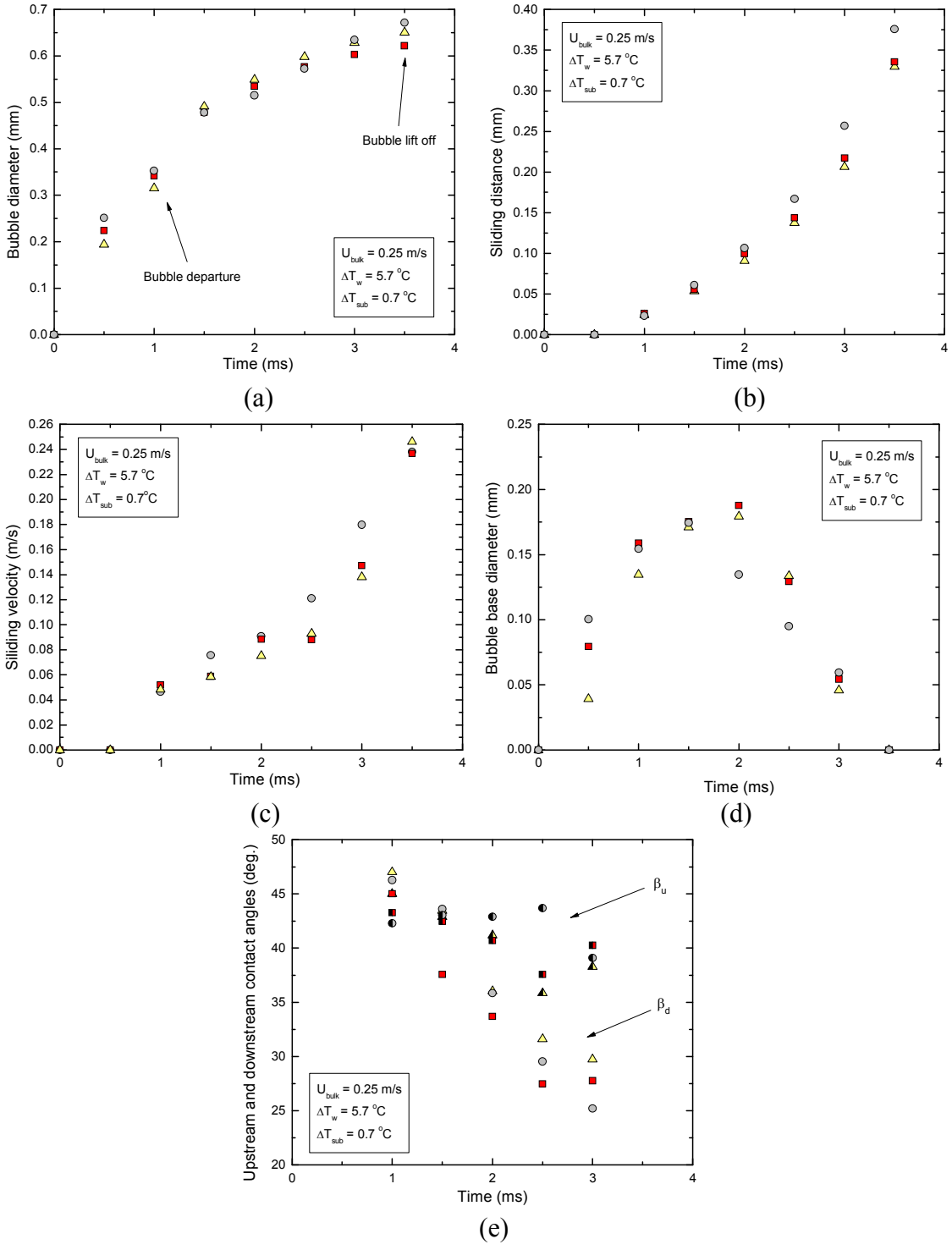

Measured quantities for 30^{o} inclined aluminum surface aluminum surface: (a) bubble diameter, (b) sliding distance, (c) sliding velocity, (d) bubble base diameter and (e) upstream and downstream contact angles, for U_{bulk} = 0.25 m/s, ΔT_w = 5.7 ^{o}C, and ΔT_{sub} = 0.7 ^{o}C.

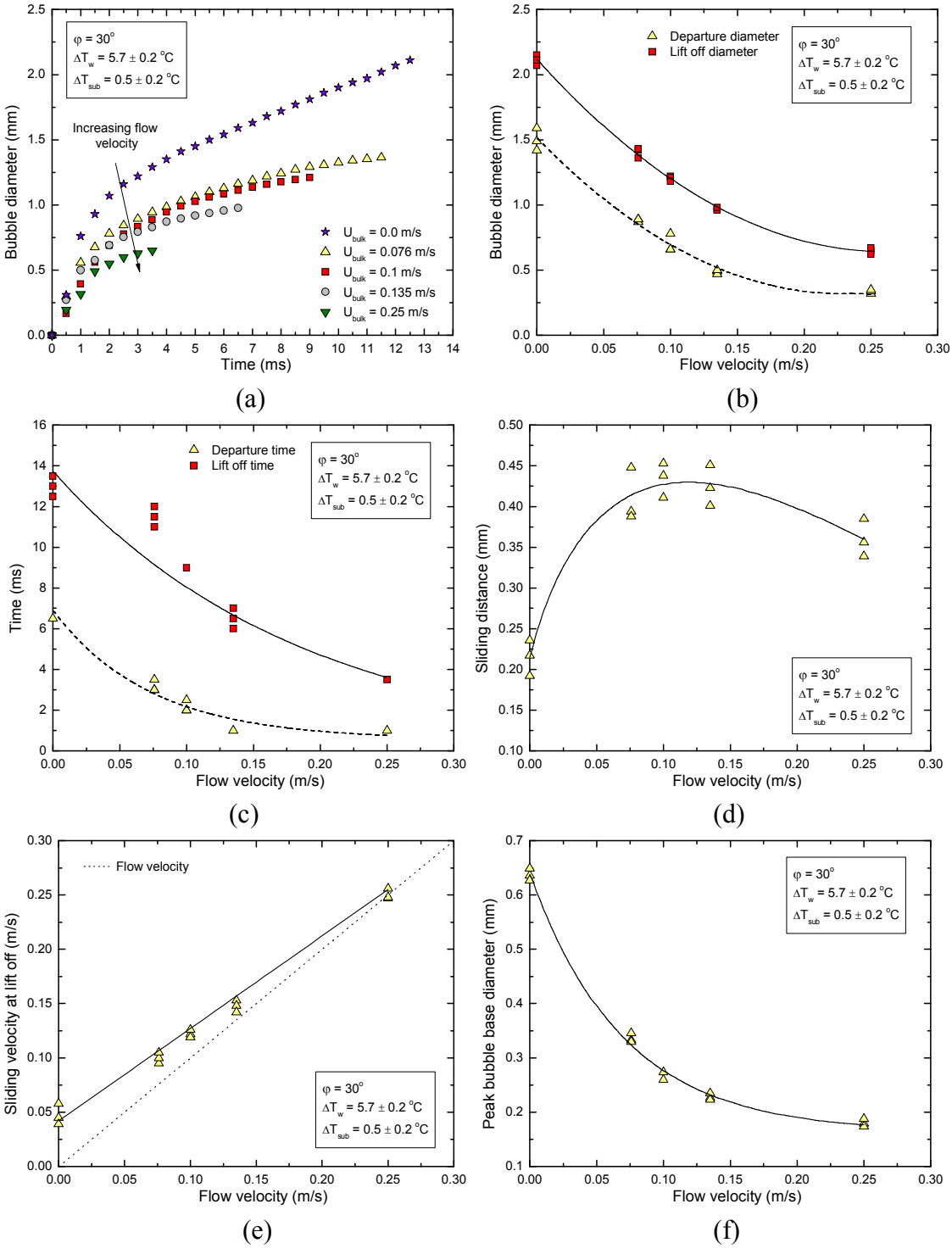

Effect of liquid bulk velocity on (a) variation of bubble diameter with time, (b) bubble departure and lift off diameters, (c) departure and lift off times, (d) sliding distance, (e) sliding velocity at lift off and (f) peak bubble base diameter – 30^{o} inclined aluminum surface.

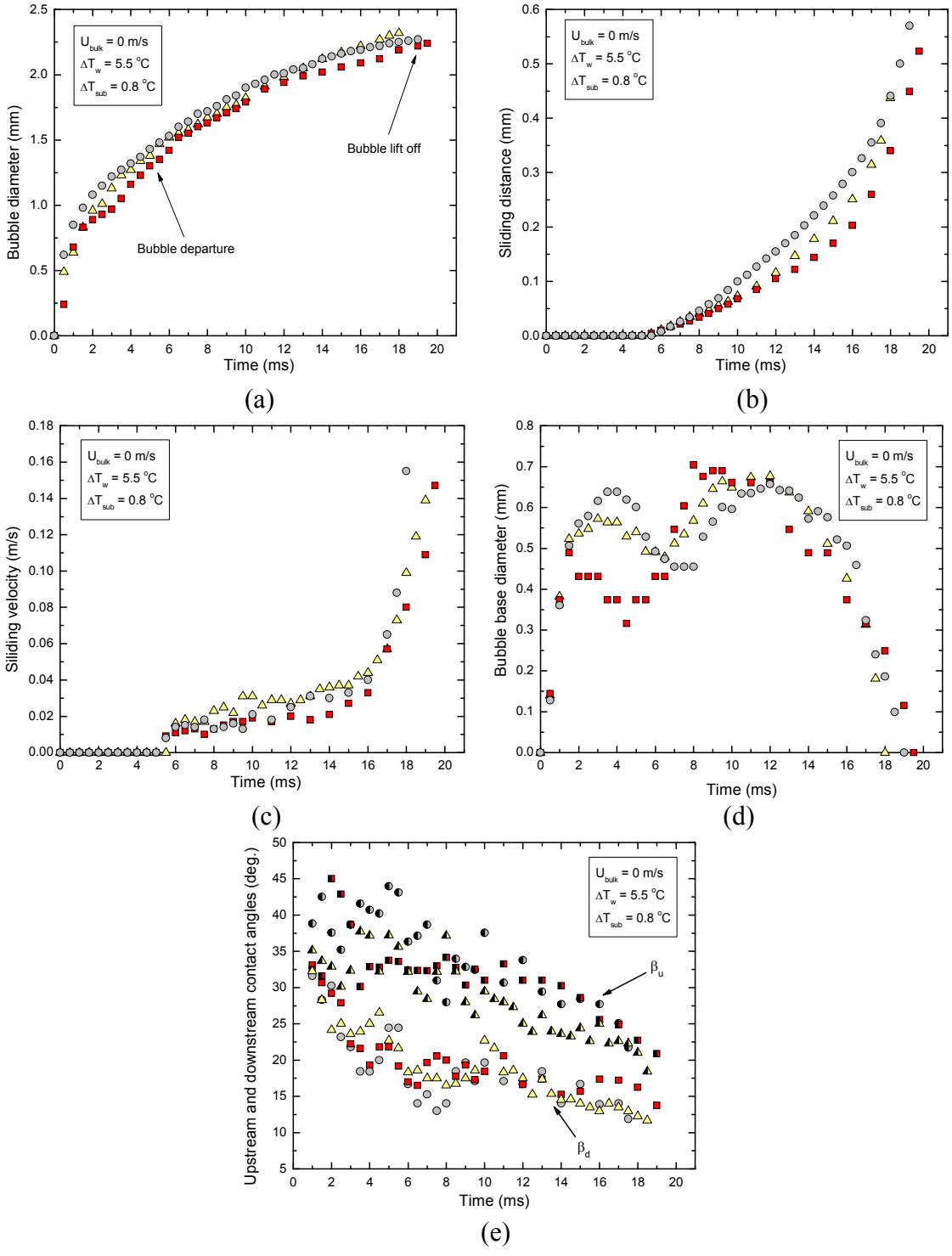

Measured quantities for 45° inclined aluminum surface: (a) bubble diameter, (b) sliding distance, (c) sliding velocity, (d) bubble base diameter and (e) upstream and downstream contact angles, for U_{bulk} = 0 m/s, ΔT_w = 5.5 °C, and ΔT_{sub} = 0.8 °C.

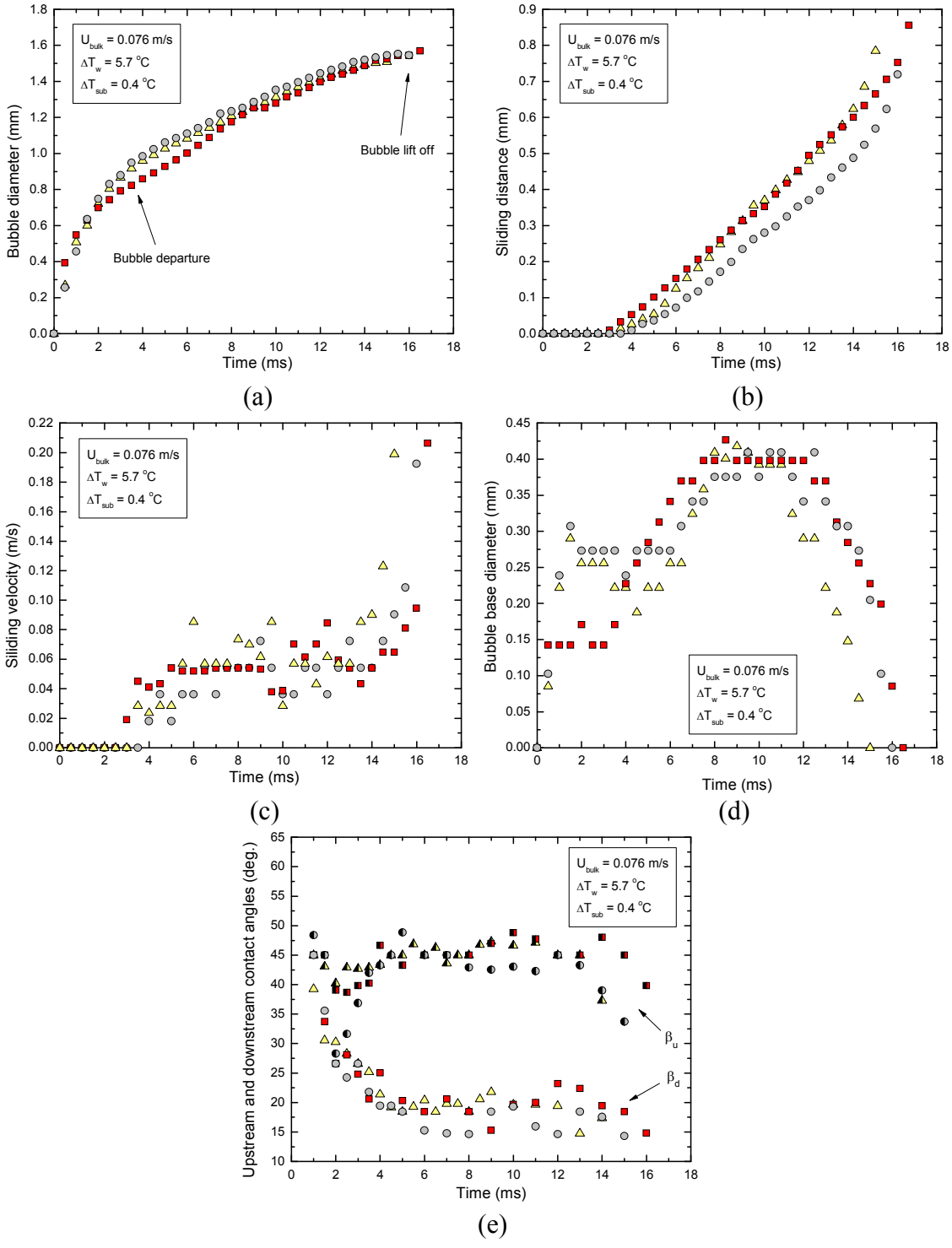

Measured quantities for 45^o inclined aluminum surface: (a) bubble diameter, (b) sliding distance, (c) sliding velocity, (d) bubble base diameter and (e) upstream and downstream contact angles, for U_{bulk} = 0.076 m/s, ΔT_w = 5.7 ^{o}C, and ΔT_{sub} = 0.4 ^{o}C.

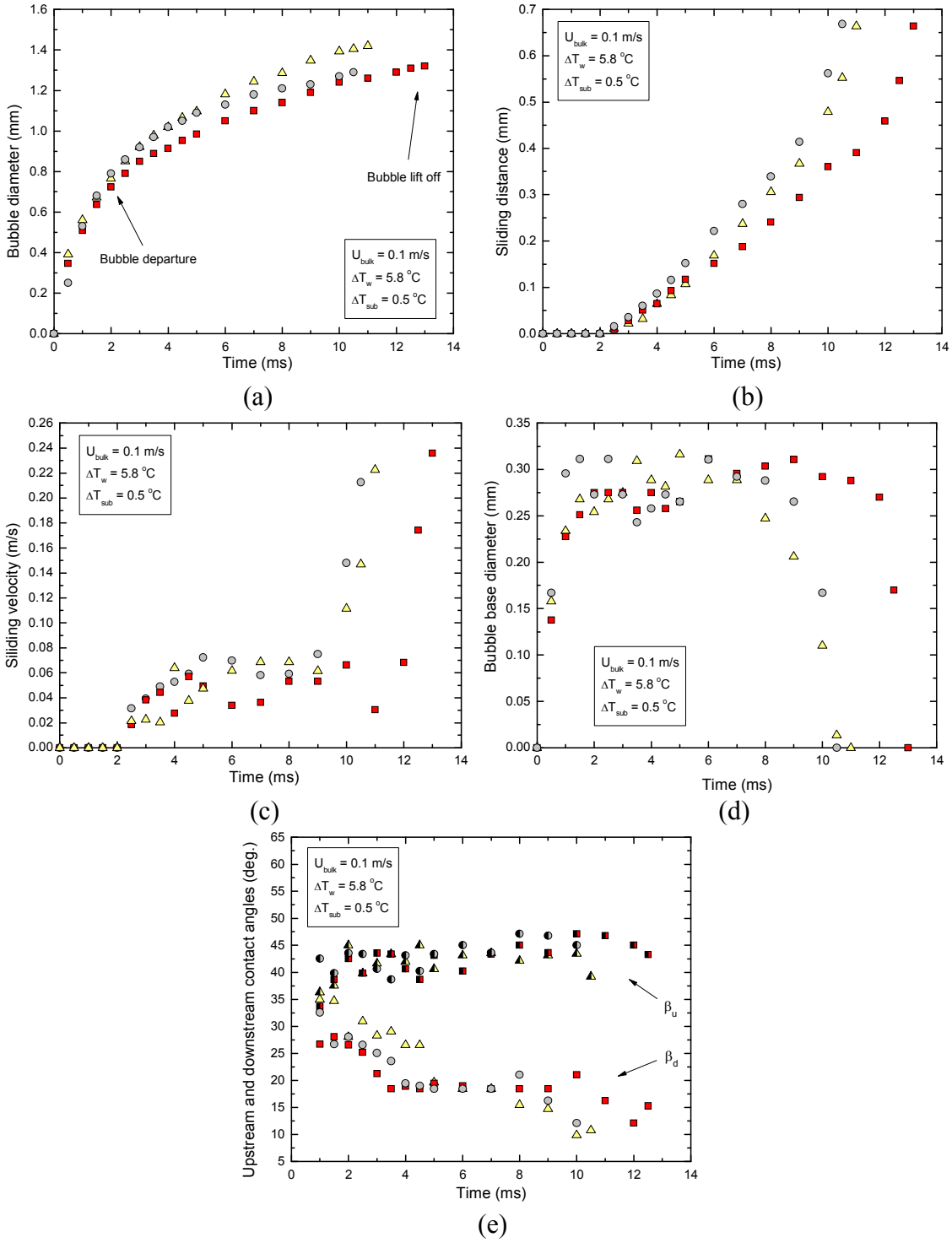

Measured quantities for 45^o inclined aluminum surface: (a) bubble diameter, (b) sliding distance, (c) sliding velocity, (d) bubble base diameter and (e) upstream and downstream contact angles, for U_{bulk} = 0.1 m/s, ΔT_w = 5.8 ^{o}C, and ΔT_{sub} = 0.5 ^{o}C.

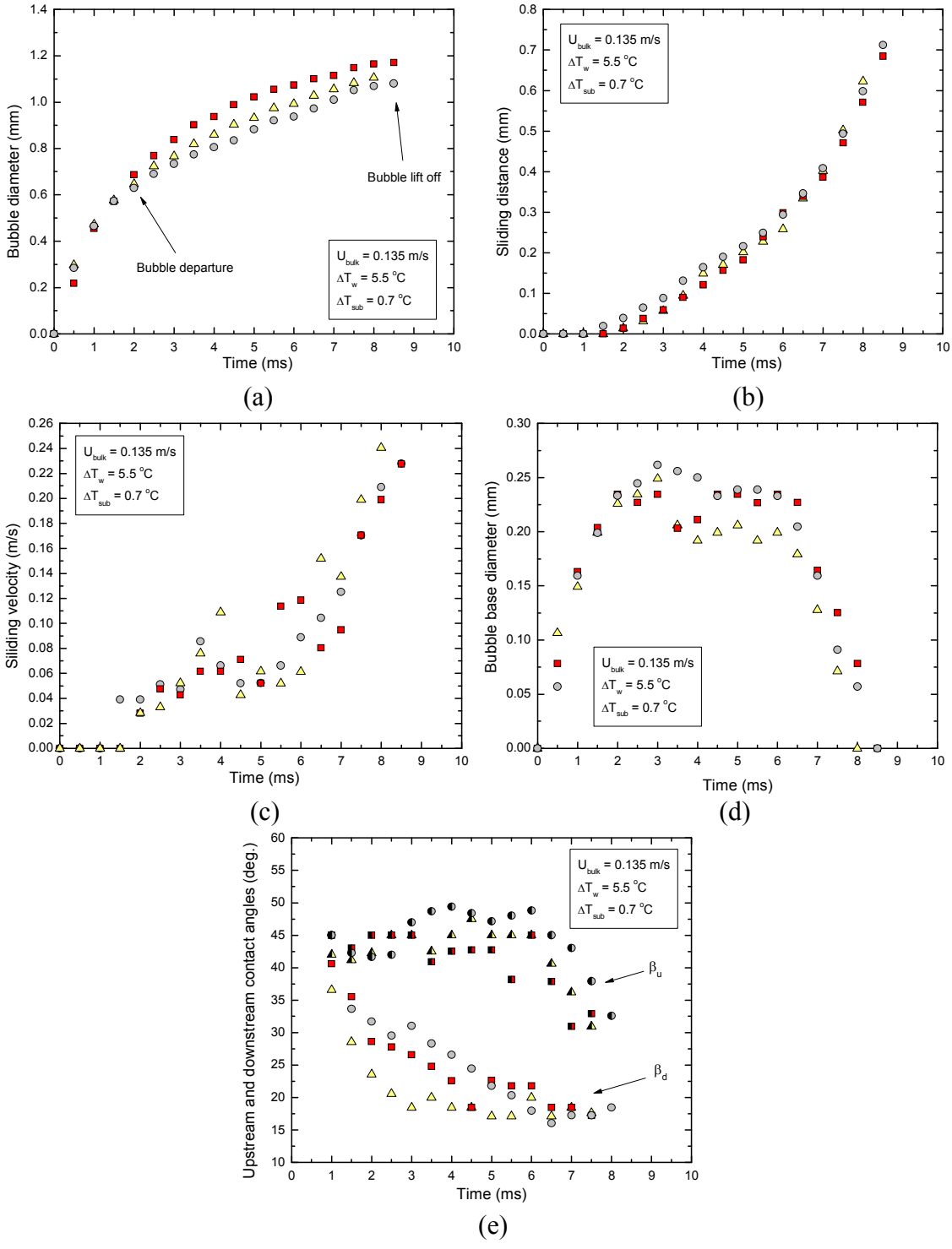

Measured quantities for 45^{o} inclined aluminum surface: (a) bubble diameter, (b) sliding distance, (c) sliding velocity, (d) bubble base diameter and (e) upstream and downstream contact angles, for U_{bulk} = 0.135 m/s, ΔT_w = 5.5 ^{o}C, and ΔT_{sub} = 0.7 ^{o}C.

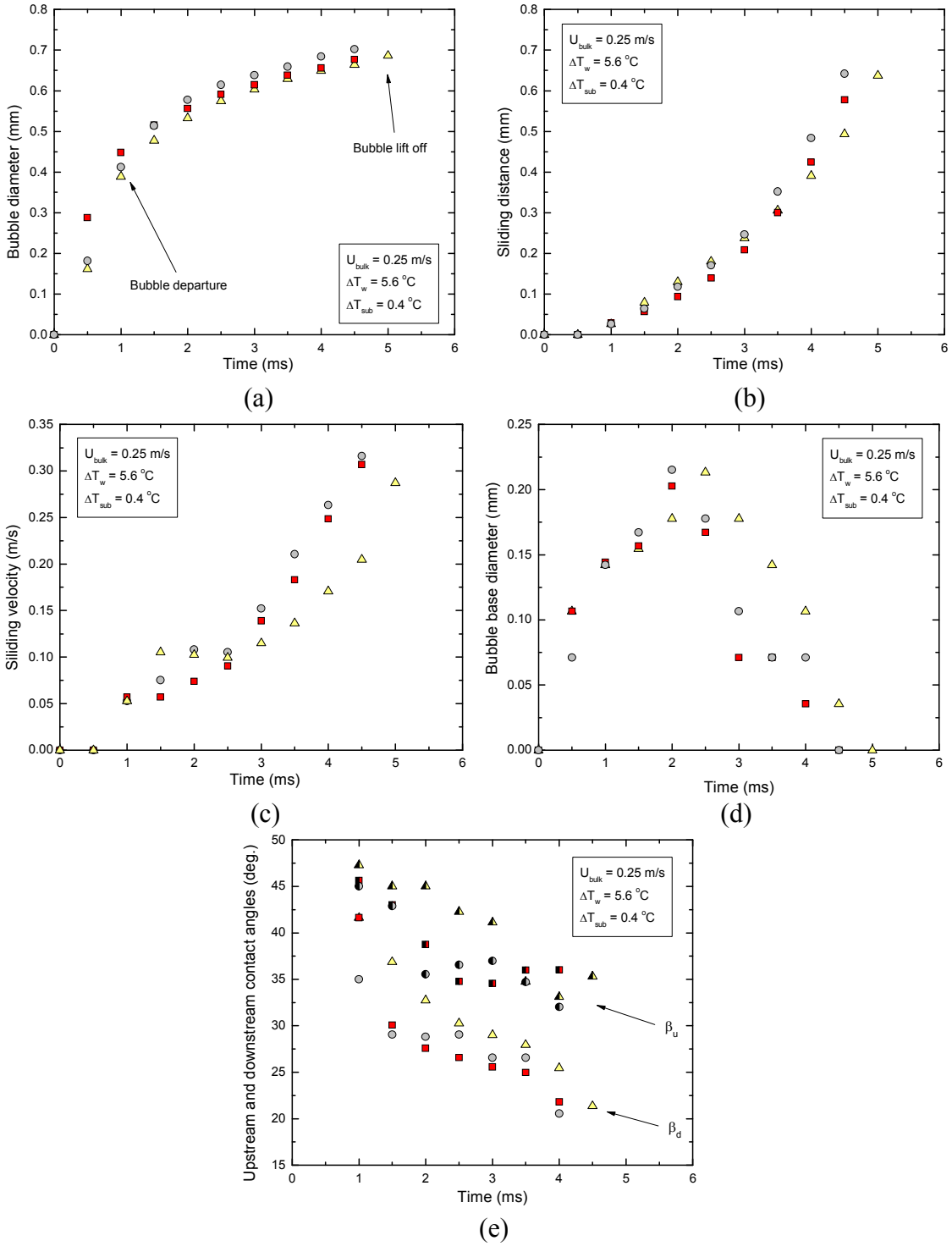

Measured quantities for 45^{o} inclined aluminum surface: (a) bubble diameter, (b) sliding distance, (c) sliding velocity, (d) bubble base diameter and (e) upstream and downstream contact angles, for U_{bulk} = 0.25 m/s, ΔT_w = 5.6 ^{o}C, and ΔT_{sub} = 0.4 ^{o}C.

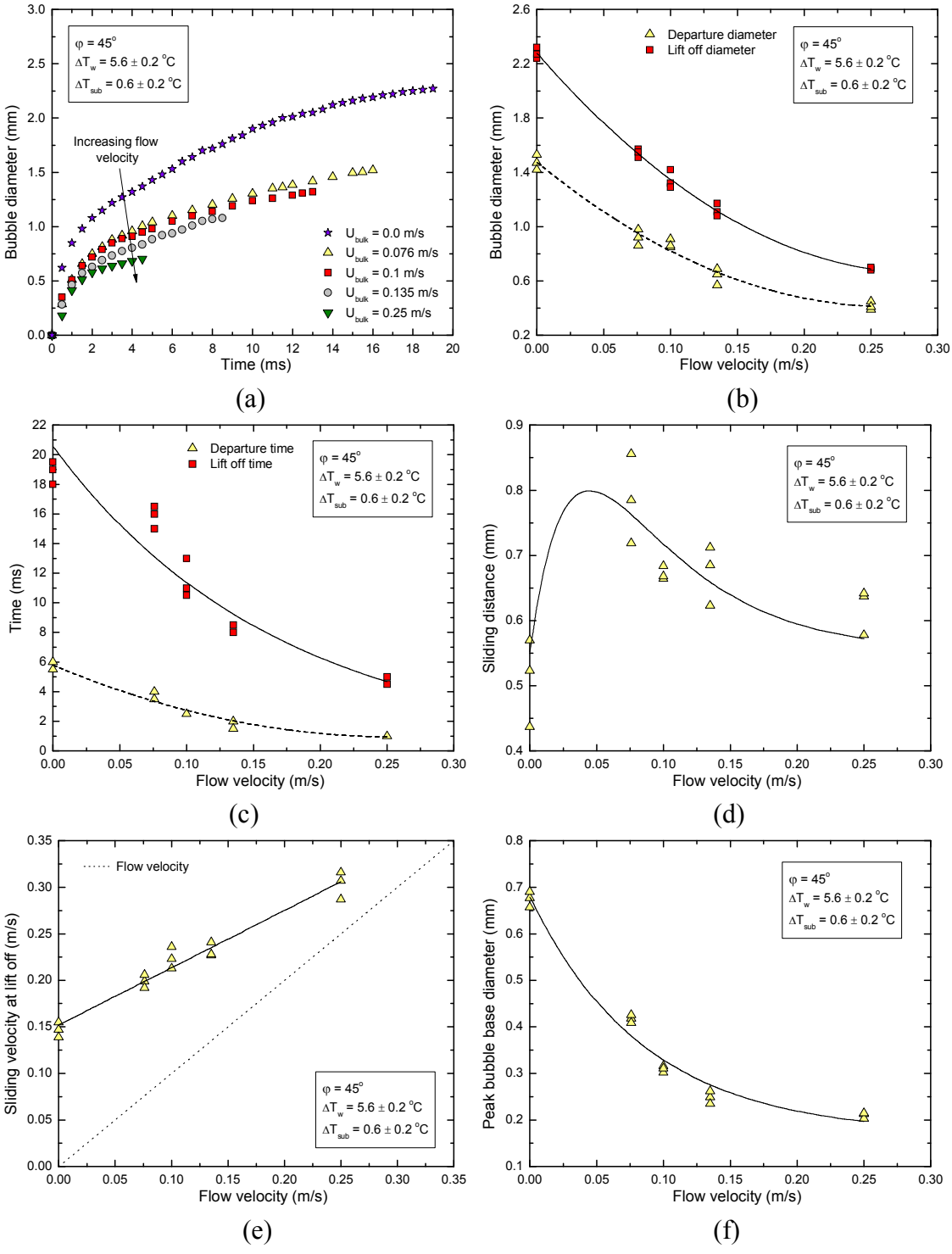

Effect of liquid bulk velocity on (a) variation of bubble diameter with time, (b) bubble departure and lift off diameters, (c) departure and lift off times, (d) sliding distance, (e) sliding velocity at lift off and (f) peak bubble base diameter – 45^{o} inclined aluminum surface.

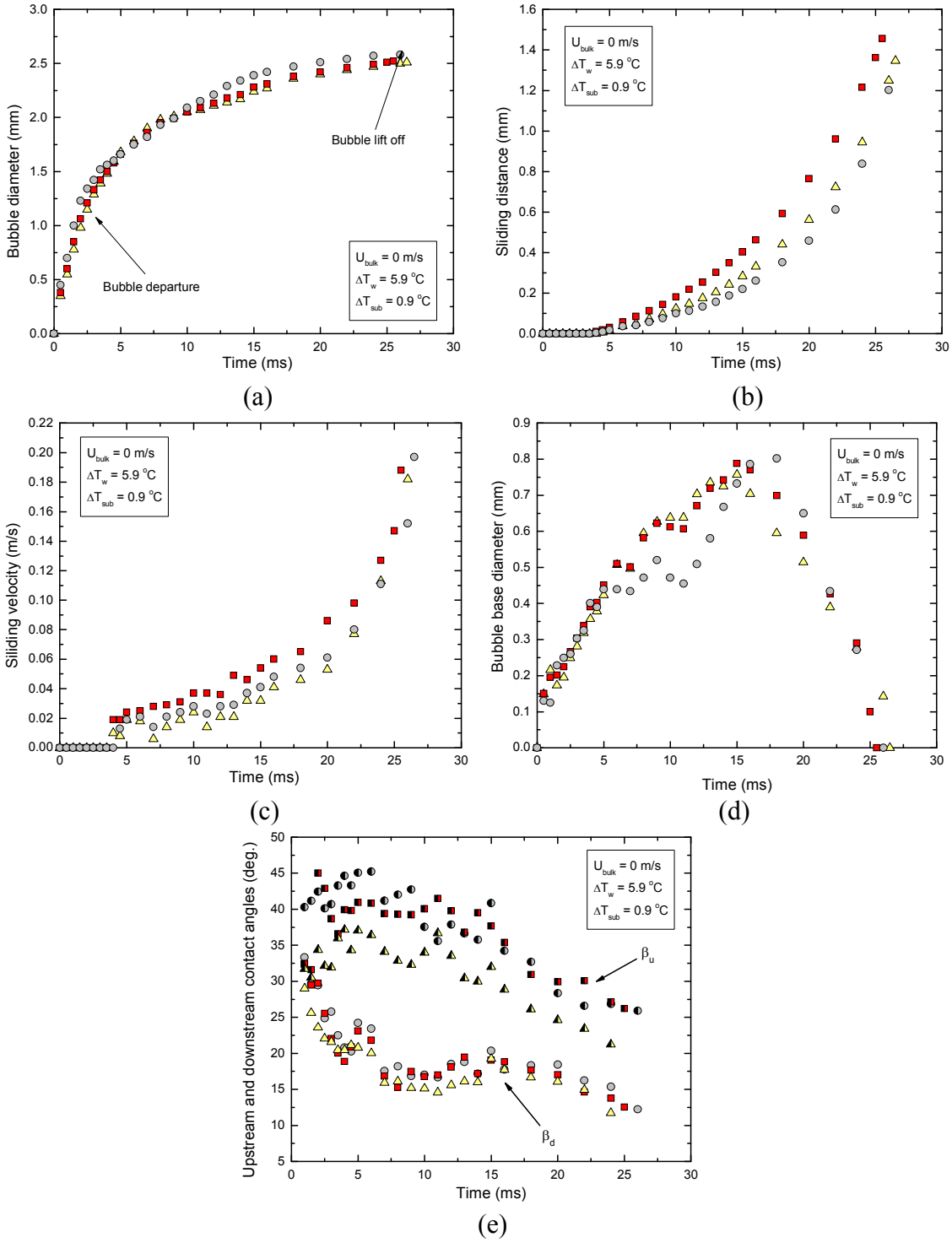

Measured quantities for 60^{o} inclined aluminum surface: (a) bubble diameter, (b) sliding distance, (c) sliding velocity, (d) bubble base diameter and (e) upstream and downstream contact angles, for U_{bulk} = 0 m/s, ΔT_w = 5.9 ^{o}C, and ΔT_{sub} = 0.9 ^{o}C.

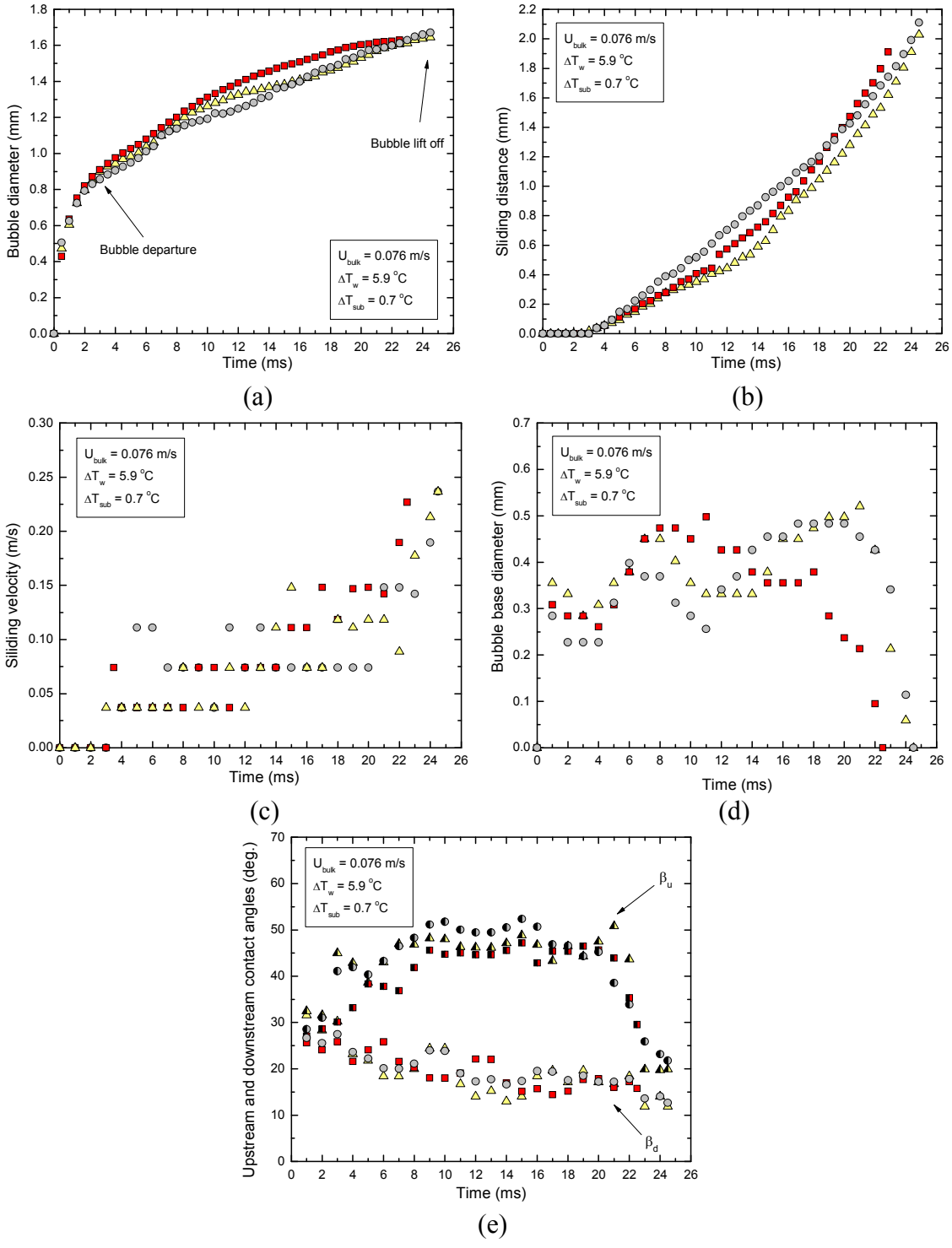

Measured quantities for 60^o inclined aluminum surface: (a) bubble diameter, (b) sliding distance, (c) sliding velocity, (d) bubble base diameter and (e) upstream and downstream contact angles, for U_{bulk} = 0.076 m/s, ΔT_w = 5.9 ^{o}C, and ΔT_{sub} = 0.7 ^{o}C.

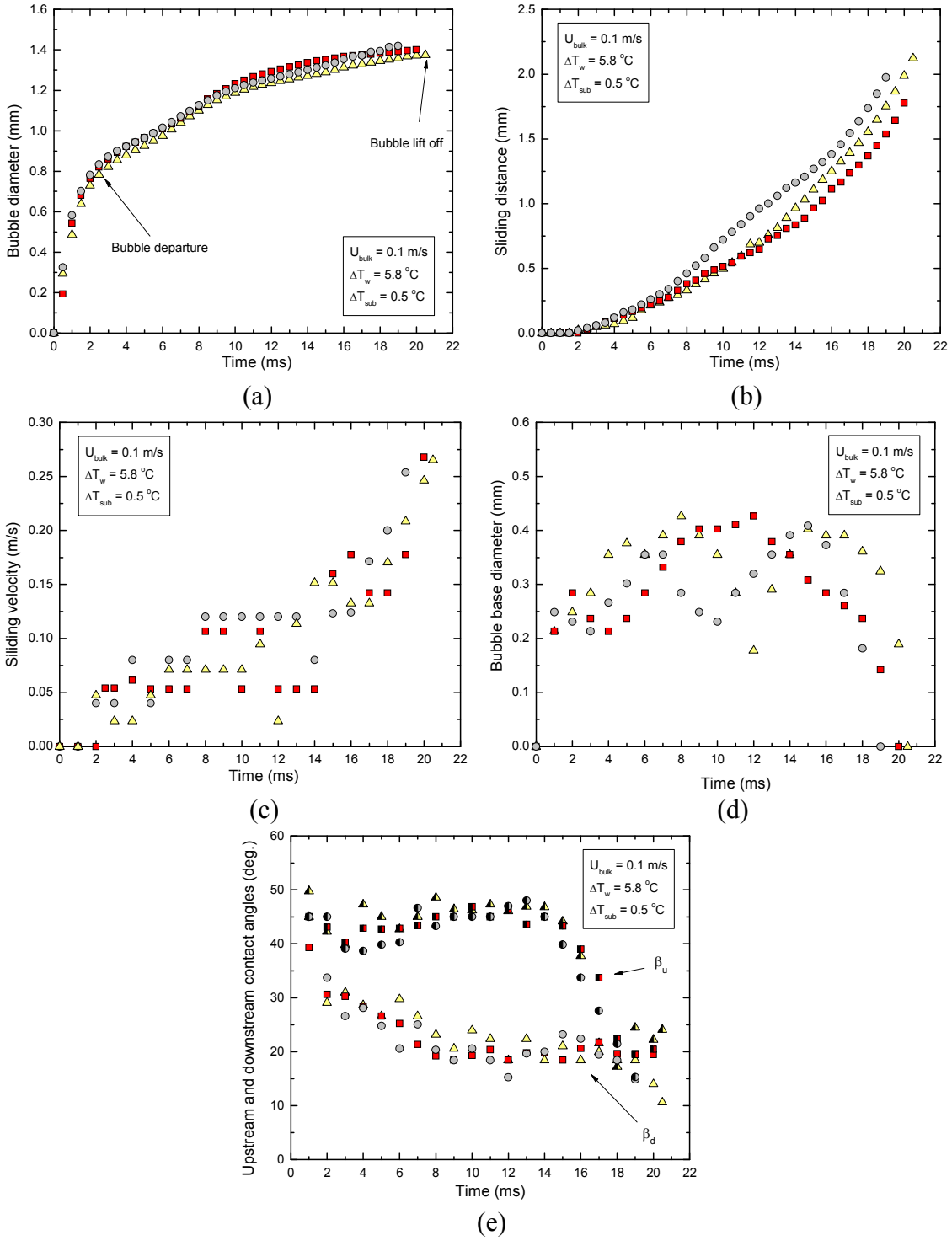

Measured quantities for 60^o inclined aluminum surface: (a) bubble diameter, (b) sliding distance, (c) sliding velocity, (d) bubble base diameter and (e) upstream and downstream contact angles, for U_{bulk} = 0.1 m/s, ΔT_w = 5.8 ^{o}C, and ΔT_{sub} = 0.5 ^{o}C.

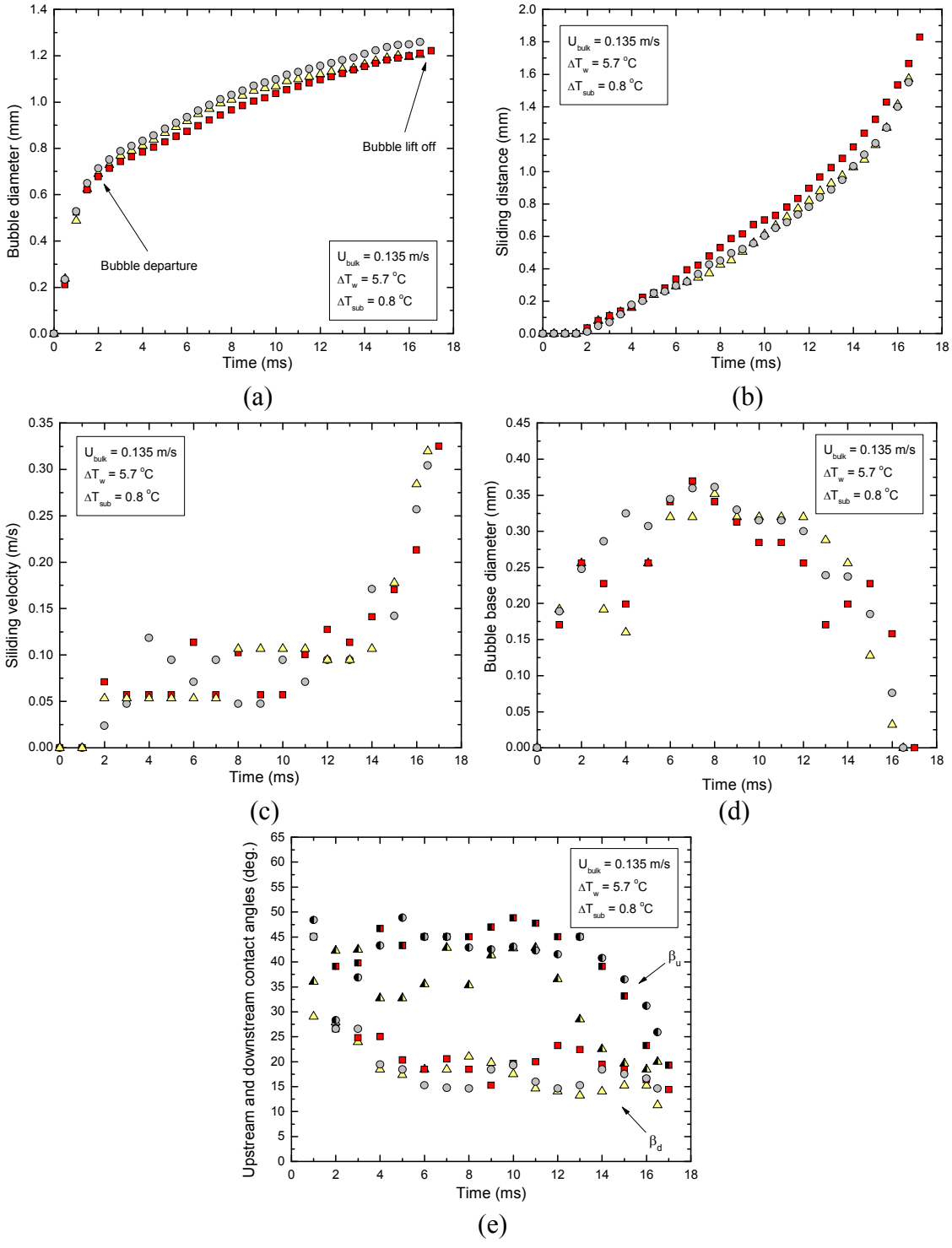

Measured quantities for 60^{o} inclined aluminum surface: (a) bubble diameter, (b) sliding distance, (c) sliding velocity, (d) bubble base diameter and (e) upstream and downstream contact angles, for U_{bulk} = 0.135 m/s, ΔT_w = 5.7 ^{o}C, and ΔT_{sub} = 0.8 ^{o}C.

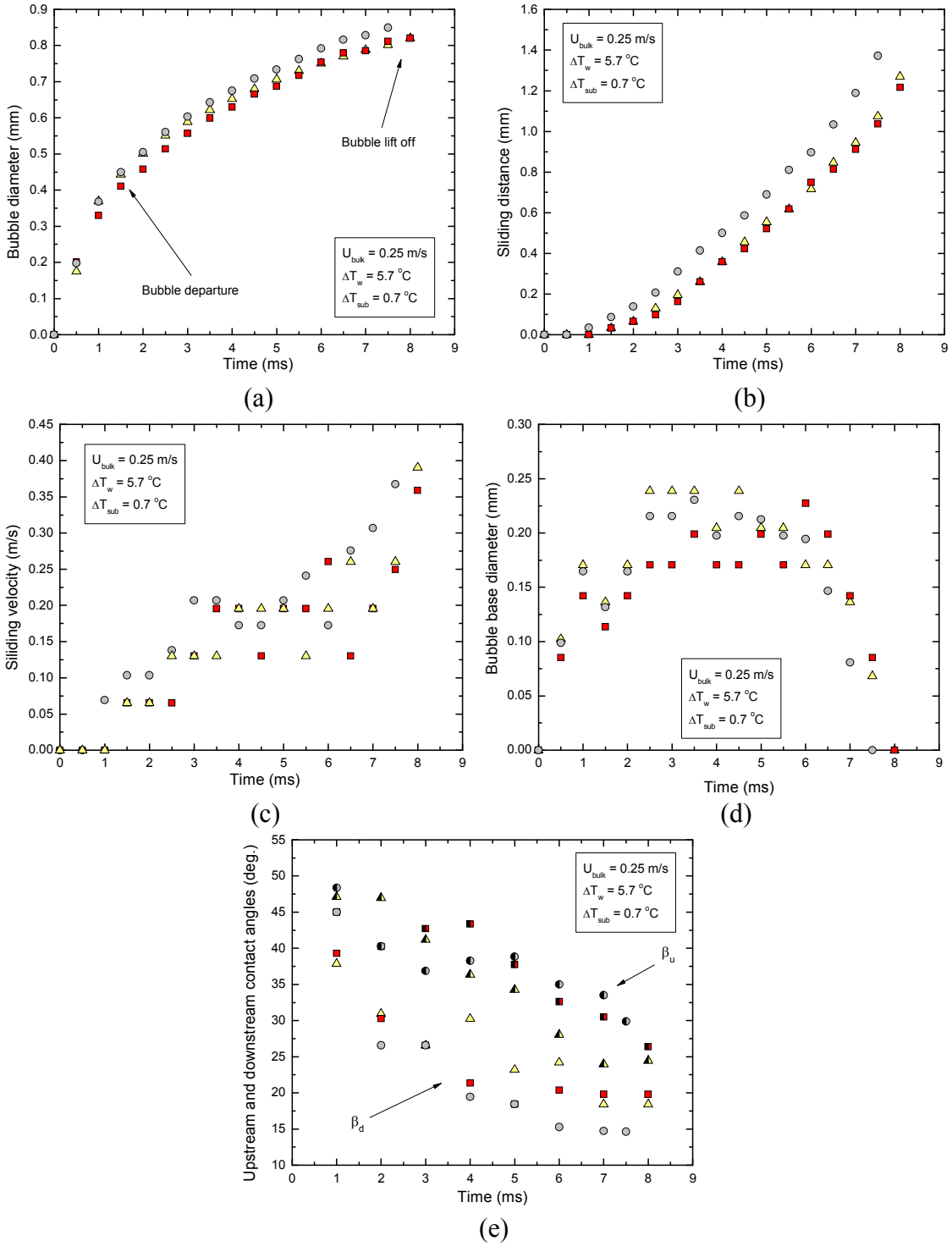

Measured quantities for 60^{o} inclined aluminum surface: (a) bubble diameter, (b) sliding distance, (c) sliding velocity, (d) bubble base diameter and (e) upstream and downstream contact angles, for U_{bulk} = 0.25 m/s, ΔT_w = 5.7 ^{o}C, and ΔT_{sub} = 0.7 ^{o}C.

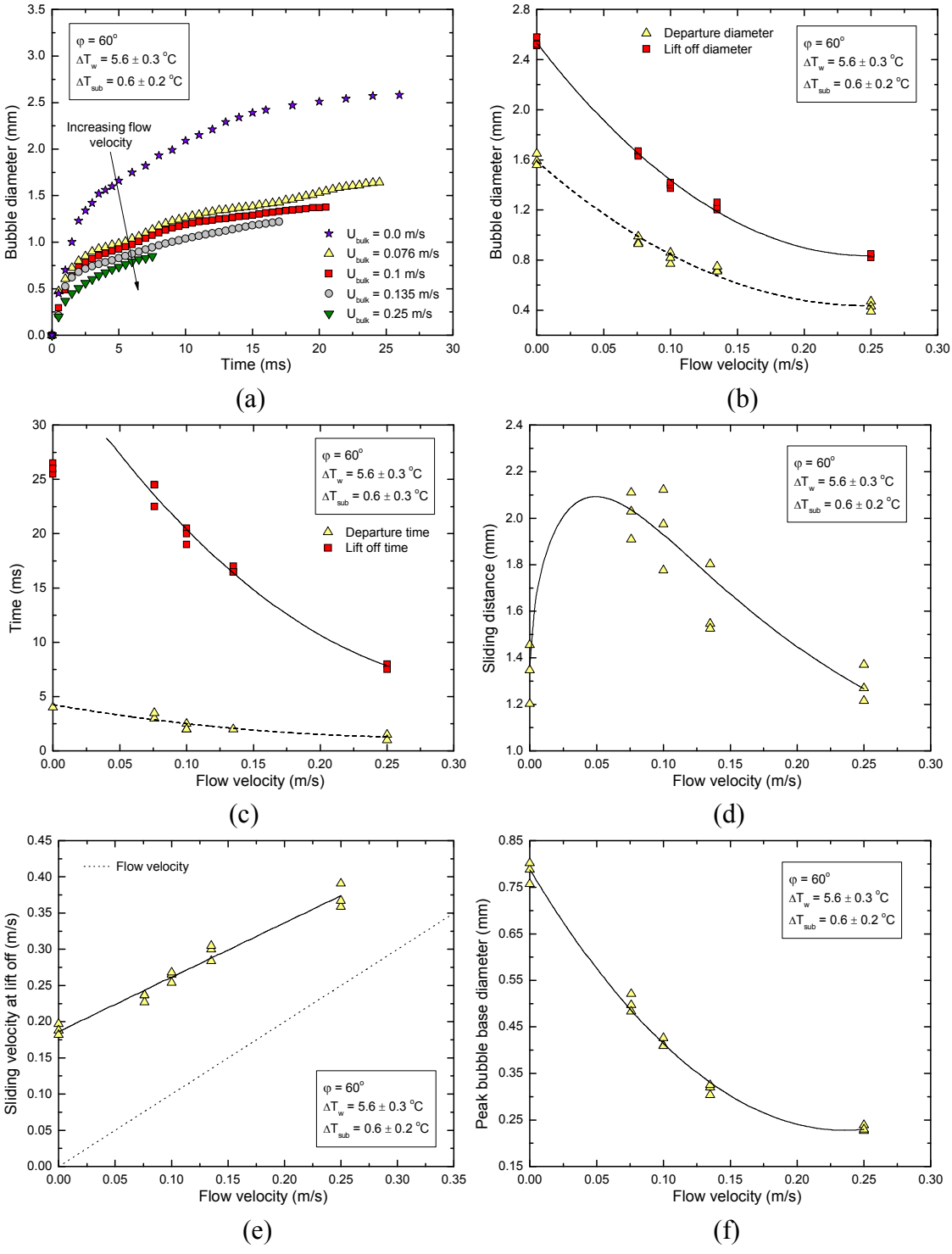

Effect of liquid bulk velocity on (a) variation of bubble diameter with time, (b) bubble departure and lift off diameters, (c) departure and lift off times, (d) sliding distance, (e) sliding velocity at lift off and (f) peak bubble base diameter – 60^{o} inclined aluminum surface.

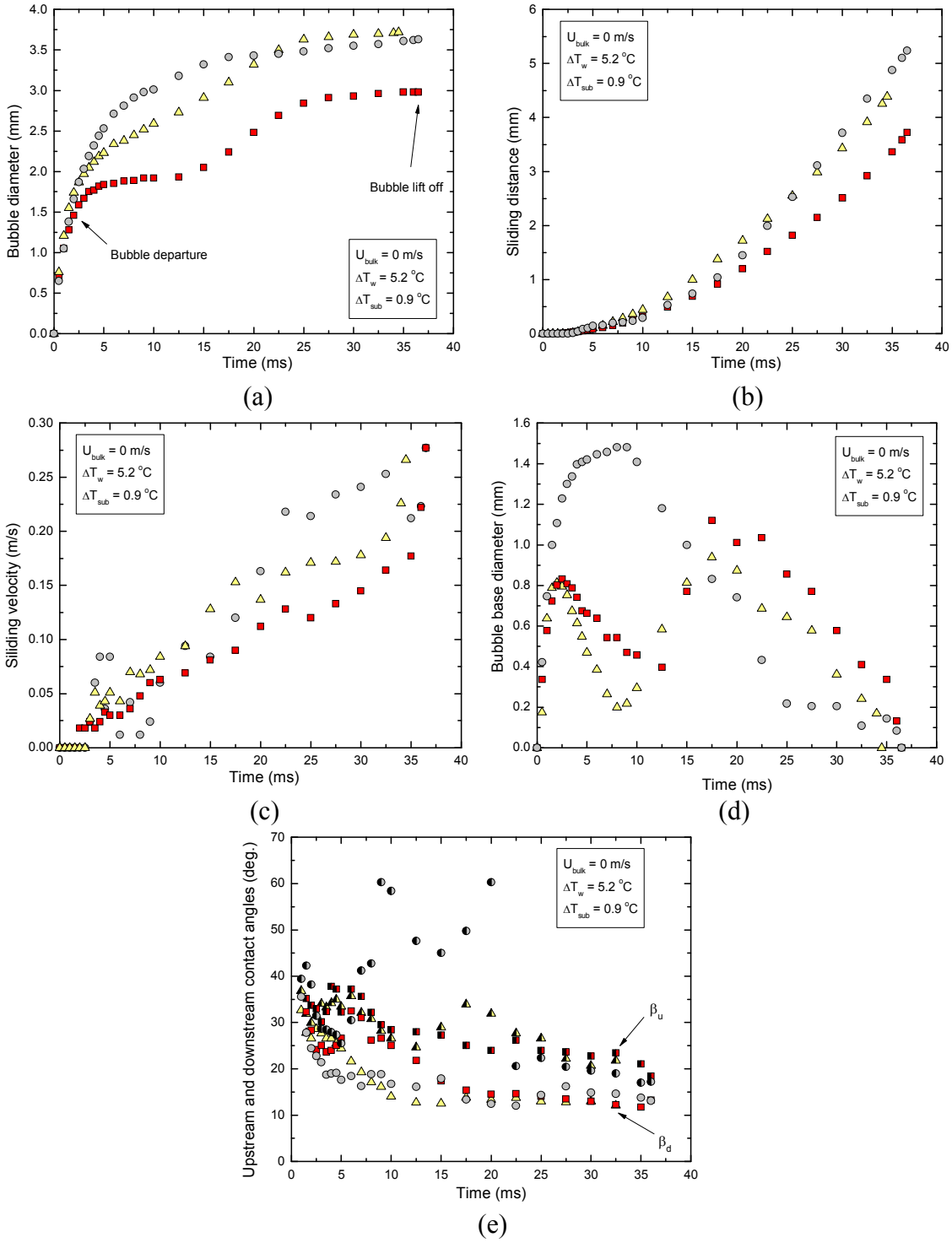

Measured quantities for vertical aluminum surface: (a) bubble diameter, (b) sliding distance, (c) sliding velocity, (d) bubble base diameter and (e) upstream and downstream contact angles, for U_{bulk} = 0 m/s, ΔT_w = 5.2 °C, and ΔT_{sub} = 0.9 °C.

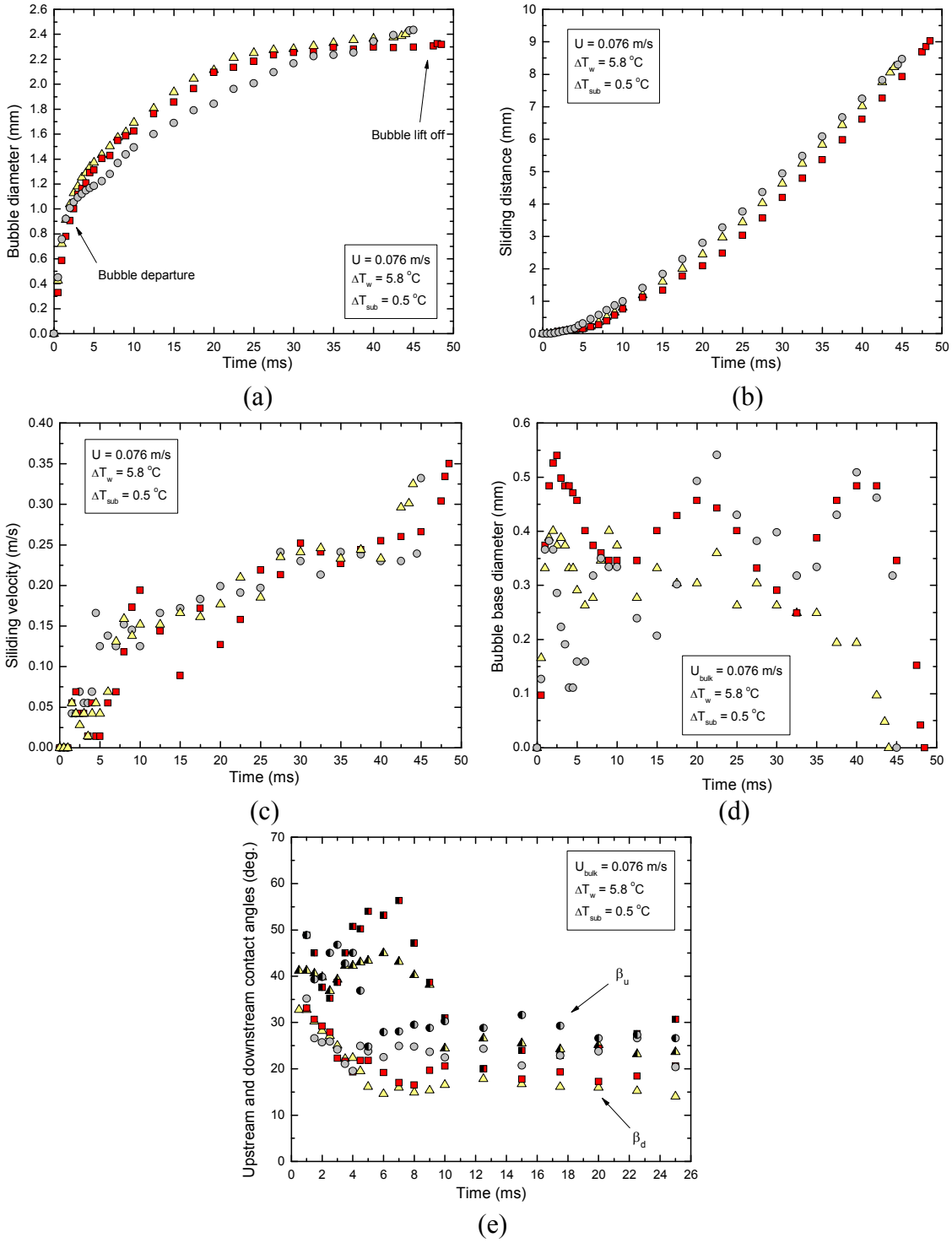

Measured quantities for vertical aluminum surface: (a) bubble diameter, (b) sliding distance, (c) sliding velocity, (d) bubble base diameter and (e) upstream and downstream contact angles, for U_{bulk} = 0.076 m/s, ΔT_w = 5.8 °C, and ΔT_{sub} = 0.5 °C.

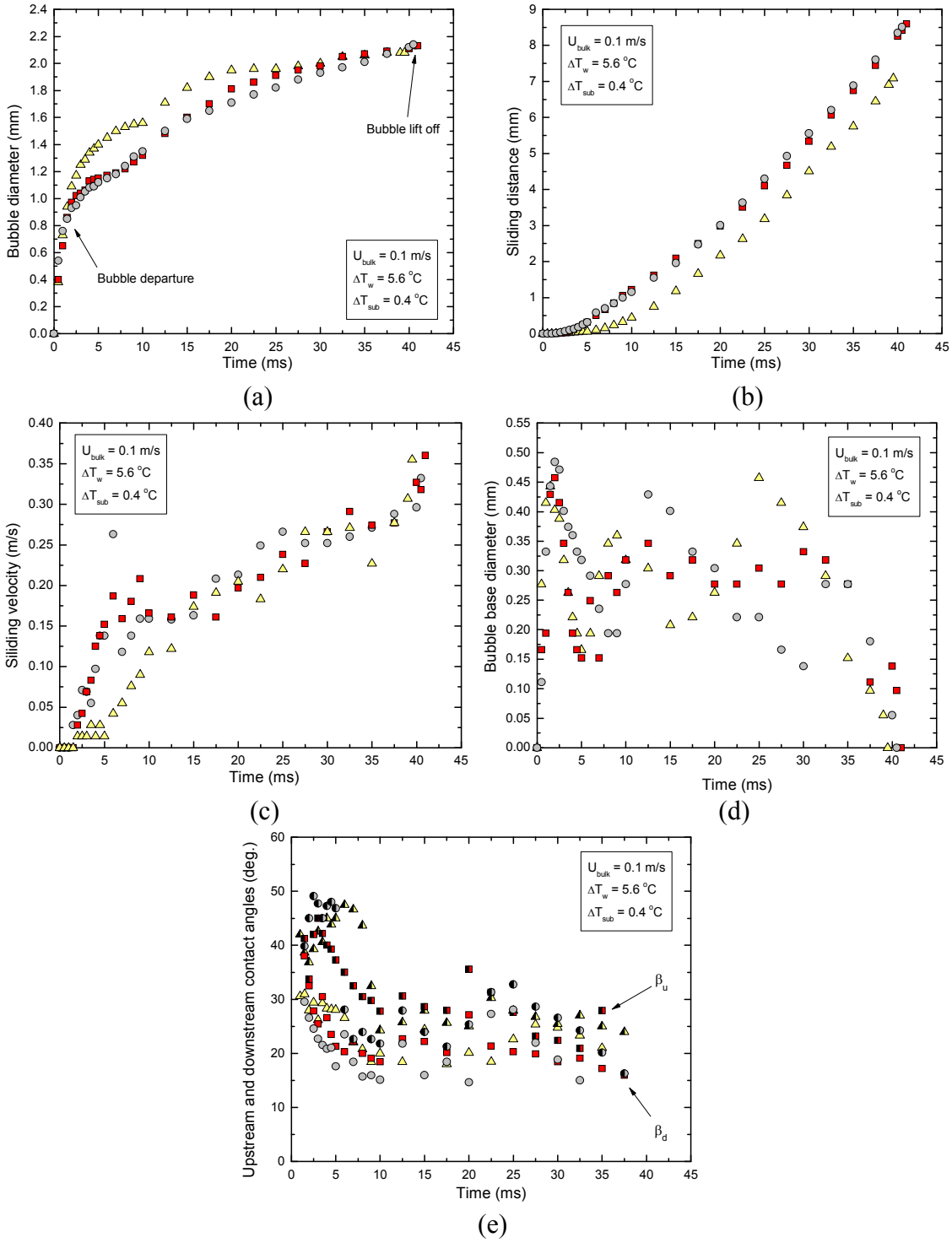

Measured quantities for vertical aluminum surface: (a) bubble diameter, (b) sliding distance, (c) sliding velocity, (d) bubble base diameter and (e) upstream and downstream contact angles, for U_{bulk} = 0.1 m/s, ΔT_w = 5.6 °C, and ΔT_{sub} = 0.4 °C.

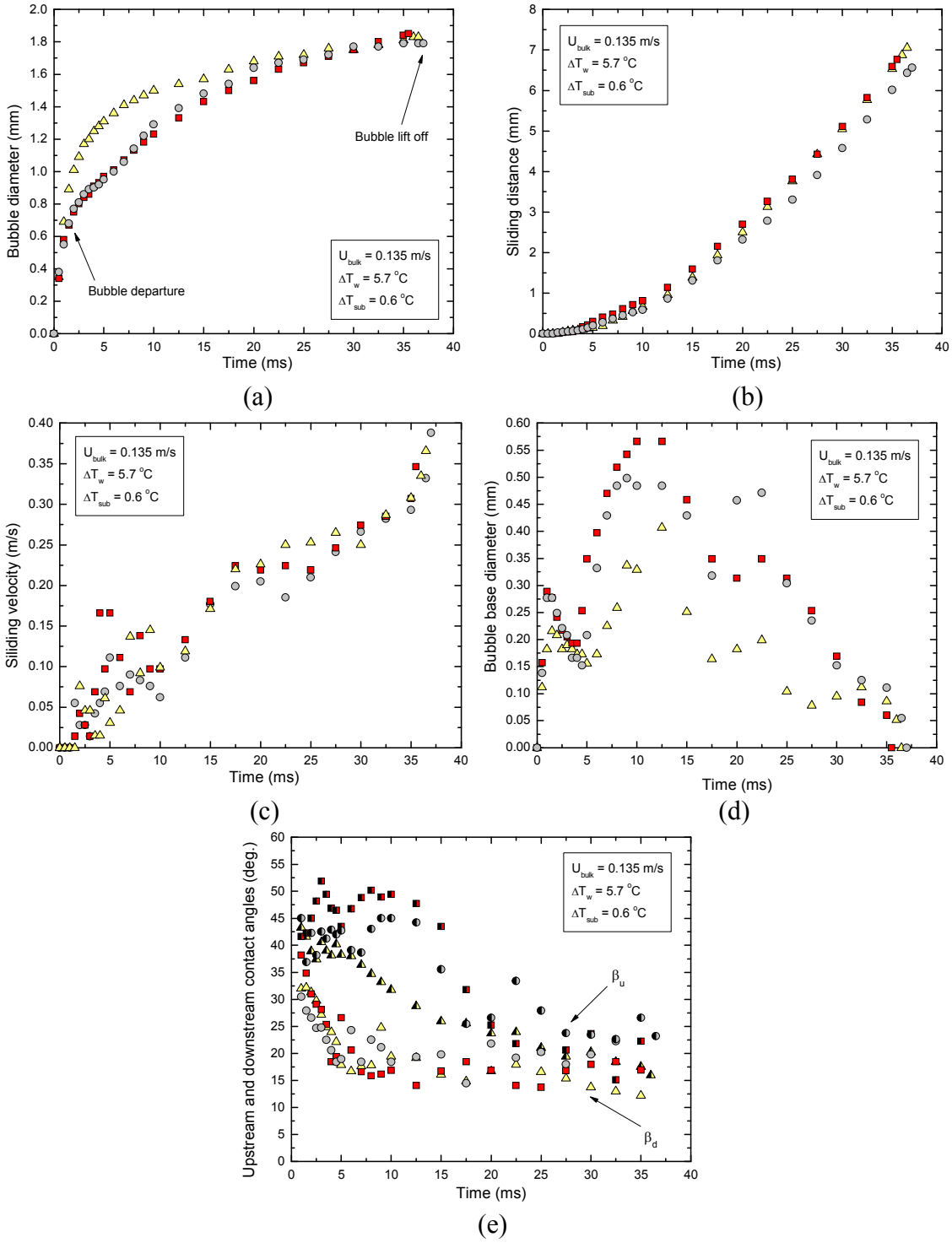

Measured quantities for vertical aluminum surface: (a) bubble diameter, (b) sliding distance, (c) sliding velocity, (d) bubble base diameter and (e) upstream and downstream contact angles, for U_{bulk} = 0.135 m/s, ΔT_w = 5.7 °C, and ΔT_{sub} = 0.6 °C.

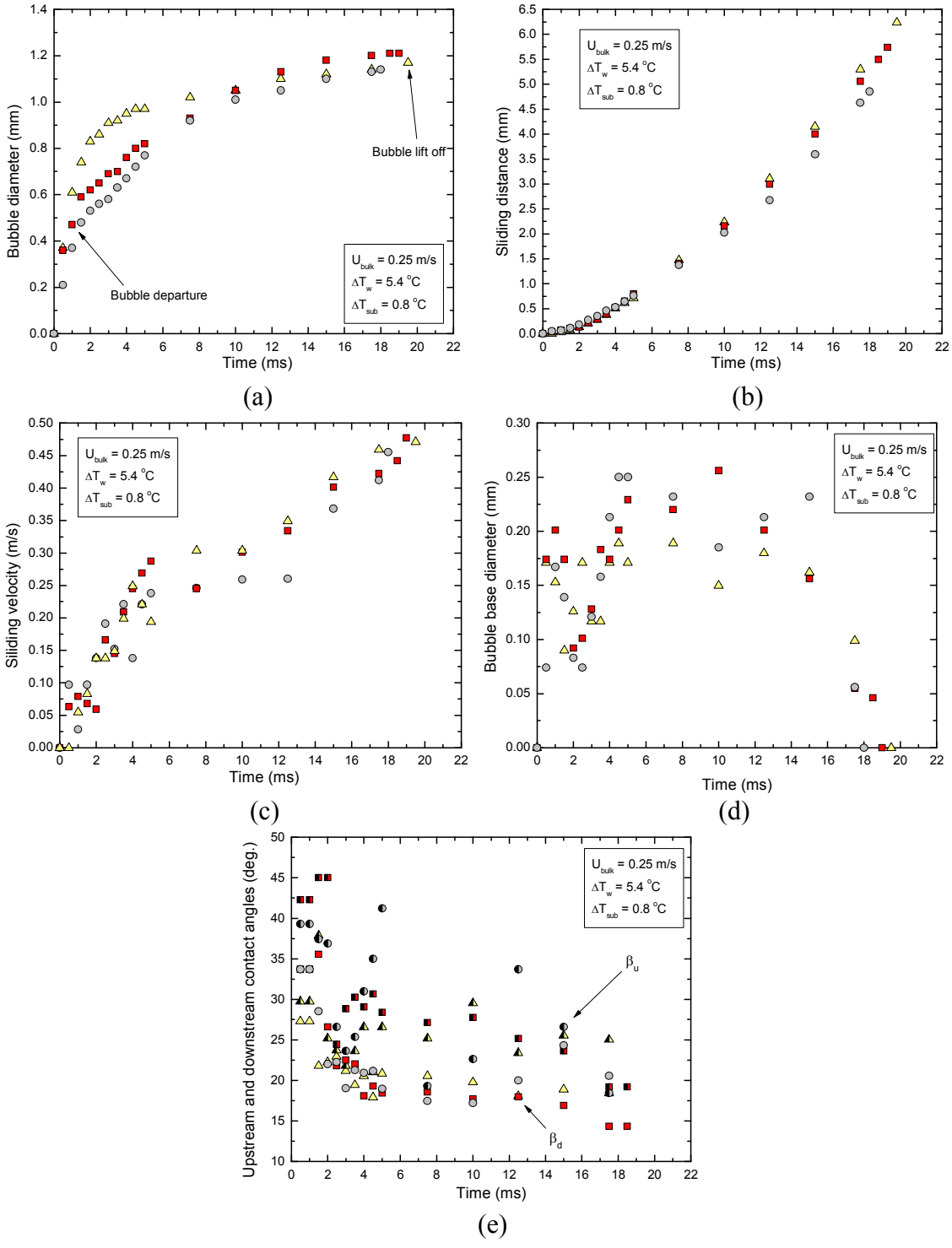

Measured quantities for vertical aluminum surface: (a) bubble diameter, (b) sliding distance, (c) sliding velocity, (d) bubble base diameter and (e) upstream and downstream contact angles, for U_{bulk} = 0.25 m/s, ΔT_w = 5.4 °C, and ΔT_{sub} = 0.8 °C.

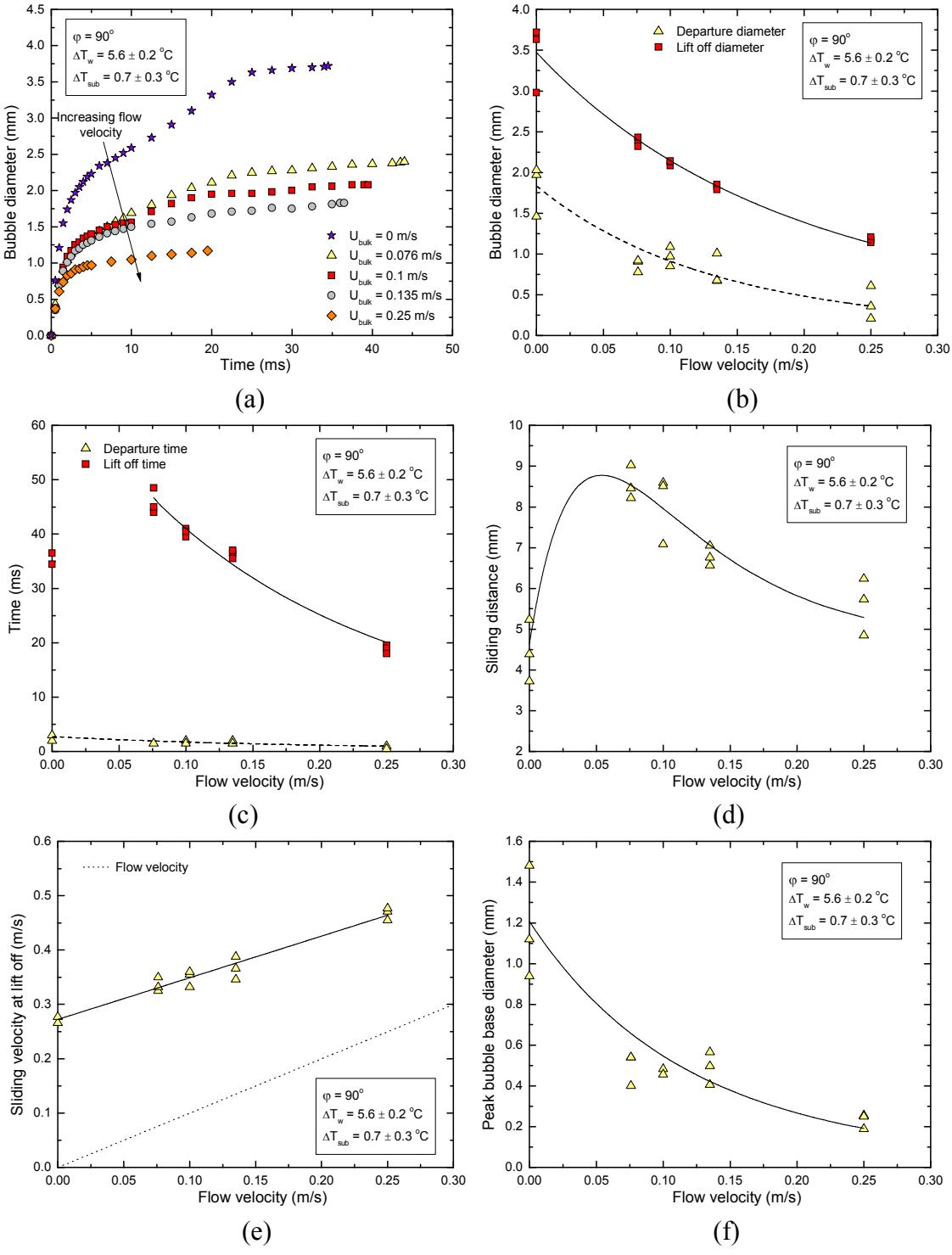

Effect of liquid bulk velocity on (a) variation of bubble diameter with time, (b) bubble departure and lift off diameters, (c) departure and lift off times, (d) sliding distance, (e) sliding velocity at lift off and (f) peak bubble base diameter – Vertical aluminum surface.

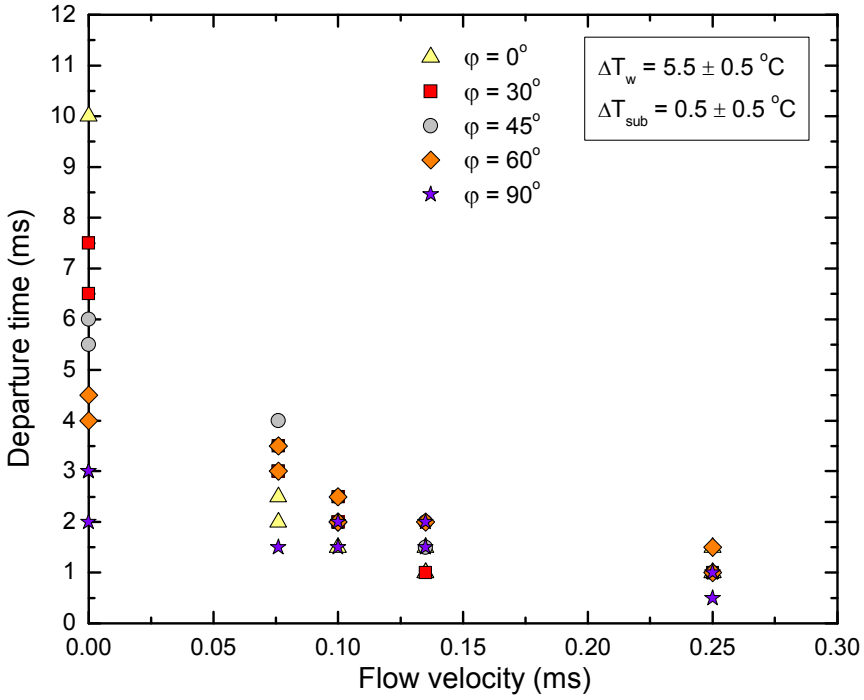

(a)

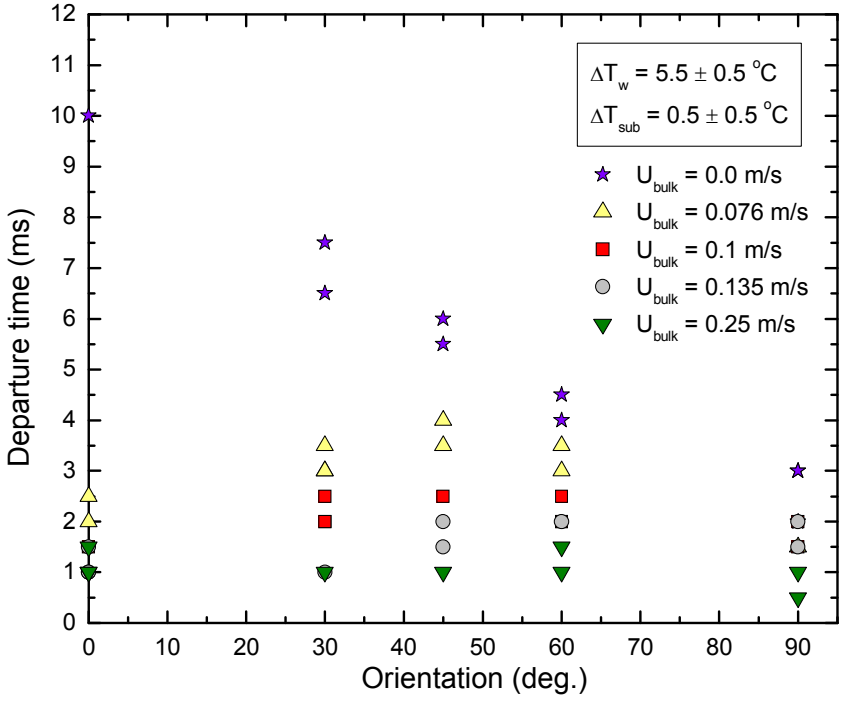

(b)

Effect of: (a) liquid bulk velocity and (b) orientation, on departure time – Aluminum surface.

REFERENCES

Abdelmessih, A. H., Hooper, F. C., and Nangia, S., 1972, "Flow Effects on Bubble Growth and Collapse in Surface Boiling," International Journal of Heat and Mass Transfer, vol. 15, pp. 115–125.

Ahmadi, R., Ueno, T., and Okawa, T., 2012, "Bubble Dynamics at Boiling Incipience in Subcooled Upward Flow Boiling," International Journal of Heat and Mass Transfer, vol. 55, Issues 1-3, pp 488–497.

Akiyama, M., and Tachibana, F., 1974, "Motion of Vapor Bubbles in Subcooled Heated Channel," Bulletin of the JSME, vol. 17, no. 104, pp. 241–247.

Al-Hayes, R. A. M., and Winterton, R. H. S., 1981, "Bubble Diameter on Detachment in Flowing Liquids," International Journal of Heat and Mass Transfer, vol. 24, pp. 223-230.

Auton, T. R., 1987, "The Lift Force on a Spherical Body in a Rotational Flow," Journal of Fluid Mechanics, vol. 183, pp. 199–218.

Auton, T. R., Hunt, J. C. R., and Prud'Homme, M., 1998, "The Force Exerted on a Body in Inviscid Unsteady Non-Uniform Rotational Flow," Journal of Fluid Mechanics, vol. 197, pp. 241–257.

Bankoff, S. G., 1958, "Entrapment of Gas in the Spreading of Liquid Over a Rough Surface," AIChE Journal, vol. 4, pp. 24–26.

Basu, N., 2003, Modeling and Experiments for Wall Heat Flux Partitioning during Subcooled Flow Boiling of Water at Low Pressures. Ph. D. thesis, University of California, Los Angeles.

Basu, N., Warrier, G.R., and Dhir, V.K., 2002, "Onset of Nucleate Boiling and Active Nucleation Site Density during Subcooled Flow Boiling," Journal of Heat Transfer, vol. 124, pp. 717–728.

Bergles, A. E., and Rohsenhow, W. M., 1964, "The Determination of Forced-Convection Surface –Boiling Heat Transfer," Journal of Heat Transfer, pp. 365–372.

Bibeau, E. L., and Salcudean, M., 1994, "A Study of Bubble Ebullition in Forced-Convective Subcooled Nucleate Boiling at Low Pressure," International Journal of Heat and Mass Transfer, vol. 37, no. 15, pp. 2245–2259.

Cooper, M.G., Mori, K., and Stone, C.R., 1983, "Behaviour of Vapour Bubbles Growing at a Wall with Forced Flow," International Journal of Heat and Mass Transfer, vol.26, no.10, pp.1489–1507.

Cornwell, K., 1977, “Naturally Formed Boiling Site Cavities,” Letters of Heat and Mass Transfer, vol. 4, pp. 63–72.

Davidson, J.F., and Schüler, B.O.G., 1960, “Bubble Formation at an Orifice in a Viscous Liquid,” Transactions of the Institution of Chemical Engineers, vol. 38, pp. 144–154.

Davis, E. J., and Anderson, G. H., 1966, “The Incipience of Nucleate Boiling in Forced Convective Flow,” AIChE Journal, pp. 774–780.

Donnelly, B., O’Donovan, T. S., and Murray, D. B., 2009, “Surface Heat Transfer Due to Sliding Bubble Motion,” Applied Thermal Engineering, vol. 29, no. 7, pp. 1319–1326.

Duhar, G., Riboux, G., and Colin, C., 2009, “Vapour Bubble Growth and Detachment at the Wall of Shear flow,” International Journal of Heat and Mass Transfer Heat Mass Transfer, vol. 45, no. 7, pp. 847–855.

Fritz W., 1935, “Maximum Volume of Vapor Bubbles,” Physik Zeitschr, vol. 36, pp. 379–384.

Gunther, F. C., 1951, “Photographic Study of Surface-Boiling Heat Transfer to Water with Forced Convection,” Transactions of the ASME, vol. 73, pp. 115–123.

Han, Y.Y., and Griffith, P., 1965, “The Mechanism of Heat Transfer in Nucleate Pool Boiling. I – Bubble Initiation, Growth and Departure,” International Journal of Heat Mass Transfer, vol. 8, pp. 887–904.

Hibiki, T., and Ishii, M., 2007, “Lift Force in Bubbly Flow Systems,” Chemical Engineering Science, vol. 62, pp. 6457–6474.

Hsu, Y., 1962, “On the Size Range of Active Nucleation Sites on a Heating Surface,” Journal of Heat Transfer, vol. 84, pp. 207–216.

Jia, W., and Dhir, V. K., 2004, “Dynamics of Contact Angle During Growth and Lift Off of Bubbles at a Single Nucleation Site in Flow Boiling”, ASME 2004 International Mechanical Engineering Congress and Exposition (IMECE2004), paper number IMECE2004-60374.

Kandlikar, S. G., Mizo, V., Cartwright, M., and Ikenze, E., 1997, “Bubble Nucleation and Growth Characteristics in Subcooled Flow Boiling of Water,” HTD vol. 342, ASME National Heat Transfer Conference, vol. 4, pp. 11–18.

Kandlikar, S. G., and Stumm, B. J., 1995, “A Control Volume Approach for Investigating Forces on a Departing Bubble Under Subcooled Flow Boiling,” Journal of Heat Transfer, vol. 117, pp. 990–997.

Kirk, K. M., Merte Jr., H., and Keller, R., 1995, "Low-Velocity Subcooled Nucleate Flow Boiling at Various Orientations," Journal of Heat Transfer, vol. 11, pp. 380–386.

Klausner, J. F., Mei, R., Bernhard, D. M., and Zeng, L. Z., 1993, "Vapor Bubble Departure in Forced Convection Boiling," International Journal of Heat and Mass Transfer, vol. 36, no. 3, pp. 651–662.

Klausner, J. F., and Zeng, L. Z., 1993, "Bubble Departure in Pool and Flow Boiling Systems: A Review and Latest Developments," ASME/JSME Nuclear Engineering Conference.

Kline, S. J., and McClintock, F. A., 1953, "Describing Uncertainties in Single Sample of Experiments," Mechanical Engineering, vol. 75, pp. 3–8.

Koumoutsos, N., Moissis, R., and Spyridonos, A., 1968, "A Study of Bubble Departure in Forced-Convection Boiling," Journal of Heat Transfer, vol. 90, pp. 223–230.

Li, D., 2005, Numerical Study of Single Bubble Dynamics during Flow Boiling. Ph. D. thesis, University of California, Los Angeles.

Ma, Y, Chung, J. N., 2001, "An Experimental Study of Critical Heat Flux (CHF) in Microgravity Forced-Convection Boiling," International Journal of Multiphase Flow, vol. 27, no. 10, pp.1753–1767

Maity, S., 2000, Effect of Velocity and Gravity on Bubble Dynamics. MS thesis, University of California, Los Angeles.

Mukherjee, A., 2004, Numerical and Experimental Study of Lateral Merger of Vapor Bubbles Formed on a Horizontal Surface during Nucleate Pool Boiling. Ph. D. thesis, University of California, Los Angeles.

Mei, R., and Klausner, J.F., 1994, "Shear Lift Force on Spherical Bubbles," Int. J. Heat Fluid Flow, vol. 15, pp. 62–65.

Montout, M., 2009, Contribution au Développement d'une Approche Prédictive Locale de la Crise d'Ebullition. PhD thesis, Institut National Polytechnique de Toulouse, Toulouse, France.

Naciri, M.A., 1992, Contribution à l'Etude des Forces Exercées par un Liquide sur une Bulle de Gaz: Portance, Masse Ajoutée. Ph.D. thesis, Ecole Centrale de Lyon, Lyon, France.

Patankar, N. A., Huang, P. Y., Ko, T., and Joseph, D. D., 2001, "Lift-Off of a Single Particle in Newtonian and Viscoelastic Fluids by Direct Numerical Simulation," Journal of Fluid Mechanics, vol. 438, pp. 67–100.

Petukhov, B. S., 1970, "Heat Transfer and Friction in Turbulent Pipe Flow with Variable Properties," Advances in Heat Transfer, vol. 6, pp. 503–564.

Qiu, D.M., Dhir, V.K., Chao, D., Hasan, M.M., Neumann, E., Yee, G., and Birchenough, A., 2002, "Single Bubble Dynamics during Pool Boiling under Low Gravity Conditions," Journal of Thermophysics and Heat Transfer, vol. 16, No. 3, pp. 336–445.

Qiu, D. and Van der Geld, C. W. M., 1997, "Bubble Shapes and Forces at Detachment," Proceedings of International Engineering Foundation Conference on Convective Flow and Pool Boiling, Irsee, Germany.

Ramanujapu, N., and Dhir, V. K., 1999, "Dynamics of Contact Angle During Growth and Departure of a Vapor Bubble at a Single Nucleation Site," Proceedings of 5th ASME/JSME Joint Thermal Engineering Conference, San Diego.

Reichardt, H., 1951, "Vollstandige Darstellung der Turbulenten Geschwindigkeitsverteilung in Glatten Leitungen," Zeitschrift fur Angewandte Mathematik und Mechanik, vol. 31, no. 7, pp. 208–219.

Situ, R., Hibiki, T., Ishii, M., and Mori, M., 2005, "Bubble Lift-Off Size in Forced Convective Subcooled Boiling Flow," International Journal of Heat and Mass Transfer, vol. 48, Issues 25–26, pp. 5536–5548.

Situ, R., Mi, Y., Ishii, M., and Mori, M., 2004, "Photographic Study of Bubble Behaviors in Forced Convection Subcooled Boiling," Int. J. Heat Mass Transfer, vol. 47, pp. 3659–3667.

Sato, T., and Matsumura, H., 1964, "On the Conditions of Incipient Subcooled-Boiling with Forced Convection," Bulletin of JSME, Vol. 7, No. 26, pp. 392–398.

Son, G., Dhir, V. K., and Ramanujapu, N., 1999, "Dynamics and Heat Transfer Associated with a Single Bubble During Nucleate Boiling on a Horizontal Surface," Journal of Heat Transfer, vol. 121, pp. 623–631.

Thorncroft, G. E., and Klausner, J. F., 1999, "The Influence of Vapor Bubble Sliding on Forced Convection Boiling Heat Transfer," Journal of Heat Transfer, vol. 121, pp. 73–79.

Thorncroft, G. E., Klausner, J. F., and Mei, R., 1998, "An Experimental Investigation of Bubble Growth and Detachment in Vertical Upflow and Downflow Boiling," International Journal of Heat and Mass Transfer, vol. 41, pp. 3857–3871.

Thorncroft, G.E., Klausner, J.F., and Mei, R., 2001, "Bubble forces and detachment models," Multiphase Science and Technology, vol. 13, pp. 35–76.

Chung, G., and Bankoff, S. G., 1990, "On the Mechanism of Forced-Convection Subcooled Nucleate Boiling," Journal of Heat Transfer, vol. 112, pp. 213–218.

Van der Geld, C. W. M.,Colin, C., Segers, Q. I. E., Pereira da Rosa, V. H., and Yoshikawa, H. N., 2012, "Forces on a Boiling Bubble in a Developing Boundary Layer, in Microgravity with G-Jitter and in Terrestrial Conditions," Physics of Fluids, vol. 24, paper number 082104.

Van Helden, W. G. J., Van der Geld, C. W. M., and Boot, P. G. M., 1995, "Forces on Bubble Growing and Detaching in Flow Along a Vertical Wall," International Journal of Heat and Mass Transfer, vol. 38, no. 11, pp. 2075–2088.

Wang, C. H., and Dhir, V. K., 1993, "On the Gas Entrapment and Nucleation Site Density during Pool Boiling of Saturated Water," Journal of Heat Transfer, Vol. 115, pp. 670–679.

Whitaker, S., 1972, "Forced Convection Heat Transfer Correlations for Flow in Pipes, Past Flat Plates, Single Cylinders, Single Spheres, and for Flow in Packed Beds," AIChE Journal, vol. 18, pp. 361–371.

Yoshikawa, H. N., and Colin, C., 2010, "Single Vapor Bubble Behavior in a Shear Flow in Microgravity," 7th International Conference on Multiphase Flow (ICMF 2010), Tampa, Fl.

Zeitoun, O., 1994, Subcooled Flow Boiling and Condensation, PhD thesis, McMaster University, Hamilton, Canada.

Zhu, M-Y., 2000, Direct numerical simulation of the solid-liquid flows of Newtonian and viscoelastic fluids. PhD thesis, University of Pennsylvania.